Atomic-Scale Control and Characterization of Oxide Heterostructures: Correlating Interfacial Structure and Novel Functionalities

MAX-PLANCK-GESELLSCHAFT

Max Planck Institute for Solid State Research

by

Y. EREN SUYOLCU

Approved dissertation to obtain the academic degree of Doctor of Natural Science

Technical University of Darmstadt (TUD) – D17

Darmstadt, 2018

This page intentionally left blank

Atomic-Scale Control and Characterization of Oxide Heterostructures: Correlating Interfacial Structure and Novel Functionalities

Dissertation submitted to the Department of Materials and Earth Sciences at Technische Universität Darmstadt

in Fulfillment of the Requirements for the Degree of Doctor of Natural Science (Dr. rer. nat.)

by

YUSUF EREN SUYOLCU

from Izmir, Turkey

Referee:	Prof. Dr. Peter A. van Aken
Co-referee:	Prof. Dr. Hans-Joachim Kleebe

Date of Submission:	13.11.2018
Date of Oral Examination:	17.12.2018

Darmstadt, 2018

Suyolcu, Yusuf Eren: Atomic-Scale Control and Characterization of Oxide Heterostructures: Correlating Interfacial Structure and Novel Functionalities

Darmstadt, Technische Universität Darmstadt

Publication Year of Dissertation at TUprints: 2019

URN: urn:nbn:de:tuda-tuprints- 89880

Date of Oral Examination: 17.12.2018

THESIS SUPERVISORS

Prof. Dr. Peter A. van Aken

Professor of Geo-Material Science
Max Planck Institute for Solid State Research
Stuttgart Center for Electron Microscopy (StEM)

Prof. Dr. Hans-Joachim Kleebe

Professor of Geo-Material Science
Geo- and Material Sciences Department
Technical University of Darmstadt

THESIS COMMITTEE

Prof. Dr. Peter A. van Aken

Referee
Professor of Geo-Material Science
Geo- and Material Sciences Department
Technical University of Darmstadt

Prof. Dr. Hans-Joachim Kleebe

Co-referee
Professor of Geo-Material Science
Geo- and Material Sciences Department
Technical University of Darmstadt

Prof. Dr. Lambert Alff

Examiner
Professor of Materials Science
Materials Science Department
Technical University of Darmstadt

Prof. Dr. Christoph T. Koch

Examiner
Professor of Physics
Physics Department
Humboldt University of Berlin

This page intentionally left blank

To my family…

This page intentionally left blank

Contents

Abstract

Complex oxide materials providing numerous physical properties can be fabricated in different forms, for instance in thin films or heterostructures, due to their highly adaptable crystal structures. In the last decade, the heterostructures of complex oxides have been in high-demand due to their large number of impressive functionalities, which do not exist in their bulk forms but emerge at the interfaces. Recent technical improvements of epitaxial growth techniques enable fabricating high-quality oxide heterostructures, where the phenomena occurring at their interfaces can be tailored depending on the choice of the constituents. However, the key factor dominating the interface functionalities is the control of the interface sharpness.

Prominent combination of state-of-the-art atomic-layer-by-layer molecular beam epitaxy (ALL oxide-MBE) and aberration-corrected scanning transmission electron microscopy (STEM) is utilized in the thesis, for the atomic-layer-precise synthesis and atomic-resolution characterization of the heterostructures, respectively. Atomically-resolved STEM imaging [i.e. high-angle annular dark-field (HAADF), annular bright field (ABF)] and spectroscopy [i.e. electron energy loss spectroscopy (EELS) and energy dispersive X-ray spectroscopy (EDXS)] techniques are combined with dedicated conductivity measurements as well as atomic force microscopy and X-ray diffraction. Using these results, the local structure, octahedral distortions, and chemical properties are correlated with the functionalities of the systems. For the STEM data analysis, "Oxygen-octahedra picker tool" and "STEM-SI Warp" software tools are used in order to quantify and to post-correct the (spectrum) images, respectively.

Complex functional oxide heterostructures consisting of iso-structural or hetero-structural contacts – mainly based on La_2CuO_4 and its derivatives – are concerned with the aim of not only tailoring the novel interface properties, which are directly linked to the local structural and chemical properties but also identifying the interface sharpness.

First, $La_{1.6}A_{0.4}CuO_4$ / La_2CuO_4 bilayers composed of a metallic (M) and an insulating phase (I), where A represents a divalent dopant (namely, Ba^{2+}, Sr^{2+}, and Ca^{2+}), are studied. After the growth optimization, detailed characterization of the structures – especially extensive STEM investigations – substantiated the importance of the elemental distribution at the interfaces: Despite the perfect epitaxial growth, the dopants were found to be inhomogeneously distributed depending on the dopant size. This distribution defines whether the final superconducting properties emerge due to the striking "interface effect" or due to "classical" homogeneous doping. Moreover, a clear correlation between dopant size, dopant distribution and local lattice deformations is underlined suggesting a relationship between the nature of superconductivity (interface vs bulk) and Jahn–Teller distortions of the anionic sublattice.

The second example of homoepitaxial (i.e. iso-structural) systems considered in this work is two-dimensionally-doped (i.e. δ-doped) La_2CuO_4 superlattices, where specified La–O atomic layers in the La_2CuO_4 crystal structure are substituted with A–O layers, in which A is an acceptor dopant (A = Ba^{2+}, Sr^{2+}, Ca^{2+}). STEM-EELS analyses substantiated that despite the differences on the cation redistribution lengths, δ-doping results in asymmetric dopant distribution profiles at the interfaces. Such distribution is correlated with a qualitative model based on thermodynamic considerations and growth kinetics: As far as the dopant redistribution mechanism is concerned, the main factor leading to intermixing in the substrate direction is thermal diffusion. On the other hand, the wider distribution in growth direction is a consequence of the high lateral mobility of the atoms, which triggers the

tendency to cationic intermixing at the surface. Moreover, the substrate temperature variation also affects the cationic distribution length, while the tensile strain induced by the substrate may influence the asymmetric profile.

Furthermore, the contacts of different materials, namely, lanthanum cuprate and lanthanum nickelate systems, are studied. High-temperature superconductivity at the interface of lanthanum cuprate (La_2CuO_4, 214-phase) and strontium (Sr)-doped lanthanum nickelate ($La_{2-x}Sr_xNiO_4$, 214-phase) heterostructures, and high-temperature thermoelectricity of lanthanum cuprate (La_2CuO_4, 214-phase) and lanthanum nickelate ($LaNiO_3$, 113-phase) heterostructures are reported. For the former, i.e. $La_2CuO_4/La_{2-x}Sr_xNiO_4$ contacts, the ability to tune the superconducting properties simply by changing the structural parameters is presented. More importantly, STEM techniques combined with dedicated conductivity measurements evidenced the decoupling between the electronic charge carrier and the cation (Sr) concentration profiles at the interface, which induces the formation of a hole accumulation layer dictating the final superconducting properties. This phenomenon is rationalized in the light of a generalized space-charge theory. As far as the $La_2CuO_4/LaNiO_3$ heterostructures are concerned, the variation of the individual layer thicknesses (with constant total film thickness) influences the physical properties: As the thickness of the individual layers is reduced, the electrical conductivity decreases and the sign of Seebeck coefficient changes.

Independent from the functionalities, the differences in chemical sharpness of lanthanum cuprate–lanthanum nickelate interfaces are further realized, although all the interfaces are structurally sharp: In the case of La_2CuO_4/La_{2-} La_2CuO_4, 214-phase $_xSr_xNiO_4/La_2CuO_4$ contacts, the La_2CuO_4–$La_{2-x}Sr_xNiO_4$ interface is sharper concerning the elemental intermixing, while the $La_{2-x}Sr_xNiO_4$–La_2CuO_4 interfaces exhibit a wider Sr distribution. On the other hand, the decrease of individual layer thickness in $La_2CuO_4/LaNiO_3$ multilayers results in strong intermixing while thicker cuprate–nickelate layers maintain sharper interfaces.

In the case of hetero-structural epitaxy of different materials (phases), e.g. superconducting–ferromagnetic $La_2CuO_4/LaMnO_3$ multilayers, substantial differences in cationic redistribution and the local octahedral network is observed. STEM investigations demonstrate that Sr redistribution in 113-$LaMnO_3$ and 214-La_2CuO_4 phases is different and this directly affects the sharpness of the interfaces. In particular, a stronger tendency of Sr segregation (in growth direction) in the 113-phase compared to the 214-phase is unveiled.

Moreover, detailed high-resolution STEM imaging and spectroscopy of PLD-grown $NdNiO_3$ epitaxial layers on [011]-oriented $NdGaO_3$ substrate experimentally show a structural re-orientation from the [011]-phase (α-phase) to the [101]-phase (β-phase), which could be understood within the framework of DFT+*U* calculations. The calculations further unveil enhanced NiO_6 octahedral breathing distortions for tensile strained α- and β-phases of $NdNiO_3$.

Zusammenfassung

Aufgrund ihrer flexiblen Kristallstrukturen können mit komplexen Oxiden Dünnschichten und Heterostrukturen mit sehr variablen physikalischen Eigenschaften, welche im Volumenmaterial nicht vorkommen, hergestellt werden. Dies hat im vergangenen Jahrzehnt zu einer beträchtlichen Forschungsaktivität geführt. Aufgrund technischer Entwicklungen können solche Oxid-Heterostrukturen inzwischen mit hoher Perfektion hergestellt werden. Dadurch wird es möglich, die Phänomene an den Grenzflächen gezielt zu kontrollieren. Hierbei kommt der Grenzflächenschärfe eine besondere Bedeutung zu.

In dieser Arbeit erfolgt die präzise Synthese mittels "atomic-layer-by-layer molecular beam epitaxy" (ALL oxide-MBE). Zur Analyse der Schichten kommt die aberrationskorrigierte Raster ("Scanning")-Transmissionselektronenmikroskopie (STEM) zum Einsatz. Diese erlaubt die Charakterisierung der Proben mit atomarer Auflösung. Für die Abbildung wird die "high-angle annular dark-field" (HAADF)-Technik sowie die "annular bright-field" (ABF)-Methode angewandt. Für die chemische Analyse kommen die Elektronen-Energieverlustspektroskopie (EELS) sowie die energiedispersive Röntgenanalyse (EDXS) zum Einsatz. Diese Messungen werden ergänzt durch Leitfähigkeitsmessungen, Röntgendiffraktometrie sowie Raster-Kraftmikroskopie. Mit all diesen Ergebnissen kann somit eine Korrelation zwischen der lokalen Struktur und Chemie und den funktionalen Eigenschaften der Systeme erarbeitet werden. Für die exakte Bestimmung der Geometrie der Metall-Sauerstoff-Oktaeder wurden die Programme "Oxygen-octahedra picker tool" und "STEM-SI Warp" verwendet. Die Messungen erfolgten an verschiedenen Systemen die im Folgenden beschrieben werden.

(i) Das $La_{1.6}A_{0.4}CuO_4/La_2CuO_4$-Schichtsystem, wobei $La_{1.6}A_{0.4}CuO_4$ metallisch ist und La_2CuO_4 ein Isolator. "A" steht für eines der divalenten Dotieratome Ba^{2+}, Sr^{2+} und Ca^{2+}. Nach Optimierung der Wachstumsbedingungen zeigten die STEM-Resultate die Wichtigkeit der Elementverteilung an der Grenzfläche auf. Denn trotz perfekten epitaktischen Wachstums zeigten die Dotieratome eine inhomogene Verteilung. Diese Verteilung bestimmt, ob die Schichten Grenzflächen-Supraleitung oder Volumen-Supraleitung zeigen. Es konnte eine eindeutige Korrelation zwischen Größe des Dotieratoms, der Verteilung der Dotieratome und der Geometrie der Metall-Sauerstoff-Oktaeder festgestellt werden. Dies deutet auf einen engen Zusammenhang zwischen dem Mechanismus der Supraleitung und Jahn–Teller-Verformung der Oktaeder hin.

(ii) In zweidimensional dotiertem La_2CuO_4 wurden einzelne La–O-Atomlagen durch A–O-Atomlagen ersetzt, wobei "A" wiederum für eines der Ionen Ba^{2+}, Sr^{2+}, Ca^{2+} steht. Mit Hilfe von STEM-EELS konnte gezeigt werden, dass die Dotierprofile asymmetrisch verbreitert sind. Dies wird mit einem qualitativen thermodynamischen Modell der Wachstumskinetik beschrieben: *Entgegen* der Wachstumsrichtung führt thermische Diffusion zu einer Umverteilung der Dotieratome, *in* Wachstumsrichtung begünstigt die hohe laterale Beweglichkeit der Oberflächenatome eine Vermischung mit anderen Atomschichten. Darüber hinaus spielt die Substrattemperatur sowie die durch das Substrat bedingte Zugspannung eine Rolle.

(iii) Es wurden zum einen Grenzflächen zwischen Lanthankuprat (214-Phase) und Sr-dotiertem Lanthannickelat ($La_2CuO_4/La_{2-x}Sr_xNiO_4$) untersucht welche Supraleitung zeigen. Zum anderen Grenzflächen zwischen Lanthankuprat (214-Phase) und Lanthannickelat (113-Phase) ($La_2CuO_4/LaNiO_3$), bei denen Thermoelektrizität nachgewiesen wurde. Für erstere wird gezeigt, dass

die Supraleitung durch Änderung der strukturellen Parameter variiert werden kann. Mit der Kombination aus STEM und Leitfähigkeitsmessungen wird gezeigt, dass elektrische Ladungsträger von Sr-Dotieratomen entkoppelt auftreten. Dies wird mittels der verallgemeinerten Raumladungstheorie erklärt. Für letztere wird gezeigt, dass die physikalischen Eigenschaften von der Dicke der Schichten abhängt: Mit abnehmender Schichtdicke sinkt die elektrische Leitfähigkeit und der Seebeck-Koeffizienten ändert sein Vorzeichen.

(iv) Trotz struktureller Schärfe sind die Grenzflächen chemisch nicht scharf. So finden wir, dass im System $La_2CuO_4/La_{2-x}Sr_xNiO_4/La_2CuO_4$ die La_2CuO_4–$La_{2-x}Sr_xNiO_4$-Grenzfläche chemisch schärfer ist als die $La_{2-x}Sr_xNiO_4$–La_2CuO_4-Grenzfläche, welche eine verbreiterte Sr-Verteilung zeigt. Generell führt eine abnehmende Schichtdicke in $La_2CuO_4/LaNiO_3$-Vielfachschichten zu stärkerer chemischer Vermischung.

(v) Im Falle der Heteroepitaxie unterschiedlicher Materialien (Phasen), z.B. bei supraleitend/ferromagnetischen $La_2CuO_4/LaMnO_3$-Vielfachschichten, finden wir erhebliche Elementumverteilung und Störungen des Oktaedernetzwerks. Die Sr-Verteilung in 113-$LaMnO_3$ ist verschieden von der in 214-La_2CuO_4 was sich direckt auf die Schärfe der Grenzfläche auswirkt. Insbesondere neigt Sr (in Wachstumsrichtung) zu stärkerer Segregation in der 113-Phase als in der 214-Phase.

(vi) $NdNiO_3$-Schichten, welche mittels PLD epitaktisch auf [011]-orientiertes $NdGaO_3$ aufgewachsen wurden, zeigten eine strukturelle Umorientierung von der [011]-Phase (α-Phase) zur [101]-Phase (β-Phase). Das Auftreten der Umorientierung konnte mittels DFT+*U* Rechnungen verstanden werden. Die Rechnungen zeigten außerdem, dass die Gitterverzerrung der Atmungsmode der NiO_6- Oktaeder, in unter Zugspannung stehenden α- und β-Phasen von $NdNiO_3$, verstärkt auftritt.

Acknowledgements

At the beginning, I would like to acknowledge many people, who supported me and my research and made this work possible…

First and foremost, I would like to express my gratitude to my supervisor Prof. Dr. Peter A. van Aken not only for his valuable support but also for giving me the opportunity to conduct my research at the Stuttgart Center for Electron Microscopy (StEM) at the Max Planck Institute for Solid State Research. He has always inspired me and guided me to pursue my ideas with great freedom. I would sincerely like to thank Prof. Dr. Hans-Joachim Kleebe for accepting me as a PhD student at the Technical University of Darmstadt and for his helpful guidance. Moreover, I would like to thank Prof. Dr. Lambert Alff and Prof. Dr. Christoph T. Koch for taking place in my thesis committee and for reading my thesis.

Secondly, I highly appreciate the noteworthy support of Dr. Gennady Logvenov: In addition to his guidance in thin film growth, it was always instructive to discuss superconductivity and magnetism with him. Although he was exposed to my crazy ideas – every time I popped up with another one in his office – he always welcomed me. I also gratefully acknowledge Dr. Yi Wang's valuable support in STEM imaging and analyses: I am thankful to both of you for your encouragement. I would like to especially thank Dr. Wilfried Sigle for the fruitful scientific discussions from the beginning and also for reading my thesis and giving valuable feedback.

It also has been my privilege to work with many prestigious scientists: I sincerely thank Prof. Dr. Joachim Maier, Prof. Dr. Bernhard Keimer, and Dr. Eva Benckiser for their great collaborations and valuable contributions to the projects. I would also like to thank and sincerely acknowledge Dr. Federico Baiutti, Dr. Matthias Hepting and Gideok Kim for the great team-play, for their worthful collaboration and friendship.

Many thanks to the people for their contribution in providing a good experimental atmosphere: Ute Salzberger and Marion Kelsch are gratefully acknowledged due to their guidance in TEM specimen preparation. Kersten Hahn and Peter Kopold in StEM group and Peter Specht in Thin Film Technology group are thanked for maintaining all the microscopes and the MBE system in good and stable conditions. Herewith, a special note to Georg Cristiani: I sincerely appreciate your assistance during the growths and I will not forget your comments on the RHEED patterns and "photography".

I thank Dr. Zhicheng Zhong and Dr. Philipp Hansmann for the first-principles calculations on $NdNiO_3$ project, Dr. Giuliano Gregori for the discussions in the La_2CuO_4-based projects, Dr. Ionela Vrejoiu for providing the manganite-ruthenate superlattice samples.

Friends are of always great importance for the difficult periods during the PhD life… First, special thanks to Dr. Pinar Kaya for the priceless support since 2011 and also many thanks to Dr. Kahraman Keskinbora, Dr. Yigit Mahsereci, Dr. Filip Podjaski, Pascal Wittclich, Dr. Umut T. Sanli, Dr. Cigdem Ozsoy-Keskinbora, Dr. Ekin Simsek-Sanli, Alp Can Karacakol, Dr. Werner Dobrautz, Dr. Matteo Minola, Dr. Alessandro Senocrate, Dr. Luzia Germann, Daniel Putzky, Julia Kröger, Katrin Fürsich, Dr. Christopher Dietl and Dr. Vesna Srot. I also want to thank whole StEM group for the nice atmosphere and also the Thin Film Technology group for nicely welcoming me. Of course, Caroline Heer is not forgotten! Thank you very much for your kind, friendly and valuable support.

Hereby, I would like to acknowledge the Max Planck Society for the Max Planck Society doctoral scholarship during my PhD.

Last but not least, I would like to thank my family for supporting me in all circumstances. Despite the 2000 kilometers distance, my father was always behind me, my mother was always with me and my sister was always close to me. Without them and their priceless support without expecting anything in return, I would not have had the opportunity to perform this study. So glad to have you…

Y. Eren Suyolcu

Stuttgart, 2018

1. Introduction

Abstract

This chapter comprises the motivation and the framework of the thesis together with giving a brief summary of the contents to the reader.

1.1 Motivation

Nowadays, the interest in semiconductor technology and semiconductor interfaces extenuates due to inherent limitations. Transition metal oxide heterostructures, as being another extensive materials family, form a multi-directional platform for the emergence of novel properties. [1,2] Bringing dissimilar constituents together in multilayer systems yields novel phenomena at the interfaces [3,4], which are normally absent in the constituent materials alone, such as metal-insulator transitions [5], orbital reconstructions [6], colossal magnetoresistance [7,8] high-temperature interface superconductivity (HT-IS) [9,10], ferromagnetism [11], formation of 2D electron gas [12], thermoelectricity [13] etc.. The use of oxide heterostructures – for instance superconducting systems – in technological applications is still partially hindered due to the lack of fundamental understanding of structural and chemical properties on the atomic scale. The phenomena occurring at oxide heterostructure interfaces can be tailored depending on the choice of the constituents; however, the key factor dominating the interface functionalities is the control of the interface sharpness and/or the interfacial intermixing.

Recently, the stupendous technical improvements in the synthesis of epitaxial oxide heterostructures with atomic layer precision, e.g. atomic-layer-by-layer molecular beam epitaxy (ALL oxide-MBE), have paved the way for fabricating stoichiometric systems and tuning their functionalities. [14,15] In addition to fabricating such valuable heterostructures, examining the interfacial structure and chemistry is of vital importance for correlating with the physical properties. Here, aberration-corrected scanning transmission electron microscopy (STEM) techniques provide a rich platform for position-sensitive probing of the interfaces with atomic resolution. The unique combination of two high-end techniques, i.e. ALL oxide-MBE and aberration-corrected STEM, is ideal for customizing and engineering the interfaces: While ALL oxide-MBE offers precise control of the heterostructures and the interfaces, STEM techniques provide not only information on the interfacial structure and chemistry but also allow the quantification of octahedral distortions at the interfaces, which mediate the properties. [16]

In this thesis, optimization of atomic layer-by-layer growth and/or atomic-resolution characterization of various complex functional oxide heterostructures – mainly La_2CuO_4 based systems in the form of either iso-structural or hetero-structural multilayers – is considered. In particular, different interfaces and their structural and chemical sharpness are correlated with the physical properties. The thesis aims at a better understanding of the complex oxide heterostructure interfaces.

1.2 Frame of the thesis

The thesis is composed of eight chapters – with individual "Introduction" and "Conclusion" sections– devoted to different oxide heterostructures and related interface examinations. The summary of the organization is the following:

Chapter 2: Background: Functional oxide heterostructures This chapter presents a background to the functional complex oxide systems and properties studied in the thesis.

Chapter 3: Experimental techniques: Growth and Characterization This chapter includes brief explanations of the experimental techniques conducted in the work such as (i) epitaxial growth, (ii) thin film characterization, and (iii) atomically-resolved aberration-corrected scanning transmission electron microscopy.

Chapter 4: Cuprate-based heterostructures In this chapter, high-temperature interface superconductivity (HT-IS) of La_2CuO_4-based heterostructures are presented. The fabrication and detailed characterization – including comprehensive STEM investigations – of bilayer systems, and the asymmetric dopant distribution profiles linked with growth kinetics at δ-doped superlattices, which are also correlated with electrical properties, are discussed.

Chapter 5: Cuprate-nickelate heterostructures This chapter discusses cuprate-nickelate multilayers, where the nickelate layers are employed as 214- and 113-phases for studying 'high-temperature superconductivity' and 'high-temperature thermoelectricity', respectively. The former, in which the presence of space-charge induced HT-IS is revealed, comprises not only the interface characterization but also the fabrication of the recent samples. For the latter, I focus on STEM investigations indicating the effect of individual layer thickness on the structural quality.

Chapter 6: Cuprate-manganite heterostructures In this chapter, superconducting-ferromagnetic heterointerfaces of La_2CuO_4-$LaMnO_3$ multilayers are presented. The realization of the structural quality and the elemental identification, as well as the octahedral distortions at the interfaces, is considered via STEM techniques.

Chapter 7: Nickelate-based heterostructures The chapter focuses on the $NdNiO_3$ thin films grown on $NdGaO_3$ substrates by pulsed laser deposition. The realization of a structural reconstruction in the $NdNiO_3$ thin films is demonstrated, and the mechanism behind the reconstruction is rationalized by DFT+*U* calculations.

Chapter 8: Epilogue The chapter summarizes the outcome and concluding remarks of the work.

This page intentionally left blank

2. Background: Functional oxide heterostructures

Abstract

This chapter gives a brief introduction to perovskite systems and presents a background of functional oxide heterostructures studied within the scope of the thesis. The structures and the main functionalities of the heterostructures including cuprate-, nickelate- and manganite-based systems are summarized. Furthermore, an introduction to the defect chemistry of related systems and thin film growth principles are presented.

2.1 Complex perovskite oxides

2.1.1 The perovskite structures

The ideal form of a "perovskite" oxide structure is formulated as ABO_3, which is composed of corner-sharing BO_6 octahedrons and A-site cations surrounded by twelve oxygen anions. The oxidation state of the A-sites occupied by a cation determines the electron count on the B-site transition metal and the valence of A and B cations give rise to the classification of ABO_3 perovskites into three groups: (i) $A^{3+}B^{3+}O_3$ (e.g. $LaMnO_3$), (ii) $A^{2+}B^{4+}O_3$ (e.g. $SrMnO_3$) and (iii)$A^{1+}B^{5+}O_3$ (e.g. $KNbO_3$). Perovskite oxides span a wide range of crystal structures including basic cubic structures or complex Ruddlesden-popper phases and different compounds can be derived starting from the highly adaptable and stable ABO_3 perovskites, either via varying the A- and B-site cations or via doping the system, i.e. via employing substitution of the cations with the dopants. Hence, the ability to tailor the structures with a variation of A- and B-site cations' size and/or valence sets the stage for tuning the functionalities.

The highly adaptable crystal structure of perovskite oxides, not only provides the opportunity of synthesizing them in different forms, such as ultrathin films and/or heterostructures, but also leads to various functionalities including ionic conductivity [17], piezoelectricity [18], ferromagnetism [11] etc. owing to sharing similar lattice parameters and structures, and thereby they can be easily integrated into each other. In such perovskite oxides, the bonding between B-cation and the O-anion, which are determined by the size of A and B cations, and correspondingly the B–O–B angle as well as the B–O bond lengths, play an important role. Relatedly, depending on cation sizes, the BO_6 octahedra are modified and the functional properties are tailored in a way that properties can be read via the interpretation of the octahedral distortions. To distinguish the origin of the distortions of the ideal structure, one can use the relative differences of the ionic radii of the constituent cations. Therefore, in order to determine the extent and structural origin of the octahedral distortions in basic ABO_3 structures, Goldschmidt's *tolerance factor* (*t*), which is defined in terms of ionic radii of the cations and anion, has been used. [19] The tolerance factor is defined as:

$$t = \frac{R_A + R_O}{\sqrt{2}\,(R_B + R_O)} \tag{2.1}$$

where R_A, R_O, and R_B refer to the ionic radii for the A cation, oxygen (O) and B cation, respectively.

The ideal cubic structure is represented by $t = 1$. In particular, although being modified by various distortions – in the cases of $t \neq 1$ – the stable ABO_3-structure is maintained for $0.8 \leq t \leq 1.0$. These octahedral deformations result in different crystal structures with lowered crystal symmetries and can be mainly exemplified as orthorhombic, monoclinic, rhombohedral and tetragonal structures.

Ruddlesden–Popper phases

In addition to the high structural adaptability of perovskites, another important feature is their easily modifiable stoichiometry, which enables different phases depending on the oxygen content or the substitution of the A cation by other cations with different valence state. Similarly, Ruddlesden-Popper (R–P) phases, which are derivatives of ideal perovskites, also exhibit structural and stoichiometric adaptability, independent of the compound.

The R–P phases are basically composed of alternating perovskite and rock-salt layers and the general formula of structures is $A_{n+1}B_nO_{3n+1}$. Importantly, due to an AO-layer "doping", the stoichiometry of the ABO_3 system evolves to A_2BO_4. In Figure 2.1.1, basic structural models of R–P phases (including fundamental ABO_3) are presented for n = 1, 2 and 3. In this thesis, the essential focus is the "n = 1" structure, namely A_2BO_4 structures, where "A" is mainly La and "B" refers to Cu (or Ni). Note that, the cubic perovskite structure is the R–P phase with $n = \infty$. The details and the experimental results that belong to these systems will be further discussed in the following sections (see Chapter 4).

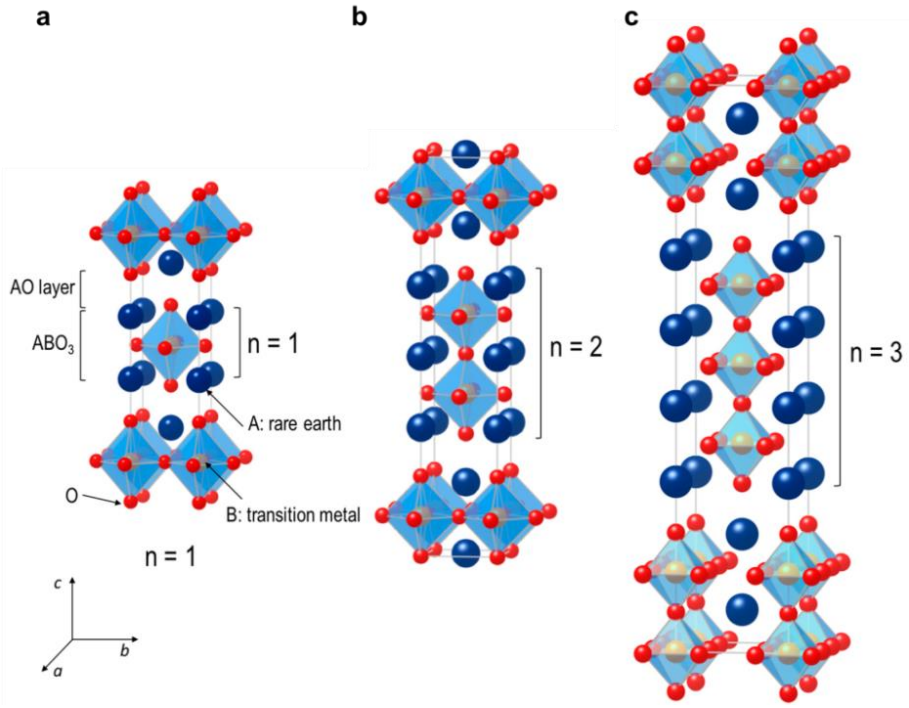

Figure 2.1.1. Structural models of (a) n =1, including ideal perovskite structure (ABO_3), (b) (n = 2) and (c) (n = 3) members of Ruddlesden–Popper phases. The denotation of n represents the number of stacked octahedral layers separated by a rock salt AO layer with different perovskite layer thicknesses. Reproduced with permission from Ref. [20]

2.1.2 Crystal-field splitting

In transition metal oxides (TMOs) the electronic transitions and bonding are dominated by partially or fully filled 3*d* orbital electrons. When ligands (in our case, oxygen anions; O^{2-}) are bonded to the TM ion in an octahedral symmetry, depending on the TM cation and its valence the energy levels of 3*d* orbitals are modified. The *Crystal Field Theory* explains these modifications via the ionic description of the bonding between TM and O^{2-}. [21] In these systems, the five-fold degenerate 3d levels are occupied by electrons that have parallel spins minimizing the Coulomb repulsion according to Hund's rule, which briefly states that the *d* orbitals are filled in a way to lower the energy of the electrons via maximized spin and angular momentum.

The *d* orbitals in TMOs (in the present case, mainly, CuO_6), are degenerated and due to the interactions (mainly electrostatic) between the B-3d (e.g. Cu 3d) orbitals and the closest O-2p orbitals, the degeneracy is broken with the octahedral crystal field effect. In other words, the oxygen anions, as being negative point charges, have a repulsive effect on 3d orbitals that gets stronger via getting closer. And, the electron-electron repulsion leads to some differences between the orbitals, i.e. the destabilization of the system and breaking of the octahedral symmetry. As a result, the energy levels are linear combinations of high-energy doublet e_g (i.e. $d_{x^2-y^2}$, d_{z^2}) and low-energy triplet t_{2g} (i.e. d_{xy}, d_{yz}, d_{xz}) states (Figure 2.1.2). The energy difference between the e_g and t_{2g} states is presented by crystal-field splitting energy (Δ_{cf}), and varies between ~1-2 eV depending on the system and the extent of the distortion. [22] In the case of electrons occupy t_{2g} orbitals (lower energies), the B cation gets more stable, whereas in the case of e_g orbital occupation at higher energies, the stabilization of the crystal field is reduced, and the system is less stable. Therefore, the extent of electron transfer in such systems is determined by the B–O bond length and B–O–B angles (see Section 2.3.2) and hence the electronic properties are designated within the 3d-orbital electrons of B-site cation and the 2p-orbitals of the oxygen.

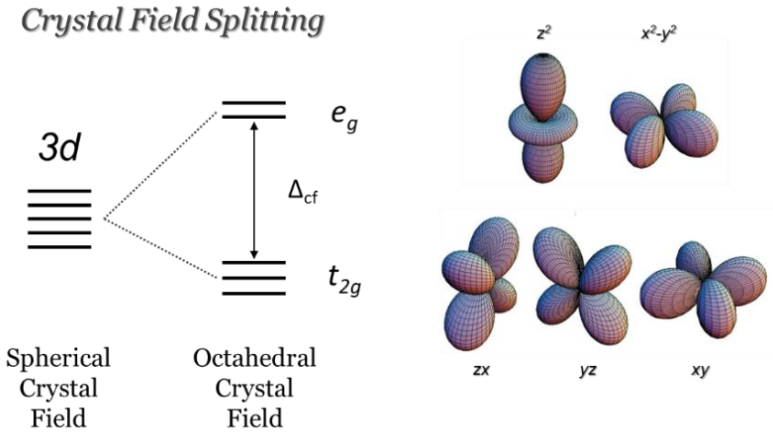

Figure 2.1.2. Illustration of the crystal field effect on d-states of a transition metal cation. The colored orbital drawings (right) are reproduced from Tokura *et al.* [22]

2.1.3 Jahn–Teller effect

The lowering of crystal symmetries is compensated by modifications of the BO_6 octahedron and these modifications take place in different forms via tilting, rotating, compressing or elongating the octahedron. In addition to the tilts and rotations of the BO_6 octahedra, the lattice symmetry can be lowered by the Jahn–Teller (JT) effect, which describes that the degenerated electronic states can accommodate a lowering of their ground-state energy by lifting the degeneracy via a lattice distortion. [23] In other words, the distortion of the ideal geometry is a consequence of removing the electronic degeneracy of the highest occupied molecular orbital via energy state splitting and lowering its symmetry, which provides energy stabilization of the system. [24]

TMOs with BO_6 octahedra surrounding the JT transition metal ions such as Mn^{3+} and Cu^{2+}, which have high-spin d^4 and d^9 configurations, respectively, exhibit JT distortions, and these distortions are intimately correlated with the physical properties. [25] For instance, the CuO_6 octahedron in the parent La_2CuO_4 is elongated along the *c*-axis by the JT effect [26] and exhibits two long and four short Cu–O bonds. [27]

In an undoped La_2CuO_4 system, the Cu^{2+} ion in the CuO_6 octahedron is mainly subject to a crystal field with tetragonal symmetry. As a consequence of that, the five-fold degenerate *d*-orbitals of the Cu^{2+} ion (with $3d^9$ electron configuration) are split into four energy levels as shown in Figure 2.1.3. The JT distortions are also a subject for $LaMnO_3$-based systems, either in a "cooperative" way or not. [28] However, the main focus of this thesis is the JT and anti-JT distortions present in the undoped and doped La_2CuO_4 systems. For further details see Section 4.2.1.

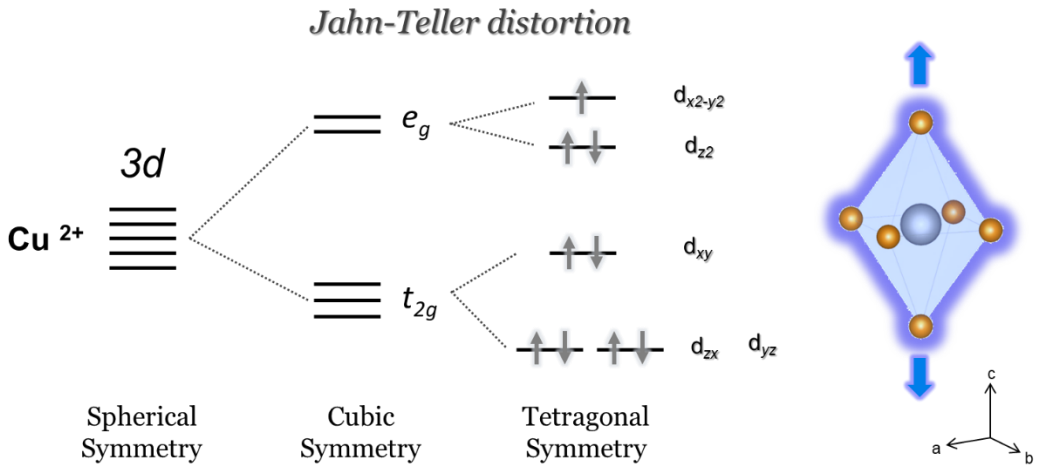

Figure 2.1.3. Illustration of the crystal-field effect on d-states of a Cu^{2+} cation with $3d^9$ configuration. The presentation of the c-axis elongated CuO_6 octahedra represents the (enhanced) JT distortion. [23,29,30]

Anti-Jahn–Teller distortion in $La_{2-x}Sr_xCuO_4$

As mentioned before, in the native lanthanum cuprate, the CuO_6 octahedra undergo JT distortions. However, via hole doping, the structure is contracted and the O–O (or $Cu–O_{apical}$) distances are modified. In order to investigate, whether the JT interaction still plays a role in the local distortion of the CuO_6 octahedra in the presence of hole carriers in ionic crystals such as cuprates, Shiraishi first performed the total energy band structure calculations of $La_{2-x}Sr_xCuO_4$ (LSCO) by varying the $Cu–O_{apical}$ distance. [31] These calculations have suggested that the Cu-apical-O distance decreases with increasing the Sr concentration in $La_{2-x}Sr_xCuO_4$.

After a while, some experimental studies were also conducted in similar systems: Distortions of CuO_6 octahedra in Sr-doped $La_{2-x}Sr_xCuO_4$ structures (x up to 0.4) and related changes in Cu–O apical distances were studied via diffraction techniques providing average structural information. [32] It is reported for this particular system that increasing the dopant concentration determines the compression of the octahedron (Figure 2.1.4), i.e. a decrease of the $Cu–O_{apical}$ distances [32], which is defined as anti-Jahn–Teller (AJT) effect. [26] Recently, the presence of JT and AJT distortions at the interface of Sr δ-doped layers was reported [33], where an anomalous elongation of the Cu–O apical distance in LCO-based structures is present, i.e. JT distortion [34] and followed by an AJT distortion contracting the CuO_6 octahedra along the c-axis. Therefore, within the scope of this thesis, the JT and also anti-JT distortions are widely studied and discussed (see Section 4.2.2), since the local JT distortions appear to be strongly related to the presence of 2D interfacial superconductivity.

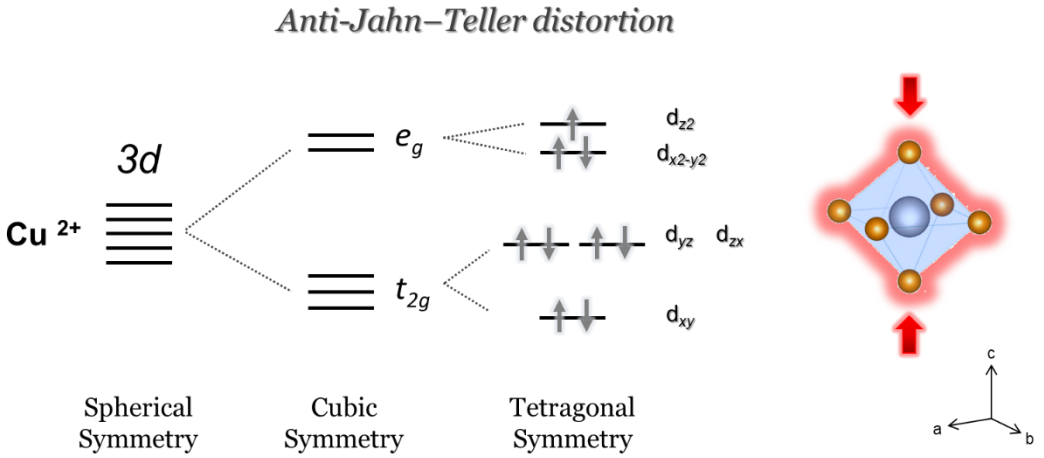

Figure 2.1.4. Illustration of the crystal field effect on d-states of a Cu^{2+} cation with $3d^9$ configuration. The c-axis-contracted CuO_6 octahedron represents the anti-JT distortion. [26,35]

2.2 Lanthanum cuprates

2.2.1 Structure of La_2CuO_4-based thin films

As briefly mentioned above, La_2CuO_4 (LCO) is a member of the R–P family with *n*=1 and presents the fundamental "214-structure" among the other cuprate-based (superconducting) systems. The La_2CuO_4 parent compound is an antiferromagnetic insulator and exhibits an orthorhombic structure, in which the CuO_2 planes are separated by rock-salt La-O blocks. For LCO the A-site is occupied by nine-fold-coordinated La^{3+} and the six-fold-coordinated B-site cation, i.e. Cu^{+2}, is placed in the center of BO_6 octahedra. A sketch presenting the structural model for La_2CuO_4 is displayed in Figure 2.2.1.

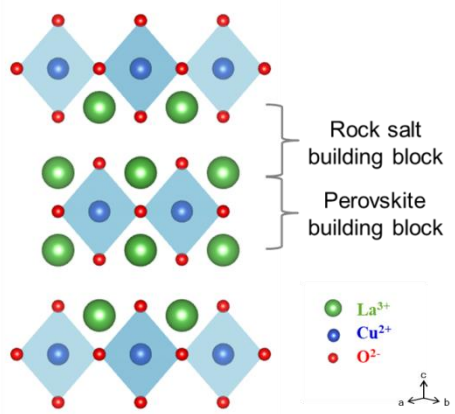

Figure 2.2.1. Structural model of La_2CuO_4. La, Cu, and O are colored with green, blue and red, respectively.

In native LCO, an elongation of CuO_6 octahedra has an impact on the *c*-lattice parameter. [36] The apical Cu–O (or O–O) bond length is expanded by the Jahn–Teller effect, whereby the system lowers its energy. As a result, a relatively long *c*-lattice parameter (~13.15 Å) is achieved compared with the other compounds, such as isostructural La_2CoO_4 and La_2NiO_4 of this family, where the *c*-axis lattice parameters are considerably smaller, i.e. ~12.60 Å [37,38] and ~12.70 [39], respectively.

2.2.2 High-temperature interface superconductivity in La_2CuO_4

The main basis of this thesis is beyond the electronic and theoretical discussions of superconductors. However, the fundamentals of the structure and the functionalities of cuprate-based high-temperature superconductor systems will be presented in this section in the form of a compact summary. The discussions based on the experimental findings are presented in *Chapter 4 and 5*.

The discovery of the high-temperature superconductivity (HTSC) in cuprates paved the way for a remarkable extent of interest in the scientific community for decades (Figure 2.2.2a). Superconductivity in a hole-doped, i.e. Ba-doped, LCO system was first discovered by the masterpiece of Bednorz and Muller. [40] The main advantage of the proposed system as a 'high-temperature superconductor' is the ability of hole (or electron) doping or oxygen intercalation to the structure owing to the easily modifiable structure of La_2CuO_4: The carrier density of the CuO_2 layer

can be altered due to doping the charge reservoir represented by the La-O blocks, which separate the CuO_2 layers from each other (Figure 2.2.2b), by holes or oxygen interstitials. The main contribution to superconductivity is provided by the CuO_2 planes, not only in the LCO system but also in other systems such as $YBa_2Cu_3O_7$, $Bi_2Sr_2CuO_6$ and $HgBa_2Ca_{m-1}Cu_mO_{2m+2+\delta}$ (Hg-Ba-Cu-O), which show even higher transition temperatures compared to LCO. For example, the highest T_c (up to ~165 K) in a cuprate-based superconductor system is the achievement recorded in Hg-Ba-Cu-O. [41–43] As also mentioned in many earlier studies, any structural disorder and chemical inhomogeneity directly affects superconducting properties and reduces T_c, therefore fabrication of high-quality structures is of great significance.

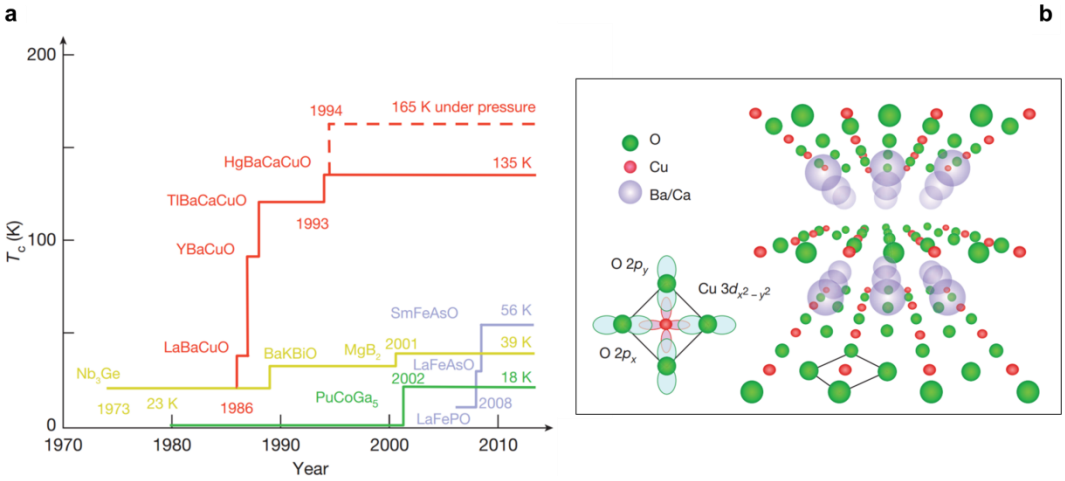

Figure 2.2.2. a) A schematic showing the superconducting transition temperatures of various classes of superconductors versus the years of each materials' discovery. b) Layered copper oxides are composed of CuO_2 planes, typically separated by insulating spacer layers. The electronic structure of these planes primarily involves hybridization of a $3d_{x^2-y^2}$ hole on the copper sites with planar-coordinated $2p_x$ and $2p_y$ oxygen orbitals. Reproduced with permission from Keimer *et al.* [44]

The superconducting phase is obtained within a certain amount of doping, i.e. $0.06 \leq x \leq 0.26$ [45–47], while the undoped LCO is an antiferromagnetic insulator and in the overdoped case the structure shows metallic behavior (Figure. 2.2.3). The hole doping is achieved via substitution of La^{3+} with a divalent cation (e.g. Sr^{2+}) or excess oxygen content. The highest T_c is realized in the optimum doping, i.e. $x \sim 0.16$. In the cases of Sr, Ba or oxygen doping, one can achieve 40 K, however, via Ca-doping the highest superconducting transition temperature achieved is around 20 K. Although numerous studies have been reported on LCO-based superconductor systems, unfortunately, in these systems the formation of *Cooper pairs* could not yet be explained with electron–phonon interactions as suggested in the Bardeen–Cooper–Schrieffer theory [48] for conventional superconductors.

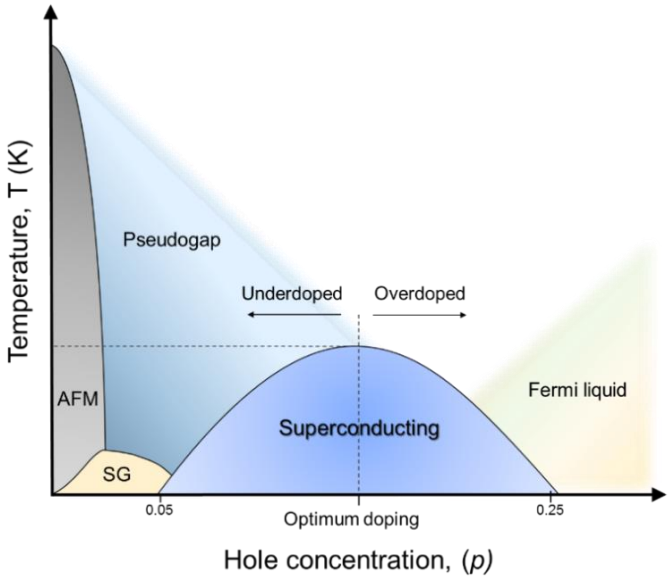

Figure 2.2.3. Illustration of a simplified phase diagram of hole-doped La_2CuO_4 systems. Different colors mark different phases (AFM, antiferromagnetic; SG, spin glass) and the dashed lines represent the optimum doping and the related T_c (~40 K for Sr-doping). The diagram is in agreement with Hashimoto *et al*. [49] and Keller *et al*. [50]

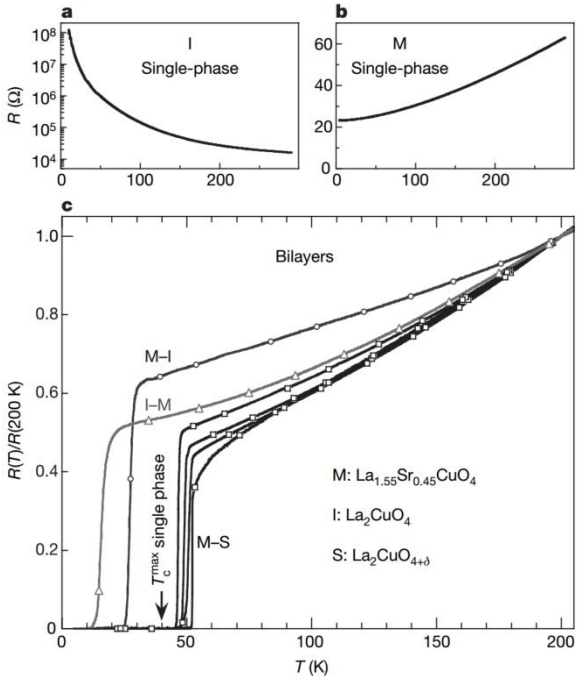

Figure 2.2.4. The dependence of resistance on temperature for single-phase and bilayer films. a) and b) display insulating and metallic single-phase films, respectively. c) includes I-M, M-I and M-S bilayers with different superconducting transition temperatures, i.e ~15 k, ~30 K and ~50 K, respectively. Reproduced with permission from *Gozar et al*. [10]

Recently, a milestone in the field of cuprate superconductivity was reached with the study of Gozar *et al*. [10], in which they reported the emergence of interfacial superconductivity as a consequence of adjoining two non-superconducting layers, i.e. one metallic (M) and one insulator (I) or superconductor (S) (Figure 2.2.4). The interface superconductivity is induced via hole accumulation and mainly based on charge transfer as a consequence of different chemical potentials of overdoped and undoped layers in such M–I bilayers. [10] It is also shown that the superconducting transition temperature depends on the layer sequence, although in all cases HTSC is reached. After this discovery, one of the principal questions was the following: "How thick is the nominal interface layer with the highest T_c?". Logvenov *et al.* answered this question utilizing "Zinc-doping" tomography and reported that HT-IS is confined to one "single" CuO_2 plane and the "hot" superconducting plane is the second CuO_2 plane after the nominal interface. [51] Later on, Butko *et al*. showed that the superconducting T_c is linearly dependent on the *c*-axis lattice parameter: The larger the *c*-lattice parameter, the higher the T_c. [52] A similar relationship between the *c*-lattice parameter and Cu–O distances has been also reported. [53,54] Analogue M–I structures were extensively investigated with the Coherent Bragg Rod Analysis (COBRA) method indicating large changes in Cu-apical-oxygen distances starting from the nominal M–I interfaces. The results in this thesis leverage and improve these findings and are presented in Section 4.1.2.

In a recent study, Bauitti *et al*. showed the contribution of the space-charge region to the HTSC in δ-doped structures. [55] They have revealed that, in the case of Sr δ-doping, an asymmetric distribution of the dopant – instead of one individual ML substitution of Sr-O and La-O – results in the formation of two different interfaces: While one of them provides ionic-intermixing-based superconductivity through homogenous doping, on the other side of the interface a space-charge layer is present (see section 4.2). All these studies indicate that the interface control and characterization is of great significance and LCO-based cuprate superconductors still provide a fruitful ground for further experiments.

2.3 Lanthanum nickelates

Another example of R–P phases is the $La_{n+1}Ni_nO_{3n+1}$ (LNO) family, which has been studied in the present thesis in two different phases: (i) $n = 1$ (i.e. Sr:La_2NiO_4) and (ii) $n = \infty$ (i.e. $LaNiO_3$). As a characteristic feature of R–P phases, the properties of different phases remarkably change from one to another for the $La_{n+1}Ni_nO_{3n+1}$ members. For example, the parent compound of the $n = 1$ phase, La_2NiO_4, is an antiferromagnetic insulator while $LaNiO_3$ exhibits paramagnetic metallic behavior. The synthesis of these two individual structures critically depends on the precise control of the growth temperature and pressure. For R–P phases with low *n*-values (e.g. La_2NiO_4) a less oxidizing environment (e.g. $P \sim 1 \times 10^{-6}$ Torr) is favorable. In the case of Sr doping of the compound (i.e. $La_{2-x}Sr_xNiO_4$), especially for increasing Sr doping levels, higher oxidizing conditions (e.g. $P \sim 2 \times 10^{-5}$ Torr) are required. Hole-doping (mainly via Sr) of the parent La_2NiO_4 is one of the main research areas of the material system; for instance, $La_{2-x}Sr_xNiO_4$ thin films with a wide range of doping concentrations have been extensively studied in terms of insulator-metal transitions or electrochemical device applications through different synthesis techniques. [56,57] The defect chemistry of $La_{2-x}Sr_xNiO_4$ is discussed in Section 2.5.

The 113-phase, i.e. $LaNiO_3$, is the most extensively studied member of the $RNiO_3$ (*R* = rare earth ion) family. In general, the family of rare-earth nickelates with composition $RNiO_3$ has recently

attracted wide-spread interest following theoretical predictions of possible high-T_c superconductivity. [58] In more detail, the RNiO$_3$ perovskite structure coordinates the Ni^{3+} ion to O^{2-} ions in an octahedral environment, providing Ni with a $3d^7$ (t_{2g}^6 e_g^1) electronic configuration with one electron in the e_g orbitals. The complex phase diagram of the RNiO$_3$ family mainly stems from emerging electronic and magnetic correlations as a function of the distortions of the perovskite lattice, with paramagnetic metallic, paramagnetic insulating, and antiferromagnetic insulating phases arising. [59] In the bulk form, the LaNiO$_3$ compound exhibits the smallest lattice distortion, and remains metallic and paramagnetic at all temperatures, while the control of the octahedral network and related Ni–O–Ni bond-angle distortions in LaNiO$_3$-based heterostructures can induce electronic and magnetic transitions. [5] The heterostructure environment enables the manipulation of intrinsic interaction parameters of all RNiO$_3$, which can significantly alter the materials' properties and new phenomena, can emerge, that are not present in the parent bulk material. In this thesis, LNO-systems (113- or 214-phases) have been used as complemental-systems to be stacked with La$_2$CuO$_4$-layers. The experimental findings and discussions can be found in Chapter 5. Moreover, for the lanthanum cuprate – lanthanum nickelate heterostructures that I contributed to the synthesis, the optimized growth parameters have benefitted from the previously gained experiences: Further details on the growth of these systems can be found in Ref. [60,61].

2.4 Lanthanum manganites

Within the scope of this thesis, in addition to cuprate and cuprate-nickelate based heterostructures, cuprate–manganite (i.e. La$_2$CuO$_4$-LaMnO$_3$) heterostructures with superconducting–ferromagnetic interfaces have also been studied (Chapter 6). Therefore, I will shortly discuss here the LMO-based systems and the exchange mechanisms that occur in manganite systems.

The general formula of perovskite manganites is AMnO$_3$ (AMO), where the B-site is occupied with the transition metal cation "Mn" and the A-site is mainly occupied with rare-earth ions. Manganate-based complex oxide systems with AMO composition have attracted wide-spread interest following the variety of magnetic functionalities. [62] In the AMO family, LaMnO$_3$ (LMO) – an antiferromagnetic Mott insulator – with Mn^{3+} and t^3_{2g} e^1_g occupancy could be named as the major actor of the playground, which exhibits attractive functionalities based on the profound interplay between local lattice and magnetic ordering (and also transport properties) that emerge a complex phase diagram with different physical properties. [63,64] The compounds with Mn^{4+} and t^3_{2g} e^0_g occupancy hindering Jahn–Teller distortions with partially filled 3d shells, in particular, BaMnO$_3$ (BMO), SrMnO$_3$ (SMO) and CaMnO$_3$ (CMO), exhibit different crystal structures. While BaMnO$_3$ favors crystallizing in the more stable hexagonal polymorph, it is less stable in perovskite structure [65,66]. SMO exhibits both cubic and hexagonal polymorphs [67,68], and CMO shows a distorted cubic structure. [69]

Exchange interactions in manganites

The complex phase diagram of Sr-doped LMO systems is a consequence of magnetic exchange interactions, which are superexchange [70,71] and double-exchange interactions mediated by O-2p orbitals, relying on the orbital degeneracy and occupancy of Mn 3d-orbitals. As mentioned in the previous section, the main use of doping manganite systems is the modification of the Mn valence in

the system. When the Mn^{3+} ion loses its e_g electron, which is the main actor in electrical and magnetic properties and is loosely bound, the system basically turns to a Mn^{4+}-bearing structure. This is the starting point of property-engineering, not only for bulk systems but also, more importantly, for LMO-based epitaxial heterostructures and interfaces. The exchange interaction between electrons is a consequence of the electron-electron Coulomb repulsion and Fermi statistics prohibiting the occupancy of an electronic state by electrons that have identical spins (i.e. two spin-up or two spin-down). [62] The *superexchange interaction* is an indirect interaction of two neighboring Mn ions through the oxygen mediation, where a one-electron-occupied 3d orbital induces the virtual transfer of two electrons as well as the dispersion of O-2p electrons to unoccupied Mn 3d-orbitals. [71] Namely, the virtual electron transfer between the TM cations is present, where the electrons are localized, and an antiferromagnetic interaction emerges. On the other hand, the mixed-valence manganite (La, A)MnO_3 (e.g. A = Ba, Sr, Ca) is a prototypical compound for the *double-exchange interaction*, in which an e^1_g electron from Mn^{3+} can hop without energy cost between Mn^{3+} and Mn^{4+} with an orbital configuration $t^3_{2g}\ e^1_g$ and $t^3_{2g}\ e^0_g$, respectively. [72] In this case, unlike the superexchange interaction, the electrons are delocalized which mediate the ferromagnetic interaction. At the end, the spins and the ions are parallel and ferromagnetically aligned, respectively.

2.5 Defect chemistry approach

Defect chemistry of doped La_2CuO_4

The properties of complex oxides strongly depend on the dopant concentration and oxygen content, and thereby, the defect chemistry plays an important role in the engineering and manipulation of their functional properties. [73–75] Hole ($h^\bullet$) doping of a parent LCO via substituting La^{3+} with divalent cations, such as Ca^{2+}, Sr^{2+}, and Ba^{2+}, (or via oxygen interstitials (O_i'')) is a common way to alter the charge carrier concentrations, as explained in previous sections. Depending on the choice of the dopant, different extent of segregation (see section 4.1.1) or different solubility limits are obtained. In this thesis, Ca, Sr, and Ba are used as dopants, where the solubility limit of Ca in LCO is the smallest ($x \sim 0.1$) and higher solubility limits ($x \sim 1.4$) for Sr and Ba are present. [76,77] Now, I will briefly present the hole doping mechanisms in our model material La_2CuO_4 from the defect chemistry approach [78], which has been explained by Maier and Pfundtner in detail. [74]

When the native La_2CuO_4 is subjected to dopant incorporation, e.g. Sr doping on a La site (Sr'_{La}), the increase of holes can be defined by:

$$2SrO + 2La^x_{La} + \frac{1}{2}O_2 = La_2O_3 + 2Sr'_{La} + 2h^\bullet \tag{2.2}$$

In the case of such doping, the formation of oxygen vacancies ($V_O^{\bullet\bullet}$) is also expected and can be defined by the following equation:

$$2SrO + 2La^x_{La} + O^x_O = La_2O_3 + 2Sr'_{La} + V_O^{\bullet\bullet} \tag{2.3}$$

Moreover, the anti-Frenkel reaction considering an oxygen site (i.e. O_O^x) should also be taken into consideration as:

$$O_O^x + V_i^x \leftrightarrow O_i'' + V_O^{\bullet\bullet} \tag{2.4}$$

As a last step considering the mass-action law, the final electroneutrality condition is defined as:

$$2[O_i''] + [Sr_{La}'] + n = p + 2[V_O^{\bullet\bullet}] \tag{2.5}$$

For a more general picture, when Sr-doped LCO is taken as a reference, the solution as a function of oxygen partial pressure can be simplified as presented in Figure 2.5.1a. For the intermediate-oxygen-pressure regime (middle), which is the most common case, the extent of hole doping is constant depending on the extent of the Sr-La substitution. However, in the high-oxygen-pressure regime (right), the main defects are expected to be the double positively charged oxygen interstitials and the dopant compensation is negligible. In the case of low oxygen partial pressures (left), the presence of oxygen vacancies is expected, and the extent of oxygen interstitials is low and constant.

In some cases, the dopant concentration may not be constant in the doped regions of epitaxial LCO systems, for instance at the interfaces, depending on the cationic intermixing. [79] Therefore, one should also consider the defect concentrations as a function of Sr-doping (Figure 2.5.1b). For this case, I take Sr-doping as a reference and refer to the study of Maier *et al.* [74] again. From the defect concentration model, it is visible, that at a fixed Sr-doping concentration for the low-doping case, the extent of oxygen interstitials accompanies the extent of Sr-doping. However, when the Sr content increase, the oxygen interstitials starts to dwindle away, and the hole formation increases in this case. Besides, very high doping of Sr results in the generation of defect associates, either neutral or not, are expected, e.g. $\{2(Sr_{La})V_O\}$.

The prediction of defect concentration in doped LCO systems is crucial since the defects directly influence structural properties that have further effects on superconducting properties. Previous reports already showed that while oxygen vacancies contract the structure, Sr-doping and/or oxygen intercalation expands the unit cell along the *c*-axis. [73,75,76,80] See Sections 2.1.3 and 4.2.2 for further literature and experimental findings, respectively.

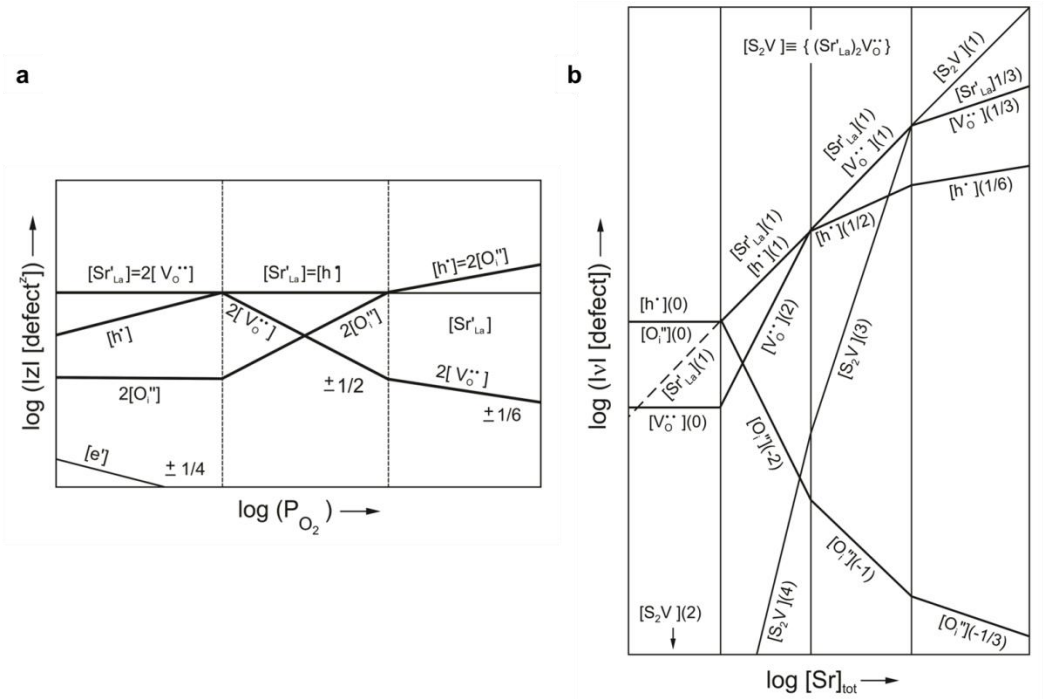

Figure 2.5.1. a) Defect concentration in La_2CuO_4 as a function of oxygen partial pressure at given Sr-content and constant temperature. b) Modeled defect concentration in La_2CuO_4 as a function of Sr-doping at constant temperature and oxygen partial pressure. Reproduced with permission from Maier *et al*. [74]

Defect chemistry of doped La_2NiO_4

Since La_2NiO_4 (LNO-214) share the same R-P structure with La_2CuO_4, it can be considered within similar chemical descriptions as well. Starting from the insulating stoichiometry compounds, an electronic phase transformation can be achieved by increasing the electron hole concentration. In particular, for (LNO-214) a transition into a metallic phase with increasing p (up to p ~1.0) has been observed. [56] Moreover, in (LNO-214), the substitution of La with an acceptor dopant (mostly Sr^{+2}) or intercalation of oxygen in the form of interstitial defects, results in hole doping, similar as for LCO. Both LSNO and LSCO can also accommodate a large amount of double-positively charged oxygen vacancies, thereby the general electroneutrality condition reads as equation (2.4). [74,81,82] By considering the above-described chemical models of LCO and of LSNO, a chemical potential gradient for holes and oxygen vacancies, as well as for Sr, is present, once a contact between these two compounds is formed. As a consequence, in order to establish equilibrium conditions, migration of defect species from LSNO in the direction of LCO should take place, [61,83] which in turn is expected to deeply affect the final functionalities of the interface region. For further details see Section 4.3.

2.6 Thin film growth: Introduction and main principles

The advantage of fabricating thin films and heterostructures of different components serves as a multifunctional platform leading to novel properties and the ability to create high-quality epitaxial heterostructures is the starting point of engineering physical properties at interfaces. As is well established, the precision of the growth techniques is a crucial factor in having an impact on the properties. Therefore, either physical [e.g. molecular beam epitaxy (MBE), pulsed laser deposition (PLD)] or chemical [e.g. chemical vapor deposition (CVD), atomic layer deposition (ALD)], different growth techniques have been developed and used depending on the choice of the material systems and applications. Some examples of interesting properties can be given as the occurrence of ferromagnetism at the interface between a paramagnetic (i.e. $CaRuO_3$) and an antiferromagnetic (i.e. $CaMnO_3$) layer [11] or the emergence of a 2D electron gas at the interface between two band insulators, namely $SrTiO_3$ and $LaAlO_3$. [12] Moreover, the interfacial superconductivity occurring at metal-insulator interfaces of La_2CuO_4-based heterostructures is another significant example, which constitutes the backbone of this Ph.D. thesis and will be further explained in the following chapters.

Growth modes

Independent of the growth technique, thin film growth modes can be classified as *island growth* (i.e. Volmer-Weber mode), *layer-by-layer* growth (i.e. Frank–van der Merwe mode) and *layer plus island* (i.e. Stranski-Krastanov mode) growth. Island growth is a consequence of the strong bonding between the particles (either atoms or molecules) on the surface of the substrate, and thus results in the formation of 3D islands and mostly causes inhomogeneous film formation. The second growth mode, i.e. Frank–van der Merwe mode, provides layer-by-layer growth generating uniform films and smooth surfaces, in which the deposition of a layer is followed by another layer and (mostly and preferably) no nucleation or island formation occurs. The third mode, namely layer plus island mode, is a mixture of two mechanisms in which layer-by-layer growth is followed by island formation. For instance, a decrease in substrate temperature may cause such a situation, where the more energetic particles on the surface start to lose their momentum and thereby start to nucleate. In a growth process at high-temperature, the high-energetic mobile particles (adatoms) on the surface move towards and stick to surface steps on the substrate, since these positions are thermodynamically favored. This type of growth is called *step-flow growth*.

Growth kinetics

The initial parameter affecting growth kinetics is the (substrate) temperature. The interaction (i.e. heat transfer) between the particles and the substrate may increase the energy of the particles and thereby contribute to the extent of surface diffusion. The kinetic energy of the particles directed to the substrate depends on the epitaxial growth technique. In the MBE growth, the thermal evaporation of the metals is the main activation factor that results in the low kinetic energy of particles around 0.1 eV. This makes a difference compared to other growth techniques. In particular, in PLD systems the energy of the particles to be deposited on the substrate is two orders of magnitude higher (i.e. ~10 eV) than in MBE.

Another crucial parameter is the gas pressure of the system. The growth of most of the oxide epitaxial systems is carried out at "high" pressures due to the involved oxidant species, where the high background pressure may cause a blocking effect for the particles on the way to the substrate. As mentioned before, the "low"-energy particles approaching the surface may be blocked due to the background pressure and may not even reach the substrate. For example, in oxide-MBE, where the ballistic transport of the ingredients from effusion cells is present, the mean free path of the particles is crucial and the pressure of the system is in the range of around 10^{-5} Torr that limits the elements to be deposited (see Section 3.1.2). Therefore, the growth kinetics and their control are the main frames of the growth success. The effect of the chamber pressure on the elemental choice and its relationship with RHEED patterns is further explained in Section 3.1.3.

Stoichiometry control is another critical factor, which is not independent of the growth technique. For instance, although the structural control of the epitaxial layers is easier in MBE-growth (due to the low growth rates), the control of the stoichiometry is more difficult since the manual control of every single layer is important. However, oppositely, in PLD growth, where the growth rate is higher than in MBE, the stoichiometry of the epitaxial film is already defined by the target, but due to the faster growth, the manual layer-by-layer control is not allowed. In other words, depending on the needs, every growth technique presents advantages and disadvantages varying on the desired achievements. For example, the control of the stoichiometry could be defined as a relative weakness of the oxide-MBE systems, especially compared to PLD systems. While perfect structural coherency is achieved at the interfaces, chemical intermixing is a matter of fact up to a certain point (~1-2 nm). [79,84] It has been shown in a recent report that while MBE yields sharper interfaces, the cation stoichiometry is more difficult to control compared to PLD growth of the same structures. [85]

Choice of substrate

To be able to grow high-quality films one needs to pay attention to the proper substrate selection first. The substrates determine mainly the expected extent of the defects, e.g. misfit dislocations or islands in the films. The worth-stressing factor in substrate choice is the lattice-match between the substrate and the film to be grown. In a heteroepitaxial growth, which is mostly the case for strain-engineered interfaces [86], the lattice parameter of the substrate (a_s) is different than the lattice parameter of the film (a_f). In a growth with a small lattice mismatch, for instance, the first layers of the epitaxial film will be strained to provide the lattice match to the substrate. The magnitude of the induced strain is usually defined by factor (f) and used for revealing the strain to be either tensile or compressive:

$$f = \frac{a_f - a_s}{a_s} \text{ x } 100 \qquad (2.5)$$

In this thesis, for the growth of LCO-based heterostructures, I mainly used $LaSrAlO_4$ (LSAO) (001) substrates since it induces compressive strain to the epitaxial layer and leads to the highest critical transition temperature (T_c) for LCO systems among other substrates. [87] LSAO has a tetragonal structure with lattice parameters a = 0.3754 nm and c = 1.2635 nm, while bulk LCO has an orthorhombic structure where Cu–O planes are separated by two La–O planes. The lattice parameters of bulk LCO are a = 0.5335 nm, b = 0.5415 nm, and c = 1.3117 nm. [52] Although LCO exhibits an orthorhombic structure at room temperature in the bulk form, it can be considered as pseudo-tetragonal: The orthorhombic LCO structure adopts the tetragonal structure of the LSAO substrate,

since it maintains an epitaxial relationship with the substrate. [88] An illustration of such situation is presented in Figure 2.6.1. On the other hand, other substrates, for instance, $(LaAlO_3)_{0.3}(Sr_2TaAlO_6)_{0.7}$ (LSAT) inducing tensile strain may cause defects in the film as discussed in Section 4.2.2.

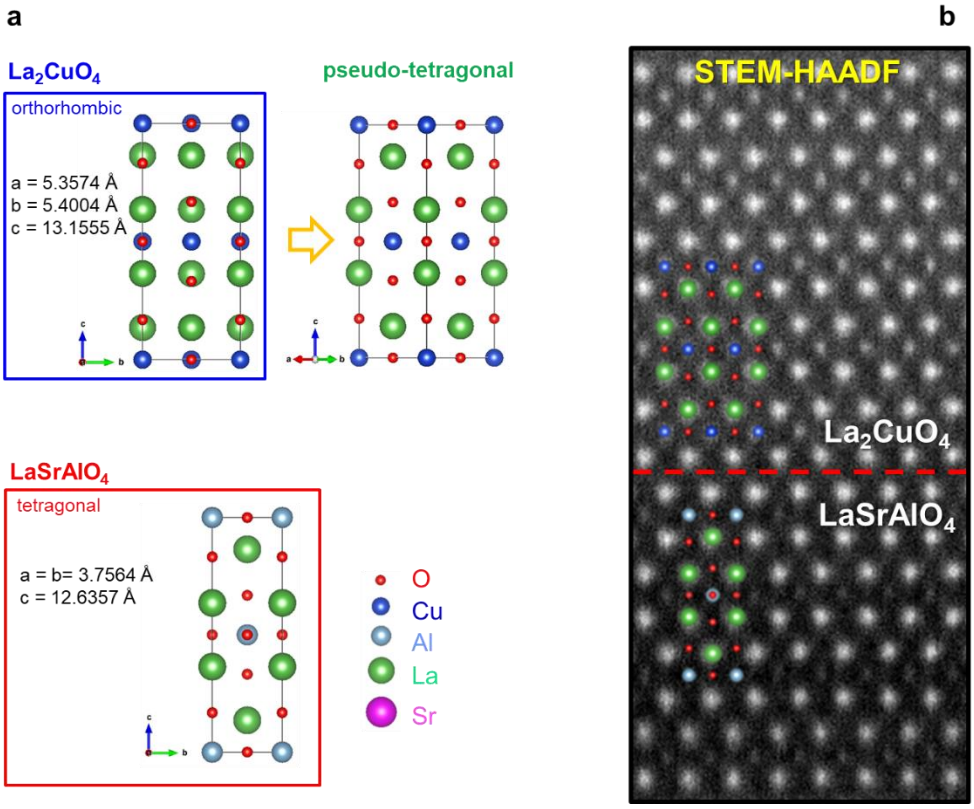

Figure 2.6.1. a) Structural models exhibiting the pseudo-tetragonal lattice representation for LCO (top) and the tetragonal LSAO (bottom). b) STEM-HAADF image representing the tetragonal (LSAO) and pseudo-tetragonal (LCO) structures on the bottom and on the top part of the image, respectively. The dashed line indicates the interface. Reproduced from *Suyolcu et al*. [89]

This page intentionally left blank

3 • Experimental techniques: Growth and characterization

Abstract

This chapter aims to give a detailed view of the experimental techniques employed within the thesis. In particular, the background and practical information about the growth of La_2CuO_4-based systems, the thin film characterization and, comprehensively, aberration-corrected scanning transmission electron microscopy methods are presented.

3.1 Oxide-MBE growth of oxide heterostructures

For high-quality thin film synthesis, one should primarily select the most appropriate growth technique depending on the choice of the layers to conjunct as heterostructures. In this thesis, the focus is on the oxide-MBE growth of epitaxial heterostructures. Therefore, the growth aspects are being discussed for oxide-MBE conditions. A basic sketch of oxide-MBE chamber ingredients, including reflection high-energy electron diffraction (RHEED), is presented in Figure 3.1.1.

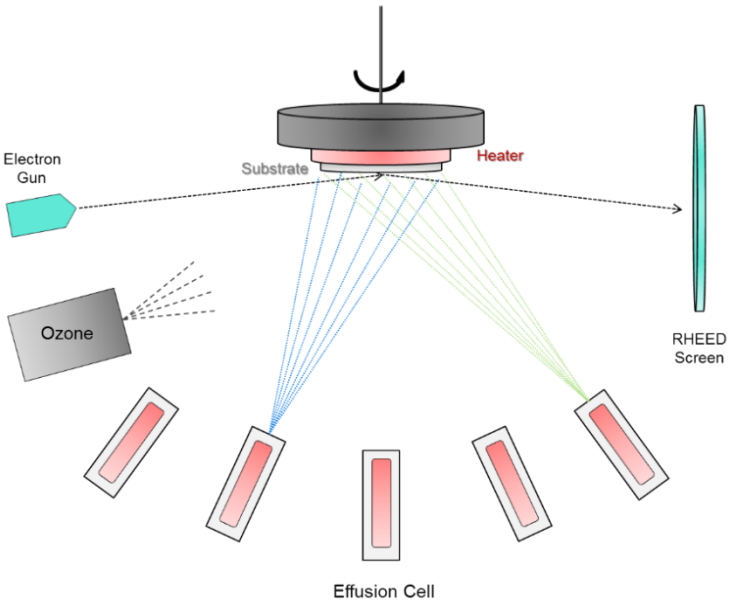

Figure 3.1.1. Basic sketch of an oxide-MBE chamber. The illustration includes effusion cells, an electron gun and a RHEED screen, an ozone delivery system and a heater as well as the substrate.

3.1.1 Growth specifics of doped La_2CuO_4

Substrate preparation

The preparation of the substrate is the first step prior to the growth. At the very beginning, the substrates are subsequently cleaned an in acetone and isopropanol in an ultrasonic bath. This cleaning procedure is followed by a $SrRuO_3$ (SRO) powder coating of the backside of the substrate (Figure 3.1.1a) via applying an SRO powder suspended in isopropanol, which is volatile and will evaporate quickly. The application of such "black" SRO powder missions enabling the absorption of the radiation emanated from the emitter as required for the appropriate and homogenous heating of the substrate. Such application is carried out by using a simple brush, which should be used carefully, since the edges and the corners of the substrate should be kept SRO free. The next step is fixing and loading the substrate into the chamber. First, the backside-coated substrate is fixed to the sample holder (Figure 3.1.2b) by using tantalum wires. Then the substrate is loaded in the load-lock, baked at 120 °C and transferred to the main chamber. This substrate preparation procedure is completed by heating the substrate to the optimum growth temperature.

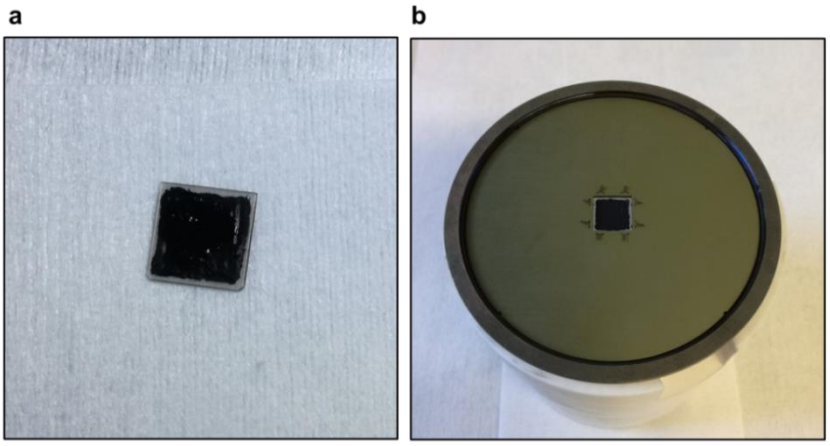

Figure 3.1.2. Photographs of (a) the backside SRO coated LSAO substrate and b) the view of the sample holder after fixing the substrate via tantalum wires.

Growth rate control and ozone production

After the substrate preparation and loading, which is followed by heating, the operator needs to further control the system and the growth parameters. The growth rate control starts even before the growth, for which the effusion cells are warmed up to the temperature values providing the appropriate vapor pressures for the elements that guarantee the desired growth rates. The optimization of the growth rates at high-oxygen-background rates is of significance on the way to high-quality growth. This is the reason why, before the growth, for each element (source), the absolute growth rates are carefully calibrated by utilizing an integrated quartz crystal microbalance (QCM) system in vacuum. It should be noted here that, the initial calibration to obtain a fudge factor for each element has been conducted by using ex-situ Rutherford backscattering analyses, which provides the absolute numbers of deposited atoms and enables the daily use of in-situ QCM. During the calibration of single sources (elements), certain pauses (~3 min) are applied in between, whereas in the case of consecutive calibration of the same elements evaporated from different effusion cells (e.g. La) such pauses are not required, since the stabilization of one cell is conducted, while the other effusion cell (of the same element) is being calibrated.

In oxide-MBE, the growth rates are ~1 Å/min and in most cases, higher growth rates are not preferred. The limited heating of the effusion cells restricts the growth rates and thereby limits the range of the elements to be grown in the system. One would normally expect the control of higher growth rates in the system. However, due to such limitation, some elements and their oxide compounds cannot be grown stoichiometrically. One example is the growth of Sr_2RuO_4 that could be conducted via PLD, but not with MBE, where the operating temperature of the effusion cells is limited (~2000 °C).

As is well established, MBE growth is in the ballistic regime and is characterized by long mean free paths of the initial (elemental) particles during the growth, in which the probability of collision of the particles is almost zero on the way reaching the substrate. This is also influenced by the pressure in the chamber. For oxidizing the evaporated elements, the oxidant species must be delivered in the system; in our system, distilled ozone, is used, which is a production of an ozone generator (discharger) system, that is stored (in liquid form) in an insulated glass still. The control of ozone delivery is critical because it is directly related to the pressure of the system and thereby is in a direct

correlation with the mean free path of the particles and the growth rate. It should be noted, that although the nominal product is ozone (O_3), in the end, a small extent of radical oxygen and molecular oxygen (O_2) accompanies the ozone. Furthermore, the system also allows tuning the delivered gas extent during the growth that enables investigating different conditions (see Section 3.1.3), while the optimum pressure is around 10^{-6} – 10^{-5} Torr.

Moreover, in complex oxide-MBE systems having several effusion cells, the optimization and the stabilization of the element fluxes are of importance. Such stabilization gets more crucial in the use of different dopants having the same valences, such as Ba, Sr, and Ca, which are widely studied in this thesis, due to different electron affinities. Therefore, the stabilization of different phases at different temperatures is required. For instance, in this work, the effusion cell temperatures are optimized at ~1650 °C, ~500 °C, ~350 °C and ~450 °C, for La, Ba, Sr and Ca, respectively. It should be noted that the *idle* temperatures of the effusion cells are different and are still higher than the room temperature. This is crucial especially for the Cu source, which is kept in a molten state at high temperatures (~950 °C) even in the *idle* mode. Because, in the case of cooling down the cell, the copper transforms into a solid state and cracks the (alumina) crucible, which requires extra maintenance at the end.

3.1.2 In–situ monitoring: Reflection high-energy electron diffraction

For oxide heterostructures, especially for superconducting systems, the structural quality of the samples has a direct impact on the properties. Therefore, the precise in-situ monitoring and control of the growth process are of great significance. In addition to the optimization of the growth parameters, one needs to take into consideration the instant control of the stoichiometry, and at that point, in-situ reflection high-energy electron diffraction (RHEED) as a monitoring tool comes to the playground. The evolution of the RHEED pattern and intensity oscillations provides feedback for precise growth control. [90–92] More specifically, the RHEED intensity oscillation enables observing the surface reconstruction, which is the ordered arrangement of the surface atoms and is crucial for understanding the growth process and the final morphology. [93–95]

In RHEED, an electron beam emanating from the electron gun is reflected from the epitaxial layers on the surface and results in specular spots (and streaks) on the fluorescent RHEED screen (Figure 3.1.1). Depending on the surface roughness the reflection varies: The rougher the surface, the less the intensity of the spots (i.e. diffuse reflection). It should be underlined that owing to the particle-wave behavior of electrons, both reflection and diffraction occur through the interaction between the surface atoms and the electron beam. The surface atoms during the growth are mobile and in order to minimize the surface energy, they change their positions on the surface. As experimental examples, the specular spot oscillations – recorded during the growth – as a function of time for a $La_{1.6}Ba_{0.4}CuO_4/La_2CuO_4$ bilayer are presented in Figure 3.1.3. In these plots, completion of each La_2CuO_4 (either doped or undoped) is represented by the maxima of the oscillations. Conversely, the minima indicate the formation of La–O blocks. Here, for further interpretation of experimental RHEED patterns, I present a preliminary case study of the surface reconstructions observed during the MBE growth of L(S)CO-based systems.

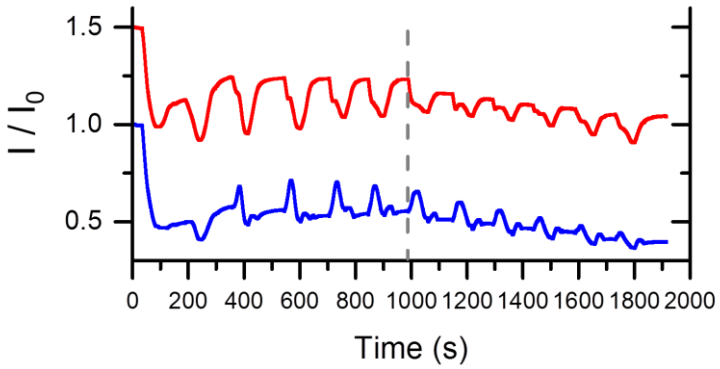

Figure 3.1.3. The specular spot (00) (red) and Bragg spot (10) (blue) oscillations are recorded during the growth of $La_{1.6}Ba_{0.4}CuO_4/La_2CuO_4$ bilayer. The intensities were integrated over selected areas, and one oscillation corresponds to a half u.c. thickness of the La_2CuO_4-based crystal structure. The dashed lines indicate the nominal M–I interface.

Surface reconstructions

In a nominal growth of LCO epitaxial thin film on (001) LSAO substrate, first, two La–O atomic layers are deposited, and this is followed by the deposition of one Cu-O atomic layer in accordance with the chemical formula of La_2CuO_4. During the growth, the substrate is heated up to ~650°C in ozone atmosphere with the pressure of ~$1.5x10^{-5}$ Torr provided by the evaporation of the liquid phase. In the case of Sr-doped LCO compounds (i.e. LSCO), a part of La atoms is replaced by Sr atoms in the co-deposition regime, i.e. simultaneous evaporation of La and Sr atoms are in a proportion corresponding to a doping level.

Concerning the growth process of optimum doped $La_{1.84}Sr_{0.16}CuO_4$, excluding the first couple of unit cells, in which the LSCO compound accommodates to the LSAO substrate, a characteristic surface reconstruction corresponding to a coherent atomic arrangement is obtained. Specifically, after the deposition of two (LaSr)–O atomic layers, the intensity of the specular spot drops to a minimum as a consequence of the destructive interference from La_2O_3 and SrO nano-islands, which cause a rougher surface, and the additional diffraction streaks disappear. After the Cu shutter is open and Cu atoms are being deposited on top and the intensity of the specular spot increases. In particular, when the deposition of half of the Cu–O atomic layer is completed, the characteristic shoulder appears in the intensity oscillation and two additional diffraction streaks develop between the Bragg diffraction and the specular spot corresponding to a surface atomic ordering with 3*a* in-plane width, where *a* is the in-plane Cu–O–Cu distance (Figure 3.1.4a). Further deposition of Cu atoms and completing a Cu–O atomic layer results in an abrupt transformation to 5*a* pattern (four additional diffraction streaks) (Figure 3.1.4b). The observation of such typical reconstructions has been an enigma of the high-quality epitaxial growth of the $(La,Sr)_2CuO_4$ compounds for a long time, however, the mechanism lying behind has not been considered, and thus, not well understood yet.

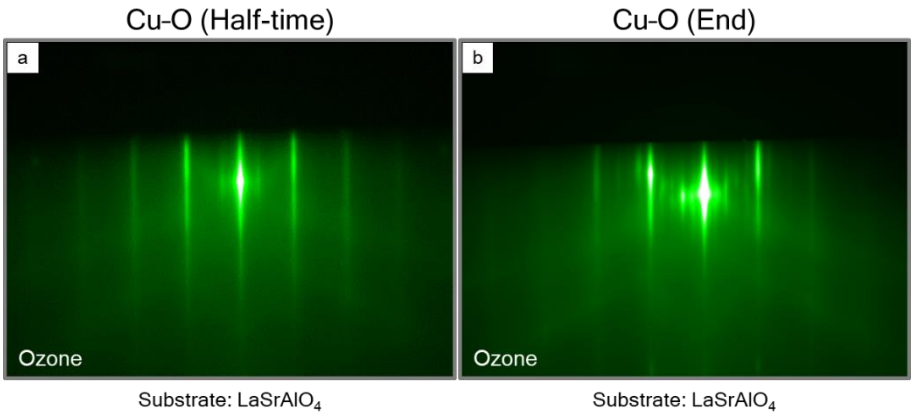

Figure 3.1.4. RHEED images obtained during the growth of optimum (x =0.16) Sr-doped La_2CuO_4. The two additional streaks in (a) and four additional streaks in (b) indicate the "half" and the "complete" deposition of the Cu–O layer, respectively.

Surface chemistry

Consecutive deposition of the constituent metals on a hot substrate (i.e. ~650° C) in oxidation conditions enables the fundamental surface chemical reactions. First, neutral nano-sized oxides (i.e. La_2O_3 and SrO) are formed following the delivery of La (or La+Sr). After the deposition of the copper (Cu) metal, one molecular layer of the L(S)CO is formed via the following surface chemical reaction due to the difference in electronegativities of La/Sr and Cu atoms:

$$\left(1-\frac{x}{2}\right)\times La_2O_3 + x \times SrO + CuO \rightarrow (La,Sr)_2CuO_{4-\delta} \qquad (3.1.1)$$

where x is the Sr doping level and δ is the oxygen non-stoichiometry (or concentration of oxygen vacancies). The entire growth process is a periodic repetition of this reaction. In the 214-structure formation, two molecular layers form "one" unit cell of a tetragonal LSCO structure (Figure 2.2.1). In other respects, the stoichiometry of LSCO compound (namely the La+Sr to Cu ratio) is also found to play a role in the determination of the surface reconstruction. At nominal stoichiometry, (La+Sr)/Cu ratio is equal to 2; however, when the amount of Cu is increased slightly, just before the nucleation of CuO precipitates, very dense reconstruction lines are visible. Such experimental observation is used for feedback and for the precise control of the molecular layers' stoichiometry during MBE growth of LSCO compounds within the scope of the thesis.

Structural origin

In addition to the previous observations, it is deduced that the lattice mismatch with the substrate has an impact on the surface atomic arrangement as well. In particular, LSCO grown on LSAO substrate inducing compressive strain (Figure 2.6.1) causes 5a width atomic arrangement (Figure 3.1.4b). However, for the growth of LSCO on other substrates, in which the film undergoes tensile strain, such as STO and $LaSrGaO_4$ (LSGO) 4a pattern (Figure 3.1.5a,b) is observed for the same doping level. This clearly indicates the influence of strain on the surface atomic arrangement. Furthermore, in order to examine the dopant size effect on the surface reconstruction, Ca^{2+} ions, which have a smaller ionic radii (90 pm) compared to Sr (131 pm) [96], are employed as a dopant for

the growth of LCCO on LSAO substrate and a 4*a* in-plane atomic arrangement is revealed (Figure 3.1.5c). All these experimental facts substantiate that surface reconstruction is influenced by structural effects.

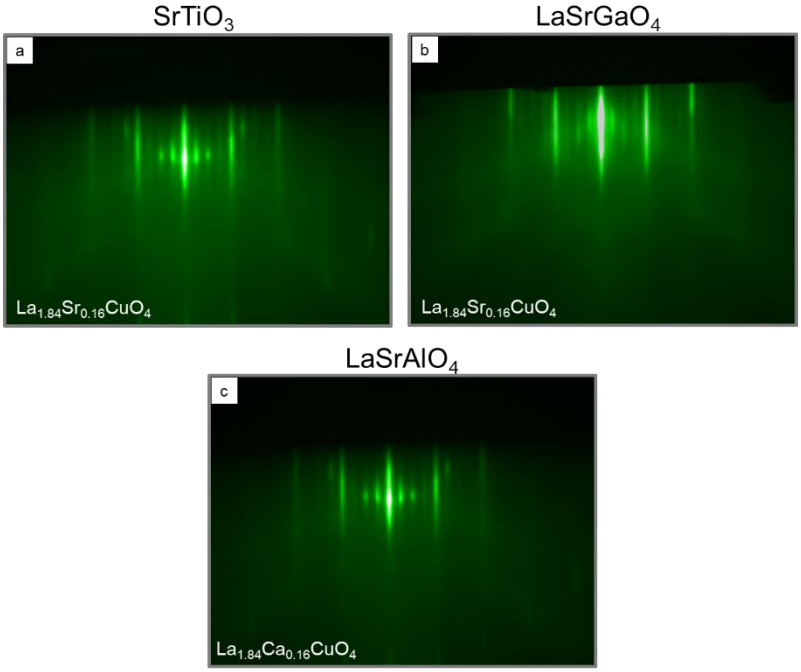

Figure 3.1.5. RHEED images obtained during the growth of $La_{1.84}Sr_{0.16}CuO_4$ films grown on (a) (100) STO and (b) (001) LSGO substrates inducing tensile strain: Three diffraction lines refer to the 4*a* width (in-plane) atomic ordering for both cases. (c) RHEED image after the deposition of the Cu layer during the growth of $La_{1.84}Ca_{0.16}CuO_4$ film on LSAO substrate exhibits three diffraction lines similarly.

Influence of oxygen pressure

Superconducting properties and for higher doping levels, one can even expect the formation of defect associates, for instance, the formation of oxygen vacancies together with the hole doping. [74,97] Therefore, considering the significant role of the oxygen and the oxygen vacancies in the surface reconstruction of LCO-based epitaxial films, further experiments are conducted via modulating the oxygen pressure. In order to verify the role of ozone assistance, as a first experiment, after depositing A-site atoms (e.g. La and Sr) under oxidation conditions, we deposit B-site (Cu) atoms in *"vacuum"*. In this case, one can still expect the reaction according to equation (3.1.1). However, the oxygen concentration will be reduced (in a more controlled way) and more oxygen vacancies will form causing a novel surface reconstruction, correlatively. The second experiment, which validates the first one, aims to compensate the lack of oxygen in the 214 structure with the delivery of ozone. The results are presented in Figure 3.1.6. Our experiments reveal that the optimum doped LSCO films lead to 4*a* width in-plane surface ordering in vacuum [Figure 3.1.6(a)] (similar to optimum doped LSCO films grown on STO substrates in ozone), which is consistent with the expected increase of oxygen vacancy concentration, whereas the visible broadening of the superstructure streaks in the RHEED image indicates the possible increase of the surface disorder in vacuum. Importantly, the post-annealing in ozone provides fast (i.e. several seconds) and clear recovery to the nominal surface ordering [Figure 3.1.6(b)], which strongly evidences the participation

of the oxygen atoms in the healing of the surface imperfections (caused by the oxygen vacancies) as well as the enhancement of the surface ordering. These observations not only provide additional information on the surface layer formation during the layer-by-layer MBE growth of LCO-based but also demonstrate the vital contribution of the oxygen atoms.

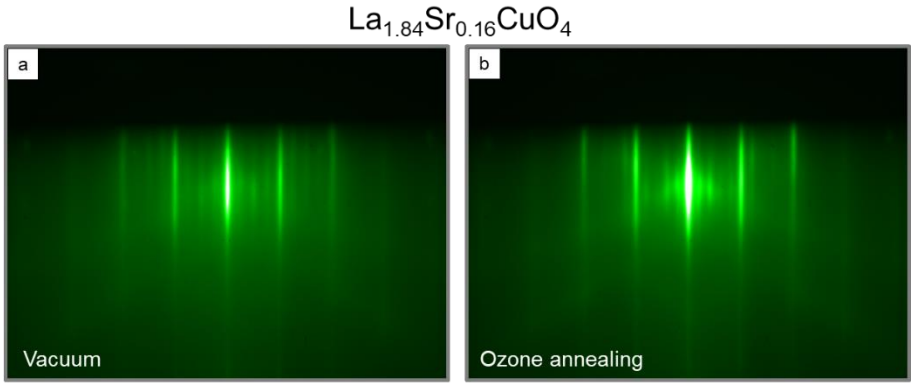

Figure 3.1.6. RHEED images of epitaxial $La_{1.84}Sr_{0.16}CuO_4$ films acquired after the Cu layer deposition in (a) vacuum and (b) after ozone annealing. The oxidation atmosphere causes different surface reconstructions.

The characteristic $5a_0$ width (in-plane) atomic ordering can be related to the size of electrostatic interactions between the dopants and the CuO_2 planes and can be correlated with the distribution of Sr dopants in the optimum doped regimes. Such reconstruction pattern is obtained almost in the entire doping range from $x > 0$ to $x = 0.2$. This is caused by the combination of oxygen interstitials and Sr dopants during the ozone-assisted growth, where the optimum doping is achieved by such a combination. In the light of these findings, one can suggest that the two dopants, i.e. created holes and oxygen interstitials, introduce local crystal distortions, which are directly displayed in RHEED screen as surface reconstruction. Furthermore, reduced dimensions in the case of vacuum growth – compared to ozone assisted growth – can be attributed to the formation of oxygen vacancies, where the post-ozone-annealing heals these oxygen vacancies. In the optimum doping case, a quasi-homogeneous superconducting ground state is observed. When one moves to the overdoped regime, supercells start to overlap, and more and more oxygen vacancies are generated to compensate valence dis-balance resulting from the substitution of La^{+3} by Sr^{+2} atoms.

These experimental observations demonstrate that for oxide heterostructures, in particular for La_2CuO_4-based HTSC systems, the precise control of the growth process and the stoichiometry can be monitored via in-situ RHEED in detail. Direct observation of many parameters affecting the surface reconstructions such as the dopant size, the choice of the substrate (i.e. the strain), the oxygen pressure and the doping concentration are revealed. Based on these comprehensive experimental observations, one can further suggest that there is a characteristic size of the surface atomic arrangements. The presence, the size and the formation of such ordering may have a crucial implication on the mechanism of HTSC. Further details are in preparation for publication. [98]

3.2 Thin film characterization

3.2.1 Atomic force microscopy

After the growth, one needs to examine the surface quality of the samples. A convenient way to examine surface morphology is performing atomic force microscopy (AFM) measurements, which provide valuable information about surface roughness and the presence of any secondary phase precipitates. AFM is a scanning probe microscopy technique which is based on the electrostatic forces between the scanning cantilever including a sharp tip and the surface of the sample. The movement (i.e. the variation of the vertical position) of the cantilever (due to surface morphology) is detected by a laser beam which is reflected towards a quadrupole detector. For the "tapping mode" used in the AFM measurements presented in this thesis, the cantilever oscillates at a resonance frequency and its amplitude is kept constant. When the tip nears the surface, depending on the electrostatic (or van der Waals) interactions, the amplitude of the cantilever oscillation varies paving the way for mapping the out-of-plane variations.

In a high-quality growth process, an atomically flat smooth surface without any secondary phases is expected. Conversely, in the case of secondary phases on the surface, one could predict a low quality of the growth. In nominal conditions, the layer-by-layer growth employed by the oxide-MBE system results in structurally sharp interfaces. However, depending on the choice of the systems to be synthesized, the formation of secondary phases in the system may be inevitable. The choice of the dopant, e.g. the variation of the dopant size, serves as an example for this situation. In particular, Ba doping of the La_2CuO_4 on LSAO (001) may result in secondary phase precipitations. [79,99] Importantly, the evaluation of the AFM images becomes more informative, when associated with RHEED patterns obtained during the growth. For a complementary example of AFM and RHEED investigations, see Section 4.1.

3.2.2 X-ray diffraction

X-ray diffraction (XRD) related techniques, which have been widely used for decades, are of importance for structural characterization of not only bulk materials but also epitaxial thin films, where the epitaxial layer thicknesses and the lattice parameters can be determined. One of the most important advantages of using XRD related techniques – with having a wavelength on the order of atomic scale – is the ability of the determination of the crystal structure of the material in a non-destructive way.

In XRD, the diffraction condition can be simply explained as a specular reflection of x-rays from periodically stacked atomic planes, from which the incident beam is diffracted. The conditions for a diffracted beam from a diffraction plane is described by Bragg's law (equation 3.2), where n is the order of the reflection, λ is the wavelength of the incident beam, d is the spacing between lattice planes, and θ is the angle of incidence of the X-rays.

$$n\lambda = 2d\sin\theta \tag{3.2}$$

For epitaxially grown structures, the orientation of the epitaxial layer is assigned by the substrate. Therefore, with prior knowledge of the substrate orientation and the expected crystal structure, the main coherent diffraction angles can be predicted. The determination of the diffraction conditions and their interpretation provides valuable information about the epitaxial relationship between the substrate and the film. For all the samples included in the thesis, XRD measurements were carried out, just after AFM measurements, in order to reveal the structural quality of the films as well as to examine the presence of any secondary phases in the samples. For the measurements, a Bruker D8 Diffractometer with a monochromator and Cu-filament source (λ = 1.5406 Å) is used.

3.2.3 Electrical conductivity

For an initial examination of the superconducting transition temperature, T_c, of the samples, mutual inductance measurements are conducted just after taking the samples out of the growth chamber, since this technique does not require deposition of Pt contacts on the surface and thus, provides quick information. This method works on the basis of detecting the mutual inductance of two Cu coils (driving and pick-up coils) placed above and below the sample. At the temperature $T \leq T_c$, where the material enters the superconducting state, the mutual inductance changes (i.e. the measured voltage drops) due to the diamagnetic screening induced by the superconducting sample. For the measurements, a system including two Agilent 34401A Multimeter and an SR850 DSP lock-in amplifier is used.

After the preliminary observations of the superconducting transition temperature of the samples, further electrical conductivity measurements are performed. For these measurements, the Van der Pauw method is used after the deposition of Pt (or Au) contacts on the samples, and a Keithley 2000 multimeter together with a Keithley 2400 sourcemeter are used. The electrical conductivity measurements of superconducting La_2CuO_4 bilayer samples (e.g. Section 4.1) presented in this thesis are mainly conducted by Georg Cristiani and Dr. Gennady Logvenov (MPI-FKF).

3.3 Scanning Transmission Electron Microscopy

Transmission electron microscopy (TEM), which has been in high demand for decades, includes numerous advantageous techniques for characterizing materials and has been considerably improved by the developments in the field. Scanning transmission electron microscopy (STEM), which can be considered as a special mode of image formation, has the advantage of probing local atomic columns. This has been made possible especially after the integration of aberration correction of the probe-forming lenses of the microscope.

In the STEM, a focused electron beam is formed by the illuminating lens system. Owing to the correction of lens aberrations, mainly the spherical aberration C_s, the electron probe can be as small as 1 Å or less. The most significant advantage of the STEM is the ability to acquire the electrons scattered to different angles as a function of the probe position on the sample. Figure 3.3.1 shows the beam emanating from the aberration corrector, which will be under the control of scanning coils just above the specimen. Moreover, the detectors, as well as the related techniques for different aims, are basically summarized including, diffraction, imaging, and electron spectroscopy.

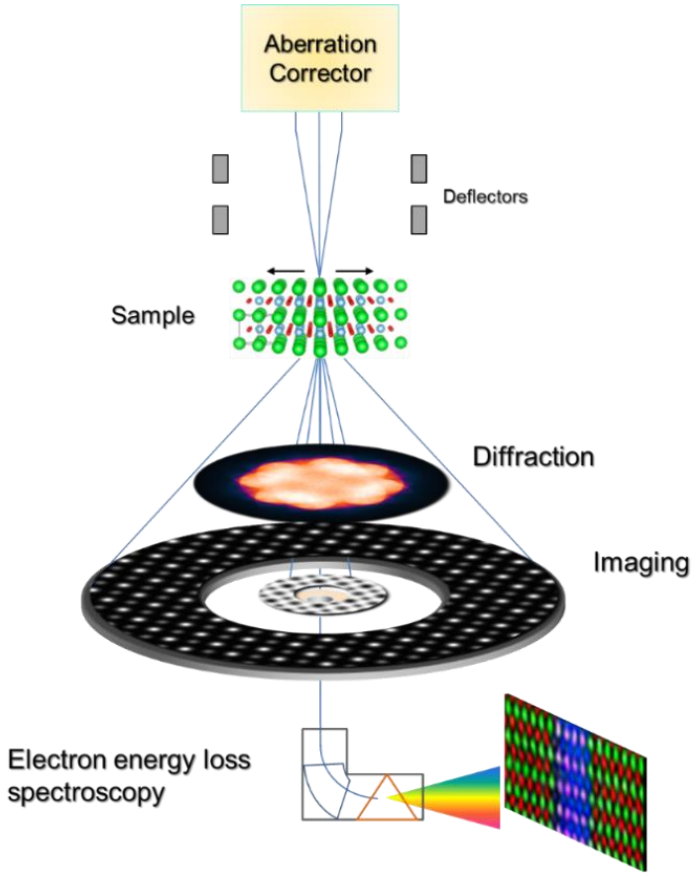

Figure 3.3.1. Cross-sectional simple illustration model of the ray diagram, optical axis, spherical aberration corrector, and detector positions for HAADF, ABF and EELS spectrum imaging. Please note that, nominally, an EEL spectrum is formed at the end of the spectrometer (see Figure 3.3.5 for an example).

In this part, I will briefly discuss the techniques and will start the TEM specimen preparation, which is critical for (S)TEM, since having thin (≤ 50 nm) electron-transparent specimen is of great significance for the analyses. For further details of TEM and STEM, and in particular, the constituent parts of the microscopes, such as guns, apertures, detectors, etc., see the textbooks *Transmission Electron Microscopy* by *Carter and Williams* [100], and *Scanning Transmission Electron Microscopy* by *Pennycook and Nellist*. [101]

3.3.1 Specimen preparation

For (S)TEM investigations, the specimen thickness directly affects the analyses and the interpretation. Within the scope of this thesis, unless indicated or acknowledged otherwise, the TEM specimens were prepared by me. Experiencing different material systems have been crucial for improving specimen preparation skills. Some parameters dramatically influence the quality of the prepared specimen. Such parameters are for oxide thin film samples the epitaxial layer thickness, the substrate material, the surface roughness, the presence of a protection layer, the growth direction and even the direction of the rotation of the tripod polishing system. For each type of sample, preparation conditions need to be optimized individually. For example, the best La_2CuO_4 bilayer samples (Chapter 4) were obtained using low-angle and low-voltage argon ion-milling.

Nevertheless, I optimized the parameters for each step and finally thin and flat high-quality samples were prepared. I mainly benefited from two facts: the very small thickness of the layered systems and the preparation method. The samples are wedge-polished [102] using very small polishing angles (~1.5–2.0º), which provide appropriately flat samples. An absolute thickness profile obtained from the Ca-doped bilayer sample is presented as an example in Figure 3.3.2, which directly proves the homogeneity of the sample thickness. Here, the absolute sample thickness is obtained by computing t / λ (where t is local thickness and λ is inelastic mean free path), obtained from the low-loss spectrum using the log-ratio method. [103] In short, for the cross-sectional electron transparent samples studied in this work, a standard sample preparation procedure including cutting, mechanical grinding, tripod wedge polishing followed by argon ion milling with a liquid nitrogen cooled stage was performed. The main steps are summarized in Figure 3.3.3 below.

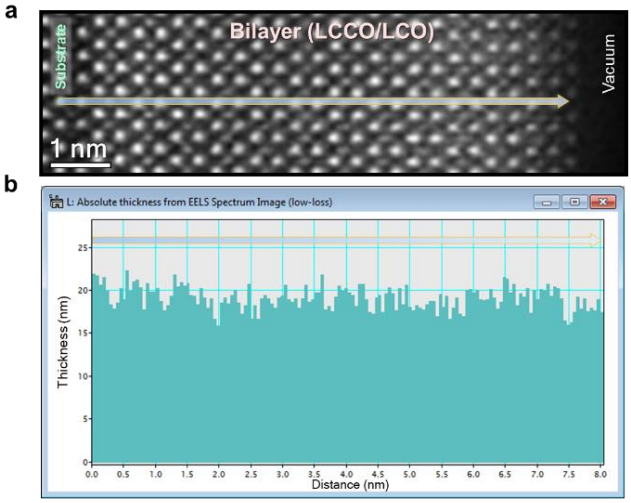

Figure 3.3.2. a) STEM-HAADF image taken of a Ca-doped bilayer and b) absolute thickness profile obtained from the EELS spectrum image showing the homogeneous thickness of the sample.

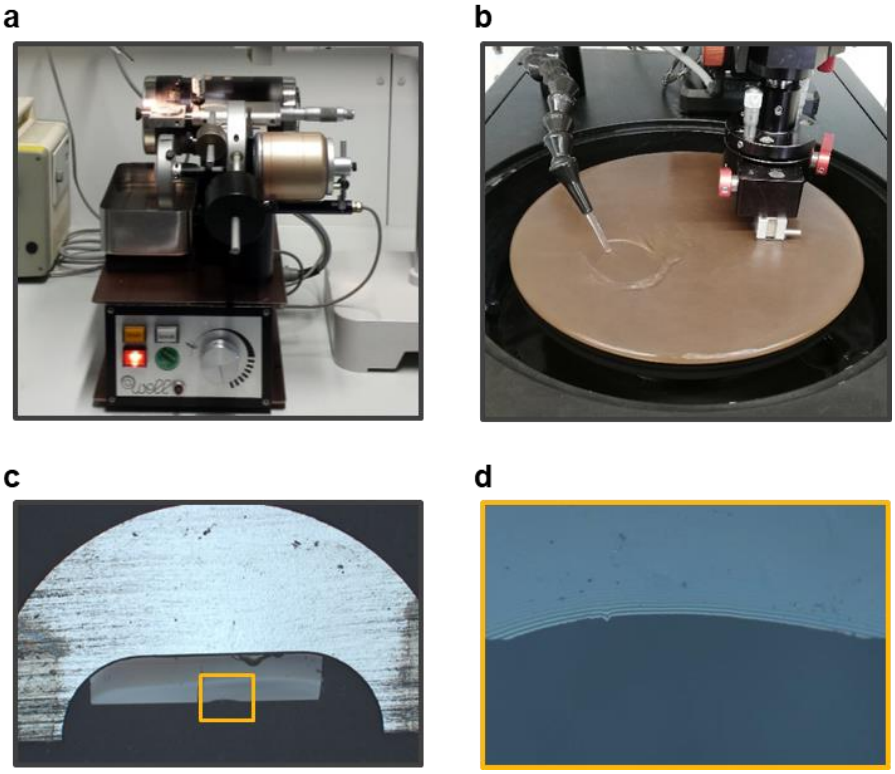

Figure 3.3.3. Steps of TEM specimen preparation: a) diamond wire saw used for cutting, b) grinding and wedge polishing with the Allied MultiPrep system [102], c) sample glued on a half grid and d) argon ion-milled sample with apparent thickness fringes as observed in the light microscope.

3.3.2 Aberration correction

One of the biggest challenges in either electron or light optics is the presence of imperfections in the optical systems. The focus and brief explanations will be about the electron optics, in particular, electron microscopy related aberrations. It is well established that aberration correctors [104] are in use not only for the STEM mode, but also for the TEM mode. The differences are basically where the correctors in the column are placed and for which purposes they are used. Namely, in STEM mode the aberration correctors are placed just after the condenser lenses and form a small electron probe that is scanned across the specimen (see Figure 3.3.1). This aberration correction is crucial since the resolution limit in the STEM is defined by the probe size. Differently, in TEM mode, the correctors are placed in the objective plane below the sample and are assigned to minimize the objective-lens aberrations.

For the alignment of the probe- and image-correction, HAADF and HRTEM images are mainly employed. The beam tilt for the Zemlin tableau measurements should start with low angles (i.e. < 20 mrad) and after reaching the desired precision, should continue with higher angles (i.e. ≥ 40 mrad). The alignment of the aberration-corrector can be summarized in three steps: (i) the initial (coarse) manual alignment of the microscope, (ii) the measurement and alignment of the aberrations up to the second order, and (ii) the use of Zemlin tableaus in order to measure high-order aberrations, starting

from low beam tilt angles ending up at higher angles. During my research, I have utilized both probe- and image-aberration-correctors integrated into two individual JEOL ARM 200CF microscopes in the Stuttgart Center for Electron Microscopy.

3.3.3 Imaging techniques

As a result of the electron beam interaction with the sample directly transmitted, scattered, and unscattered electrons carrying precious information are generated. Detection of such electrons is carried out via detectors placed in different planes. A variety of imaging techniques are available in the STEM, which differs according to the detector positions and collection angles. Some prominent examples are high-angle annular dark-field (HAADF) [105], annular bright-field (ABF) [106–108], and low-angle ADF (LAADF) [109]. Throughout my research, all abovementioned imaging techniques have been employed. However, the focus of this thesis will be on HAADF and ABF imaging techniques, which can be considered as being inspired by hollow-cone illumination in conventional parallel illumination mode. [100] Even though imaging of heavy elements by atomic resolution using HAADF imaging has been achieved long time ago, recent enhancement in spherical aberration (C_s) correctors [104] have paved the way for reaching even picometer-scale resolution, which also allows light-element imaging by ABF imaging [107].

One of the crucial points during STEM operation is the stability of the microscopes. Moreover, the stability of the specimens and the specimen holders/stages are of great importance, especially for concomitant imaging and spectroscopy measurements. These measurements additionally require temperature stability of the lenses, which should carefully be taken into consideration.

Figure 3.3.4. A plan-view illustration of HAADF and ABF detectors. Representative HAADF (darker, outer) and ABF (inner, brighter) experimental images taken from the $SrTiO_3$ specimen are bestrewed on the detector schematics. Please note that the experimental images are illustrated for a better presentation; nominally, there is no image formation on the detector, instead, a diffraction pattern is detected.

High-angle annular dark-field imaging

HAADF imaging, so-called "*Z*-contrast imaging", is mostly used for differentiating heavier and lighter elements. In this technique, the detected electrons are the ones being scattered to high angles that are larger than Bragg scattering angles. For such large-angle scattering, coherent effects of elastic scattering are negligible. The image mode and contrast, and the information that can be gathered vary depending on the scattering angles. For instance, while ADF images are formed using collection angles from elastically Bragg-scattered electrons, the HAADF range covers incoherent thermal diffuse scattering. Moreover, it is well-established that HAADF images provide atomic number contrast reflecting the nucleus potential, called Rutherford scattering for which the image intensity is proportional to the atomic number of the constituent elements with being approximately proportional to $\sim Z^{1.7-2}$. [110] There are also some other experimental parameters influencing the STEM-(HA)ADF imaging, which have been reported in previous studies, such as tilt [111,112], contamination [113] etc. A collection angle range of 75–310 mrad is employed for the HAADF images acquired and presented in this thesis.

HAADF imaging is also used for strain analyses as well as the quantification of local distortions [33,89] recently. Some examples of the quantification of local crystal lattice distortions at interfaces of superconducting La_2CuO_4 bilayers and $NdNiO_3$ thin films showing collinear magnetic properties are presented in sections 4.1.2 and 7.1, respectively. One of the biggest challenges confronted for such quantification is the scan distortions during the acquisition as well as the physical drifts of the samples during the experiments. Therefore some post-processing methods are developed [114] as well as the usage of multi-frames acquisition [115] to minimize such effects and to enhance the precision (Section 3.3.5).

Annular bright-field imaging

Simultaneous acquisition of ABF and HAADF images, which displays both light and heavy elements, is one of the most noteworthy improvements achieved in the field during the last years. As discussed for HAADF imaging, the collection semi-angles define the extent and contrast of the images in STEM imaging. In the very first reports on ABF imaging, the angle limitations for this technique were explained in detail. [106,107] The collection angles of the scattered electrons in ABF images are considerably small compared to (HA)ADF imaging. For instance, for the ABF images acquired and presented in this thesis, a collection angle range of 11–23 mrad is employed, which is narrower compared to HAADF range (cf. Figure 3.3.4). In ABF imaging, not only the low-angle-scattered electrons are collected but also the directly transmitted electrons are blocked, e.g. with a beam stopper, for a better contrast formation [106,107]. Similar to HAADF imaging, such scattering is also related to the atomic potential. However, the correlation between the contrast and the atomic number is different, being proportional to $\sim Z^{1/3}$. [107,108]

One of the prominent benefits of STEM imaging is the precise measurement of interatomic distances. Different experimental variants such as convergence and collection angles [108], sample tilt [116], scan distortion [114,115] and specimen thickness [108] are crucial experimental factors that can affect the image contrast and atom shape in the image. Recently it has been also comprehensively reported that small tilts on the order of ~ 6 mrad can cause dramatic artificial displacements of atom columns in the image. Moreover, the tilt-induced asymmetric dechannelling along the beam propagation can be defined by the atom position shift and artificial displacements, while the lattice

constant measurements are not drastically affected by specimen tilt effect. [117] The experimental conditions for ABF imaging are more difficult compared to HAADF imaging. In other words, while one can easily acquire a prominent HAADF image, the accompanying ABF image may not be as conclusive as the HAADF. Some prominent examples of simultaneously acquired ABF and HAADF images at the interfaces of LSMO/SRO superlattices are presented in Figure 3.3.5.

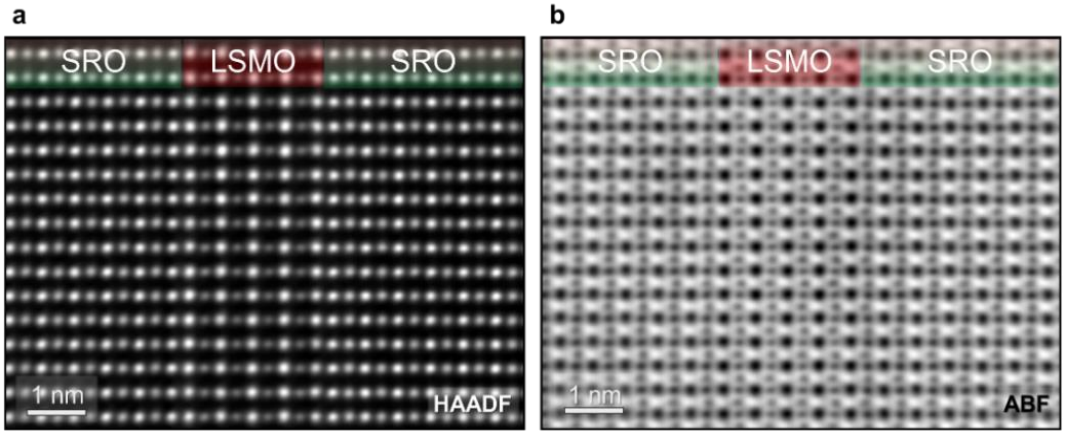

Figure 3.3.5. a) Simultaneously acquired STEM-HAADF and b) STEM-ABF images of (4) LSMO / (8) SRO multilayer sample presenting the coherent interfaces as well as projecting all possible atomic column positions. The images taken in [1-10] direction were processed with a multivariate weighted principal component analysis routine (MSA Plugin in Digital Micrograph) to decrease the noise level.

3.3.4 Spectroscopy

Energy-loss spectroscopy (EELS) and energy-dispersive x-ray spectroscopy (EDS) are both powerful techniques providing atomic-resolution information. EELS has a better spatial resolution, even ~10 meV resolution has been reached nowadays. [118] Furthermore, while the signal-to-background ratio is smaller than in EDS, EELS provides a better precision for light elements. However, due to the small collection solid angles of the EDS detectors, longer dwell times during the acquisition, are necessary. This is a disadvantage which may end up with beam damage during the experiment. Further details of these extensive techniques can be found in previous reviews [119,120].

Electron energy-loss spectroscopy

After the electron-sample interaction, some extent of energy will be lost due to the inelastic scattering as a result of Coulomb interactions between the impinging atoms and the atomic electrons of the sample. In other words, in such interaction, the electrons of the sample are excited into states above the Fermi level, due to the energy gained from the impinging electrons (Figure 3.3.6). [121] The spectroscopy technique measuring these energy losses of the inelastically scattered electrons is called EELS. In EELS, inelastically scattered electrons are dispersed into a spectrum, which is composed of characteristic edges based on the energies they have transferred, reflecting the electronic energy levels as shown in Figure 3.3.6. Therefore, through the aberration-corrected STEM-EELS analyses, atomically-resolved chemical and electronic information could be obtained.

The EELS spectrum can be classified into three different regions providing a variety of information: (i) zero-loss region, (ii) low-loss region and (iii) core-loss (high-loss) region (Figure 3.3.6a). The zero-loss peak (ZLP) is the strongest peak of the spectrum, which mostly arises from directly-transmitted (unscattered) or elastically scattered electrons. The ZLP is used to determine the energy broadening of the beam and the energy resolution of the spectrum (via the width of ZLP) as well as to calibrate the energy scale. The low-loss region at energy losses up to about 100 eV contains single-electron excitations from the valence to the conduction band and includes collective electron excitations (plasmon losses) which represent the oscillations of the free electrons in the material. For the atomic resolution studies, core-loss ionizations are mainly investigated and are further explained below.

The core-loss region from ~100 eV to several thousand electron volts contains the characteristic absorption edges of the constituent elements including information about the chemical bonds. Here, electrons are excited deep core levels to unoccupied electronic states above the Fermi level (Figure 3.3.6b). The core-loss edges are composed of two main structures: (i) the electron energy loss near edge structure (ELNES) and (ii) the extended electron energy loss fine structure (EXELFS). [121] The edge shape i.e. ELNES reflects the density of unoccupied states (DOS). In other words, this region exhibits the "personal" codes of the specimen reflecting the ionization edges that correspond to the excitation of inner shell electrons. [120,121]

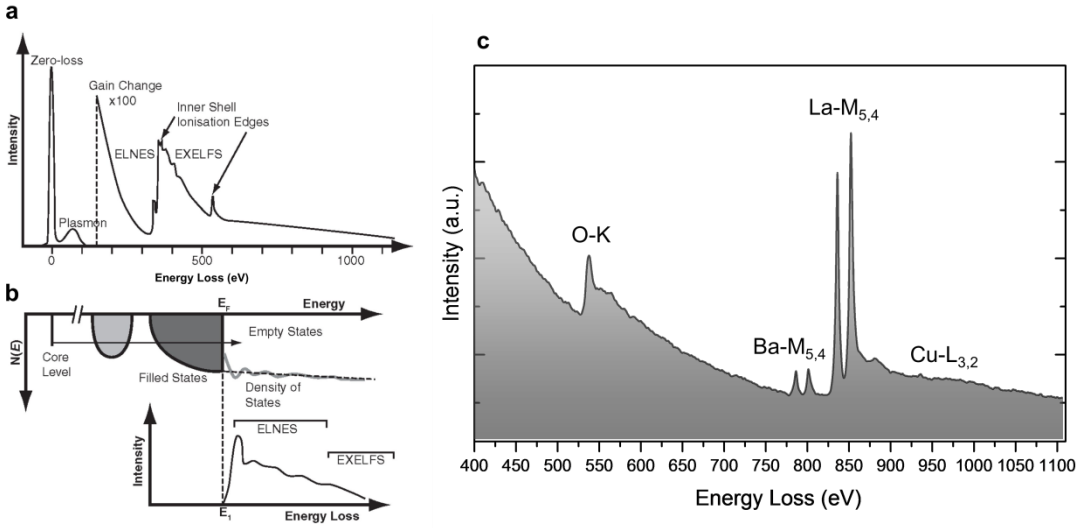

Figure 3.3.6. a) Schematic diagram of a general EELS spectrum. b) The origin of the ELNES intensity which reflects the unoccupied DOS above the Fermi level. Reproduced with permission from Ref. [120]. c) Experimental EELS spectrum from obtained Ba-doped La_2CuO_4 bilayer sample showing O-K, Ba-$M_{5,4}$, La-$M_{5,4,}$ and Cu-$L_{3,2}$ edges.

The core-loss edges for the materials studied in this work (e.g. La-$M_{5,4}$, Cu-$L_{3,2}$, Ba-$M_{5,4}$) are close to each other and even overlap (Figure 3.3.6c). Therefore, to separate the overlapping edges, I used the multiple linear least square fitting (MLLS) [122] (Section 4.1). The possible beam damage of the specimen for the core-loss investigations is another parameter to be considered. The signal in the core-loss region is quite weak compared to the ZLP and longer acquisition times are needed, which may cause damage on the sample. In addition to optimizing the acquisition times for specific samples, acquiring multi-frames [123] may improve the signal-to-noise ratio.

For the EELS experiments, a Gatan GIF Quantum ERS spectrometer was employed. EELS analyses were conducted at probe semi-convergence angle of 28 mrad (or 20.4 mrad in some cases) and a collection semi-angle of 111.5 mrad (or 68.5 mrad in some cases) were used. EEL spectrum images were processed using the multivariate weighted principal component analysis routine (PCA) (MSA Plugin in Digital Micrograph) developed by M. Watanabe [124] to reduce the noise in the data.

3.3.5 Data analysis

With high-quality image acquisition in electron microscopy, fast processing of the data and enhancing the accuracy and the precision as well as improving post-process tools are of great significance recently. In this section, I will present two different software tools developed by Dr. Yi Wang (MPI-FKF). The first software package is for detecting the atomic column positions in order to quantify the local distortions with a precision of 3-4 pm and the second software script is a post-process tool for correcting any kind of linear or nonlinear distortions present in (spectrum) images.

Oxygen octahedra picker tool

In oxide heterostructures, revealing the octahedral distortions, which requires accurate measurements of atomic column positions, crucially helps to evaluate and to tune the functionalities correlatively. For this purpose, a software tool, which is called "oxygen octahedra picker tool" to obtain quantitative information of the local lattice and BO_6 octahedral distortions from STEM-HAADF and STEM-ABF images has been developed.[125]

In this software two methods have been implemented to determine the center of the individual atomic columns: (i) the center-of-mass and (ii) two-dimensional (2D) Gaussian fitting. In the center-of-mass method, the peak center of an atomic column is given by:

$$C_x = \frac{\Sigma_i \Sigma_j (x_i \cdot I_{ij})}{\Sigma_i \Sigma_j I_{ij}} \quad \text{and} \quad C_y = \frac{\Sigma_i \Sigma_j (y_i \cdot I_{ij})}{\Sigma_i \Sigma_j I_{ij}}, \tag{3.3}$$

where x_i and y_j are the positions of the pixel (i,j) along the x- and y-axes, and I_{ij} is the image intensity of the pixel (i, j).

Secondly, for the 2D-Gaussian method the individual atomic column intensities are fitted to 2D Gaussian function with a constant summation as follows:

$$I(x,y) = I_0 + A * \exp\{(-\frac{1}{2}\left[\left(\frac{x-x_0}{x_w}\right)^2 + \left(\frac{y-y_0}{y_w}\right)^2\right]\} \tag{3.4}$$

The working principle of the software contains two different steps, where the default routine is the center-of-mass method that is followed by a 2D Gaussian fitting iteration optionally. The method was verified on different type of heterostructures and interfaces. Here to present some example images and related image quantification results presenting the octahedral changes of the interfaces of LSMO/SRO superlattice structures (Figure 3.3.7). The simultaneously acquired HAADF (Figure

3.3.7a) and ABF (Figure 3.3.7b) images clearly show all atomic columns in this particular projection. Importantly, while the in-plane La–La (Figure 3.3.7a) and O–O (Figure 3.3.7b) interatomic distances indicate perfect epitaxial relationship, clear variations are observed in the out-of-plane interatomic distances, especially at the interfaces. Detailed examples employed on different systems and interfaces are comprehensively discussed in Chapter 4 and 5. Lastly, I should underline that the accuracy and the precision of the methods are studied on both HAADF and ABF images with experimental and simulated images. Further information about the software can be found in Ref. [125].

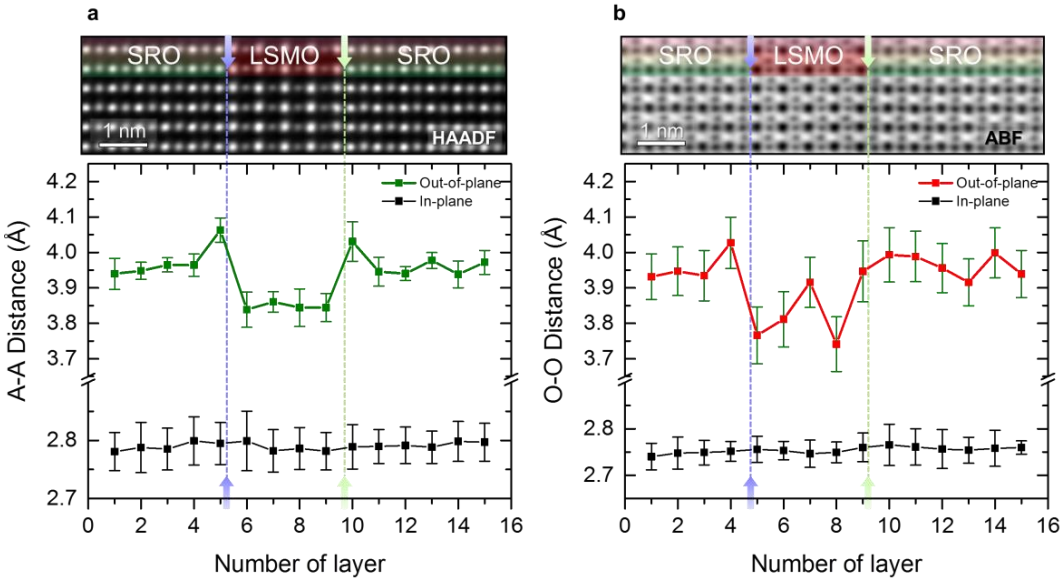

Figure 3.3.7. Sr (La)–Sr (La) (a; left column) and O-O (b; right column) interatomic (out-of-plane and in-plane) distances obtained from (4) LSMO / (8) SRO PLD grown samples. The interatomic distances measured by the O–O picker tool reveal the "constant" in-plane interatomic distances substantiating the epitaxial growth. Out-of-plane measurements employed for both on HAADF and ABF images show interesting local distortions: (i) the La (Sr)-La (Sr) interatomic distances in SRO/LSMO are different from those in LSMO/SRO, (ii) similar to La(Sr)–La(Sr) interatomic distances, O–O distances are larger in the SRO/LSMO interface compared to LSMO/SRO. The blue and green arrows on the images indicate the nominal SRO–LSMO and LSMO–SRO interfaces.

Spectrum image warper

Specimen drift and scan distortions can contribute to a discrepancy between true and desired electron beam positions in the STEM and that may result in both linear and nonlinear distortions in the experimental images. Despite various state-of-the-art improvements in aberration-corrected electron microscopy and related tools such as holders, microscope columns, etc., the experimental artifacts caused by the raster scanning owing to drifts (stage or sample) or to fly-back distortions during scanning of the beam cannot be prevented. [126] A basic schematic of "raster scanning" is presented in Figure 3.3.8. Such problems make spectrum imaging, employing EELS or EDS, more difficult since the pixel exposure times (dwell times) are longer compared to imaging techniques.

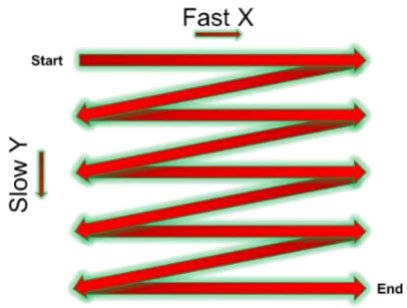

Figure 3.3.8. Illustration of a raster scan in scanning transmission electron microscopy. The schematic presents the fast and slow scanning directions. Note that the fast scan direction is composed of many small steps instead of one long scan.

Recently, in various post-processing software rigid and non-rigid registration techniques [114,115,127,128] are developed and served for use in the field. Additionally, a new post-processing software for image and spectrum image corrections called "STEM-SI warp" has been developed by Dr. Yi Wang (MPI-FKF). [129] The software enables corrections of both linear and non-linear image distortions. During my thesis, I have also utilized this software. An example of a non-linear correction of an EELS-SI acquired from an NVO thin film on an NGO substrate is presented in Figure 3.3.9.

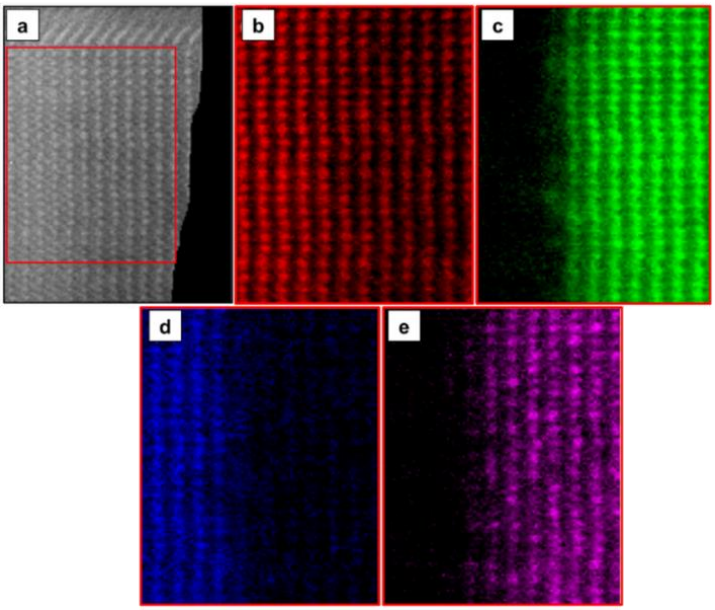

Figure 3.3.9. (a) Non-linear distortion partially corrected STEM-EELS SI data, (b)–(e) atomic-column-resolved Nd-$M_{4,5}$ (red), V-$L_{2,3}$ (green), Ga-$L_{2,3}$ (blue), and La-$M_{4,5}$ (magenta) elemental maps extracted from the distortion-corrected SI.

4 • Cuprate-based heterostructures

Abstract

The discovery of novel phenomena occurring at interfaces in complex oxide heterostructures has stimulated large interest in recent years due to the prominent possibilities of tuning functionalities at the atomic layer scale. This illustrates the predominant role played by the local structural parameters. Tuning the network of metal-oxygen octahedra is a promising route for achieving new properties and functionalities in perovskite-based oxide hetero-structures. In this chapter, the focus is on the high-temperature interfacial space-charge induced superconductivity which is one of the most exciting interface effects. The extensive investigations on the local chemistry and crystal structure including octahedral distortions across La_2CuO_4-based superconducting interfaces using high-resolution analytical scanning transmission electron microscopy techniques are presented.

4.1 High-temperature superconducting La_2CuO_4 bilayers

4.1.1 Dopant size effects on interface functionalities

Depending on the choice of the constituents, numerous microscopic phenomena can occur at oxide heterostructure interfaces. [9,12,17,130–133] In this context, one recent exciting finding was the observation of high-temperature interface superconductivity (HT-IS) at the interface between epitaxially grown strontium-overdoped metallic (M) lanthanum cuprate ($La_{1.55}Sr_{0.45}CuO_4$) and underdoped insulating (I) La_2CuO_4 (LCO) layers [10], none of which is superconducting if taken alone. The full understanding of HT-IS is a very important step towards the understanding of the HTSC mechanism [10,134], being potentially able to shed light on questions related to the formation of superconducting interfaces [10,135], its dimensionality and locus [51] and the impact of the crystal structure and atom positions on the superconducting properties. [34,52] Numerous studies employing advanced experimental methods as well as innovative approaches have addressed these questions [51,52,136–141] and the state-of-the-art of the common understanding of such phenomena can be found in several review articles. [142–148]

In order to explain the HT-IS in M–I lanthanum cuprate bilayers, a model based on electronic charge transfer due to the difference in the hole chemical potentials of the carriers between the overdoped and the underdoped phases has been invoked. [51,140] As a consequence of such a charge redistribution, a doped region having optimal hole concentration for HTSC (namely, the second CuO_2 plane in LCO away from the interface) is formed in the nominally insulating phase. Notably, in such bilayers, the superconducting critical temperature (T_c) was also found to be dependent on the deposition sequence, being about 15 K in I–M structures (in which the LCO layer is deposited first) and >30 K in M–I structures, in which overdoped LSCO is employed as a bottom layer. [52] Remarkably, despite the two phases exhibit quite different *c*-axis parameter (~13.25 Å and ~13.15 Å for LSCO and LCO, respectively), a common *c* can be assigned to both phases, according to X-ray diffraction (XRD) analysis, in the case of epitaxial bilayers. Namely, the top layer adopts the out-of-plane lattice parameter of the bottom phase as a consequence of electrostatic interactions ("Madelung strain"). [52] Here, the dependence of T_c on the deposition sequence was attributed to such an effect, with T_c being higher (lower), when the out-of-plane lattice constant of the structure is expanded (shrunk) due to Madelung strain (i.e. when the M layer is deposited first). Notably, a linear relation between T_c and *c* was pointed out.

Such findings open an exciting scenario for the enhancement of the superconducting critical temperature in M–I lanthanum cuprate heterostructures, which could in principle be obtained by appropriately tuning the out-of-plane lattice parameter of the bottom layer. In particular, a promising route is represented by the possibility of realizing overdoped $La_{2-x}Ba_xCuO_{4+\delta}$ (LBCO) thin films, as demonstrated by Sato *et al*. [149], which was found to have *c* as high as ~13.5 Å for strongly overdoped (x = 0.35) layers under compressive strain (grown on $LaSrAlO_4$ (001) substrates). In the light of these considerations, the extrapolated T_c value for the M–I bilayer with LBCO being the bottom layer could lead to a giant enhancement up to ~65 K.

In this work, $La_{1.6}A_{0.4}CuO_4$ – La_2CuO_4 bilayers (with A = Ca, Sr, Ba), which were grown by atomic-layer-by-layer oxide molecular beam epitaxy (ALL-oxide MBE) [150], are investigated by several and complementary experimental techniques: atomic force microscopy (AFM), XRD, low-temperature direct current (DC) resistance measurements, magnetic susceptibility measurements and

high-resolution scanning transmission electron microscopy (STEM). A structural model of the ALL-oxide MBE grown bilayers is given in Figure 4.1.1. It should be noted here that, whereas the successful synthesis of high-quality Sr-doped [87] and Ba-doped [149] La_2CuO_4 epitaxial films have been achieved by several groups, there are no reports about MBE-grown Ca-doped LCO epitaxial films, possibly as a consequence of low Ca solubility [77] or due to the tendency of the formation of a highly defective structure (high concentration of oxygen vacancies). [75] Note also that Ca^{2+}, Sr^{2+}, and Ba^{2+} ions have the same formal charge, but different cationic radii, namely 118 pm, 131 pm, and 147 pm, respectively, for nine-fold coordination. [96] The mismatch with the host La cation, whose ionic size is 121 pm, is -2.47%, +8.3%, and +21.5%, respectively.

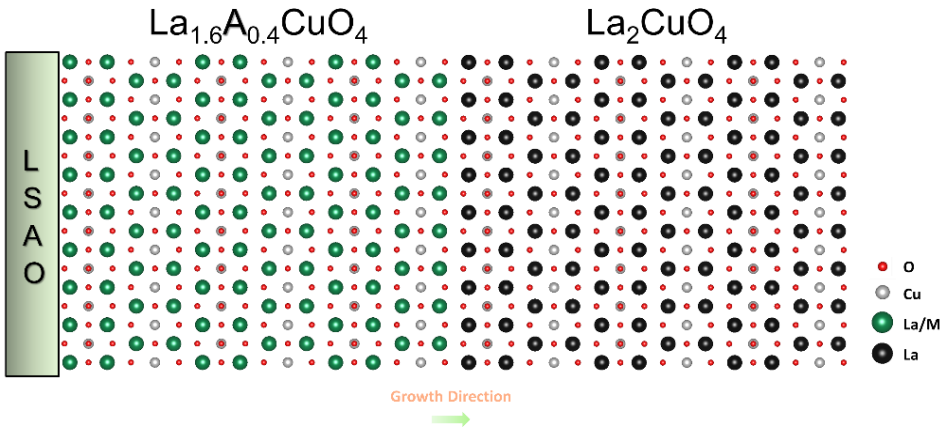

Figure 4.1.1. Structural model of the $La_{1.6}A_{0.4}CuO_4/La_2CuO_4$ bilayers grown on the LSAO substrate. The bilayers are composed of two different layers: (i) overdoped (metallic, M) $La_{1.6}A_{0.4}CuO_4$ and undoped (insulator, I) La_2CuO_4, respectively.

Results

The growth of each M–I bilayer was monitored by in-situ reflection high-energy electron diffraction (RHEED). The final RHEED patterns of each bilayer, namely LCCO/LCO, LSCO/LCO, LBCO/LCO, are displayed in Figures 4.1.2a-c, respectively. For Ca- and Sr-doped bilayers, no additional diffraction spots apart from the ones attributed to the typical perovskite-type LCO were observed, which indicates no secondary-phase precipitate formation. However, during the growth of Ba-doped bilayers, such spots were observed as displayed in Fig. 4.1.2c. These additional spots are related to the presence of secondary phase precipitates.

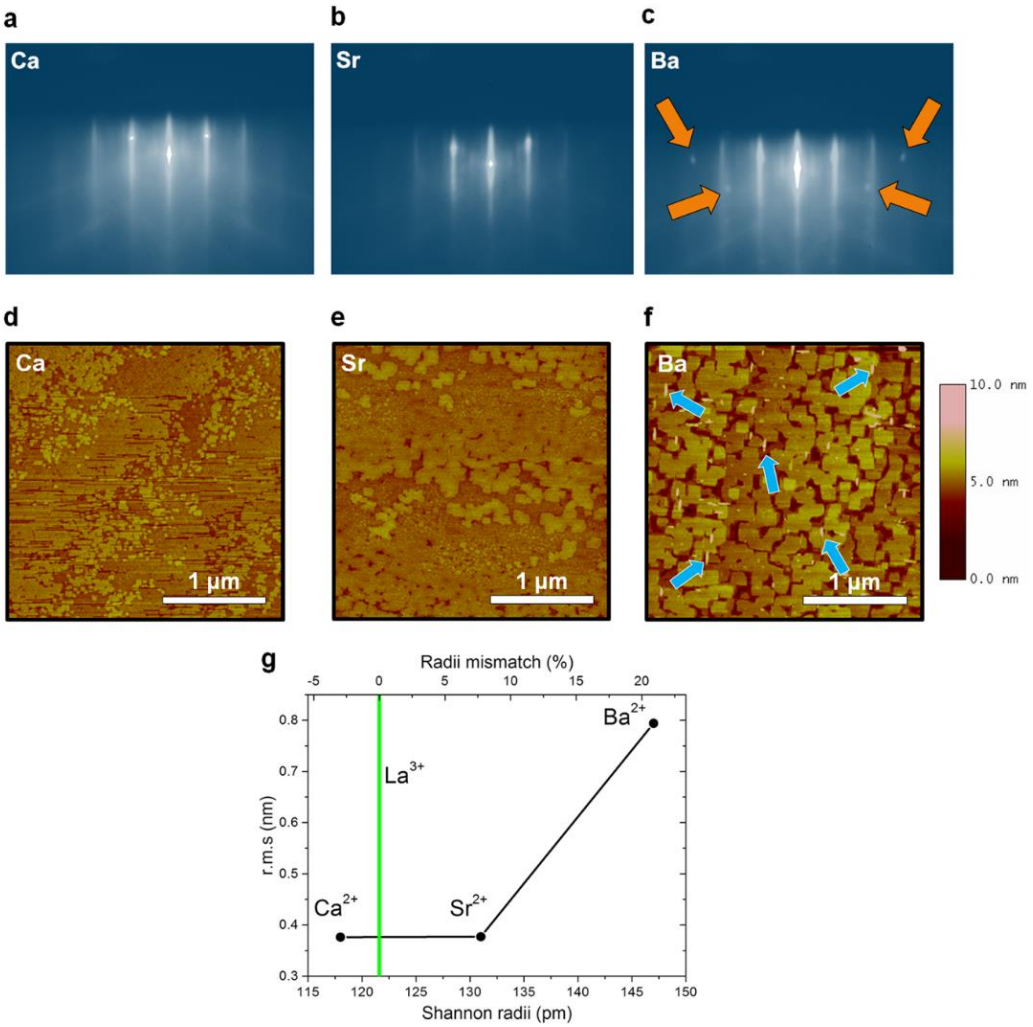

Figure 4.1.2. RHEED patterns of the three different bilayers: a) LCCO/LCO, b) LSCO/LCO, c) LBCO/LCO. AFM images of the top surface of the three different bilayers: d) LCCO/LCO, e) LSCO/LCO, f) LBCO/LCO. One can observe the different surface morphology, in particular, in the case of LBCO/LCO, secondary phase precipitates can be observed (some are marked by blue arrows). The atomic steps with heights of less than one unit cell (u.c.) are attributed to a small substrate miscut angle (~0.1°). g) rms roughness values of three bilayers versus cation radius (pm). Reproduced from *Suyolcu et al.* [79].

In order to rationalize such findings, a systematic investigation on the surface morphology of each bilayer is performed by means of AFM. Typical AFM images of three different bilayers are presented in Figures 4.1.2d–f for LCCO/LCO, LSCO/LCO, LBCO/LCO bilayers, respectively. Indeed, these three different bilayers have slightly different surface morphology, i.e. as the dopant size increases from Ca to Ba one can see that the surface becomes visually rougher. This indicates the influence of the dopant on the surface mobility of incoming atoms. Additionally, in Figures 4.1.3a–c higher magnification AFM images and in Figures 4.1.3d–f related, representative linescan profiles are displayed for Ca-, Sr-, and Ba-doped bilayers, respectively. The linescan profiles are obtained along the blue arrows indicated on the AFM images. Such profiles demonstrate that in the case of the Ba-doped bilayer, one can see relatively high (~3-4 nm) secondary-phase precipitates, while the roughest points in the case of Ca- and Sr-doped bilayers are measured as ~1 nm. To quantify the surface roughness, the root mean square (rms) value is used over the full scanning area. The images (and the

linescan profiles) clearly demonstrate that Sr-doped and Ca-doped samples have atomically smooth surfaces, whereas the Ba-doped sample is characterized by a remarkably rougher surface. In the case of LCCO/LCO and LSCO/LCO bilayers, the rms roughness was measured as 0.377 nm and 0.376 nm over a scanning area of 6.25 μm^2. In the case of the LBCO/LCO bilayer, instead, the rms roughness is 0.805 nm, i.e. twice as large over the same scanning area. Most importantly, in the latter, secondary-phase precipitates (indicated with light-blue arrows on Figure 4.1.2f), are detected as already observed by RHEED during the growth. A plot of the rms surface roughness of the bilayers vs. the dopant cation radius (pm) is presented in Figure 4.1.2g.

Moreover, with the aim of specifically addressing the Ba segregation issue, we have grown more than 50 single-phase Ba-doped LCO epitaxial films with different Ba concentrations in the range from 0.05 to 0.35 on LSAO (001) substrates. None of these films show ideal growth and are free from formation of secondary phase precipitates. However, the critical thickness, at which secondary phase precipitates nucleate, decreases linearly as the Ba concentration increases (Figure 4.1.3g). A typical RHEED image of a precipitate-free single-phase LBCO (x = 0.18) film with a thickness less than the critical thickness (<5 u.c.) is shown in the bottom inset in Figure 4.1.3g, while the upper inset is an RHEED image of a film thicker than the critical thickness of precipitate formation for this doping level (> 6.5 u.c.). Note that the diffraction from the LBCO/LCO bilayer exhibits a similar pattern with characteristic spots (cf. Figure 4.1.2). A typical AFM image of the 15 u.c. LBCO single-phase film, in which secondary-phase precipitates are clearly observed, is shown in Figure 4.1.3h. For this particular sample, the rms surface roughness is ~1.74 nm, which is twice as large as in an M–I bilayer with a 3 u.c. thick overdoped Ba layer. Furthermore, indirect observations claiming that the precipitates are Ba-rich compared to precipitate-free areas are confirmed by using Auger electron spectroscopy (AES). However, quantifying the chemical composition more precisely is beyond the AES resolution. [79]

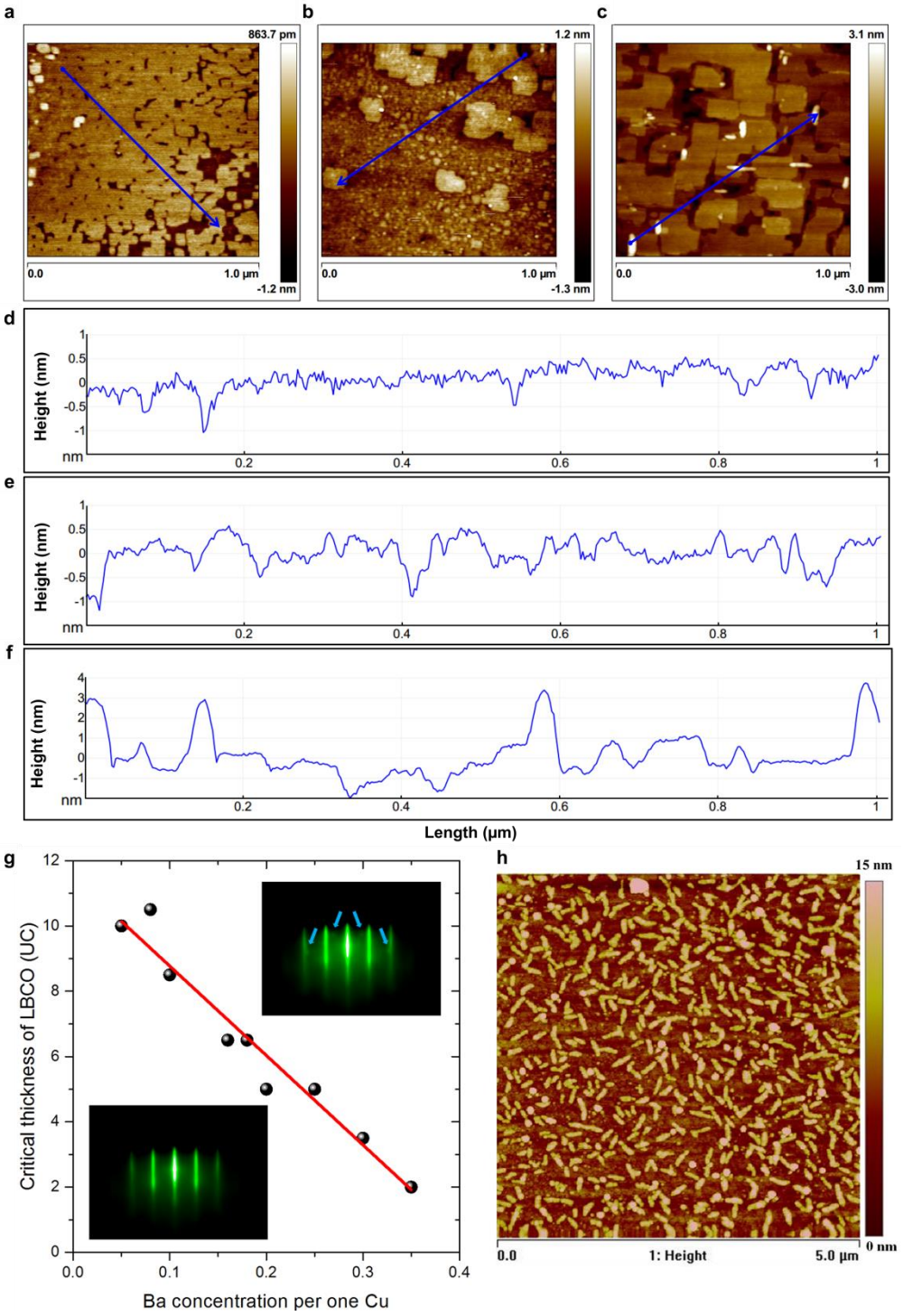

Figure 4.1.3. High magnification AFM images of three different bilayers: a) LCCO/LCO, b) LSCO/LCO, c) LBCO/LCO. Line scan profiles obtained from the AFM images given in a-c: d) LCCO/LCO, e) LSCO/LCO, f) LBCO/LCO. One can observe the different surface morphology. In the case of LBCO/LCO, secondary phase precipitations can be observed with up to 3-4 nm height. g) The critical thickness of the LBCO film versus Ba concentration at which RHEED patterns indicate nucleation of secondary phase precipitates. The top inset RHEED image has extra diffraction spots in comparison to the bottom RHEED image. h) AFM image of a 15 u.c. thick LBCO (x = 0.18) film on LSAO (001) substrate. Reproduced from Suyolcu *et al.* [79].

For structural quality determination, first, XRD measurements are figured out, and the results are compiled in Figure 4.1.4. From the position of Bragg peaks (00l), where l = 2, 4, 6, and 8, the average *c*-axis lattice parameter for each bilayer was calculated and the results are presented in Figure 4.1.4a-c for Ca-, Sr- and Ba-doped bilayers, respectively. [52] Through the data, the shortest *c*-axis lattice constant (13.22 Å) was observed for the LCCO/LCO bilayers, whereas the *c*-axis lattice parameters are measured as 13.28 Å and 13.37 Å for the LSCO/LCO and LBCO/LCO bilayers, respectively. XRD Θ–2Θ diffraction scans for three different bilayers demonstrate a single peak for the two phases in a similar way to what was reported by Butko *et al*. [52]. Such findings nicely correlate with the nominal cationic radii in nine-fold coordination as a consequence of Madelung strain (Figure 4.1.4d).

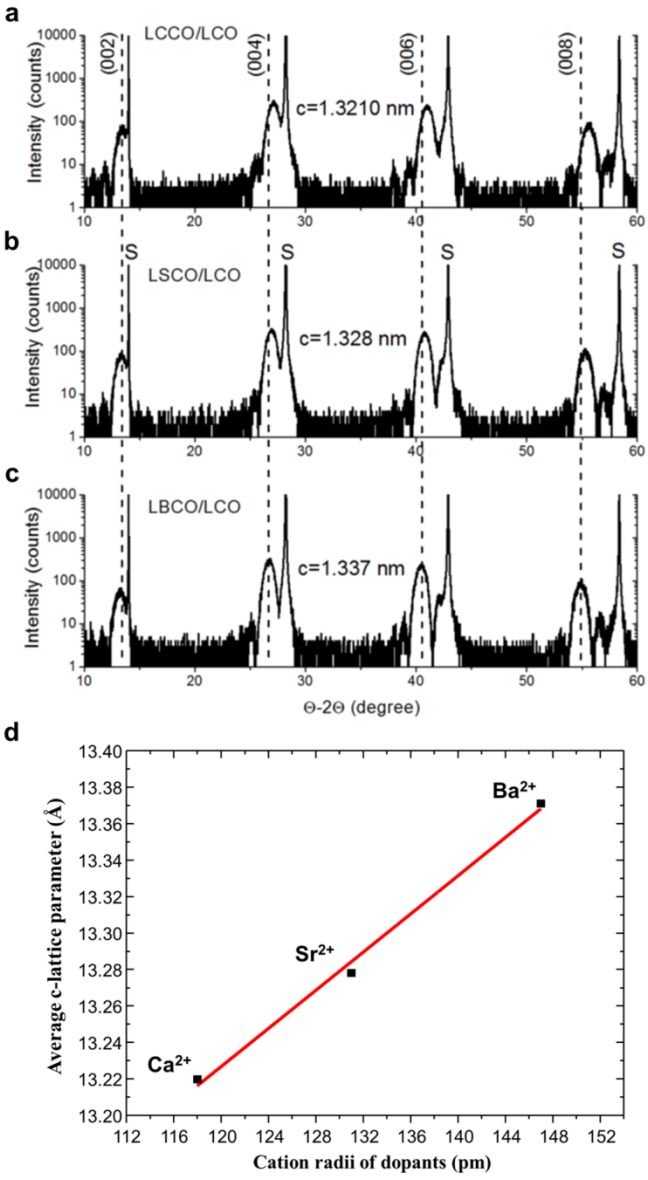

Figure 4.1.4. XRD θ-2θ scans for three different bilayers: a) LCCO/LCO, b) LSCO/LCO, and c) LBCO/LCO and d) *c*-axis lattice parameter versus ionic radii of dopants in three different bilayers: LCCO/LCO, LSCO/LCO, and LBCO/LCO. Reproduced from Suyolcu *et al.* [79].

DC resistance and magnetic susceptibility measurements in a parallel geometry provided information regarding the superconducting properties of such samples. The most significant data are presented in Figure 4.1.5. In panels a, b, c, the temperature dependence of the electrical resistance is shown for LCCO/LCO, LSCO/LCO, and LBCO/LCO, respectively; the corresponding magnetic susceptibility measurements are displayed in panels d, e, f. The superconducting transition temperature, T_c, was determined from the resistivity measurements as the temperature at which the resistance drops to zero. Notably, these values coincide with the temperatures where the real and the imaginary parts of the mutual inductance signals start to deviate from the normal state values.

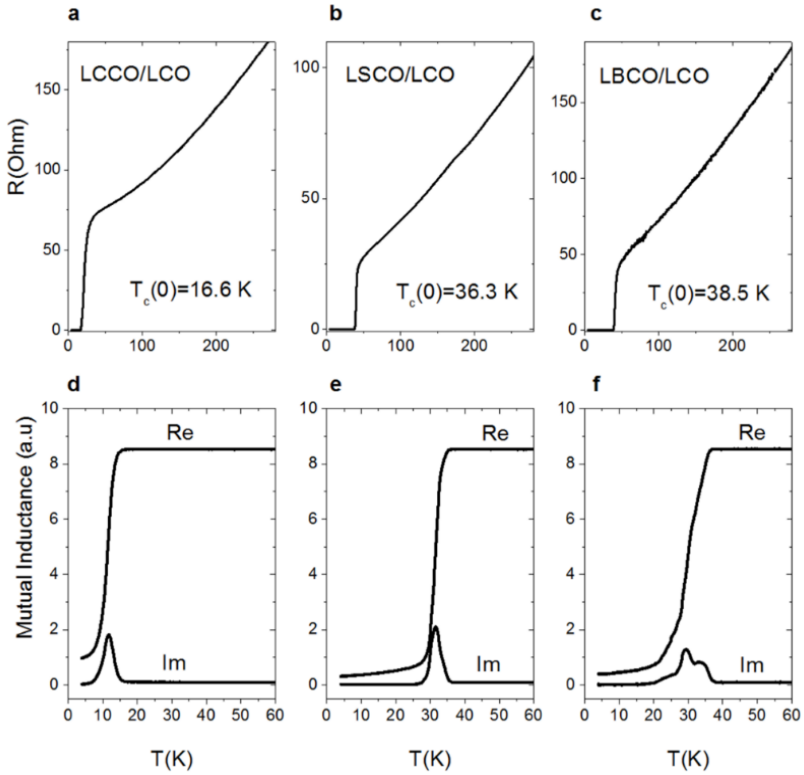

Figure 4.1.5. Transport measurements for three different bilayers. The upper panels show resistance versus temperature for a) LCCO/LCO, b) LSCO/LCO, c) LBCO/LCO, whereas the bottom panels show the real (Re) and imaginary (Im) parts of mutual inductance measurements for d) LCCO/LCO, e) LSCO/LCO, f) LBCO/LCO. Reproduced from Suyolcu *et al.* [79].

For the LCCO/LCO system, the superconducting critical temperature, T_c, is ~17 K, whereas it is ~36 K in the case of the LSCO/LCO bilayer, which is consistent with the literature [51]. For the LBCO/LCO bilayers, a ~10% enhancement of the T_c value compared to the T_c for LSCO/LCO bilayers was obtained (T_c ~39 K). Most importantly, the linear correlation between the *c* axis parameter and T_c, as it was proposed in the literature (Ref. [52]), does not hold in the present case (see Figure 4.1.6). Lastly, a small systematic shift of Sr- and Ca-doped bilayers' *c*-lattice parameters compared to the literature data was observed. This could be ascribed to the difference in the layer thicknesses, since the layers grown in Ref. [52] are 20 u.c. thick, whereas in our case they are just 3 u.c. thick, thus being possibly affected by a different in-plane strain state.

While the linear extrapolation of T_c vs c data would lead to a $T_c \sim 65$ K, the measured value is remarkably lower (only ~39 K). In addition, the transition to the superconducting state in the mutual inductance measurements of LBCO/LCO bilayer is broad ranging from 38.6 K to 20 K with several peaks in the real part, suggesting the presence of regions having different superconducting critical temperatures (Figure 4.1.5f). An overview of the main results including surface roughness, average *c*-axis lattice constant, and T_c is presented in Table 1. There exists a strong impact of different cations on the superconducting and structural properties of bilayers grown under the same conditions.

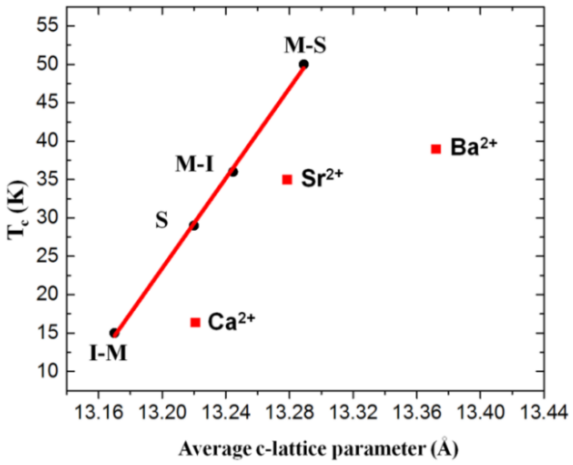

Figure 4.1.6. Dependence of T_c on the average *c*-axis lattice parameter. The red squares show the T_c values measured in Ca-, Sr-, and Ba-doped bilayers in the present study, whereas the black circles refer to I–M (La_2CuO_4 / $La_{1.56}Sr_{0.44}CuO_4$), S (superconducting; $La_2CuO_{4+\delta}$), M–I ($La_{1.56}Sr_{0.44}CuO_4$ / La_2CuO_4) and M–S ($La_{1.56}Sr_{0.44}CuO_4$ / $La_2CuO_{4+\delta}$) structures as reported in Ref. [52]. Reproduced from Suyolcu *et al.* [79].

Table 1. Summary of electrical and structural measurements for Ca, Sr, and Ba doped bilayers.

Structure	T_c (K) (from inductance)	T_c (K) (from resistance)	Roughness [nm]	*c*-axis parameter [Å]
LCCO/LCO	16.1	16.6	0.37(7)	13.21(98)
LSCO/LCO	35.8	36.3	0.37(6)	13.27(53)
LBCO/LCO	38.1	38.6	0.80(5)	13.37(01)

In order to gain deeper insight on the interfacial situation and possibly on the discrepancy between the present *c* vs T_c dependence in comparison with the literature, atomically resolved imaging and spectroscopy were carried out by high-resolution STEM. High-angle annular dark-field (HAADF) images taken from each bilayer proved the growth quality and defect-free structures. Figure 4.1.7a depicts the microstructure of the LCCO/LCO bilayer. All atomically resolved HAADF images were taken along the [100] direction of the LSAO substrate. The HAADF image, where the contrast slightly changes in the first two unit cells from the substrate/LCCO bilayer interface, demonstrates the high epitaxial quality of the LCCO/LCO bilayer, a coherent interface, and the absence of extended defects such as misfit dislocations and/or stacking faults. An atomically resolved

image at a higher magnification of the highlighted region in Figure 4.1.7a is presented in Figure 4.1.7b. Figure 4.1.7c shows the intensity profile of the HAADF image taken from the Ca-doped bilayer presented in Figure 4.1.7a. The black arrow indicates the vertical length used for averaging (Figure 4.1.7a). On the HAADF image, Ca-doped areas exhibit a darker contrast, while undoped LCO layers appear brighter. Because the HAADF image intensity is approximately proportional to $Z^{1.7-2}$ (where $Z_{La} = 57$ and $Z_{Ca} = 20$)) [33,105], the intensity increase in the first 1-2 unit cells corresponds to the Ca-depleted region followed by a Ca-doped region with lower intensity. To the best of our knowledge, this is the first example of a successfully grown overdoped LCCO epitaxial layer.

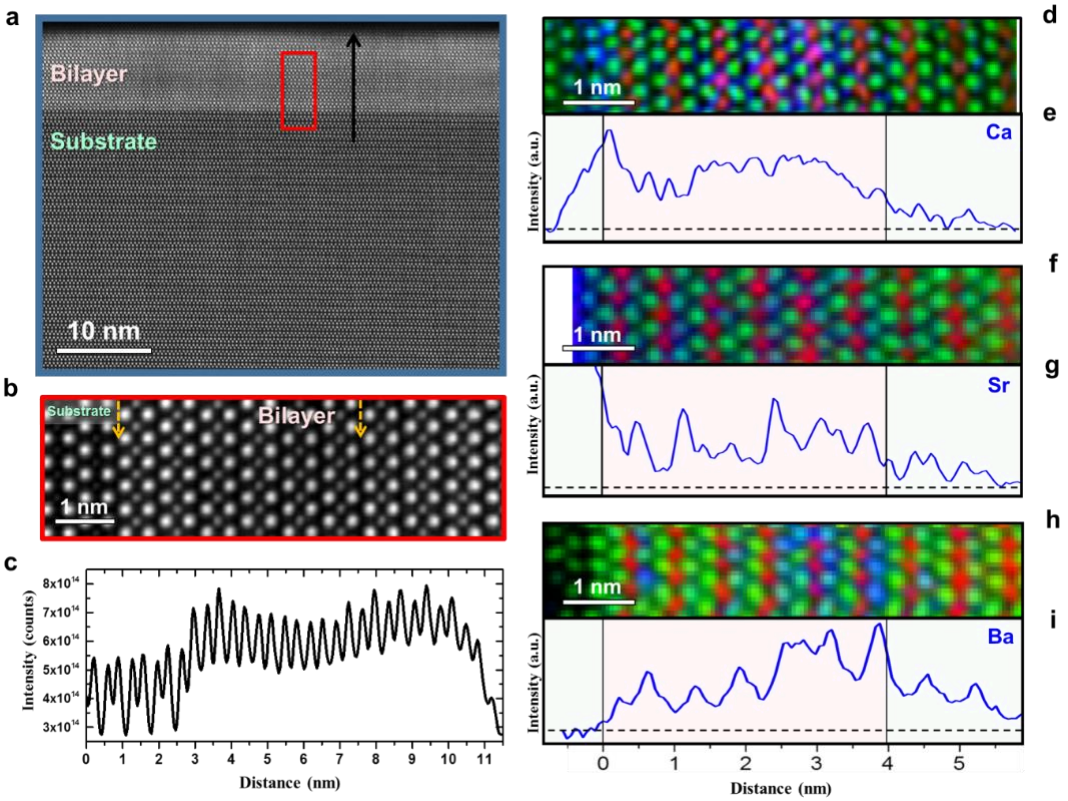

Figure 4.1.7. Atomically resolved STEM imaging and EELS spectrum imaging. a) HAADF image showing the growth quality, a defect-free structure and coherent interfaces of LCCO/LCO. b) High magnification of the area highlighted by the red rectangle in a. In d, f, and h, RGB elemental maps (La = green, Cu = red, dopant = blue) are shown. In e, g and i the Ca-, Sr- and Ba-doped bilayers dopant distributions, as obtained from the maps in (d), (f), and (h), are displayed. Reproduced from Suyolcu *et al.* [79].

Figures 4.1.7d, 4.1.7f, and 4.1.7h show RGB (red is Cu, green is La, and blue is dopant) atomic resolution maps of Ca, Sr, and Ba-doped bilayers as measured by EELS. The average profiles of the dopant distributions obtained from the EELS maps are shown below each RGB map in Figures 4.1.7e, 4.1.7g, and 4.1.7i. The nominal interfaces are shown by black lines. To exemplify the base level for the dopant signal observed, the Ba profile averaged from the RGB map of the Ba-doped bilayer (see next section, Figure 4.2.2d) is presented in Figure 4.1.8 below.

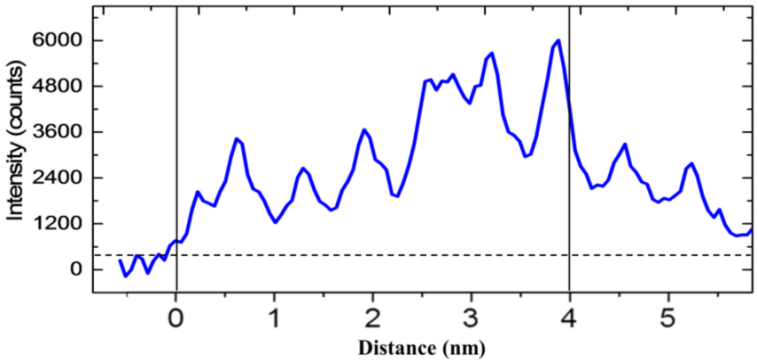

Figure 4.1.8. Dopant distribution of the Ba-doped bilayer as a plot of intensity vs. distance obtained from the map in Figure 4.2.2d. The vertical lines indicate the nominal interfaces and dashed lines indicate zero intensity. Reproduced from Suyolcu *et al.* [79].

The RGB maps and the average profiles of dopant distributions for Ca-, Sr-, and Ba-doped bilayers exhibit characteristic differences. Sr-doped bilayers show the most homogeneous distribution among the dopants (see Figures 4.1.7f and 4.1.7g). The abruptness of the LSCO/LCO interface can be estimated from the decay of the Sr distribution from the M layer into I layer as ~1.6 ± 0.4 nm, which is in fairly good agreement with the values reported in the literature [10] for a related system. Conversely, the distribution of Ca and Ba dopants in LCCO/LCO and LBCO/LCO bilayers is less homogeneous. For averaging the distribution lengths from EELS line scans (for each dopant) several line scans acquired from different regions of the samples are used.

The atomically resolved EELS RGB map shown in Figure 4.1.7h shows that the Ba concentration increases in the M phase towards the LBCO/LCO interface. This trend is also confirmed by the averaged profile of the Ba dopant presented in Figure 4.1.7i and clearly demonstrates the tendency of Ba to segregate towards the free surface of the film. Most importantly, as a consequence of such Ba migration, the LBCO/LCO interface is quite smeared, i.e. the decay length of Ba ions, obtained as an average from several EELS linescans, is 2.6 ± 0.6 nm, which is considerably larger with respect to the other dopants. Note that some linescans – as the one displayed in Figure 4.1.8 – exhibit a Ba distribution involving the whole nominally undoped area. This may be related to the presence of secondary phase precipitates at the film free surface as observed by RHEED and AFM (see Figure 4.1.2).

As far as the LCCO/LCO bilayer is concerned, a tendency to Ca accumulation at the interface between the substrate and the epitaxial layer is observed and is followed by a depletion of Ca on the 1st and 2nd unit cells (see Fig. 4.1.7a-c). This is visible in the magnified RGB EELS map and average Ca profile in Figures 4.1.7d and 4.1.7e, respectively. Such an anomalous behavior may be connected with the compressive in-plane strain in the film and will be the object of further investigations. In this case, the extent of cationic intermixing at the M–I interface can be estimated to be ~1.4 ± 0.4 nm. Please note that in this section, the RGB elemental maps obtained from each bilayer were presented, however, in the next section, all elemental maps, i.e. La, Cu and each dopant Ba, Sr and Ca, for individual atoms are displayed (Figures 4.2.3–4.2.5). The EEL spectrum images were processed using the multivariate weighted principal component analysis routine (PCA) (MSA Plugin in Digital Micrograph) developed by M. Watanabe [124] to reduce the noise in the data. In order to separate overlapping edges in each spectrum, such as La-$M_{5,4}$, Cu-$L_{3,2,}$ and Ba-$M_{5,4}$, multiple linear least square fitting (MLLS) [122] was used. For overlapped signals, MLLS fitting windows of 650–1100

eV for Ba-$M_{5,4}$, La-$M_{5,4}$, Cu-$L_{3,2}$, 305–390 eV for Ca-$L_{3,2}$, and 1750–2100 eV for Sr-$L_{3,2}$ edges were used. The integration windows used for Ca-$L_{3,2}$, Ba-$M_{5,4}$, La-$M_{5,4}$, Cu-$L_{3,2}$, Sr-$L_{3,2}$, and edges are 343–394 eV, 772–815 eV, 822–868 eV, 935–961 eV, 1935–2066 eV, respectively.

Discussion

The present investigations highlight the profound impact that the choice of the dopant has on the final structural properties of the bilayers, and how this affects the resulting electrical transport properties of the system. In particular, it is observed that the average out-of-plane *c*-axis lattice parameter as measured by XRD (Figure 4.1.4), which is an average over the whole thin-film volume, exhibits a strong dependence on the dopant species, i.e., *c* is proportional to the dopant ionic radius (the larger the dopant radius the larger is the lattice parameter) (Figure 4.1.4d). This allows us to tune *c* simply by changing the dopant species while keeping the ionic charge constant. Interestingly, although Ca^{2+} ions are smaller than La^{3+} ions, the Ca-doped bilayer has a larger *c*-axis lattice parameter than pure LCO. This can be explained by the different valences of Ca (2+) and La (3+). Ca^{2+} replaces La^{3+} and maintains the nine-fold coordination. Therefore, Ca^{2+} constitutes a negative charge on the A-site. The electrostatic repulsion of this negative charge with neighboring oxygen ions results in a lattice expansion.

A major impact of the dopant size on the in-plane strain state of the films is expected in a similar way as was already demonstrated by Lee *et al*. for a related perovskite system. [99] In particular, when Ba^{2+} is employed as a dopant, i.e. in the case of LBCO/LCO bilayers, the maximum in-plane strain is induced. As the HAADF images show perfect epitaxial growth of all films without formation of misfit dislocations or other defects which could relieve strain, the only way to obtain strain relaxation in the case of the Ba-doped system is by the rearrangement of dopants within the film, i.e. the segregation of excess Ba towards the film surface. This explains the formation of a secondary phase (likely Ba-based) at the surface [75,77], as shown by AFM and RHEED images (Figure 4.1.2c–f) and revealed by AES. [79] It also explains, why in the case of single-phase films, the critical thickness of precipitate formation during the growth is decreasing with increasing Ba concentrations (see Figure 4.1.3g). The absence of such precipitates in LCCO and LSCO films indicates that Ca^{2+} and Sr^{2+} ions, whose ionic size is more similar to La^{3+}, are accommodated in the thin film, i.e. the in-plane strain is maintained. Our results are consistent with those of Lee *et al*. [99] who found that the smaller size mismatch between the La^{3+} host and dopant cations reduces the segregation level of the dopants. Notably, whereas a homogeneous dopant profile was found in the Sr-doped bilayers, also the Ca-doped bilayers exhibit a certain tendency to inhomogeneity, i.e. Ca^{2+} accumulates towards the substrate possibly as a consequence of the strain state at the substrate-film interface.

A strong deviation from the expected linear dependence of T_c on the *c*-axis lattice parameter for M–I bilayers is revealed – with T_c of the LBCO/LCO bilayer being lower than expected – while the *c*-axis lattice parameter is increased. Whereas the linear extrapolation of T_c vs *c* leads to a predicted T_c ~65 K, the measured value is only ~39 K. In order to explain this, one needs to consider the dopant distributions at each interface. The average cationic intermixing extent is as high as 2 u.c. in the case of LBCO/LCO bilayers (the wide Ba distribution is also detected by EELS line scans (see Figure 4.1.8)). This anomalous Ba redistribution is a consequence of Ba segregation towards the film surface, which eventually results in a particularly smeared M–I interface. Such a finding can account for the reduced T_c for the LBCO/LCO bilayers as demonstrated recently for a related LCO-based

system, for which a smeared interface leads to classical doping, the so-called "homogeneous doping" [55]. At equilibrium, the hole concentration is increased in correspondence to the randomly distributed ionic dopant point defects, rather than to an interface effect, and defines the final local physical properties. In such a situation (only homogeneous doping is active), one expects T_c not to exceed the values which are normally obtained in doped single-phase systems, i.e. max T_c ~40 K for optimally doped LBCO samples epitaxially grown on $LaSrAlO_4$ (001) substrates [149]. The two superconductivity mechanisms are illustrated in Figure 4.1.9 below.

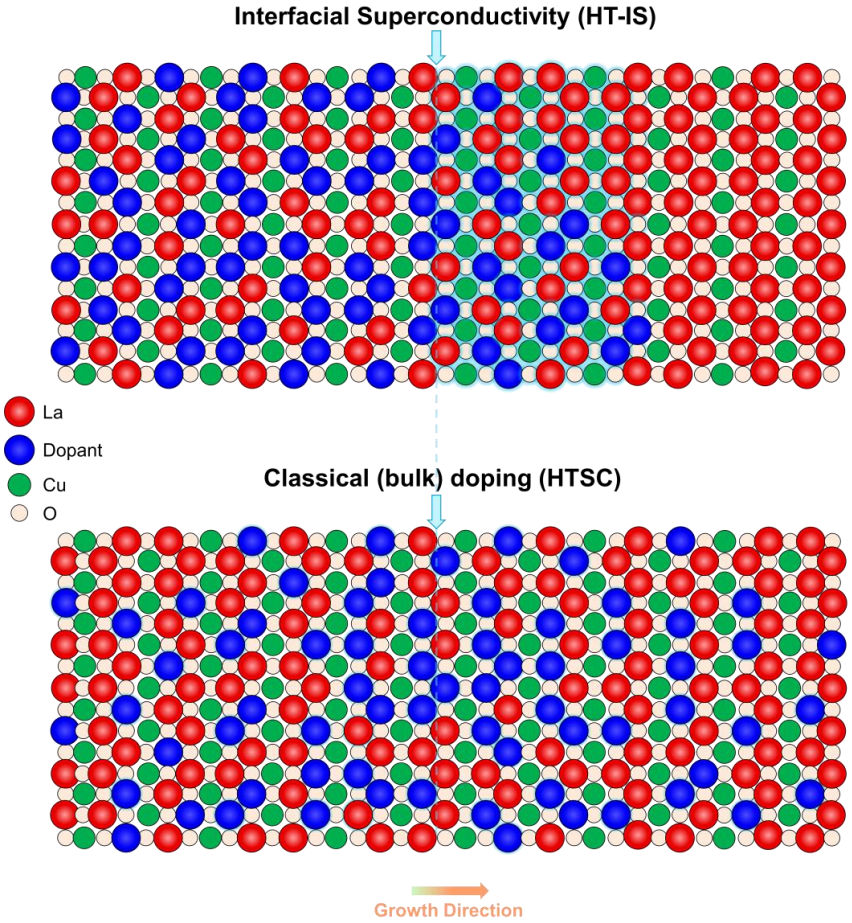

Figure 4.1.9. Illustration of two different superconductivity mechanisms observed in M–I bilayers: Interface superconductivity (HT-IS; i.e. Sr- and Ca-doping, top) vs. bulk superconductivity (HTSC; i.e. Ba-doping, bottom). Due to different dopant distribution based on the dopant size (i.e. Ca and Sr vs. Ba), different superconducting mechanisms are induced. The turquoise arrows indicate the nominal M–I interface position.

For both systems, despite a certain dopant redistribution is present at the interface, the behavior is believed to be consistent with the typical HT-IS. In the case of the LSCO/LCO interface, as investigated by *Gozar et al*. [10,136], Sr spread into the nominally undoped phase for about 1 u.c., i.e. 1.3 nm, in agreement with our observations on both LCCO/LCO and LSCO/LCO structures. Nonetheless, these findings undoubtedly enable to ascribe the HT-IS to an electronic effect, rather than to ionic doping. Therefore, in the present work, the reduced T_c of the LCCO/LCO interface (the dopant spread beyond the interface is 1.4 nm), may be linked to the small *c*-axis parameter, in agreement with the linear *c*–vs–T_c relation. The Sr-doped bilayers show consistency with the previous studies, not only in T_c but also in the Sr redistribution length. [10]

Conclusions

In conclusion, a number of complementary experimental methods, including high-resolution XRD, AFM, transport measurements and spherical aberration-corrected STEM-EELS is used in order to study high-temperature superconducting interfaces in $La_{1.6}A_{0.4}CuO_4$/ La_2CuO_4 bilayers grown by atomic-layer-by-layer oxide MBE, where A = Ca^{2+}, Sr^{2+}, and Ba^{2+}. It is found that the *c*-axis lattice parameter increases linearly with the dopant size. T_c was found to depend non-linearly on the average *c*-axis lattice constant and saturates at about 40 K, whereas T_c was expected to rise up to about 70 K for the LBCO/LCO case, due to the interplay between the hole leakage and Madelung strain. This is assigned to a different redistribution of the dopant ions across the interface. In particular, as a consequence of the large ionic size mismatch between the dopant and the host cation, Ba segregation occurs and gives rise to a smeared interface. In the case of LCCO/LCO and LSCO/LCO systems, the interfaces were found to be sharper (yet not atomically sharp). As a consequence of such a different interface structure, distinct phenomena occur for inducing the interface superconductivity: in the LCCO/LCO and LSCO/LCO cases, interface effects, i.e. electronic redistribution, are predominant, whereas, in the case of LBCO/LCO, HTSC is rather ascribed to the "classical" homogeneous doping determined by cationic intermixing. In such a "conventional" situation, the expected T_c enhancement due to the interface effect is prevented.

This work highlights the profound impact that ionic intermixing may have on the definition of the final properties of oxide epitaxial interfaces and demonstrates that future studies of ionic effects at interfaces, in particular on cationic redistribution during growth, are of paramount importance for the full understanding of such structures.

4.1.2 Visualizing Jahn–Teller and anti-Jahn–Teller distortions

Introduction

Key properties of complex perovskite oxide structures are strongly influenced by small structural changes of the BO_6 octahedral network [151–155] and tailoring and tuning lattice distortions can be achieved by strain states imposed, e.g., by the lattice mismatch between substrate and film in epitaxial systems.[86,152,156–158] Thus, understanding how octahedral distortions are correlated with dopant distribution and how they modify the functionality of complex oxide heterostructures is of great significance.

The Jahn–Teller (JT) effect is a spontaneous geometric distortion of a non-linear system in an electronic state with orbital degeneracy and results in removing the degeneracy via energy state splitting and lowering its symmetry. [23] TMOs with octahedral coordination, in which the metal ion has high-spin d^4, low-spin d^7, and d^9 configurations, show JT distortions, which can be intimately correlated with the physical properties [25]. For instance, the CuO_6 octahedron in the parent La_2CuO_4 (LCO) is elongated along the *c*-axis by the JT effect [26] and exhibits two long and four short Cu–O bonds. [27] Distortions of CuO_6 in Sr-doped $La_{2-x}Sr_xCuO_4$ structures (x up to 0.4) and related changes in Cu–O apical distances were studied via diffraction techniques providing average structural information. [32] It is reported that, in such systems, increasing the dopant concentration determines the compression of the octahedron (i.e. a decrease of the Cu–O apical distances) [32] defined as anti-Jahn–Teller (AJT) effect. [26] Recently it was shown that, in the presence of interfacial electronic redistribution leading to a decoupled concentration profile between electron holes and dopant ions (striking interface effects), an anomalous elongation of the Cu–O apical distance in LCO-based structures is present (JT distortion). [33,34] Thus, local JT distortions appear to be strongly related to the presence of 2D interfacial superconductivity. Moreover, investigations on $La_{2-x}A_xCuO_4$ (LACO)–LCO bilayers [79] (where A is a divalent cation A = Sr, Ba, Ca) and two-dimensionally doped La_2CuO_4 superlattices [33,55] pointed out that the dopant size and dopant distribution directly influence the interface functionalities, i.e., the occurrence of the bulk-like or interfacial superconductivity, as discussed in the previous section. In particular, the interfacial superconductivity is induced only in the presence of a sharp interface. These findings pave the way for new promising investigations on local distortions at such interfaces induced by different dopant distributions. In this context, it is essential to probe the cation displacements and the octahedral tilts via a precise determination of the atomic column positions and to correlate this with atomically resolved information of the chemical composition.

In this work, new insights into LACO–LCO bilayers with differently sized dopants, i.e. A = Ba, Sr, and Ca, having same formal valence state (2+), which allows systematically studying the effect of the dopant size on octahedral distortions, are provided. Although octahedral distortions at the interface of various heterostructures have been widely studied recently [151–153,159–161], the present understanding of A_2BO_4 systems is, in this sense, still limited. Previous investigations of LCO-based bilayers have been limited to Sr-doped systems [34] or, in the case differently sized dopants have been used, no insights have been gained regarding the local lattice structural parameters [79]. Here, by analyzing the cationic and anionic deformations with atomic resolution, it is shown that the size mismatch between the dopant and the host La^{3+} cations directly affects the structure and in particular the out-of-plane strain state. [99] It is further demonstrated that the dopant size locally distorts both cationic (La–La) and the anionic (O–O sublattice) and different JT distortions are

present. A comparative study gathered from hole-doped La_2CuO_4 structures combining different STEM techniques (i.e. EELS, ABF, and HAADF imaging) which link the distribution of the dopants with the CuO_6 octahedral distortions is described.

Results

The substrate used for all the samples, i.e. LSAO, has a tetragonal structure with lattice parameters a = 0.3754 nm and c = 1.2635 nm and bulk LCO has an orthorhombic structure, where Cu–O planes are separated by two La–O planes. The lattice parameters of the bulk LCO are a = 0.5335 nm, b = 0.5415 nm, and c = 1.3117 nm. [52] Because of the small difference between the in-plane lattice constants of LSAO and LCO and the existent epitaxial strain, the LCO film can be considered as tetragonal. [88] Perfect coherent interfaces between the LSAO substrates and the epitaxial layers are revealed through atomically resolved HAADF images (Figure 4.1.10. a–c), which cover the substrate and the nominal metallic and insulating phases, and demonstrate the high quality of the bilayers. The substrate gives rise to a darker contrast as compared to the epitaxial layer due to the difference of the mean atomic weight. [105]

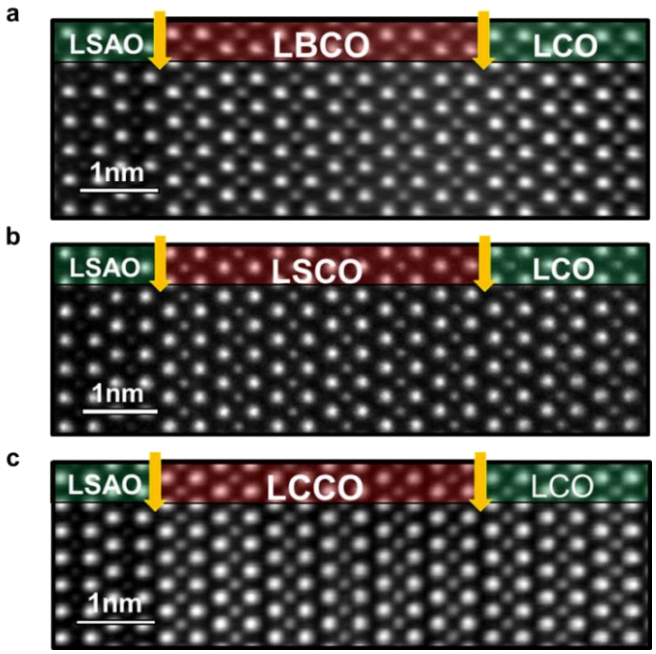

Figure 4.1.10. STEM-HAADF images showing coherent interfaces of a) Ba- (LBCO), b) Sr- (LSCO), and c) Ca- (LCCO) doped bilayers. The HAADF images were taken along the [100] direction of the LSAO substrate. Reproduced from Suyolcu *et al.* [89].

Not only the temperature dependence of the electrical resistance for the samples, where all of them exhibit a superconducting transition with critical transition temperatures (T_c) of ~39 K, ~36 K, and ~17 K for Ba-, Sr-, and Ca-doped bilayers, respectively, but also their correlation with the dopant size and distribution are discussed in the previous section. Now, the focus will be linking the dopant distribution and the correlated lattice deformations, i.e. local lattice and octahedral distortions. First, I start with the examination of the elemental distribution of each element employed in the structures,

where the comprehensive EELS analyses evidence a certain redistribution of dopants with respect to the nominal composition. Figures 4.1.11–4.1.13 exhibit atomically resolved elemental maps of Ba-, Sr-, and Ca-doped bilayers, which were all extracted from the EEL spectrum images (SIs) by fitting the EELS data to reference spectra using a multiple linear least-squares fitting procedure**.** The reference spectra were directly extracted from the experimental EELS SI. [79,122] Note that in the previous chapter the RGB elemental maps obtained from each bilayer were presented. However, in this section, all elemental maps, i.e. La, Cu, and each dopant as being Ba, Sr and Ca, for individual atoms are presented.

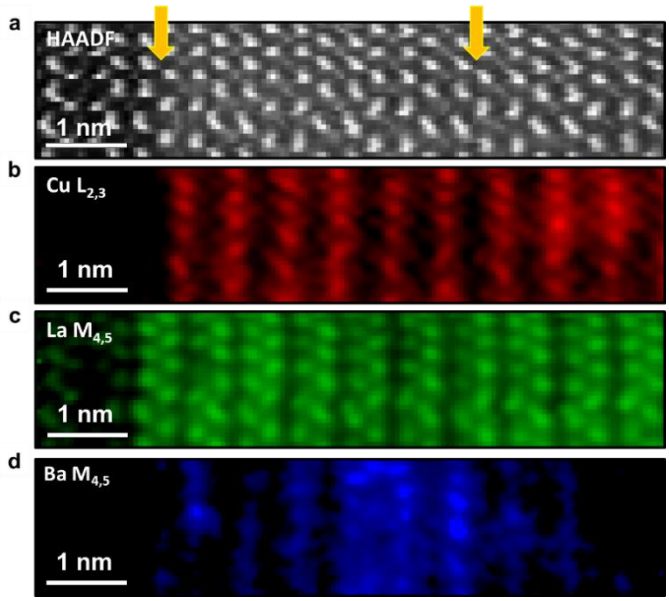

Figure 4.1.11. Atomically resolved EELS spectrum image of the Ba-doped bilayer. a) Simultaneously acquired HAADF image. (b–d) Atomically resolved Cu-L_{23} edge, La-M_{45} edge, and Ba-M_{45} edge elemental maps. The arrows indicate the nominal interface positions. Reproduced from Suyolcu *et al.* [89].

The reference HAADF survey images of the analyzed regions are presented in Figures 4.1.11a, 4.1.12a and 4.1.13a for Ba-, Sr-, and Ca-doped samples, respectively. In Figure 4.1.11b–d, atomically resolved Cu, La, and Ba elemental maps obtained from an EELS SI across the interfaces of the Ba-doped bilayer are presented. The atomically resolved La (green) and Ba (blue) maps depict a decrease in the La concentration and a concomitant increase of Ba (blue) (Figure 4.1.11d) near the nominal M–I interface within the doped phase (note that Ba^{2+} acts as a substitutional defect for La^{3+}). As a result of Ba migration, the LBCO/LCO interface appears to be smeared with 2.6 ± 0.6 nm width of the Ba distribution (Section 4.1.1). Figures 4.1.12c and 4.1.12d present the distribution of La and Sr cations in the structure, respectively. One can see that the Sr distribution at the M–I interface is more abrupt than for the Ba-doped case, despite a certain redistribution of Sr into the I phase (~ 1.6 ± 0.4 nm) is present. Finally, for the Ca-doped bilayer, a slightly lower width of Ca ions across the M–I interface (1.4 ± 0.4 nm) is observed. It should be noted here that such results are in a very good agreement with the 2D-doped La_2CuO_4 system [84], in which differently sized dopants have been introduced in the form of atomic layers in the La_2CuO_4 parent structure and the dependence of the cationic redistribution width with the dopant size has been explained on the basis of thermodynamic

considerations, i.e. equilibrium conditions establishing at the film surface during the growth process (see the Section 4.2.1 for further details).

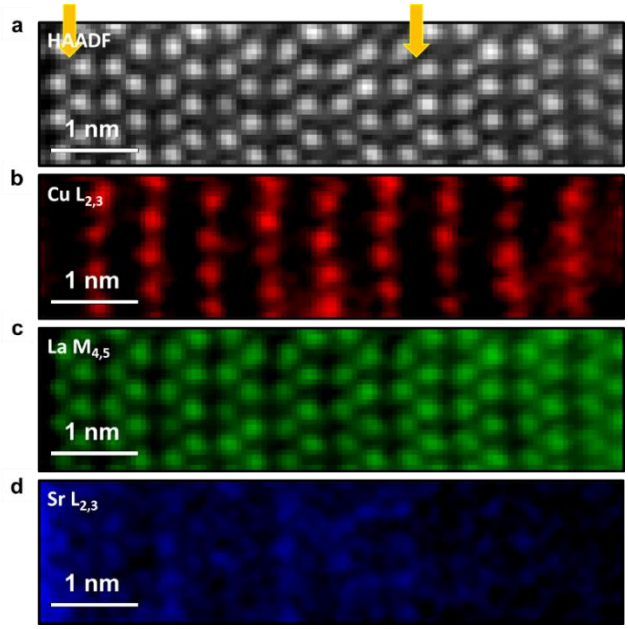

Figure 4.1.12. Atomically resolved EELS spectrum image of the Sr-doped bilayer. a) Simultaneously acquired HAADF image. (b–d) Atomically resolved Cu-$L_{2,3}$ edge, La-$M_{4,5}$ edge, and Sr-$L_{2,3}$ edge elemental maps. The arrows indicate the nominal interface positions. Reproduced from Suyolcu *et al.* [89].

The substrate-film interface (indicated by the left-hand side arrows in Figures 4.1.11 to 4.1.14) presents a peculiar behavior depending on the dopant of choice: The Ba concentration is depleted in the first layers of the M phase next to the substrate (see Figure 4.1.11), whereas a certain dopant segregation (followed by a dopant depleted region) is observed at the substrate-film interface in the Ca-case (see Figure 4.1.13). The Sr distribution in Sr-doped bilayers shows the most homogeneous distribution within the nominally doped phase.

To evaluate the dopant distribution effect on the structure of the octahedral network, HAADF (e.g. Figure 4.1.10) and ABF images (Figure 4.1.14) of the interfaces of all samples are simultaneously acquired. Thus, all atomic columns in the crystal structure, namely La/Sr–O, Cu–O, and O, were imaged. Subsequently, the interatomic apical (out-of-plane) and basal (in-plane) oxygen-to-oxygen (O–O) distances were measured by using the O–O picker software. [125] Figure 4.1.14a–c shows the atomically resolved ABF images, where all atomic columns are unambiguously resolved, showing both nominal interfaces (i.e. substrate–M layer and M–I interfaces, for Ba-, Sr-, and Ca-doped bilayers, respectively) confirming the high structural quality. In Figure 4.1.14d, the measured interatomic distances are defined (the red arrow shows the distance between apical oxygen atoms, the green arrow shows the distance between oxygen atoms in the basal plane).

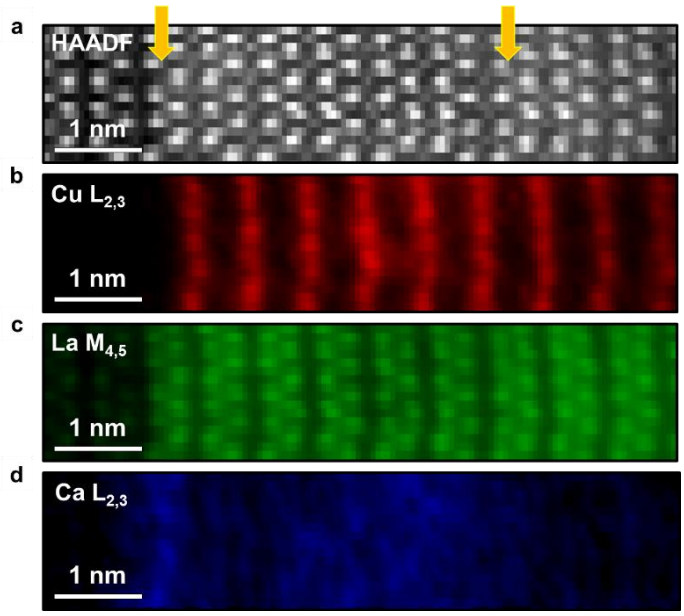

Figure 4.1.13. Atomically resolved EELS spectrum image of the Ca-doped bilayer. a) Simultaneously acquired HAADF image. (b–d) Atomically resolved Cu-L_{23} edge, La-M_{45} edge, and Ca-L_{23} edge elemental maps. The arrows indicate the nominal interface positions. Reproduced from Suyolcu *et al.* [89].

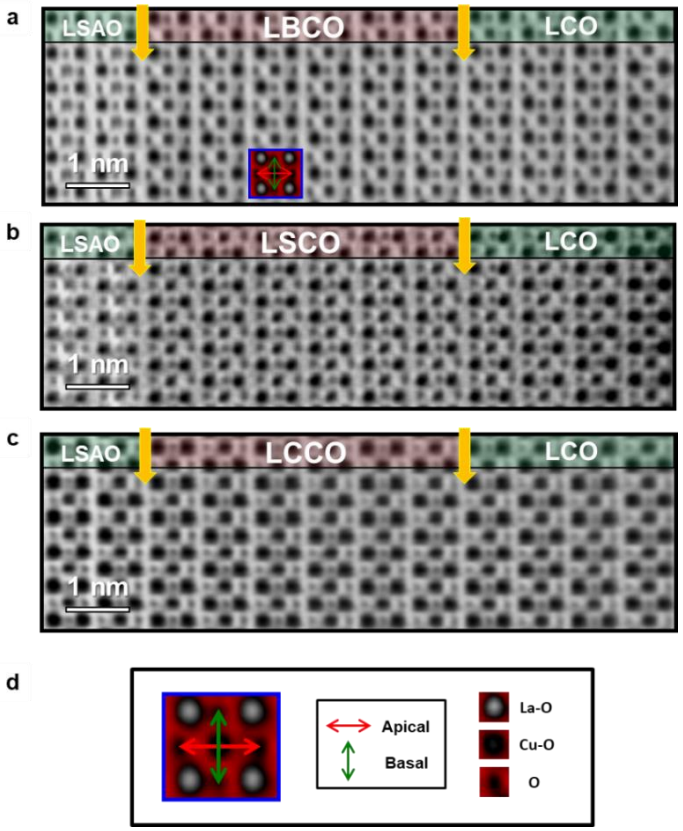

Figure 4.1.14 ABF images showing coherent interfaces and all atomic column positions including O-positions for the a) Ba-, b) Sr-, and c) Ca-doped bilayers. The yellow arrows indicate the nominal interface positions. d) Illustration of measured apical and basal O–O distances on a magnified (and colored) section obtained from (b). Reproduced from Suyolcu *et al.* [89].

By averaging the dopant intensity profiles (i.e. Ba-$M_{4,5}$, Sr-$L_{2,3}$, Ca-$L_{2,3}$) from elemental EELS SIs (e.g. Figures 4.1.11–4.1.13), integrating the intensities for each constituting block (i.e. half unit cell), summing up the values of all the constituting blocks, and scaling the doping concentration profiles in order to preserve the global stoichiometry, the dopant concentrations (x) for each constituting block, as shown in Figure 4.1.15a–c, are obtained. Measured interatomic distances vs. number of CuO_2 planes (or LCO blocks) are displayed in Figure 4.1.15d–f. The basal and apical O–O interatomic distances are plotted in green and in red, respectively. Each data point corresponds to one measured LCO block (i.e. half unit cell). The O–O interatomic distances were calibrated according to the distances measured in the LSAO (001) substrate.

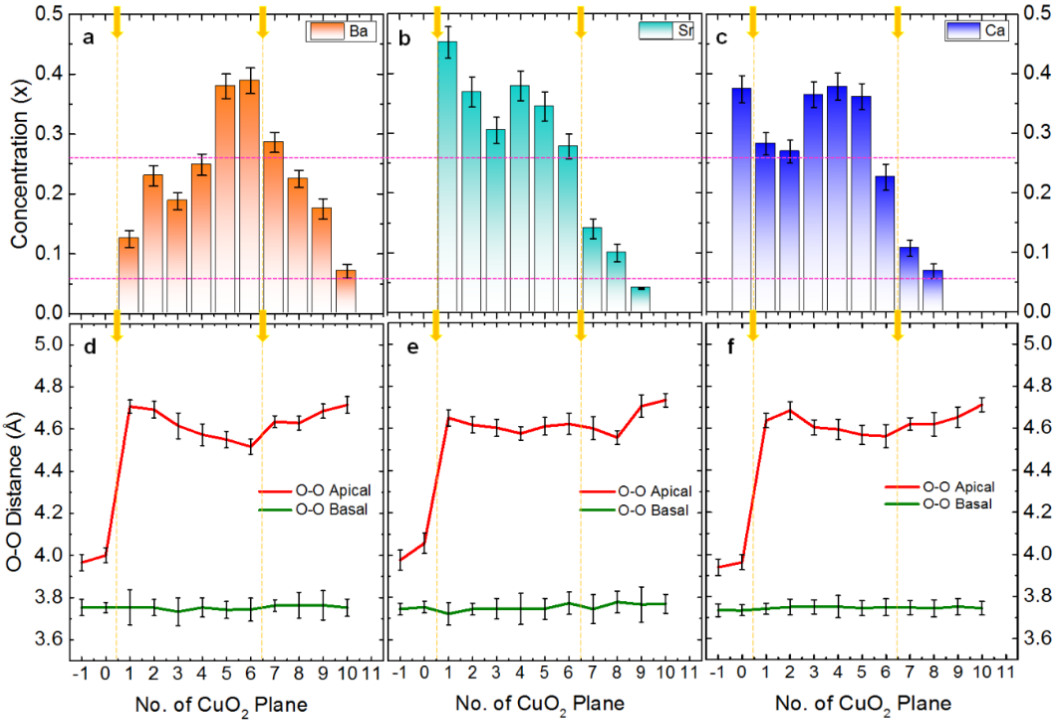

Figure 4.1.15 Graphs showing the concentration per CuO_2 block for the a) Ba-, b) Sr-, and c) Ca-doped bilayers. The horizontal dashed lines delimitate the region corresponding to the superconducting phase. (d–f) O–O atomic column spacing along the apical (red) and basal (green) directions for the LBCO/LCO, LSCO/LCO, and LCCO/LCO bilayers, respectively. The yellow arrows indicate the nominal interface positions. The error bars represent the 95% confidence interval (corresponding to 2 times the standard error) of the average of 14 unit cells of LCO along the basal direction. Reproduced from Suyolcu *et al.* [89].

All measurements of the basal in-plane O–O distances for the three different bilayers exhibit the same value within the error bars, namely 3.75 Å and exhibit a perfect coherency with the LSAO substrate. These findings show that all films are under compressive in-plane strain. [33] Conversely, in the LBCO/LCO system, a dramatic decrease of the apical oxygen distances with increasing Ba concentration (Figure 4.1.15d) is observed. In the first half unit cell (i.e. the first LCO block) of the epitaxial layer, the measured spacing is 4.72 ± 0.03 Å, whereas it is 4.51 ± 0.04 Å in the 6th LCO block (next to the nominal interface). In the following column (the one just above the nominal LBCO/LCO interface) the O–O apical distance is measured as 4.69 ± 0.030 Å. As far as the LSCO/LCO bilayer is concerned, in the highly doped region, the O–O interatomic distances remain constant (Figure 4.1.15e). However, a clear increase by 15 pm from the 8th (4.55 ± 0.03 Å) to the 9th atomic row (4.70 ± 0.05 Å) is found. Figure 4.1.15f indicates changes in the out-of-plane interatomic distances in the LCCO/LCO bilayer related to the Ca dopant distribution. In particular, large O–O distances were obtained for the first two unit cells, where the Ca concentration is less than the nominal doping level. The value measured for the 2nd epitaxial block is 4.68 ± 0.042 Å and the lowest values of around 4.56 Å are obtained for the 5th and 6th blocks yielding a decrease of the O–O interatomic distance of 12 pm. Lastly, a gradual increase starting from the 6th block is observed and the difference between 6th (4.56 ± 0.04 Å) and 10th (4.71 ± 0.03 Å) blocks is measured as 15 pm.

In order to gain deeper insights into the effects of dopant size and distribution on local A-site displacements, the basal and apical La–La atomic distances are measured. Figure 4.1.16 presents the measured distances for each sample along with one representative HAADF image (from the LBCO/LCO bilayer, Fig. 4.1.16a). The graphs (Fig. 4.1.16b–d) show La–La distances vs. number of CuO_2 planes (each plane corresponding to a building block of the LCO structure). In the LBCO/LCO bilayer, the largest and the smallest interatomic La–La apical distances are measured for the 2nd and 10th blocks as 3.73 ± 0.03 Å and 3.63 ± 0.02 Å, respectively, and exhibit a difference of ~10 pm between nominally overdoped and undoped regions (Figure 4.1.16b). Moreover, a decrease of ~7 pm is measured from the 6th block (3.71 ± 0.04 Å) to the 7th block (3.64 ± 0.03 Å), which corresponds to the nominal M–I interface. In the LSCO/LCO system (Figure 4.1.16c), the La–La distances in the overdoped layers are slightly smaller than the LBCO/LCO system (i.e. ~3.67 Å). Also here, lower La–La distance values (up to 7–8 pm difference for the 10th block (3.61 ± 0.03 Å, where x (Sr) = 0), are found for the undoped region with respect to the doped one. Figure 4.1.16d shows the results for the LCCO/LCO bilayer: Here, only a slight monotonic increase of the La–La distance in the growth direction is observed, yet mostly lying within the experimental error bars. The average La–La distance is 3.64 Å, where the highest value obtained is 3.66 ± 0.03 Å (5th block). To specifically address the dopant size effect on local La–La distortions, the local apical distances averaged from the six nominally overdoped layers (blocks 1–6) of each sample are compiled. The measurements reveal that the largest La–La apical spacing (average) (3.71 ± 0.01 Å) is observed for the Ba-doped bilayer, whereas the measured spacings are 3.67 Å and 3.63 Å for the Sr- and Ca-doped bilayers, respectively. Figure 4.1.17 shows a plot of La–La distances vs. cation radii indicating the linear correlation.

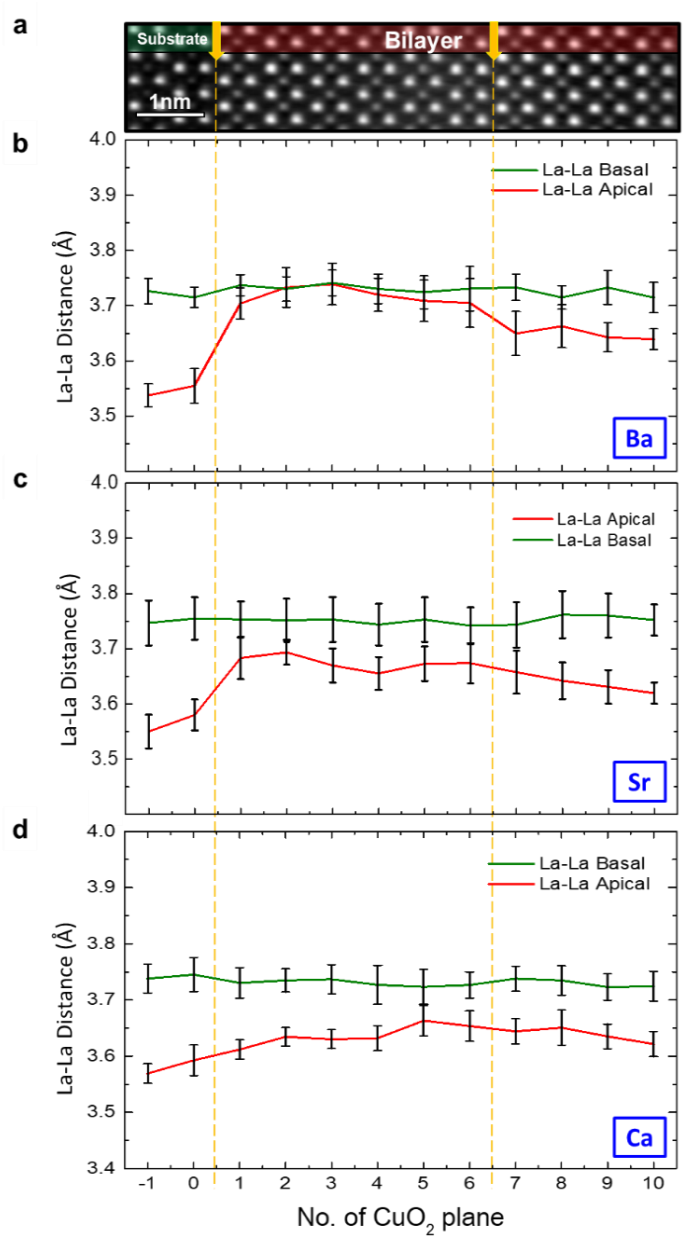

Figure 4.1.16. High-resolution STEM-HAADF image and quantitative analyses of the structural distortion in the Ba-, Sr-, and Ca-doped bilayers: a) representative STEM-HAADF image of LBCO/LCO bilayer given as a guide for the eyes; b), c) and d) La–La atomic column spacings along the basal (green) and apical (red) directions for the Ba-, Sr-, and Ca-doped bilayers, respectively. The error bars represent the 95% confidence interval (corresponding to 2 times the standard error) of the average of 14 unit cells of LCO along the basal direction. Reproduced from Suyolcu *et al.* [89].

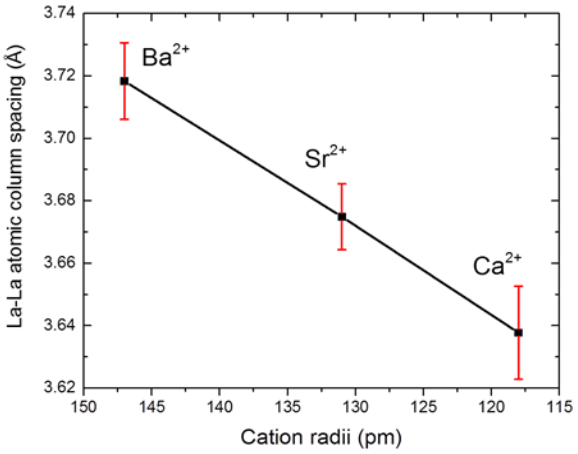

Figure 4.1.17. Dependence of local lattice parameter on the cation radii of dopants (i.e. Ba^{2+}, Sr^{2+}, and Ca^{2+}). Reproduced from *Suyolcu et al.* [89].

Discussions

Previous investigations pointed out that the choice of the dopant has a profound impact on the interface functionalities of the system. [79] From the EELS investigations, different profiles of dopant distribution for Ba-, Sr-, and Ca-doped bilayers were obtained. Figure 4.1.15a–c summarizes the dopant concentrations and gives quantitative information about the composition of each block. It is known from the electronic phase diagram of the hole-doped lanthanum cuprate system that the superconducting phase in bulk systems occurs when the doping level of a La_2CuO_4 unit cell lies between $0.05 \leq x \leq 0.26$. [47] At lower doping levels an insulating phase is present (underdoped), whereas a metallic (overdoped) phase appears at $x > 0.26$.

Let us first consider the LBCO/LCO system. According to the dopant concentrations from the EELS analyses (Figure 4.1.15a), it is evident that the blocks mostly exhibit metallic and superconducting phases. This is a consequence not only of Ba distribution at the M–I interface but also of Ba depletion at the substrate–M region. Moreover, blocks 5 to 7 are overdoped (i.e. metallic), whereas most of the other columns (blocks 1 to 4) and in the nominally undoped phase (blocks 8 to 10) show compositions which can be ascribed to the superconducting phase. This indicates that, due to ionic intermixing (i.e. to ionic doping), superconductivity should not be ascribed to effects arising at the M–I interface, rather it is a bulk phenomenon involving several unit blocks which is also evidenced via previous mutual inductance measurements. [79]

If we now turn the attention to the O–O distances of the LBCO/LCO system, the measurements performed on the ABF images (Figure 4.1.14) (with an assumption that no significant displacement of Cu atoms occurs from the center of the CuO_6 octahedron) demonstrate the decrease of the apical O–O distance with increasing Ba doping along the growth direction. The smallest apical O–O distance appears at the 6^{th} constituting block, where the highest Ba concentration is present. Above the nominal interface position (indicated by the yellow arrows in Figure 4.1.15a,d), the apical Cu–O distance starts to increase with a gradual decrease of the Ba concentration. This relationship between the Ba concentration and the apical Cu–O distance presents a clear example of an AJT distortion. [26] Therefore, the correlation between the gradient in the Ba distribution and apical O–O distances on both sides of the M–I interface could be ascribed to the AJT effect, which results in localization of holes in both $d_{x^2-y^2}$ and d_{z^2} orbitals. [89] At that point, one can argue that although a larger *c*-lattice

parameter is obtained via Ba doping in both bulk [149] and epitaxially grown structures (e.g. single phase films, M–I structures etc.), intense AJT distortions causing shorter Cu–O distances prevent probable T_c enhancements. Such suggestion may be the object of further studies performed on Ba-doped lanthanum cuprate systems similar to Sr-doped structures. [162]

As far as the Sr-doped bilayers are concerned, the obtained concentration profile shows a homogeneous distribution in the overdoped layer, which exhibits the metallic composition (x >0.26, see Figure 4.1.14), so that the HTSC stemming from "bulk" doping in the M-phase can be certainly ruled out (unlike the above-described LBCO–LCO system). A rapid fall-off in Sr concentration at the M–I interface is present. The compositional analysis suggests that blocks 7 and 8 (nominally undoped) exhibit a non-negligible Sr concentration due to dopant redistribution in growth direction (Figure 4.1.15b) [84]. It should be noted that the system under consideration is very similar to the one which has extensively been studied by Gozar *et al*. [10], in which it was demonstrated that, despite a certain ionic intermixing (whose width is very similar to what is reported here), hole redistribution from the metallic into the insulating phase was highlighted and indicated as responsible for the HT-IS. This has seen further confirmation in recent studies on related systems. [55,136]

Given the homogeneous Sr distribution in the overdoped layer, the AJT effect for the Sr-doped sample cannot be discussed directly, as the O–O distance variations are almost as small as the measurement precision (about 4 pm). [125] However, a considerable increase of the O–O apical distance starting from the 9th block is observed. Such an "anomalous expansion" has been previously reported for similar systems [33,34], in which the relation with the occurrence of HT-IS as a consequence of interface effects (i.e. interface hole redistribution) was clearly demonstrated. [51] Therefore, the observed sharp increase in apical O–O distance starting from the 9th block (JT distortion indicating localized holes in $d_{x^2-y^2}$ orbitals) can be considered as a fingerprint for a superconducting transition induced by interface phenomena, not by "ordinary" ionic intermixing. Notably, this sets a clear difference between the LBCO–LCO system and the LSCO–LCO system.

For the LCCO/LCO interface, a combination of both AJT (in the metallic phase) and JT (starting from the interface) distortions is revealed. The situation in the M-phase is similar to what has been described for the LSCO–LCO case, i.e. the dopant concentration x lies above the limit for HTSC, thus HTSC has to be ascribed to the M–I interface region. In order to rule out any contribution to superconductivity stemming from the presence of interstitial oxygen in LCO, all the samples have been post-annealed in vacuum after the growth process (see Bauitti *et al*. [150]). Also, the dopant redistribution length of the Ca-doped bilayer at the M–I interface is comparable to the Sr-doped one. A certain Ca accumulation at the substrate-film interface (zeroth block in Figure 4.1.14c – due to epitaxial compressive stress, which may be partially accommodated by the substitution of La with smaller Ca), is noticed and followed by the presence of a Ca-depleted region (i.e. 1st and 2nd blocks). An increase (~ 10 pm) of the apical O–O distances that is accompanied by such a lower dopant concentration is followed by a decrease starting from block 3, in which a higher dopant content is present. This again represents an AJT effect similar to the overdoped layer of the Ba-doped sample. A monotonic increase (up to 15 pm) of the apical O–O distance is present from the 7th block (4.56 Å) to the 10th block (4.71 Å). Importantly, blocks 9 and 10 do not exhibit the presence of any Ca-dopant, thereby a typical JT distortion is observed, which – unlike what was observed for the M phase – cannot be ascribed to the presence of dopant. Rather, given the superconducting character of the interface, such a JT distortion may be related to 2D interfacial superconductivity in a similar way as discussed for the Sr-case.

It is revealed by detailed analyses that the JT distortion is present only in the case of Sr- and Ca-doped M–I bilayers. In the case of the Ba-doped bilayer instead, AJT distortions characterize both sides of the nominal interface of LBCO/LCO. Such a relationship between the dopant concentrations and the out-of-plane O–O distances points towards two different superconducting mechanisms, activated by the different dopant distributions leading to different JT distortions. In particular for bulk superconductivity for the Ba-doped case, a typical AJT distortion (holes located in both $d_{x^2-y^2}$ and d_{z^2} orbitals with parallel spins, resulting in shorter O–O distances) [29] is observed, whereas for the Sr and Ca case a combination of AJT and JT is revealed, where the holes are located only in $d_{x^2-y^2}$ orbitals and the apical oxygens are shifted away from the La sites resulting in larger O–O (apical) interatomic distances. As described above, this may be related to the presence of interface effects characterized by electronic redistribution.

Another point regards the local effect of substituting La^{3+} cations with differently sized dopants having the same valence states (i.e. Ba^{2+}, Sr^{2+}, and Ca^{2+}). Figure 4.1.16 presents quantitative information on local lattice deformation obtained from the HAADF images. Figure 4.1.16b shows that the La–La apical distance in the LBCO system sharply decreases from the doped (M) to the undoped (I) phase, substantiating that the large Ba dopant expands the lattice dramatically. A similar effect, yet less pronounced, can be observed for the LSCO/LCO system, in which a decrease of apical La–La distances from the M to the I phase is unveiled, again highlighting the lattice expansion due to Sr substitution. The almost constant La–La spacing obtained from the Ca-doped bilayer instead (Figure 4.1.16d) can be explained by the relatively small size difference between Ca^{2+} and La^{3+}, which does not induce very large A-site displacements. These findings further suggest that apical O displacements are more sensitive to the dopant size compared to La^{3+} displacements, indicating that A-site deformations are relatively less affected (Figures 4.1.15 and 4.1.16).

Conclusions

In conclusion, the effect of dopant size and dopant distribution on the structure and the octahedral network of ALL-oxide MBE grown $La_{1.6}M_{0.4}CuO_4$ / La_2CuO_4 bilayers with M^{2+}= Ba^{2+}, $Sr^{2+,}$ and Ca^{2+} is studied. It is found that the different dopant size remarkably affects the structure as a consequence of different dopant distribution in the structure. Atomically resolved EELS analyses allowed us to reveal the elemental distributions across the interfaces and to measure the redistribution lengths of the dopants in the growth direction as well as in the substrate. The interatomic distance measurements performed on the ABF and HAADF images enable us to precisely determine the atomic column positions and to quantitatively investigate the octahedral distortions and local lattice deformations. Our findings revealed that the dopant distribution has a remarkable effect on the O–O distance (JT and anti-JT effects), which can be related to the occurrence of different mechanisms leading to superconductivity, and also unveiled the correlation between the dopant size and the local lattice parameter. This work underlines the crucial effect of the dopant distribution on the octahedral network and, in turn, on the final superconducting properties, and highlights the importance of complementary advanced STEM techniques for the study of oxide interfaces.

4.2 *δ*-doped high-temperature superconducting La_2CuO_4 interfaces

Introduction

Two-dimensional doping, i.e. "delta (δ)-doping", which has been firstly reported for the semiconductor field, is based on placing a very thin (i.e. single) layer of the dopant in a matrix or substituting an atomic layer of the dopant with the host atoms, and suggests a new approach for oxide materials. [163–167] At oxide materials interfaces, as a consequence of charge redistribution, a spatial separation between ionic and electronic dopants may be obtained leading not only to increased electronic mobility due to reduced scattering [168–170] but also to the occurrence of significant functionalities. Recently, implementation of such an approach for achieving two-dimensional doping (δ-doping) in lanthanum cuprate (La_2CuO_4), which yielded the occurrence of HTSC upon the substitution of selected single LaO planes with SrO ones, [55] is achieved. It is great of importance to observe the formation of the space-charge zone on the downward side of the two-dimensionally Sr-doped layers [17,171], resulting in single-layer confinement of superconductivity. [51]

Previous STEM investigations already substantiated the asymmetric Sr profiles at the interfaces, where the dopant concentration profile is abrupt at the downward side of the interface and rather spread in the growth direction. [33] Similar (asymmetric) profiles have been reported in the literature for semiconductors and oxides, not only the δ-doped structures but also for heterostructures in which different phases are combined consecutively [172,173]. It is also shown that the choice of the layer sequence directly influences the sharpness of the interfaces [163,172–176]. For the evaluation of the experimental findings, various models have been proposed such as a kinetically limited process [177,178], surface Fermi-level pinning [163], surface roughness [179], surface diffusion as a consequence of intrinsic defects [172,180]. It is well known that the local chemistry at the interfaces has a direct impact on the functionalities of oxide heterostructure interfaces [181–185], and thus, it is of crucial importance to investigate the cationic intermixing at such interfaces. In this work, ALL oxide-MBE grown δ-doped La_2CuO_4 structures [150] are investigated, in order to reveal the role played by different parameters on the chemistry of the interfaces. The growth optimization and the fabrication of the structures have been already performed by Dr. F. Baiutti (MPI-FKF) [61] and the details of the growth of the heterostructures can be found in Ref. [84]. The nominal composition of the grown structures can be written as follows:

$$[AO\text{-}LaO\text{-}CuO_2 + N \times (LaO\text{-}LaO\text{-}CuO_2)] \times M,$$

in which *N* and *M* represent the spacing between the doped layers (expressed in a number of constituting La_2CuO_4 "blocks" i.e. half of the unit cell) and *M* represents the number of superlattice repetitions, respectively. For systematic investigations of the structure and the properties of the samples, a combination of various techniques was carried out such as in-situ RHEED during growth, AFM, electrical conductivity measurements, and atomically-resolved STEM imaging and spectroscopy. The choice of the dopants and the synthesis conditions enabled evaluating the influence of different parameters on the final dopant profiles. In this study, the focus is on the impacts of (i) dopant size, (ii) valence of A cation, (iii) growth temperature and (iv) tensile strain induced by the substrate on the dopant distribution profiles.

4.2.1 Effects of dopant size and valance on cationic distribution

To elucidate the influence of the cationic size mismatch between the dopant and the host cation on the distribution characteristics, similar to *Suyolcu et al*. [79], a series of samples have been investigated, where the elastic strain, induced by the cationic substitution is expected to be the driving force for the segregation of the dopant. [99] Here, the effect of the substitution of La in the doped layer with differently-sized dopants, namely, Ca, Sr and Ba, is studied. Note that the size mismatch is calculated as $(R_A - R_{La}) \times 100 / R_{La}$, in which R_A and R_{La} are the ionic radii of the A and the La cations (9 - fold coordinated) respectively, according to *Shannon*. [96]

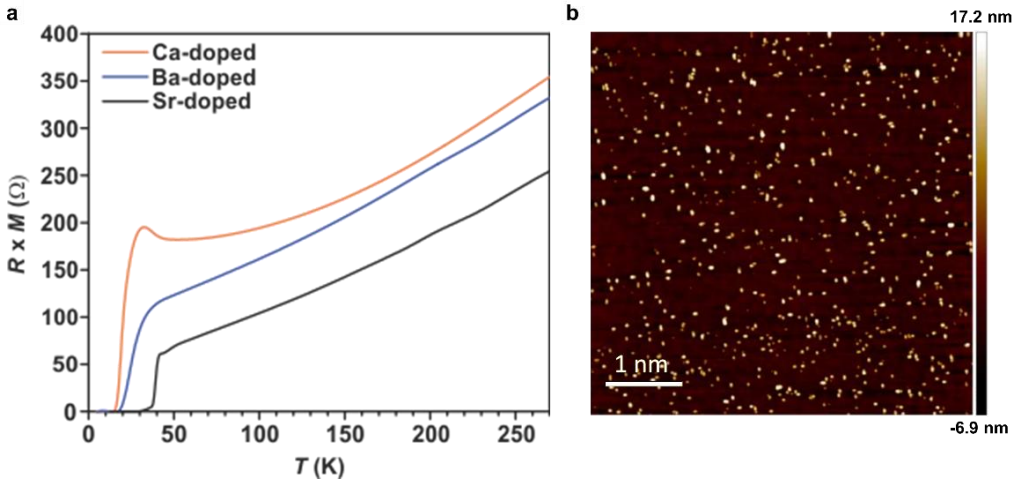

Figure 4.2.1. a) Resistivity vs temperature curves for Sr (black line), Ba (blue line), Ca (orange line) two-dimensionally doped La_2CuO_4 (N = 9). The resistance values have been normalized by multiplication with the number of superlattice repetitions (M). b) AFM micrograph of Ba δ-doped La_2CuO_4 multilayer indicating the high tendency of secondary phase formation in the structure. Reproduced from *Bauitti et al*. [84].

In Figure 4.2.1a, the low-temperature resistance curves of representative samples are given presenting the HTSC transition for all samples. [61] For the Sr-doped case, the temperature of zero-resistance, T_c, reaches the highest value ~ 41 K as a consequence of space-charge effects and ionic redistribution [55]. Lower T_c values are measured in the case of Ba- (T_c ~ 21 K) and of Ca-doped (T_c ~17 K) samples. For the Ca δ-doping case, the value of the critical temperature is found to be consistent with the previous findings obtained for single-phase Ca-doped bulk La_2CuO_4 structures. [77] In the case of Ba-doped samples, the reduced T_c with respect to single-phase Ba-doped La_2CuO_4 may be ascribed to the strong tendency of forming secondary phases during the growth which is also revealed via AFM investigations (Fig. 4.2.1b), which may be destructive for the transport properties. [149]The structure of the samples together with the concentration profile of each dopant has been investigated by atomically resolved STEM imaging and spectroscopy. STEM-HAADF images and atomically-resolved EELS elemental maps (i.e. spectrum images) obtained from all samples are presented in Figure 4.2.2 and Figure 4.2.3, respectively. HAADF images for Ca-, Sr-, and Ba- two-dimensionally doped La_2CuO_4 are displayed in (a), (b), and (c) of Figure 4.2.2, respectively. The images exhibit that, in all three cases, high-quality epitaxial growth without any structural defects on the $LaSrAlO_4$ (001) substrates were achieved. The different contrast due to the different atomic numbers, (Z_{Ca} = 20, Z_{Sr} = 38, Z_{Ba} = 56, and Z_{La} = 57) the doped regions seem darker; especially for Ca and Sr doping cases (see Figures 4.2.2.a–b).

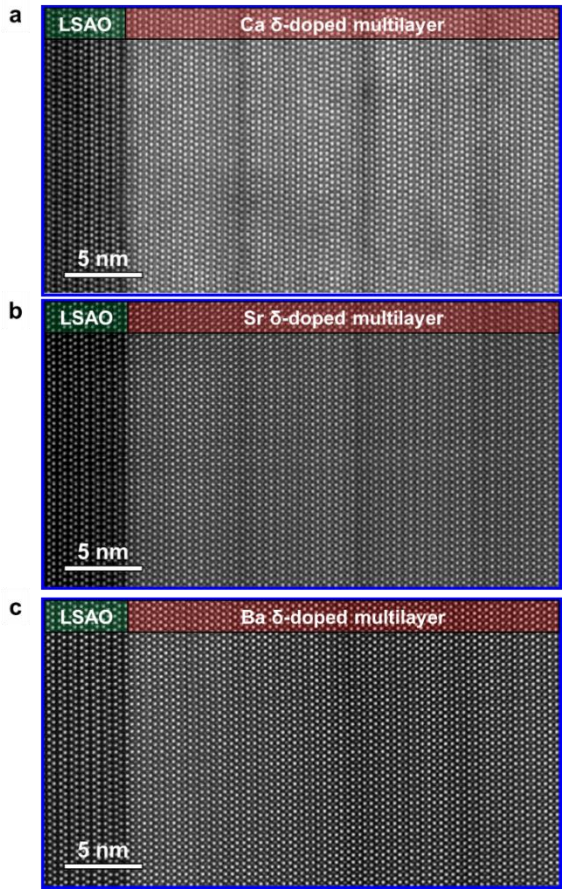

Figure 4.2.2. HAADF images for a) Ca, b) Sr, and c) Ba δ-doped multilayers. All images exhibit the structural quality of the samples. [84]

Furthermore, the results of the atomically resolved EELS analyses (i.e. elemental maps) and related averaged profiles obtained for different elements, are respectively presented in panels a and b of Figure 4.2.3 for the Ca-doped, in Figure 4.2.3c–d for the Sr-doped and in Figure 4.2.3e–f for the Ba-doped cases. From the EELS analyses, it is clearly seen that the dopant distribution is not confined in a single atomic plane, but it is rather spread (i.e. the asymmetric profile). This is valid not only for the Sr-doped case as previously reported but also for the Ca- and the Ba-doped samples. For quantifying the amount of the abovementioned redistribution in both the substrate (downward side of the interface) and growth directions (upward side of the interface) EELS linescans have been analyzed. The results of the averaged linescans are presented in Figure 4.2.3g, in which the redistribution width is shown as a function of the dopant ionic size mismatch with La. Let us first focus on the upward side of the interface (solid diamonds). Here, the results of Ca- (2.65 ± 0.34 nm) and Sr-doped (2.25 ± 0.54 nm) heterostructures show the independent behavior of the redistribution length on the cation size, while in the case of Ba (2.97 ± 0.60 nm) a wider distribution of the dopant is observed. At the backward side (open circles), a remarkably larger redistribution length is measured for Ca (1.89 ± 0.31 nm) with respect to Sr (0.96 ± 0.33) and Ba (1.23 ± 0.26). The trends highlighted by the analysis of the redistribution width ratio (upward/downward) displayed in Figure 4.2.3h, which shows very similar values for the Sr- and Ba-doped cases (highly asymmetric distribution, width ratio ~ 2.4), whereas, in the case of Ca, the distribution is more symmetric (width ratio ~ 1.4). Dr. Yi Wang (MPI-FKF) is gratefully acknowledged for the support on Figure 4.2.3.

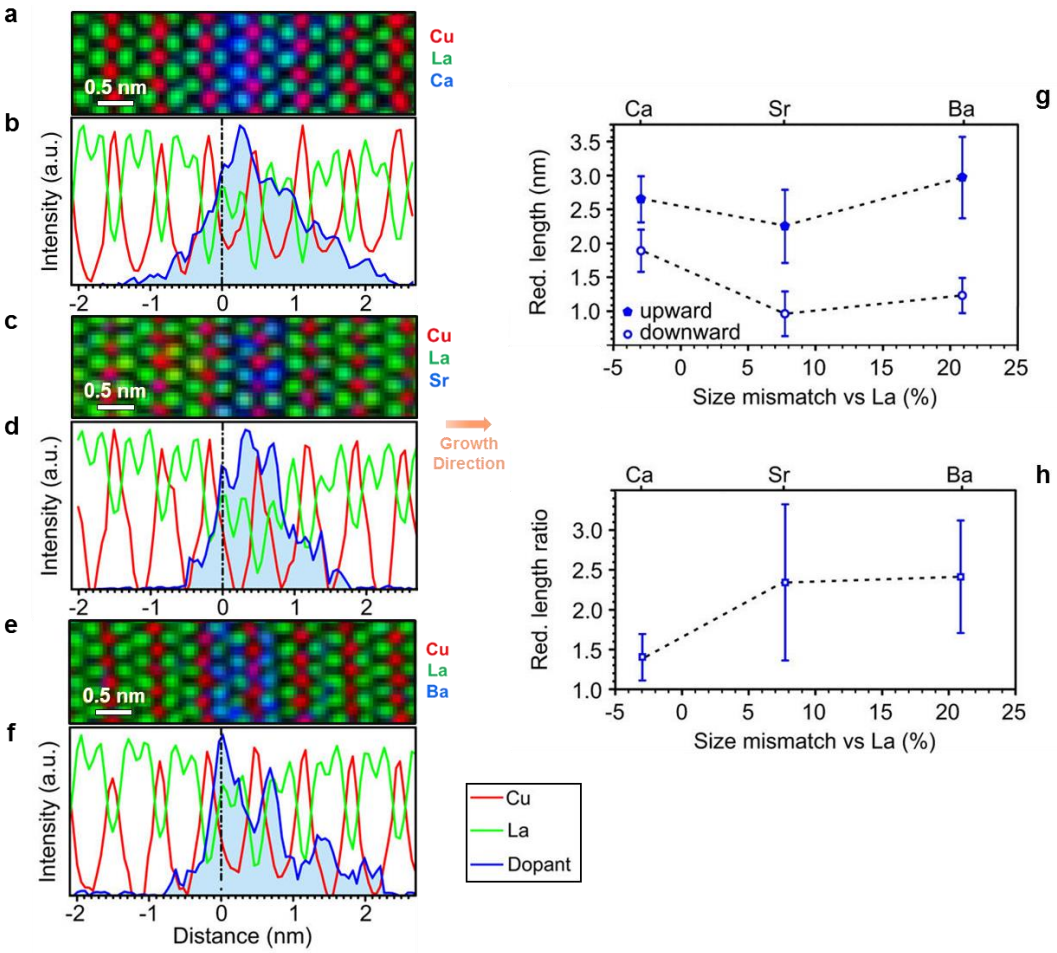

Figure 4.2.3. The respective elemental maps and averaged concentration profiles from atomically resolved EELS spectroscopy are shown in (a, b), (c, d), and (e, f) for Ca-, Sr-, and Ba- doping, respectively. Black dashed lines are used as a guide and indicating "0" nm. (g) Average extension, resulting from EELS data analysis, of the, Ca, Sr, and Ba redistribution widths at the upward side (solid diamonds) and at the downward side (open circles) of the interface, as a function of the dopant ionic size mismatch with La. (h) Redistribution width ratio (upward/downward) for Ca-, Sr-, and Ba- two-dimensionally doped La_2CuO_4. Error bars express the standard deviation of the mean. Reproduced from *Bauitti et al*. [84].

The second target is focusing on the charge of the dopant. It is well known that a local charge may occur on the free surface of crystalline materials, which has been shown for oxides. For instance, the segregation of oxygen vacancies results in positively charged surfaces [163,186–188]. The charge interaction between these polar surfaces and the acceptor dopant acts as a driving force for cationic segregation in single-phase perovskite thin films [99], and may, therefore, be accounted as an explanation for the spread of the dopant in the growth direction also in the present case. Thus, here, this idea is pursued and a δ-doped structure, where the substitution of La with an isovalent cation, namely Dy, is discussed. Since the La/Dy substitution leads to the formation of a neutral defect [84], the surface electric field is expected not to contribute to the Dy migration and thereby, a narrower concentration profile in comparison to the divalent dopant case may be predicted. It should be noted that, when attempting to realize the full substitution of a LaO layer with DyO, the formation of secondary phase precipitates was always detected (see Figure 4.2.4a). Therefore, in order to avoid such an undesired effect, only a partial substitution of La was employed ($La_{0.5}Dy_{0.5}O$), which yielded a better sample quality. An HAADF image acquired from such a defect-free region (including the substrate) and an EDX Dy-L edge intensity linescan acquired along several interfaces is presented in Figure 4.2.4b,c, respectively. Due to the similar atomic number ($Z_{La} = 57$, $Z_{Dy} = 66$), no strong contrast is visible between doped and undoped regions in the HAADF image (Figure 4.2.4b). The darker area on the left-hand side corresponds to the substrate. The resulting average redistribution width (obtained from several EDX linescans) was found to be 1.07 ± 0.23 nm and 2.24 ± 0.31 nm for the backward and the upward side of the interface, respectively. Despite the lower initial dopant concentration, such values are very similar to the typical ones found for the Sr, Ba, Ca cases (see above) indicating that the cation redistribution at the interface cannot be ascribed to the presence of a charged surface during growth.

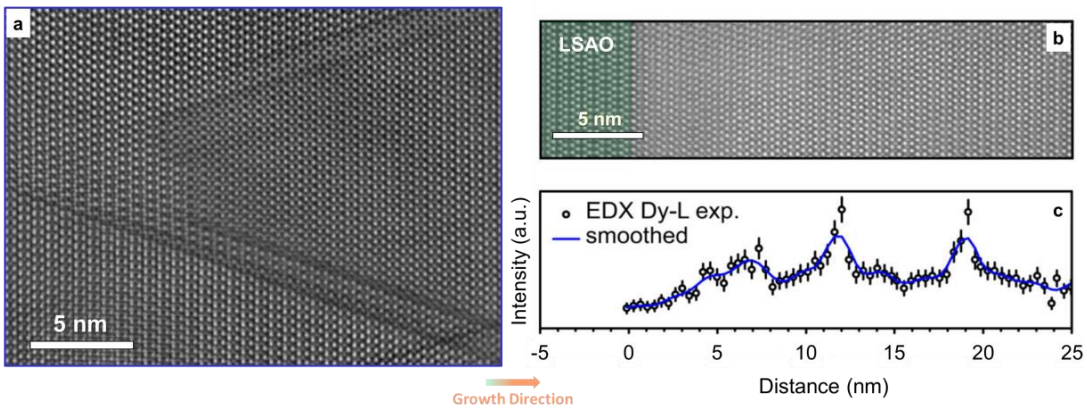

Figure 4.2.4. a) HAADF image showing some extended defects originating from Dy-doped area b) HAADF image of Dy two-dimensionally doped La_2CuO_4. c) Dy-L intensity profile acquired by EDX during a linescan across several Dy-containing planes in a defect-free region. Reproduced from *Bauitti et al.* [84].

4.2.2 On the effect of growth temperature and tensile strain

In the field of semiconductors it is generally accepted that, by decreasing the substrate temperature during the growth, a sharp delta dopant distribution can be obtained [163,189] due to the decreased atom mobility. [177] In this section, I consider the effect of the growth conditions and the choice of the substrate on dopant concentration profiles and thus on the final sample properties, as well as examining whether a sharper delta dopant distribution could be achieved (similar to semiconductors) by lowering the substrate temperature. Moreover, it is also examined how a substrate inducing tensile strain (i.e. LSAO in our case) on the structure affects the dopant distribution. Thus, first, the effect of the substrate temperature on cationic intermixing in the Sr δ-doped La_2CuO_4 was studied in which, during the growth of the heterostructure, a systematic decrease of temperature was carried out with 30-35ºC steps from the nominal growth temperature (about 600ºC) to 500ºC. With the aim of avoiding the formation of structural imperfections due to low-temperature growth, only a portion of the superlattice, namely, the doped and the following two La_2CuO_4 blocks (in which most of the redistribution process is expected to occur) was deposited at reduced temperature, whereas for the rest of the structure the nominal growing temperature was re-established.

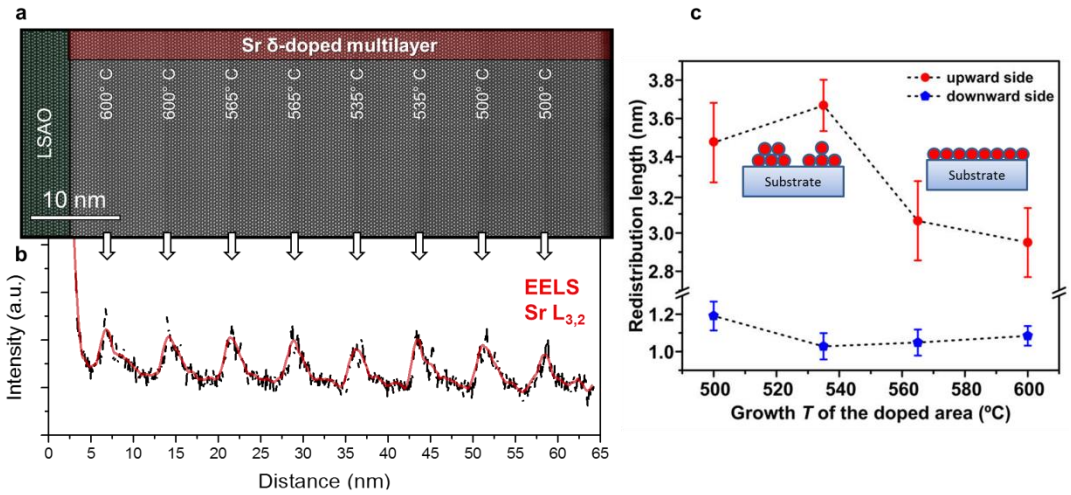

Figure 4.2.5. a) HAADF image of a Sr δ-doped La_2CuO_4 structure, in which the doped regions (collimated with arrows) have been deposited at gradually decreasing (~35 ºC) temperatures. b) Sr-$L_{2,3}$ EELS profile linescan acquired along the growth direction. The smoothed data (red) is given with the raw data (black) and the error bars are smaller than the symbols. c) The Sr average redistribution length as resulting from EELS analyses for the downward and upward sides of the interface are reported in (b). Reproduced from *Bauitti et al.* [84]. In order to allow for a better comparison, the data have been normalized with respect to the reference values (interfaces grown at 600 ºC).

In Figure 4.2.5a, the HAADF image demonstrates an overview of the heterostructure, which is explicitly representing a defect-free structure. As mentioned previously, due to the different atomic number of the constituents, the darker areas indicate the doped layers. In Figure 4.2.5b, the EELS linescan profile of Sr is presented clearly showing the typical asymmetric profile, respectively. The average extents of the dopant redistribution as a function of the growth temperature for the downward and the upward side of the interface, obtained by averaging several line scans, are given in Figure 4.2.5c. Please note that, in order to avoid any contribution from specimen thickness, each δ-doped layer is examined individually. One can observe that a remarkable increase of the intermixing extent

(up to 25% increase with respect to the interfaces grown at 600 ºC) can be found for the upward side of the interface, while for the downward side the redistribution width does not exhibit a clear trend by decreasing the growth temperature. This is in contrast with some experimental observations (and relative models) related to semiconductor systems, which revealed, instead, the tendency of the dopant to "freeze-in" closer to the nominal doped layer by lowering the growth temperature. [177] Instead, it is observed that a change in the Sr concentration profiles occurs at the upward side of the interface if the growth temperature is decreased below 565 °C. Moreover, the redistribution width increases from about 3 nm (for growth T = 565−600 °C) to about 3.5 nm (for growth T = 535−500 °C) (see Figure 4.2.5d). Such a remarkable change can be attributed to the activation of the island growth mode because of atoms clustering at low temperatures. [190] Correspondingly, when two samples' superconducting critical temperature (T_c) values are compared, lower T_c values are realized for the sample grown in reduced (i.e. T = 500 °C) temperature. This can be again ascribed to the activation of the island growth mode, having by virtue of the worsening of the sample crystallinity. It should be noted here that, as far as the downward interface side is regarded, the independence of the redistribution width with temperature can be easily explained by considering that during growth only the upward side of each interface was deposited at reduced temperatures. Moreover, for what concerns the portion of the structure which was grown under optimal conditions (T = 600 °C), the slightly larger redistribution width which was observed here (~2.95 nm) with respect to the values reported above (see Figure 4.2.3; □2.25 nm), could be ascribed to the different sample thickness (~50 nm here and ~25 nm in Figure 4.2.3), i.e., different times employed for the growth. As a consequence, a longer time for thermal diffusion was allowed here.

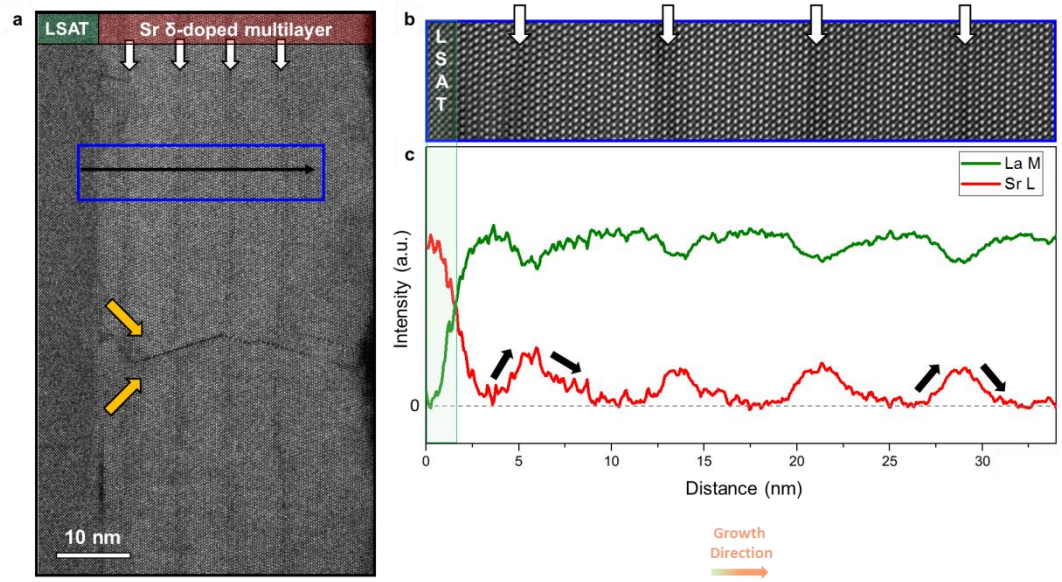

Figure 4.2.6. a) HAADF image of a Sr δ-doped La_2CuO_4 multilayer grown on LSAT substrate presenting the overview of the sample. White arrows indicate the δ-doped regions and orange arrows indicate the structural defect. b) High magnification of the area highlighted by the blue rectangle in a. c) Sr-$L_{3,2}$ (red) and La-$M_{5,4}$ (green) EELS profile linescans acquired along the growth direction. Black arrows indicate the Sr distribution tendencies on both sides of nominal δ-doping and dashed lines indicate zero intensity.

The constructive effect of compressive strain (i.e. LSAO substrate) on HTSC in La_2CuO_4-based systems is clearly shown [87] and such substrates have been highly in use. [16,79] The effect of tensile strain on similar structures to unveil the influence on structural properties is studied as well. For this purpose, the same structures (i.e. Sr δ-doped multilayers) grown on LSAT substrate, which provides tensile strain instead of compressive strain as obtained by LSAO substrates, are examined. Through the STEM investigations (Figure 4.2.6), two important findings based on imaging and chemical analyses were obtained. First of all, in contrast with high-quality structures usually achieved by using LSAO substrates, the epitaxial multilayers grown on LSAT substrates are characterized as defective structures. Figure 4.2.6a demonstrates a defective region and orange arrows are used as guides signaling the defect on the image. Atomically-Resolved EELS investigations also provide interesting information. Such investigations, which are performed on defect-free regions along growth direction (Figure 4.2.6c) substantiates the difference (i.e. change) in the Sr distribution in the structure. In particular, the asymmetric profile tends to disappear in the growth direction. While the first δ-doped layer in the structure provides a clear asymmetry in the profile, the redistribution profile turns to a Gaussian-like distribution in the 4^{th} two-dimensionally doped layer, which is proved by both Sr and La linescan profiles (Figure 4.2.6c).

Discussion

A detailed investigation of the possible mechanisms determining the formation of cationic intermixing at δ-doped La_2CuO_4 interfaces, in which the nominal structure is formed by substitution of single LaO planes with AO dopant planes, is conducted. This enables addressing the main mechanisms responsible for the dopant distribution at the downward side (substrate direction) and at the upward side (growth direction) of the interface. The distribution in the substrate exhibits a higher tendency to cationic intermixing in the case of the dopant having the smallest ionic radius (Ca) (see Figure 4.2.3). Notably, in the substrate direction, the specific ALL-MBE growth kinetics, where the dopant layer is deposited only once the underlying unit cell is completed, one can expect that the intermixing occurs only either as a consequence of the roughness of the layer or due to thermal diffusion (i.e. time-temperature dependent migration of the dopant into the bulk crystal). However, detailed high-resolution STEM investigations do not indicate increased layer roughness for the Ca-doped sample. Thus, it can be concluded that, on this side of the interface, intermixing occurs mainly due to thermal diffusion (typically by the A-site vacancy hopping mechanism [191]). In this framework, a smaller atomic radius is expected to lead to a reduced enthalpy in the diffusion process, as already observed for related perovskite systems. [192] This may be also connected with the compressive strain state (-1.4%) of the thin films, which may favor the substitution of La with a cation having a smaller ionic radius. [193]

Importantly, if the Sr distribution is considered across the interface as reported by *Wang et al*. [33], one can see that the distribution at the downward interface side can be satisfactorily fitted by using a Gaussian distribution profile with a standard deviation $\sigma = 0.43$ nm as shown in Figure 4.2.7 (red line). Such a spatial distribution is expected by applying Fick's law to an initial delta distribution. By considering the usual growth time ($t \sim 10^4$ s), one can also estimate the diffusion coefficient $D = \sigma^2/2t \sim 9 \times 10^{-20}$ cm^2/s. This is in good agreement with the typical diffusion coefficient value,s which can be found in the literature for A_2BO_4 systems [143,192], referring to a counter diffusion of Sr^{2+} and La^{3+}. The reason, why the differences between Ca, Sr, and Ba distribution profiles are rather limited, could be the significant contribution of the La^{3+} migration. At the upward side of the interface,

thermal diffusion is not explanatory itself alone, as it would lead to a symmetric Gaussian distribution of the dopant cation across the nominal doped AO plane, whereas highly asymmetric profiles are experimentally observed (see e.g. Figure 4.2.3k). According to the results obtained from Dy-doping (cf. Figure 4.2.4), one can also conclude that the presence of a surface charge (during the growth) cannot account for the dopant spread in the growth direction.

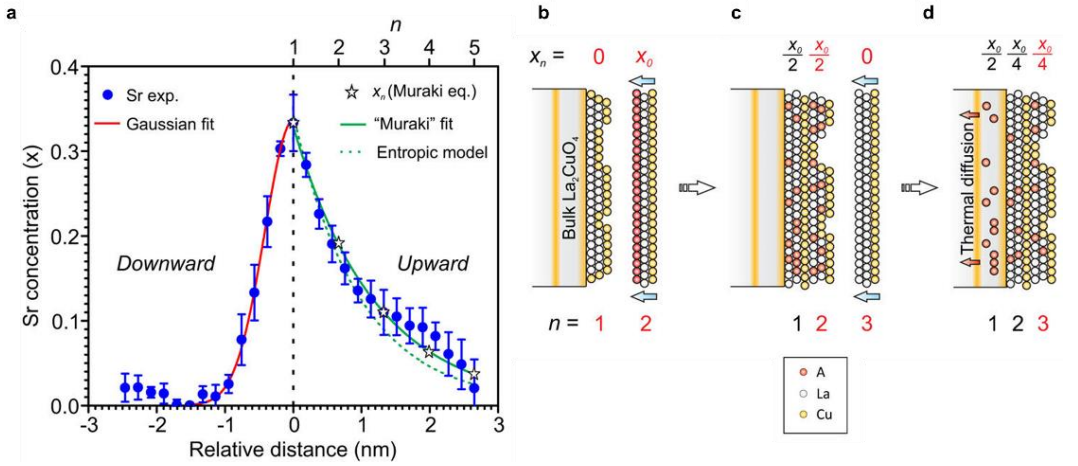

Figure 4.2.7. (a) Fitting of the Sr concentration profile across the nominally doped interface (marked by the black dotted line). The blue circles represent the Sr experimental profile as retrieved from the STEM-EELS analysis reported in ref 16. At the downward interface side, the experimental data are fitted using a Gaussian function, which simulates the evolution of a delta-dopant profile upon thermal diffusion. At the upward interface side, the fitting curve (green line) stems from the Muraki equation, $x_n = x_0(1 - P)\, P^{n-1}$, with fitting parameters $x_0 = 0.78$ and $P = 0.58$. In particular, the stars represent the resulting concentration of each (La,A)O−(La,A)O−CuO_2 constituting block (labeled with n). In panels b−d, a sketch of the cationic intermixing process based on thermodynamical considerations is shown ("entropic model"). In panel b, the last undoped La_2CuO_4 constituting block (labeled with n = 1) is depicted on the surface of the film, together with the incoming two-dimensionally doped La_2CuO_4 block (n = 2) (note that, for simplicity, the growth process is pictured as "block-by-block" deposition, rather than as the real atomic-layer by atomic-layer). Here the film (excluding the last La_2CuO_4 constituting block) is labeled as "bulk La_2CuO_4". Imposing the equilibrium conditions to be verified between the surface and the incoming block (n = 1 and n = 2) results in the A-cation being equally distributed between these two, as shown in panel c. Afterwards, when the next block (n = 3) is deposited, the situation evolves as follows: n = 1 now pertains to the bulk phase, i.e., is no more involved in the mixing process, whereas the blocks n = 2 and n = 3 share the same A-cation amount in order to establish conditions of thermodynamic equilibrium. The resulting dopant distribution after this iteration is sketched in panel d (for each step, the "active" blocks are highlighted in red). Such a process can be formally described by the Muraki equation having P = 0.5 (dotted green line in panel a, resulting $x_0 = 0.69$). Reproduced from *Bauitti et al.* [84].

Furthermore, the in-plane strain induced by the ionic size mismatch between the host dopant cation plays only a secondary role as demonstrated by the slightly larger redistribution width of Ba with respect to Sr and Ca (in the growth direction, Figure 4.2.3). Rather, a mechanism that is based on lateral diffusion during the growth should be taken into account, i.e. intermixing is allowed only between the free film surface and the incoming particles (thus being limited to the topmost layer of the film). This is justified by the fact that atom displacement at the surface requires only a limited number of bonds to be broken, because of the lower coordination. Moreover, surface defects such as steps or vacancies, which may arise as a consequence of growth imperfections, substrate morphology,

or surface reconstruction, could favor intermixing at the surface level. [61,172,194] Such a situation can be formally described by using the phenomenological model of Muraki *et al*. [173], which has been already implemented for delta-doped systems in the field of semiconductors. According to such a model, the dopant concentration x_n of the n^{th} layer (in the present case of each (La,A)O−(La,A)O−CuO_2 constituting block) can be expressed as a function of a parameter P, which describes the probability of atoms at the topmost layer to segregate to the next layer in the growth direction, and of the nominal dopant concentration of the δ-doped layer x_0 according to $x_n = x_0(1-P)P^{n-1}$. In Figure 4.2.7a, The Muraki equation has been employed for fitting the Sr experimental profile at the upward interface side upon imposition of appropriate constraints on the values of x_0 in order to keep the total dopant stoichiometry. [84] A good agreement between the fitting curve (solid green line in Figure 4.2.7a; resulting fitting parameters $x_0 = 0.78$, $P = 0.58$, in agreement with the fitting constraints) and the experimental data can be observed, showing that such a model holds in our case. The resulting segregation probability deriving from the fitting ($P = 0.58$) allows for further considerations regarding the possible mechanisms of dopant migration in the growth direction. In particular, a value of $P = 0.5$ could be explained by simply considering a process based on lateral diffusion, as described above, in which thermodynamical equilibrium is allowed to be established between the last La_2CuO_4 block on the film surface and the incoming particles. Such an assumption is justified by the very slow kinetics, which is typical of the ALL-MBE growth process, having a growth rate of about 1 Å.min^{-1}. In this case, as long as cationic solubility limitations can be ruled out, configurational entropy drives the A-cation to equally distribute between the surface La_2CuO_4 block and the growing block. In this framework, additional factors such as the ionic size mismatch or thermal diffusion determine an increased probability for atoms to migrate to the surface layer ($P > 0.5$). The Muraki equation for such an "entropic" model assumes the simplified form $x_n = x_0/2^n$ (dotted green line in Figure 4.2.7a). A final graphic representation of the suggested process for interface cationic intermixing is depicted in Figure 4.2.7b−d. As far as the growth conditions, and in particular the growth temperature, are concerned, one would expect slower kinetics of lateral diffusion by decreasing the growth temperature, in turn leading to a sharper dopant distribution. This is in contrast with the experimental observations (cf. Figure 4.2.5d) and may be explained by the higher tendency to the formation of clusters on the surface, rather than of a two-dimensional layer, by lowering the growth temperature. [172,195] In addition, surface reconstruction, which may act as an additional factor for the surface intermixing by determining the formation of a surface layer having different stoichiometry with respect to the bulk, was found to be dependent on the growth conditions in related oxide systems. [196] Finally, by comparing the dopant concentration profiles of the different cations (Ca, Sr, and Ba) as reported in panels b, d, and f of Figures 4.2.3, respectively, one can infer a certain tendency to broken symmetry in the dopant spatial distribution by increasing the dopant size (i.e., within a single CuO_2−(La,A)O−(La,A)O block, the dopant concentration is systematically larger in the first layer above the CuO_2 plane in the growth direction). [33,139] This effect is particularly evident in the case of the Ba doping and will be the object of further investigations. Lastly, the applied tensile strain to the structure via LSAT substrates results in relatively (cf. the structures grown on LSAO (001) substrates [55,79,87]) defective and less uniform structures as well as emerging a distribution of the dopant different from the asymmetric behavior. One can suggest that the tensile strain in thicker samples with more repetitions could have a stronger effect on cationic intermixing at the interfaces. That issue could also be an interesting subject for further investigations in order to interpret the structural relationship between transport properties.

Conclusion

In conclusion, a detailed investigation of the possible parameters affecting the redistribution of the dopant in δ-doped La_2CuO_4 structures has been performed. Scanning transmission electron microscopy investigations suggest that, in the direction of the substrate (downward interface side), thermal diffusion is active and leads to the formation of a rather abrupt profile, if dopant substitution is performed with cations having large ionic radii. On the other side, where the dopant is spread across several unit cells, a thermodynamical model dominated by entropic effects is proposed. In addition, layers roughness appears as a major factor in the cationic intermixing, whereas a prominent role played by a surface space-charge layer and effects due to in-plane strain can be ruled out. Our results emphasize the significant influence that interface chemistry plays in the definition of the final properties of complex oxide heterostructures and may be employed for achieving better control of the growth processes and of the final interface functionalities, e.g. by appropriately choosing the dopant species, the growth conditions, and the substrates.

5 • Cuprate-nickelate heterostructures

Abstract

In this chapter, heteroepitaxial contacts of lanthanum cuprate and lanthanum nickelate systems are presented. In particular, high-temperature superconductivity at the interface of lanthanum cuprate (214) and strontium (Sr)-doped lanthanum nickelate (214) heterostructures, and high-temperature thermoelectricity of lanthanum cuprate (214) and lanthanum nickelate (113) heterostructures are discussed. Atomically resolved scanning transmission electron spectroscopy and microscopy techniques are combined with dedicated conductivity measurements, and local structure and chemical properties are correlated with the functionalities of the systems.

5.1 High-temperature superconductivity at $La_2CuO_4/La_{2-x}Sr_xNiO_4$ interfaces

Introduction

The approach of materials engineering through the introduction of an interface has seen early development in the field of ionic and mixed ionic-electronic conductors, [171,197] which find wide application e.g. in energy transformation and storage systems. In this class of functional materials, significant deviations of the concentration profiles for the mobile ionic and electronic species may occur at material discontinuities (e.g. grain boundaries and dislocations), potentially leading to huge changes in the overall system functionalities (ionic and electronic conductivities). [198–201] Such effects have been described in the light of the space-charge theory, according to which the interfacial crystallographic discontinuity represented by an interface inherently determines the presence of an electrical potential gradient that affects the concentration profiles of the mobile charge carriers in the so-called space-charge zones in the interface region. [83,202]

La_2CuO_4-based HTSC systems are one of the widely studied oxide systems, where La_2CuO_4 (LCO) undergoes an insulator to high-temperature superconductor transition upon hole ($h^\bullet$) doping. [40] Electron holes are normally introduced in the system (in the bulk form) as a compensating charge for aliovalent ionic substitution or by introducing excess interstitial oxygen [74], but recent reports importantly demonstrated that HTSC can be locally induced in LCO by taking advantage of interface effects. [10,55,89,136] However, so far, such interfacial contribution has been limited to homoepitaxial systems, in which the only employed phase was LCO-based, while the studies on heterojunctions are still missing. Only one study of non-superconducting La_2CuO_4/La_2NiO_4 structures was reported by Smadici *et al.* [203].

La_2CuO_4 and La_2NiO_4 (LNO) can be addressed by similar chemical and defect-chemical considerations. Starting from the insulating stoichiometric compounds, an electronic phase transformation can be achieved by increasing the electron hole concentration $p = [h^\bullet]$. In particular, for the case of LNO a transition into a metallic phase with increasing p (up to $p \sim 1.0$) is observed, [56] whereas high-temperature superconductivity (for $0.05 \leq p \leq 0.26$) and metallicity ($p > 0.26$) appear in LCO. [45,74] A hole increase can be generated in LCO and LNO by substituting La with an acceptor dopant (mostly Sr^{+2}, denoted by Sr'_{La} i.e. Sr on La-site with a negative excess charge) or by intercalating oxygen excess in the form of interstitial defects (O_i'') [81,204,82] Taking into account that both LSCO and LSNO can also accommodate a large amount of double-positively charged oxygen vacancies ($V_O^{\bullet\bullet}$), the electroneutrality condition reads:

$$p + 2\,[V_O^{\bullet\bullet}] = 2\,[O_i''] + [Sr'_{La}] \qquad (5.1.1)$$

The coupling between the various defect concentrations is determined by the mass action laws of the respective interaction reactions (Frenkel-disorder reaction and oxygen incorporation reaction). As a consequence, Sr-doping leads to an increased vacancy and decreased interstitial concentration. [74] At interfaces equation 5.1.1 has to be replaced by Poisson's equation leading to a redistribution of all mobile charged defects. Therefore, a chemical potential gradient for holes and oxygen vacancies, as well as for Sr, is present once a contact between nominally undoped LCO and LSNO is formed. In

order to establish equilibrium conditions, an interdiffusion of all the mobile defect species between LSNO and LCO should take place, [83] which in turn is expected to affect the final conduction properties of the interface region.

In order to investigate such a situation, superlattices of lanthanum cuprate (La_2CuO_4) and lanthanum-strontium nickelate ($La_{2-x}Sr_xNiO_4$) have been realized by atomic-layer-by layer oxide MBE, which allows for precise control of the film stoichiometry at the atomic layer level. [150] For the first time, it is demonstrated that interface HTSC can be induced in LCO at the heteroepitaxial contact with LSNO. Furthermore, it is revealed that the final superconducting properties of the LCO/LSNO interface can be effectively tuned by simply changing the structural parameters, (doping level *x* of the nickelate phase, layers sequencing, and spacing), while leaving the stoichiometry of LCO unchanged, unlike the "classical" bulk-doping picture.

In this part of the project, the main focus is established on high-resolution STEM investigations (combined with other complementary techniques) including atomically-resolved imaging and spectroscopy, which link the local structure and chemistry with the present functional properties. Finally, the experimental findings are rationalized by discussing possible mechanisms for interface charge redistribution. Superconductivity is rationalized by considering a mechanism for hole accumulation at the interface based on local cationic intermixing but also on space-charge considerations. The growth details and elementary characterization of the samples have been previously initiated and discussed in Ref. [61]. In the latter stage of this project, I partially contributed to the growth of the samples as well.

Results

All the superlattice structures are grown on LSAO (001) substrates inducing compressive strain and the nominal composition of the superlattices can be written as:

$$1 \text{ x } La_{1.56}Sr_{0.44}CuO_4 + S \text{ x } (2.5 \text{ x } La_{2-x}Sr_xNiO_4 + N \text{ x } La_2CuO_4)$$

Here, *S* represents the number of superlattice unit repetitions, whereas *N* defines the thickness of the LCO phase (expressed in the number of unit cells – u.c.).

The resistance data for a representative set of samples having different doping level *x* of LSNO are shown in Figure 5.1.1a, which demonstrates that HTSC forms with increasing *x*. In Figure 5.1.1b, the T_c values as a function of the doping level are summarized. Superconductivity is found for $x > 0.5$, reaching the plateau value of ~35–40 K for $x > 0.8$. While it is well known that single-phase LCO undergoes an insulator-to-high-temperature-superconductor transition upon electronic doping, it is important to note here that none of the constituting materials is expected to exhibit superconductivity. Rather, HTSC is induced in the LCO phase at the interface region as a consequence of the contact with the nickelate phase. As far as the temperature dependence of the resistance is concerned ($\partial R / \partial T$), one cannot infer a clear correlation with the doping level *x* of LSNO. This, together with a certain broadness, which characterizes the superconducting transition, is suggestive of spatial inhomogeneities in the charge distribution or to a certain crystallographic disorder at the interface. In Figures 5.1.1c and 5.1.1d, the electrical behavior of bilayers having different content *x* for LSNO is reported. Such structures, in which LCO is either deposited as a bottom or as a top layer for LSNO, allows for addressing the electrical properties of single-phase contacts. In Figure 5.1.1c (d), the *R* vs *T* curve for a structure in which LCO is a bottom (top) layer is displayed. By comparing the two figures, one can notice the superconducting properties are only slightly affected by the sequence of the layers,

i.e. the maximum T_c is in both cases 24 K. The analysis of the dependence of T_c on x suggests that the minimum doping level for the occurrence of HTSC is slightly lower in the case of the LCO / LSNO structure than in LSNO /LCO, as can be inferred by comparing the resistivity curves obtained for x = 0.7. As far as lower doping levels are concerned, one can expect T_c to exhibit a similar dependence on x, as for what was already pointed out in the case of the superlattice structures (i.e. absence of superconducting transition for $x < 0.5$ for both the LCO/LSNO and the LSNO/LCO contacts).

The dependence of T_c on the thickness of the LCO phase has been studied for the case of superlattices in which x = 1.3 (Figure 5.1.2). The highest T_c values ($T_c > 30$ K) are obtained for 2.5 u.c. < N < 4.5 u.c.. For lower N values, T_c decreases (and the structure eventually becomes non-superconducting for N = 1 u.c.). For large N (> 4.5 u.c.), T_c tends to saturate at 25 K. This is comparable with T_c obtained for the bilayers (cf. Figures 5.1.1c, and 5.1.1d).

In order to explain the dependence of T_c versus doping level x (cf. Fig 5.1.1b), dedicated STEM investigations on LCO/LSNO/LCO interfaces (in the form of trilayer structures) – with compositions x = 0.8 and x = 0.4 – are performed. Low-magnification STEM-HAADF images of each sample covering the substrate and the epitaxial trilayers are displayed in Figure 5.1.3 demonstrating the high structural quality of the films. Due to the different Sr concentrations (i.e. x = 0.8 and x = 0.4) employed in the LSNO structures, the different contrast in the images is discernable: In the higher doping case stronger contrast (Figure 5.1.3a) is obtained.

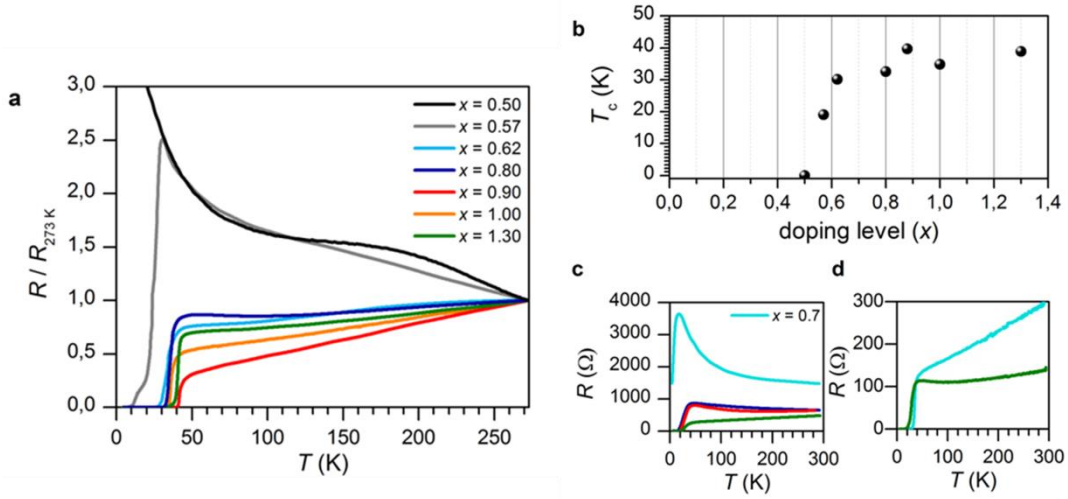

Figure 5.1.1: Electrical properties of LCO / LSNO structures. a) Resistance curves as a function of temperature, for a set of superlattices (N = 2.5) having different doping levels x of LSNO. In order to allow for a direct comparison between the curves, the resistance values have been normalized to R (T = 273 K). b) Dependence of T_c on the doping level x for LCO / LSNO superlattices for a set of representative samples (the corresponding R vs T curves are reported in (a)). c) R vs T for LCO (bottom layer) / LSNO (top layer) bilayers and d) R vs T for LSNO (bottom layer) / LCO (top layer) bilayers for representative doping levels x (refer to Figure 5.1.1a for the color legend). Reproduced from Bauitti *et al*. [205].

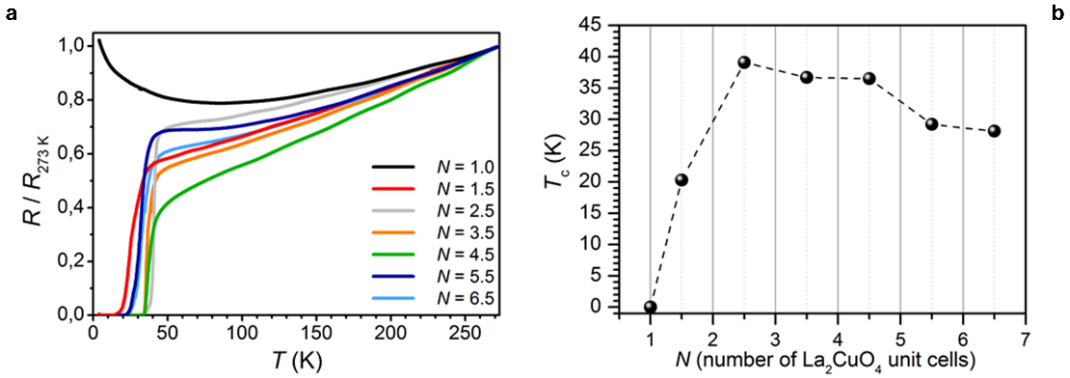

Figure 5.1.2. Dependence of T_c with the LCO thickness for LCO / LSNO superlattices. a) R vs T curves for 1 x $La_{1.56}Sr_{0.44}CuO_4$ + S x (2.5 x $La_{0.7}Sr_{1.3}NiO_4$ + N x La_2CuO_4) superlattices, for different LCO thicknesses N. b) T_c values as a function of the thickness of the LCO phase N for the $La_{0.7}Sr_{1.3}NiO_4/La_2CuO_4$ superlattices, whose R vs T curves are reported in (a). Reproduced from Bauitti *et al.* [205].

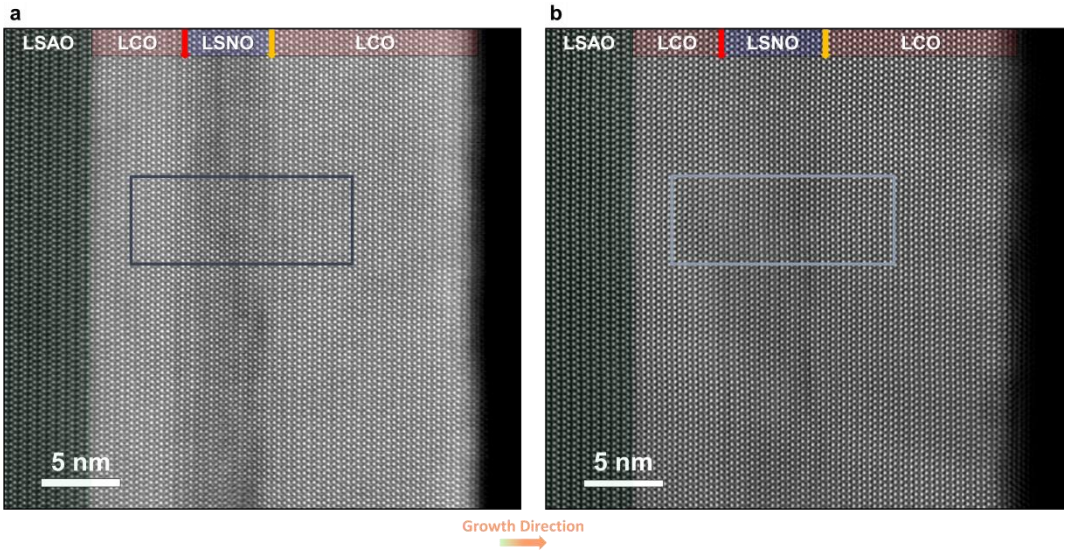

Figure 5.1.3. Low-magnification STEM-HAADF images of (a) x = 0.8 and (b) x = 0.4 LCO/LSNO/LCO trilayers. The images demonstrate the epitaxial quality and the defect-free structures for both samples. Depending on the different doping (i.e. Sr doping) of the samples the image contrasts are different.

Higher-magnification images focusing on both LCO/LSNO and LSNO/LCO interfaces as well as related EDS linescans across the interfaces of each sample (i.e. x = 0.8 and x = 0.4) are presented in Figure 5.1.4. In particular, for x = 0.8 (Figures 5.1.4a and 5.1.4b for HAADF imaging and EDX linescan, respectively) HTSC arises, whereas insulating behavior is observed for x = 0.4 (Figures 5.1.4c and 5.1.4d for HAADF imaging and EDX linescan, respectively). On the HAADF images (Figs. 5.1.4a,c) the nominal interface positions, identified by taking into account the LSNO thickness and the number of Ni intensity maxima in the EDX linescans (cf. Figs 5.1.4b,d), are marked by red and yellow arrows. While the Sr concentration initially undergoes a sharp drop on both interface sides, whose spread has an upper limit of ~1 nm regardless of the doping level (by taking the nominal interface positions as a reference), an additional Sr "tail", indicated by a shaded blue arrow in Fig.

5.1.4b and 5.1.4d characterizes the LSNO / LCO contact (LCO as a top layer). This is wider for x = 0.8 (~2.5 nm) than for x = 0.4 (~1.5 nm). Such an asymmetric profile may be due to the combined effect of thermal diffusion acting on both interface sides and of a "Muraki segregation effect", the latter acting in the growth direction only (i.e. at the LSNO/LCO contact), in analogy with a previous study. [84] More interesting is the comparison between the Ni and Sr profiles, in consideration of the fact that Ni impurities are known to act as a suppressor of HTSC in LCO. [206,207] In particular, the redistribution length of the two species at the LCO/LSNO contact is of the same extent. Conversely, the Sr migration width at the LSNO/LCO interface is larger (about 1 extra u.c.) than the Ni redistribution width.

At this point, it is worth to focus on the comparison between the electronic and ionic concentration profiles. For this purpose, a detailed examination of the O-K edge prepeak via EELS analysis is performed on a LCO/LSNO superlattice having x = 1.3. In Figure 5.1.5, the STEM-HAADF image and Sr, Ni and O-K edge prepeak profiles obtained from EELS are presented. The STEM-HAADF image (Figure 5.1.5a) reveals the high-quality epitaxial relationship between the substrate (dark region on the left-hand side) and the film, where the strong image contrast (cf. Figure 5.1.3) clearly shows the individual LCO and LSNO layers. An important point is the decoupling between the Sr distribution (blue line in Figure 5.1.5c, top panel) and the O-K edge prepeak (red line in Figure 5.1.5c, bottom panel), which indicates the decoupling between Sr and hole distribution profiles, that is present at both interface sides.

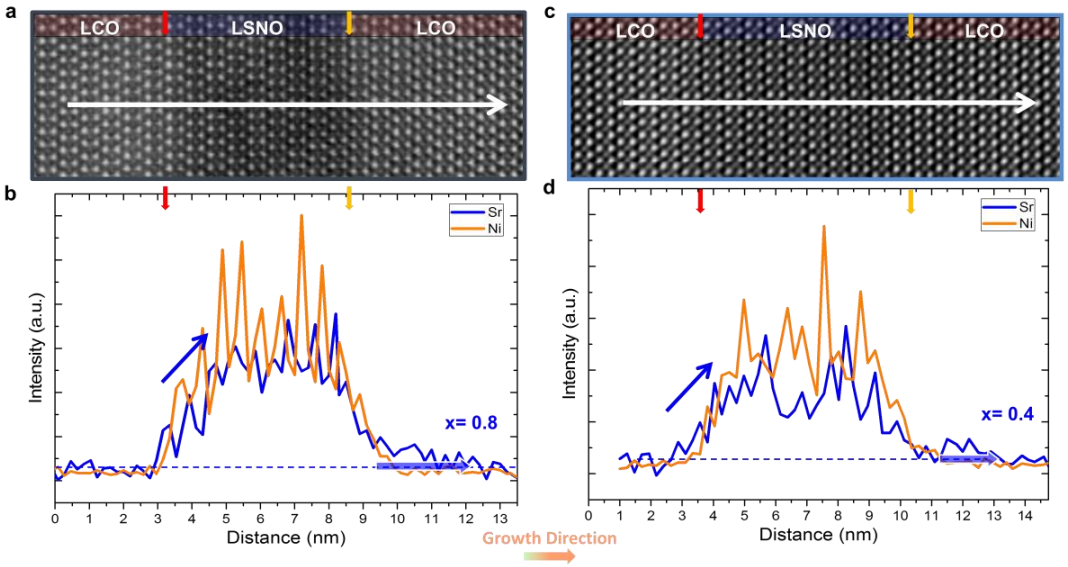

Figure 5.1.4. STEM imaging and EDX spectroscopy for LCO / LSNO / LCO trilayers. In panels a) and c), HAADF images of structures in which the doping level of LSNO are x = 0.8 and x = 0.4, respectively, are displayed. EDX linescans for Ni and Sr are shown in panels b (for x = 0.8) and d (x = 0.4). Reproduced from Bauitti *et al.* [205].

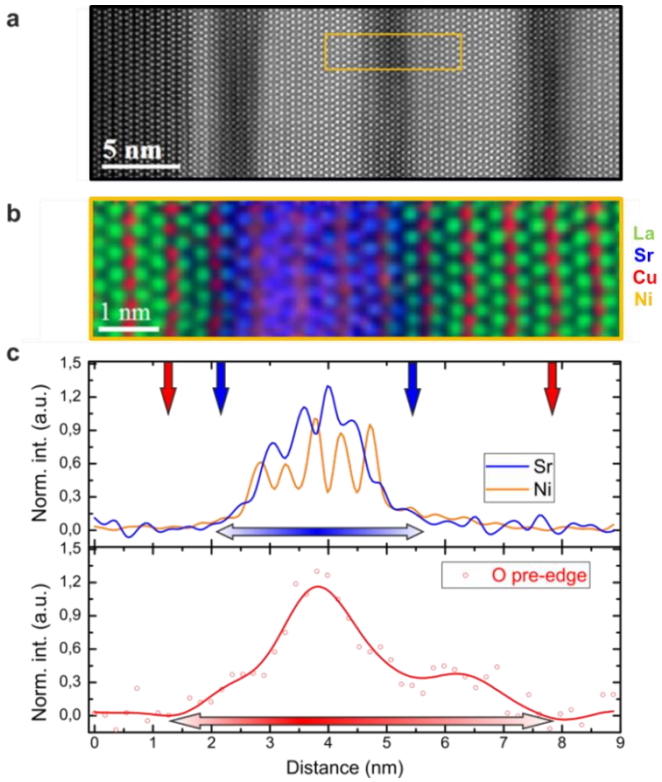

Figure 5.1.5. **HR-STEM investigations at the La_2CuO_4 / $La_{0.7}Sr_{1.3}NiO_4$ / La_2CuO_4 interfaces**. a) HAADF image of a the superlattice structure (N = 9). b) Spatial elemental distribution, extracted from the EELS spectrum image across a $La_{0.7}Sr_{1.3}NiO_4$ region and neighboring LCO areas (the analyzed region is highlighted by the orange rectangle in panel (a)). The color code is as follows: La-green, Cu-red, Ni-orange, Sr-blue. c) EDX signal for Sr (blue) and Ni (orange) (top panel), together with the simultaneously acquired O-K edge prepeak profile as obtained by an EELS linescan (red line, bottom panel). The blue and red arrows indicate the upper limits for the Sr and holes distributions, respectively. Reproduced from Bauitti *et al.* [205].

For precise evaluation of the O-K edge prepeak and Sr distribution simultaneous acquisition of STEM-EDXS and STEM-EELS spectrum images are carried out across the interfaces (Figure 5.1.6). The experimental (STEM-HAADF) survey image is presented in Figure 5.1.6a. Raw EDXS spectrum images including all elements and background-subtracted EELS spectrum images of the O-K edge are displayed in 5.1.6b,c, respectively. The O-K edge profiles obtained from different positions, i.e. from the LCO and LSNO layers as well as both interfaces, LCO/LSNO (bottom) and LSNO/LCO (top), are presented in Figure 5.1.6d, which demonstrates clear differences in the prepeaks. In particular, the presence of the prepeak formation at both interfaces and in the LSNO layer confirms the O-K edge prepeak mapping given in Figure 5.1.5, while no prepeak formation is observed in the LCO layer. Dr. Yi Wang (MPI-FKF) is acknowledged for the valuable contribution on Figure 5.1.5.

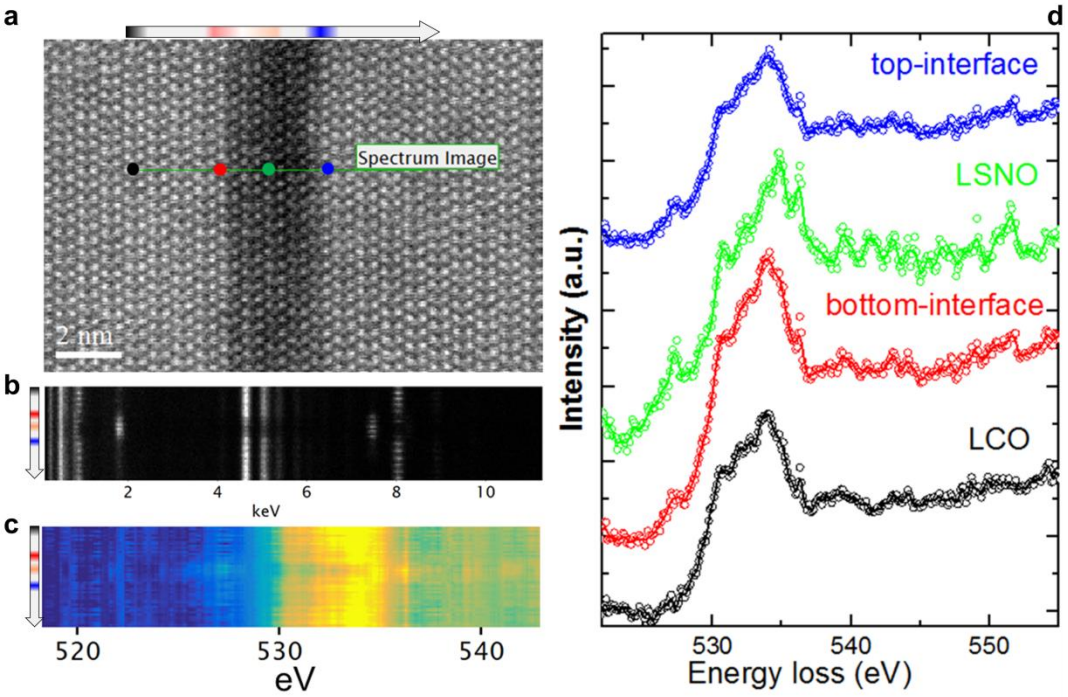

Figure 5.1.6. (a) HAADF image showing the line along which the EELS and EDXS line scan was acquired. (b) Raw EDXS spectrum image. (c) EELS spectrum image of the O-K edge after background subtraction. (d) Oxygen-K edge from different positions as indicated in Figure (a). The intensity of the pre-edge peak has been quantified by multi-Gaussian peak fitting using a non-linear least square (NLLS) routine for all spectra in the line scan profile across several interfaces. Reproduced from Bauitti *et al*. [205].

Discussion

Comprehensive STEM investigations clearly substantiate the elemental intermixing – especially the Sr redistribution – across the interfaces. Although the occurrence of HTSC can be partly attributed to the unintentional Sr doping of LCO, such Sr intermixing alone does not provide a sufficient explanation for a number of experimental findings, therefore cannot be accounted as the only responsible factor for the HT-IS.

In particular, as far the LSNO/LCO contact is concerned, a greater (~1 nm) Sr redistribution width for the superconducting interface (when x = 0.8) with respect to a non-superconducting contact (x = 0.4) is observed, and no difference in the chemical abruptness at the LCO/LSNO interface can be detected, when comparing the superconducting interface (i.e. x = 0.8; Figure 5.1.4b) and the non-superconducting interface (i.e. x = 0.4; Figure 5.1.4d). Therefore, the electrical properties are not directly coupled to the Sr concentration profiles. Most importantly, the LCO/LSNO interface is not only chemically sharper as for Sr, but it is also characterized by a similar migration width of Sr and Ni, i.e. Ni impurities are present in the same LCO region, which is also doped by Sr. As it is well-known in literature and as further corroborated by our experimental evidence, the presence of a small percentage of Ni replacing Cu in the CuO_2 planes is expected to determine a strong decrease of the superconducting critical temperature, T_c. [206,207] Therefore, if cationic interdiffusion is taken as the only responsible for the effects, superconductivity with T_c up to 40 K stemming from such Ni-containing LSCO areas should be ruled out. Lastly, the comparison between the Sr dopant and the hole profiles, as retrieved by STEM-EDXS profiles (Figure 5.1.5), indicates that an evident

decoupling between the two, i.e. the formation of a hole accumulation layer, is present at the interface. Such a finding is clearly not ascribable to "simple" homogeneous doping, in which charge neutrality is locally fulfilled according to equation (2.5) (which can be simplified as $p = [Sr'_{La}]$ in the hole compensation regime).

A generalized thermodynamic picture that takes into account all these constituting elements has to be paid attention to, [83] since in these systems both the ionic (cationic and anionic) and the electronic species are sufficiently mobile to redistribute. [204] In order to describe the thermodynamic equilibrium at an interface, one needs to consider the electrochemical potential $\tilde{\mu}_k$ (for simplicity for one direction, "*x*") for each defect species *k* having effective charge z_k:

$$\tilde{\mu}_k(x) = \mu_k + z_k e\varphi(x) = \mu_k^0 + RT \log c_k(x) + z_k e\varphi(x) \tag{5.1.2}$$

in which the electrochemical potential at distance *x* from the interface is expressed as a function of the standard chemical potential μ_k^0, of the defect concentration c_k and of the electrical potential $\varphi(x)$ (here μ_k represents the chemical potential for the defect *k*). In equation 5.1.2, the dilute carrier's concentration and hence the Boltzmann distribution are assumed for simplicity. In equilibrium, the condition of a constant electrochemical potential demands

$$\tilde{\mu}_k(x) = \tilde{\mu}_{k,\infty}, \tag{5.1.3}$$

$\tilde{\mu}_{k,\infty} = \tilde{\mu}_k(x = \infty)$ being the electrochemical potential in the bulk ($x = \infty$).

The chemical potential gradient for the defect species (holes, oxygen vacancies, and Sr), which is present at the interface between LSNO and LCO, is not only a driving force for the migration of Sr in the direction of LCO, but also for the transfer of holes and oxygen vacancies. Owing to the mobilities involved, the latter is expected to occur even at room temperature, while a Sr transfer requires higher temperatures (possibly reached during preparation).

As far as the charge transfer direction is concerned, the entire free-energy picture has to be considered. Here, the direction on the basis of the doping conditions (configurational entropy) is estimated, supported by the chemical similarity of the base-materials. As the substantial Sr doping of LNO enforces a very high hole and a very high vacancy concentration as long as electroneutrality has to be fulfilled, suspending the latter condition is expected to result in a transfer of both carriers to the undoped LCO provided Sr remains frozen (or to a Sr redistribution if sufficiently mobile). For the Boltzmann distribution, the equilibrium spatial distribution in such a space-charge region follows from combining equations 5.1.2 and 5.1.3:

$$\frac{c_k(x)}{c_{k,\infty}} = \exp\left(-\frac{z_k e\Delta\varphi(x)}{kT}\right) \tag{5.1.4}$$

$c_{k,\infty}$ being the defect concentration in the bulk and $\Delta\varphi(x) = \varphi(x) - \varphi(x = \infty)$ the space-charge potential.

Equation 5.1.4 shows that oxygen vacancies and holes perceive the space-charge in a qualitatively similar way, but the profile for $V_O^{\bullet\bullet}$ (z_k = 2) is steeper than for $h^{\bullet}$ (z_k = 1). A net transfer

of oxygen vacancies and holes from LSNO to LCO leads to the formation of a negatively charged region at the LSNO side of the interface. For compensation, a region where oxygen vacancies and especially holes (the holes being the majority defect in the system) are accumulated, establishes in LCO. Such a situation with an enriched *p*-type charge carriers concentration eventually leads to the occurrence of HTSC in LCO at the interface. A schematic picture of the thermodynamic situation at the interface is depicted in Figure 5.1.7.

Such a space-charge situation is able to explain all the experimental findings: (I) From the experimental data, it is evident that the key element for the appearance of superconductivity is the enhanced hole concentration in LSNO. This suggests electron transfer (electronic space-charge): In order to maintain the hole electrochemical potential constant (see equation 5.1.4) holes are transferred from LSNO into the LCO phase leading to the appearance of HTSC. [84] Such a mechanism has already found experimental proof in other oxides.[131,208] Interestingly, for high doping level ($x \geq 0.9$), single phase LSNO undergoes an insulator-to-metal transition as reported in literature [56] and as confirmed by previous studies on MBE-grown LSNO films. [150] Such a value is very similar to the doping level at which the superconducting state is fully developed in the structure studied here, therefore suggesting that a charge transfer mainly involves delocalized holes from the metallic LSNO phase to LCO. It should be noticed that this is also in line with previous contributions on a related system (i.e. interface HTSC in LSCO/LCO bilayers), [140] in which a similar dependence of T_c with the electronic carrier density of LSCO was found. (II) The hole–Sr decoupling (cf. Figure 5.1.4d) can be fully explained by considering that, in the space-charge regions, the concentration profiles of the mobile defects are not dictated by the condition of local electroneutrality (cf. equation 5.1.1 and equation 5.1.4). Rather, the migration of negatively charged Sr defects from LSNO to LCO is expected to simply lower the space-charge potential $\varphi(x)$, but to not directly influence the local hole concentration. (III) As far as the effect of Ni impurities on HTSC is concerned, it is evident from Figure 5.1.4d that the extent of the hole accumulation (space-charge) zone at the interface, in which HTSC is expected to appear, is larger than the Ni redistribution width. (IV) The dependence of T_c with the superlattice spacing N (Figure 5.1.2) can be explained by taking into account that for low spacing (for which reduced T_c was found) one expects the space-charge zones to overlap leading to high hole concentration. The reduced $T_c \sim 25$ K which has been observed for very large spacing ($N > 5$), as well as for the bilayers (Figure 5.1.1c and 5.1.1d), may instead be ascribed to out-of-plane adjustments of the lattice bond lengths as a consequence of the epitaxial relation between the layers. [52,61] Few very recent studies have dealt with the origin of the electrical and magnetic properties of oxide epitaxial heterostructures in the light of the space-charge theory. [209,210]

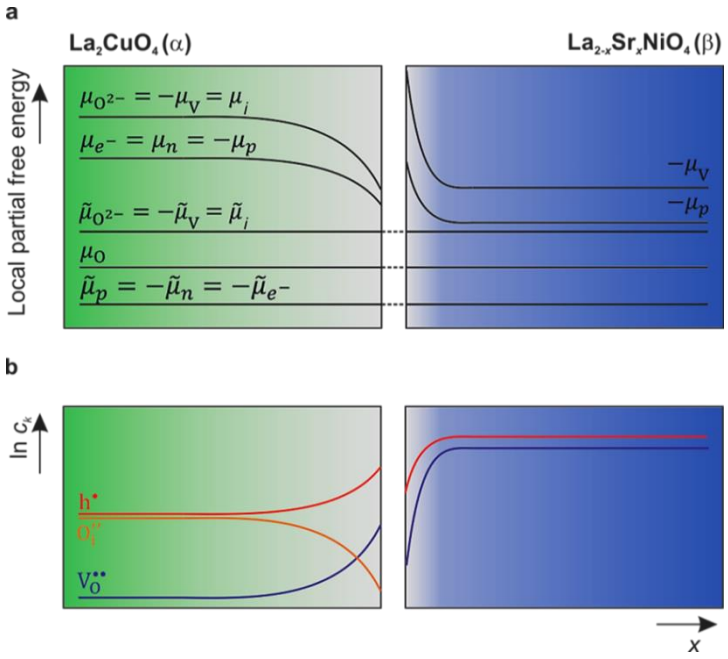

Figure 5.1.7. Sketch of the thermodynamic situation at the boundary layers of LCO and LSNO (if both are equilibrated with the same oxygen partial pressure and a net transfer of holes and vacancies occurs from LSNO to LCO). a) The condition of thermodynamic equilibrium for the defect species (the abbreviations *v, i, p, n* are used for the building units oxygen vacancies, oxygen interstitials, electrons and holes respectively) and with the external oxygen partial pressure defines a horizontal profile for the electrochemical potential of V ($\tilde{\mu}_V = \mu_V + 2F\varphi$) and p ($\mu\tilde{}\_p = \mu\_p + F\varphi$), as well as for the chemical potential of oxygen $\mu_O = -\mu_V + 2\mu_p$. Therefore, as a consequence of the difference in the bulk chemical potentials for the defect species, the bending of μ_V and μ_p at the interface is expected. b) Resulting charge concentration profiles at the interface. Reproduced from Bauitti *et al*. [205].

According to the condition of electrochemical potential constancy, also $V_O^{\bullet\bullet}$ (which are abundant in LSNO due to the high doping level) [82,210] are expected to rearrange at the interface together with holes. A redistribution of both according to equation 5.1.4 automatically fulfills the condition of the constant chemical potential of neutral oxygen at the interfaces, provided that both materials are in equilibrium with the same oxygen partial pressure (Figure 5.1.7). A higher interface electrical potential and consequently a greater hole accumulation, if both $V_O^{\bullet\bullet}$ and $h^{\bullet}$ redistribute, are expected, while a partial Sr-redistribution would lower the space-charge effect. According to Figure 5.1.5, the estimated hole decay length for LCO is ~1-2 nm. It should be noted that the expected steeper concentration profile of $V_O^{\bullet\bullet}$ with respect to $h^{\bullet}$ (cf. equation 5.1.4) may affect the final properties of the LCO region which is adjacent to the interface, leading to overdoping. [97]

In addition, it should be mentioned that a certain role in the definition of the interface HTSC could be played by nanoscale phase-separation, according to which separated LSCO and LSNO nano-islands form at the interface. Under such an assumption, a percolation between LSCO nano-islands may favor the formation of an HTSC path. Notably, such a scenario would explain the appearance of HTSC at the interface even in the presence of Ni and the suppressed diamagnetic response of the superconducting phase, as measured by using mutual inductance set-up, due to the lack of a continuous superconducting layer. [211]

Conclusion

In conclusion, a study on the structural and electrical properties of lanthanum cuprate/Sr-doped lanthanum nickelate epitaxial heterostructures, grown by ALL oxide-MBE is presented. The structures exhibit high-temperature superconductivity with T_c up to ~40 K (onset) as a consequence of local hole accumulation and T_c can be tuned by changing the doping level x in the nickelate or by varying the supercell thickness. In particular, HTSC occurs only, when highly doped (metallic) LSNO composition is employed. Structural analysis by HR-STEM showed that a certain cationic interdiffusion (~1 u.c.), involving both the A-site (La, Sr) and the B-site cations is present. A certain tendency for Sr to migrate further from LSNO into LCO in the growth direction was detected, while the LCO/LSNO interface is chemically sharper. Moreover, EELS investigations suggest the presence of the hole accumulation layer at the interface, which is decoupled from the ionic dopant profile. Simple cationic interdiffusion does not satisfactorily explain all the experimental findings. Rather the system can be fully described if a mechanism for which space-charge effects (i.e. migration of holes and oxygen vacancies from the LSNO into the LCO phase) is taken into account. These findings not only represent an unprecedented case of interface HTSC in the case of heteroepitaxy, but may also shed light onto the complex interplay between ionic and electronic effects at oxide interfaces, and in particular on typically neglected effects of oxygen vacancies redistribution.

5.2 High-temperature thermoelectricity at $La_2CuO_4/LaNiO_3$ heterostructures

Introduction

It is well-established that transition metal oxides and their epitaxial heterostructures are in high demand due to their substantial variety of electronic, chemical, and mechanical properties. Nevertheless, despite their desirable characteristics including low cost, chemical, and physical stability at high temperatures and oxidizing conditions [212], oxides were believed to be poor thermoelectrics (TEs) because of their low charge carrier density and mobility as well as the relatively high lattice thermal conductivity. [213] The breakthrough for thermoelectricity of oxides occurred, when the first studies on Na_xCoO_2 single crystals were published and since then a novel interest for thermoelectric applications of oxide materials has sparkled. [214]

The energy conversion efficiency of thermoelectric materials is described with the figure of merit:

$$ZT=\frac{PF}{\kappa}T=\frac{S^2\sigma}{\kappa}T \tag{5.2.1}$$

where PF is the power factor, S is the Seebeck coefficient, σ is the electrical conductivity, κ is the thermal conductivity, which consists of the lattice and electronic contributions. [215] Since the higher the ZT the better the thermoelectric performance, materials operating at higher temperature (T), with large S, high σ, and low κ are desired. One way to optimize the thermoelectric properties is using oxide heterointerfaces, where intriguing electronic phases can be stabilized that are not present in the constituent compounds. One key example is given by the study of Ohta *et al*. [13], where the large electrical conductivity and thermopower in the $SrTiO_3$ (STO) / Nb-doped STO superlattice (SL) structures caused by the existence of a two-dimensional (2D) electron gas confined within one unit-cell thick interface was obtained. Another interesting 2D electronic interface forms between $LaAlO_3$ (LAO) and STO. [12] Pallecchi *et al*. [216] reported the high negative thermopower values at the LAO/STO interface on the order of 10^4- 10^5μV/K oscillating at regular intervals as a function of the applied electric field at low temperatures. The insensitivity of thermopower to surface scattering mechanisms is verified by studying the thickness dependent thermoelectric properties in cobaltite films. [217,218] Moreover, the substantial Seebeck coefficient found at the $Ca_3Co_4O_9$–$SrTiO_3$ interface underlines the importance of oxygen stoichiometry and exchange dynamics. [219]

The most straightforward approach to understand the electrical and thermoelectric properties of SLs considers a slab model, where the effective conductivity $\sigma_{total}(T)$ and the Seebeck coefficient $S_{total}(T)$ is calculated based on the Kirchhoff's law for parallel connected layers and can be expressed as: [220]

$$\sigma_{total}(T)=\frac{\sum_i \sigma_i(T)\cdot d_i}{\sum_i d_i}, \tag{5.2.2}$$

$$S_{total}(T)=\frac{\sum_i S_i(T)\cdot \sigma_i(T)\cdot d_i}{\sum_i \sigma_i(T)\cdot d_i}, \tag{5.2.3}$$

where $\sigma_i(T)$, $S_i(T)$ and d_i are the electrical conductivity, the Seebeck coefficient, thickness of the constituent layers, respectively. Thereby, the design of novel thermoelectric systems by stacking different oxide layers is a promising direction. [221]

In this work, insulating lanthanum cuprate La_2CuO_4 (LCO) and lanthanum nickelate $LaNiO_3$ (LNO) that exhibits metallic conductivity at room temperature [222] have been chosen for building oxide multilayers up. Although the thermoelectric properties of LCO have been investigated over the last two decades and several groups have reported large positive Seebeck coefficients [223–231], the Seebeck coefficient of the LNO compound is small and negative. [232] Another difference of these two oxides is the oxygen exchange dynamics: LCO has a tetragonal structure and excess oxygen can easily be in-corporated (ex-corporated) into (from) interstitial sites. The incorporation to the unoccupied interstitial positions (V_i) can be formulated by:

$$\frac{1}{2}O_2+V_i \rightleftharpoons O_i^{''}+2h^{\bullet} \tag{5.2.4}$$

and in the bulk of pure materials, holes ($h^{\bullet}$) and oxygen interstitials $\left(O_i^{''}\right)$ have to obey electroneutrality, [233]

$$[h^{\bullet}]=2[O_i^{''}] \tag{5.2.5}$$

The introduction of excess interstitial oxygen makes LCO a conductor and even a high-temperature superconductor (see the previous sections). Unlike LCO, it is not possible to incorporate interstitial oxygen into the dense cubic LNO perovskite [234,235] and the excorporation of oxygen is typically achieved by utilizing a hydrogen atmosphere [236]. Besides, heating of the stoichiometric LNO in an oxygen atmosphere has no significant effect on the oxygen content. [237]

By taking into account different electrical and thermo-electrical properties as well as different oxygen stability of LCO and LNO, different LCO–LNO multilayers were synthesized by means of ozone assisted atomic-layer-by-layer oxide molecular beam epitaxy (ALL-oxide MBE) with in-situ reflection high energy electron diffraction (RHEED) control in order to understand the relationship between different parameters and thermoelectric properties at different temperatures. All heterostructures were characterized by employing several and complementary experimental techniques such as X-ray diffraction (XRD), high-temperature Seebeck coefficient and electrical conductivity measurements. Selected heterostructures were investigated using aberration corrected STEM imaging and energy dispersive X-ray spectroscopy (EDXS), which are the main focus of this section.

Results & Discussion

Four LCO-LNO heterostructures with different individual layer thicknesses were deposited on $LaSrAlO_4$ (LSAO) (001) substrates by keeping the total thickness constant. The growth of the samples are conducted by Dr. Pinar Kaya and Dr. Gennady Logvenov (MPI-FKF). In Figure 5.2.1 the conductivity and Seebeck coefficient of the LCO–LNO heterostructures are shown as a function of temperature (in the range from 300K to 800K). As the thickness of the constituent LNO and LCO layers was decreased, the conductivity gradually decreases and the Seebeck coefficient changes sign

from negative to positive. In addition, both heterostructures exhibit a non-monotonic temperature behavior for $\sigma(T)$ and $S(T)$ in characteristic temperature regions, which becomes apparent as the thickness of LCO and LNO layer decreases. A similar temperature dependence was observed in the single LCO layers, while this is not the case for a single layer LNO suggesting that LCO is responsible for this behavior. [238]

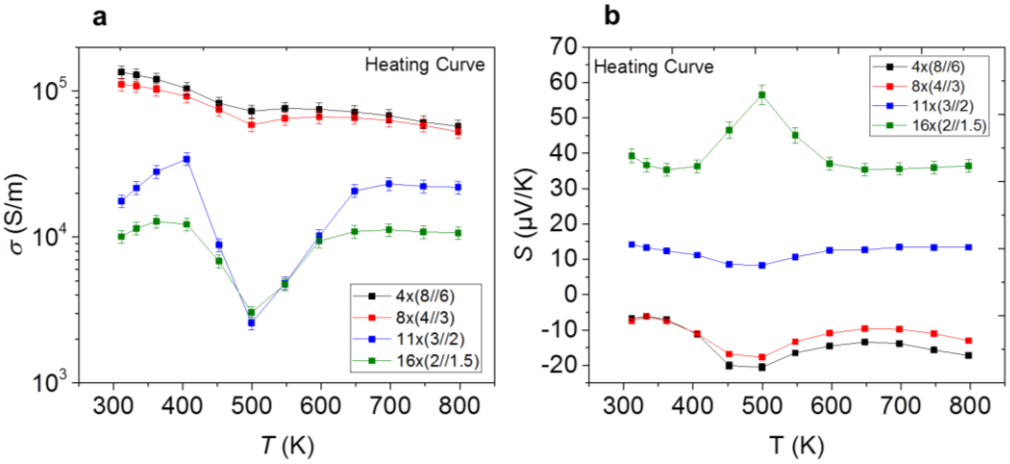

Figure 5.2.1. a) Electrical conductivity and b) Seebeck coefficient of superlattices with different individual layer thicknesses, as a function of temperature. Reproduced from Kaya *et al.* [238]

For further evaluation of the thickness and temperature dependencies of the electrical conductivity and Seebeck coefficients, atomically-resolved STEM investigations of the samples are performed in order to reveal possible interface effects such as cationic intermixing. For STEM investigations I focus on two "end-members" of the sample set: One sample is composed of thicker LCO and LNO layers (i.e. thick-layered; total thickness (u.c.) = 4 x (8xLNO/6xLCO)); the other one has thinner LCO and LNO layers (i.e. thin-layered; total thickness (u.c.) =16 x (2xLNO/1.5xLCO)), where the total thickness of the epitaxial film is constant. XRD patterns, STEM-HAADF images, and EDXS line scan profiles of these two samples are presented in Figures 5.2.2 and 5.2.3. One can notice the high-quality epitaxial relationship between the substrate and both LCO–LNO heterostructures. Corresponding superlattice (SL) peaks (Figure 5.2.2c), and sharp interfaces (Figures 5.2.2b,d), can be recognized in the thick-layered sample, while the thin-layered sample shows strong chemical intermixing through the film (Figures 5.2.3b,d) and also less pronounced SL peaks (Figure 5.2.3c). Moreover, one can see in the HAADF image inset in Figure 5.2.3b for the thin-layered sample that LNO adopts the nominal 113 cubic structure only in the very first layers, while the rest of the sample exhibits the 214-tetragonal structure, in which intermixing of Cu and Ni atoms is spread through almost the entire film.

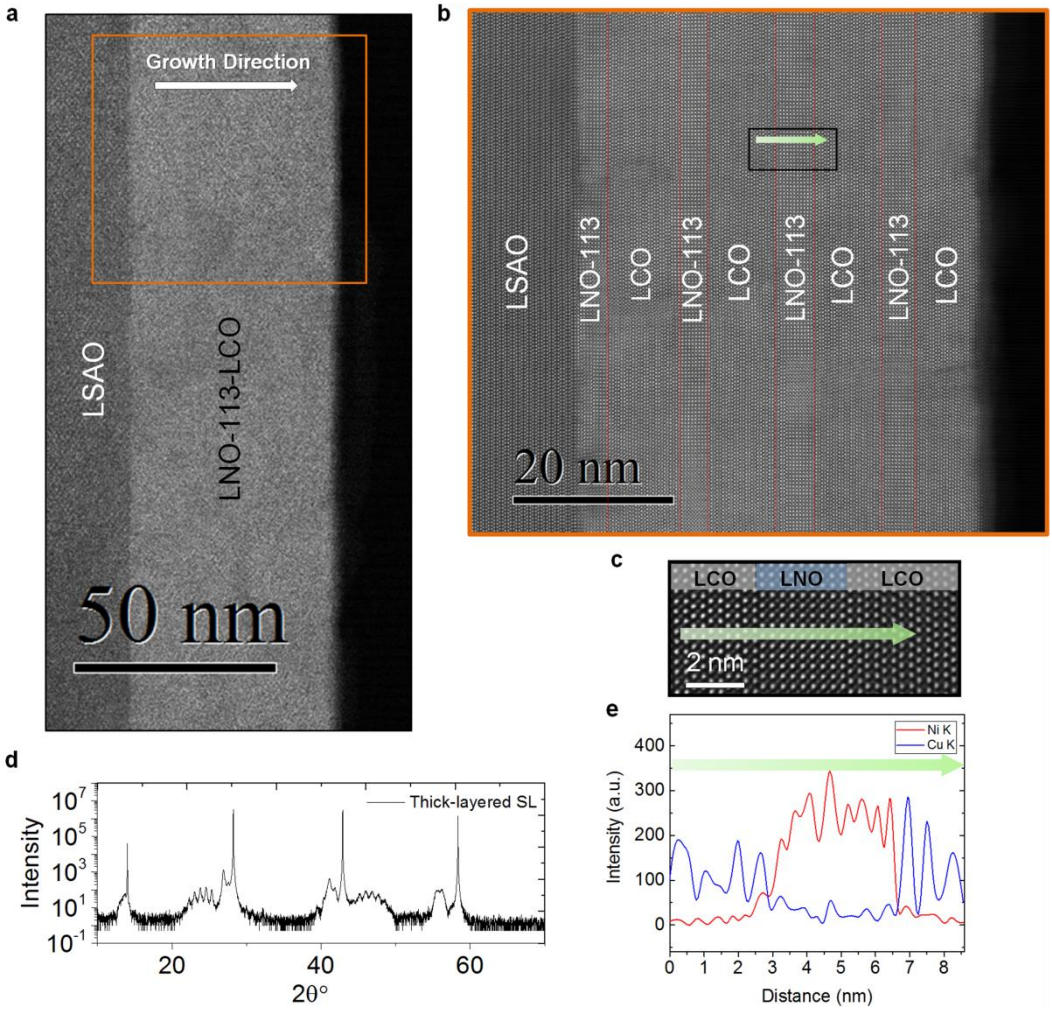

Figure 5.2.2. a), b) and c) low, intermediate and high-magnification HAADF images of the thick-layered sample grown on LSAO substrate, respectively. d) XRD pattern of the sample and e) EDXS line scan profiles of Ni (red) and Cu (blue) along the green arrow in (b) and (c). Reproduced from Kaya *et al*. [238].

In a previous study of LCO–LNO SLs grown on LSAT (001) substrates, the 113-LNO structure was maintained throughout the structure, and the intermixing was much more limited. [239] However, the heterostructures grown on LSAO substrates indicates almost complete transformation to the 214-phase after the first LNO (113) layers with strong Cu-Ni intermixing in thin-layered sample (Figure 5.2.2). Thus, a substitutional solid solution of $La_2(Cu,Ni)O_4$ with 214 crystal structure was formed during the growth of the thin-layered heterostructure, which is also supported by the XRD measurements employed before and after the thermal cycling indicating no structural and/or phase change. [238] Therefore, for the thin-layered SL (i.e. 16 x (2xLNO/1.5xLCO)), the parallel slab model – using the data of LCO and LNO single phase films with the corresponding thicknesses – is not applicable due to the strong Cu–Ni intermixing, where the sign change of the Seebeck coefficient from negative to positive is present in LCO–LNO heterostructures with very thin LCO and LNO layers (as explained by a substitutional solid solution [240,241]). Nevertheless, the parallel slab model was applied for the thick-layered SL, to further evaluate the contributions of different layers, where the interfaces are sharper. For that, the electrical conductivity and the Seebeck coefficient of the individual LCO and LNO layers with related thicknesses were used, and the model yields a good

agreement for the Seebeck coefficient (Figure 5.2.4a), while the agreement is interestingly less satisfactory for the electrical conductivity (Figure 5.2.4b)). These measurements and calculations were performed by Dr. Pinar Kaya (MPI-FKF).

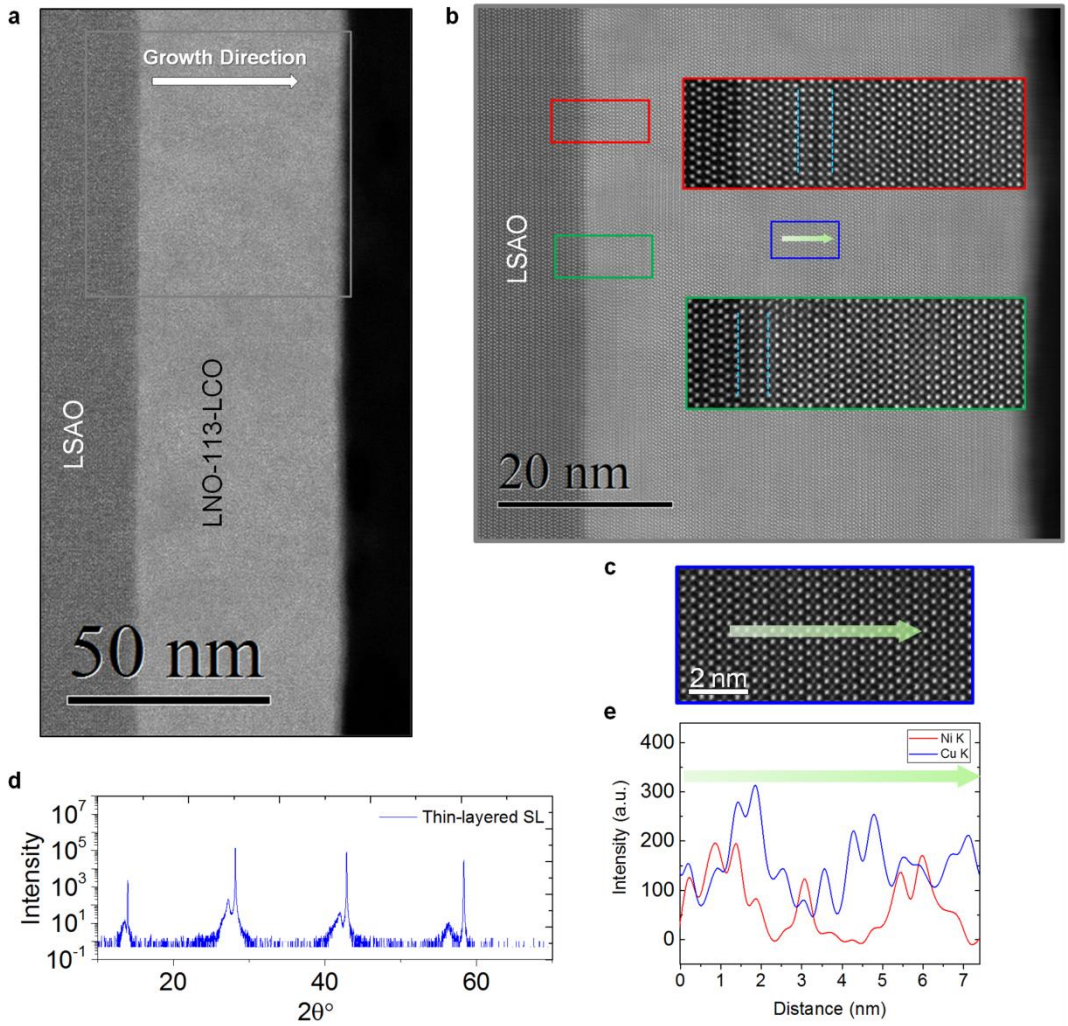

Figure 5.2.3. a), b) and c) low-, intermediate- and high-magnification HAADF images of the thin-layered sample grown on LSAO substrate (inset images indicate the corresponding red and green rectangular regions, blue dashed line indicates the 113-structure). d) XRD pattern of the sample and e) EDXS line scan profiles of Ni (red) and Cu (blue) along the green arrow in (b) and (c). Reproduced from Kaya *et al*. [238]

On the other hand, the experimental conductivity of the thick-layered superlattice is higher than the calculated value, which implies that the conductivity of one (or both) of LCO and LNO layers in the heterostructure is higher than the conductivity of single phase reference layers with corresponding thickness. This could be related to the different scattering behavior of carriers in the single-phase films and heterostructures or the small difference in carrier concentration (n) and/or mobility (μ) or due to interfacial effects. Please note that, the Seebeck coefficient does not show such an anomaly, which is simply due to the fact that it is less sensitive in this respect. [242] Such differences can be due to a variation of the slab properties in the thick-layered heterostructure compared with the single phase LCO and LNO reference slabs, and at that point, one can consider several reasons such as

chemical intermixing, space charge effect, effect of epitaxial strain and different oxygen concentration and/or different scattering in the heterostructure compared with the reference layers. A specific local interfacial contribution cannot be the main reason, because that would require very high conductivity.

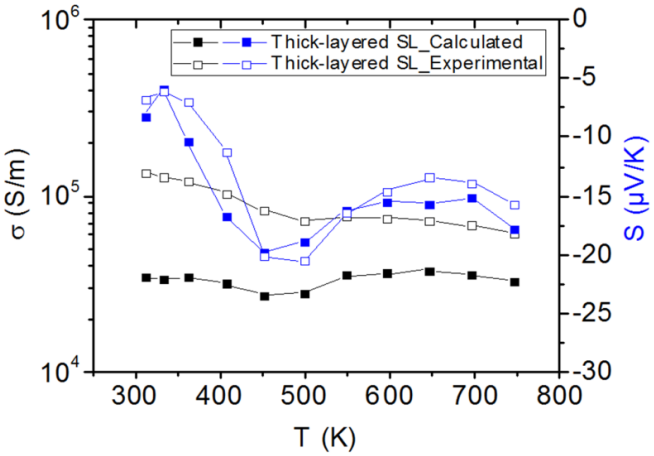

Figure 5.2.4. Seebeck coefficient (blue) and electrical conductivity (black) of superlattices with thick constituent layer as a function of temperature obtained experimentally and calculated by applying the parallel slab model. Reproduced from Kaya *et al*. [238]

Summary and conclusions

In this section, the relationship between constituent layer thickness and the thermoelectric properties of LCO–LNO multilayers grown by ozone-assisted MBE are studied in the temperature range from 300 to 800 K. It is demonstrated that, in LCO–LNO heterostructures with relatively thick LCO and LNO layers the thermoelectric properties are mainly dominated by the more conducting LNO layers and can be described by the parallel slab model. In the multilayers, a sign change of the Seebeck coefficient was observed depending on the thickness of the constituting layers: As they get thinner the Seebeck coefficient changes from negative to positive numbers, which is explained by the intermixing of Cu and Ni atoms resulting in a p-type Cu-rich substitutional solid solution of the form $La_2(Cu_{1-x}Ni_x)O_{4+\delta}$ and by the formation of the 214 structure, when the individual layers become very thin. Moreover, the non-monotonic temperature dependencies of $\sigma(T)$ and $S(T)$ in LNO–LCO heterostructures, which are attributed to the oxygen exchange dynamics in the 214 crystal structure of the LCO layers, revealed that the oxygen stoichiometry can decisively modify the electrical conductivity and the Seebeck coefficient of the constituent oxide layers.

This study demonstrates that the design of artificial thermoelectric materials is possible by stacking oxide layers, but in order to optimize the functional thermoelectric properties one needs to pay attention to: (i) Possible formation of solid solutions in heterostructures, especially if the constituent layer thickness is very small. (ii) The oxygen stoichiometry owing to the comparatively large temperature range targeted for applications, where both kinetic and thermodynamic aspects are crucial for a description of the thermoelectric properties.

6. Cuprate-manganite heterostructures

Abstract

The interfaces of epitaxial complex oxide systems inducing intriguing functionalities, which are dominated by the local properties at the contacts of heterojunctions, require atomic resolution identification. In this chapter, structural and chemical properties of superconducting-ferromagnetic, i.e. cuprate-manganite, heteroepitaxial interfaces probed with comprehensive aberration-corrected STEM techniques is presented. The investigations demonstrate that Sr redistribution in 113-$LaMnO_3$ and 214-La_2CuO_4 phases is different: Sr is strongly redistributed in 113-manganite heterostructure floating over the later-deposited La-O layers. This trend in 113-$LaMnO_3$ is very distinct from that in 214-La_2CuO_4 phases. Such distribution not only affects the sharpness of the interfaces but also influences the local octahedral distortions and the physical properties, correlatively.

6.1 Anomalous Sr distribution at $La_2CuO_4/LaMnO_3$ heterostructures

Introduction

The phenomena occurring at oxide heterostructure interfaces can be primarily tailored by the choice of the constituents. However, the key factor dominating the interface functionalities is the control of interface sharpness, which can be identified by the order of cationic intermixing, i.e. elemental redistribution. Therefore, examining the interfacial structure and chemistry is vital for correlating the physical properties. For instance, in La_2CuO_4 (LCO) based, i.e. 214-type, high-temperature superconducting (HTSC) interfaces, the importance of dopant distribution in overdoped-undoped LCO bilayer systems [79,89] and the mechanism of cationic distribution in 2D-doped LCO systems [84] for iso-structural cuprate-cuprate interfaces have been reported recently (see chapter 4). In these studies, aberration-corrected [104] scanning transmission electron microscopy (STEM) has provided local-probing techniques such as high-angle annular dark-field (HAADF) imaging [105], annular bright-field (ABF) imaging and electron energy-loss spectroscopy (EELS) with subatomic precision. [89]

In addition to the iso-structural systems, hetero-structural systems exhibit intriguing properties as well. One of the most important example of such heteroepitaxial systems is the interfacial contact of HTSC $(Y,Ca)Ba_2Cu_3O_7$ (YBCO) and a ferromagnetic $La_{0.67}Ca_{0.33}MnO_3$ (LCMO), where orbital reconstruction and charge transfer take place at the interface. [243] Recently, the antiferromagnetic coupling between Cu and Mn spins was also demonstrated in a similar heterostructure with another type of cuprate, $(La,Sr)_2CuO_4$, and considered as a "ubiquitous" behavior of cuprate/manganite interfaces. [244] The charge transfer within the layers can be tuned via controlling the compositions of the superlattices with sub-unit cell precision [245] and it is natural to connect the local lattice/chemical structure to such physical phenomena.

To understand the mechanisms of the formation of hetero-structural interfaces and their influence on the functionalities, cuprate-manganite superlattices with different cuprate layer thicknesses are fabricated by an ALL-oxide MBE system, that enables precise control (i.e. atomic layer level) of the film stoichiometry. In order to realize the cationic distribution and related local distortions at the interfaces of different phases, i.e. 113- and 214-phases, comprehensive aberration-corrected STEM techniques are applied. The Sr distributions in 113-manganite and 214-LCO phases are found to be dissimilar. In particular, Sr-O layer of $SrMnO_3$ deposited on top of 214-cuprates strongly segregates in the growth direction, floating through the $LaMnO_3$ layers deposited on top. The Sr-O layer (i.e. δ-doping) of $LaSrCuO_4$ deposited on top of 113 manganites shows different elemental distribution and chemical sharpness compared to the conventional case.

Results & Discussion

The superlattices are grown on LSAO (001) substrates and the nominal composition of the superlattices can be written as:

$$21 \text{ x } (2 \text{ x } SrMnO_3 / 6 \text{ x } LaMnO_3 / 1 \text{ x } LaSrCuO_4 / N \text{ x } La_2CuO_4)$$

Here, N represents the thickness of the LCO phase (expressed in number of half unit cells – u.c.). For both of the samples, the thickness of $SrMnO_3$ (SMO) - $LaMnO_3$ (LMO) layer and δ-doped layer were kept constant, while the LCO layer is designed as three monolayers (MLs) for "thin" and nine MLs for "thick" layers. For clarity of the presentation, samples are defined as thin-LCO and thick-LCO, respectively. Basic sketches of the samples are presented in Figure 6.1.1.

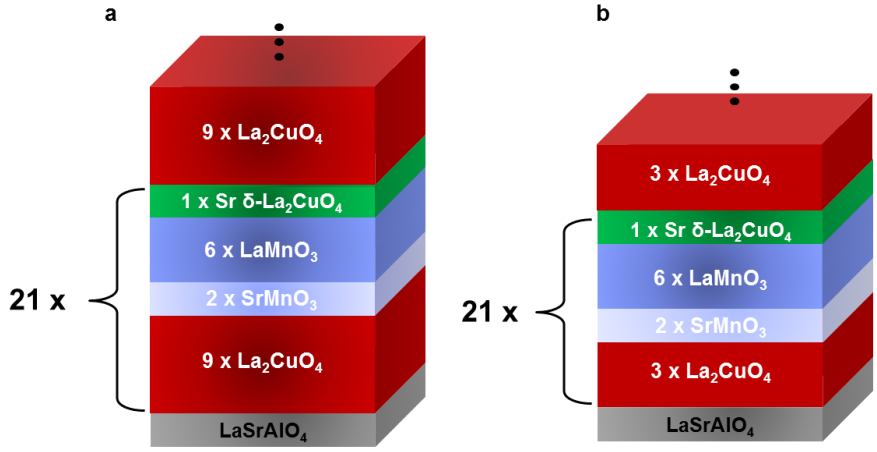

Figure 6.1.1. Basic sketches of the (a) thick-LCO (N = 9) and (b) thin-LCO samples (N = 3). Both of the samples are composed of 21 repetitions.

To investigate the atomic arrangement of the samples, I first conducted STEM-HAADF imaging that not only demonstrates the epitaxial quality of the samples but also reveals how the adjacent layers are grown structurally. Figure 6.1.2 and Figure 6.1.3 demonstrate the high quality of the samples without extended defects, where the LSAO substrate (darker) and the epitaxial multilayers (lighter) can be distinguished via their contrast due to the difference of the mean atomic weight. The image intensity profiles averaged along the growth direction (indicated with the orange arrows) exhibit a regular contrast owing to the Sr distribution across the 214-113 and 113-214 interfaces. In particular, the decrease in the image intensity is visible (darker contrast) at the Sr-containing layers. Such obvious contrast for the thick-LCO SL structure substantiates the structurally sharp interfaces (e.g. Figure 6.1.2c).

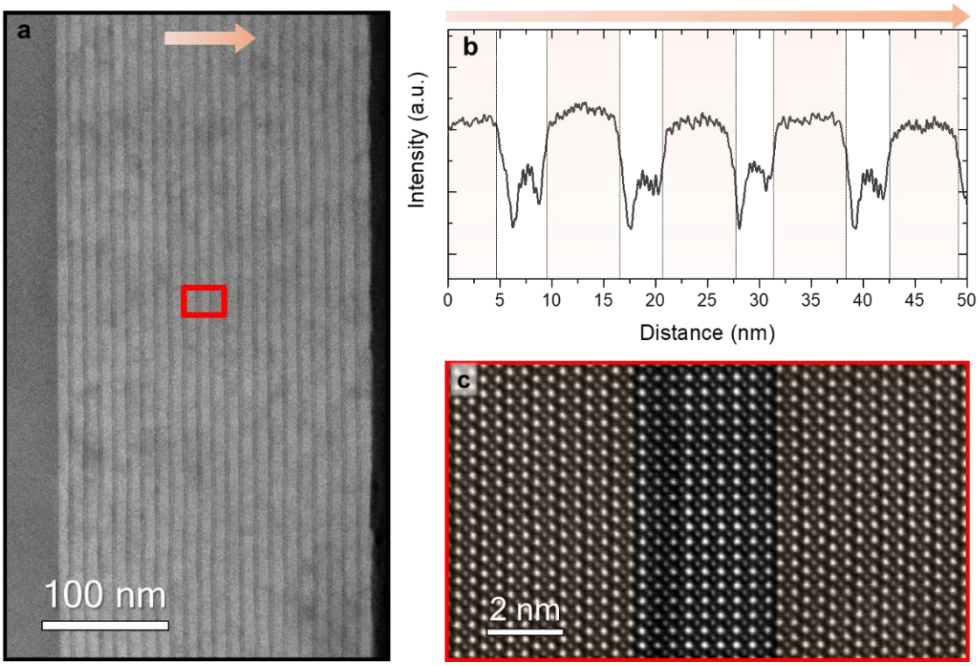

Figure 6.1.2. (a) Low magnification STEM-HAADF images of the thick-LCO SL demonstrate the high-quality epitaxy. (b) STEM-HAADF image intensity profile along the orange arrow in Fig. 1a, averaged along the perpendicular direction. The image intensity indicates the periodicity of the contrast related to the Sr distribution at the interfaces. (c) High-magnification image of the area highlighted by the red rectangle in (a) confirming the structurally coherent 214-113 and 113-214 interfaces.

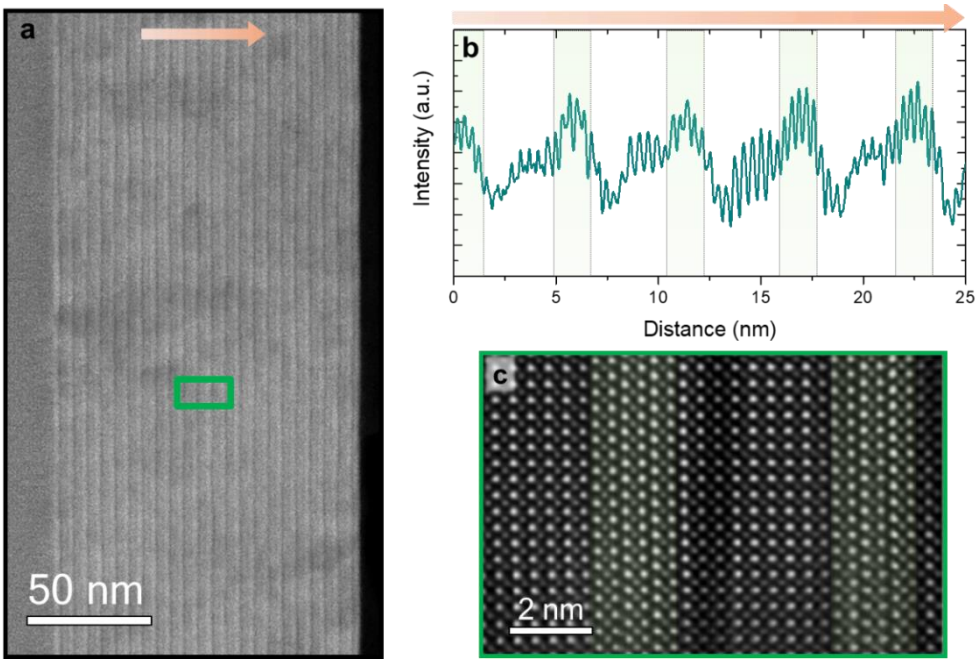

Figure 6.1.3. (a) Low magnification STEM-HAADF images of the thin-LCO SL demonstrate the high-quality epitaxy. (b) STEM-HAADF image intensity profile along the orange arrow in Fig. 1a, averaged along the perpendicular direction. The image intensity indicates the periodicity of the contrast related to the Sr distribution at the interfaces. (c) High-magnification image of the area highlighted by the red rectangle in (a) confirming the structurally coherent 214-113 and 113-214 interfaces.

After revealing the structurally coherent interfaces, atomically-resolved STEM-EELS investigations are performed in order to evaluate the elemental intermixing (i.e. the chemical sharpness) at the interfaces. Figure 6.1.4a-d show atomic resolution maps of Sr (blue), La (green), Mn (red), Cu (cyan) and the overlay (RGB) of these elements as obtained via STEM-EELS, respectively. The La and Sr substitution in the manganite phase (Figure 6.1.4a,b) and the eight-monolayer-thick Mn distribution (Figure 6.1.4c) are revealed. Here, the substitution of La^{3+} with Sr^{2+} (divalent alkaline-earth metal), which provides potential charge carriers for electrical conductivity [246], results in a mixed valance of Mn^{3+} and Mn^{4+}, where the ions exchange the carriers via O-2*p* orbitals as explained by the double-exchange mechanism. [72,247,8] Moreover, as a consequence of such atomic intermixing emerging at the SMO-LMO interface, the expected electronic structure is a mixture of $t_{2g}^3e_g^1$ and $t_{2g}^3e_g^0$ configurations. EELS results clearly indicate that the elemental intermixing is mostly confined to 2-3 UC (Figure 6.1.4). That is in a good agreement with the polarized neutron reflectometry (PNR) measurements demonstrating the magnetic profile of the individual layers as employed for identical systems. [245]

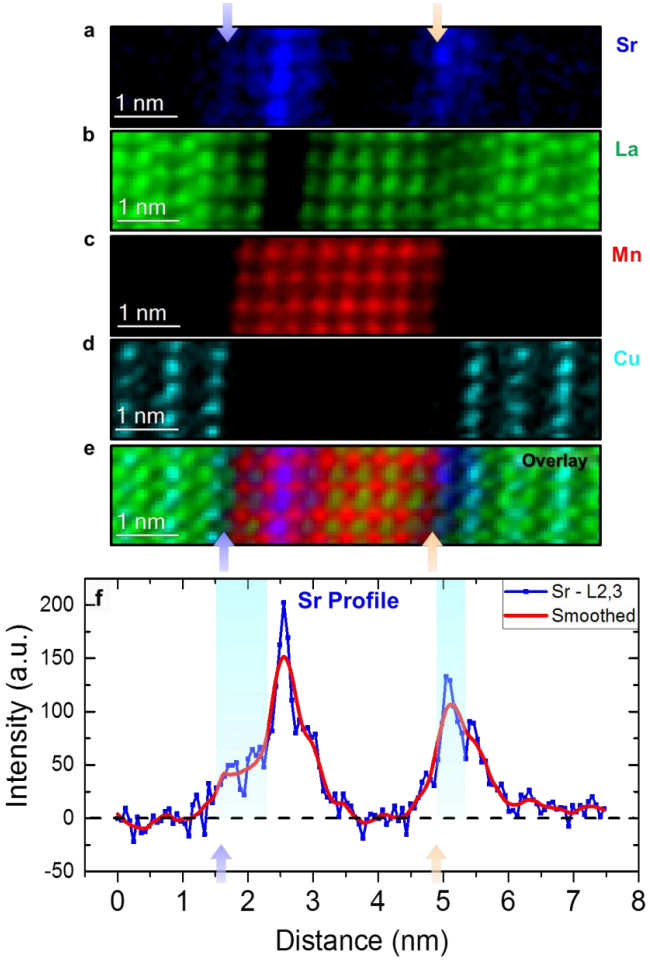

Figure 6.1.4. The atomically resolved elemental maps obtained via EELS spectroscopy, are displayed in panels a), b), c) and d) for Sr (blue), La (green), Mn (red), and Cu (cyan) respectively. e) displays the overlay of the three elements. f) shows the Sr distribution profiles across both interfaces. The linear distortion in the experimental spectrum image is corrected via STEM SI Warp software [129] for the Sr profile plot in (f). Please note that, for clarity, the nominal $SrMnO_3$ and Sr δ-doped La_2CuO_4 layers are shaded light-blue.

Furthermore, in the 113-phase (i.e. SMO-LMO contact) the increased Sr concentration in growth direction is noteworthy, in which the position of the Sr-O layers are majorly deviated from the position they were nominally deposited (Figure 6.1.4). This is an example of Sr segregation towards the surface triggered by the locally induced in-plane strain via La and Sr substitution. In particular, the larger Sr atoms [96] – compared to La – are re-arranged in the structure, in order to relieve the strain and the system is relaxed via the mild modification (i.e. segregation) instead of any defect formation, as high-epitaxial quality is evidenced via STEM-HAADF imaging (Figure 6.1.2, 6.1.3). This behavior is similar to the Ba segregation in epitaxial La_2CuO_4-based systems. [89] The difference in the present case is the sudden stop of Sr distribution after 4 MLs. The importance of the interface sharpness (smoothness) for SMO-LMO superlattices, which directly affects the enhancement (reduction) of the ferromagnetic moment at the interfaces, have been reported. [176,248] But our observation is slightly different from that of the SMO-LMO interfaces reported before. [249]. Such difference could be due to the compressive strain induced by the LSAO substrate and LCO interlayers, which maximizes the effect of the local strain. These findings suggest that the interface sharpness can be further tuned via heteroepitaxial contacts, which influences the magnetic profiles.

Simple segregation is not enough to explain the obvious presence of La-rich (or Sr-deficient) A–O column detected on the first nominal SMO layer and the sudden termination of the SrO segregation. In addition to the HAADF image contrast (Figure 6.1.3), STEM-EELS analyses clearly evidence the La-rich first layer and the Sr segregation in growth direction as well as the A- and B-type interface formation [244] at two interfaces (Figure 6.1.4). Here, one can suggest that the local charge of the layers (polar and unipolar layers) plays a role in this case. The negatively charged CuO_2 layers attract the positively charged LaO layers and the SrO layers are pushed upwards. [139] The abrupt termination of the SrO segregation takes place after the charge is compensated by the LaO layers. Therefore, one can speculate that in addition to the elastic strain energy induced by the size difference of La^{3+} and Sr^{2+}, the local charge difference triggered by La^{3+} and Sr^{2+} substitution plays role in this picture as well. Nevertheless, these interfaces need further examination for detailed evaluation of the mechanism lays behind.

On the other hand, the elemental intermixing on the next interface (i.e. 113-214 interface; manganite-cuprate) shows an interesting contrast at the SMO-LMO interface. The Sr distribution in the system clearly demonstrates the dissimilarity of Sr profiles in two different phases (Figure 6.1.4). In particular, the 2D-doping of Sr in the La_2CuO_4 phase exhibits an asymmetric profile, as reported in previous studies. [55,84] However, our results demonstrate different redistribution lengths in both substrate and growth directions. The distribution in the growth and substrate directions are measured around 1.3 nm (~2 uc) and ~0.65 nm (~ 1 uc), respectively, which gives rise to a sharper interface similar to that of Sr and Ca-doped M-I bilayer structures reported recently. [79] Such difference can be ascribed to the epitaxial strain from $LaMnO_3$, since the growth conditions (~600-650 °C, $3x10^{-5}$ Torr) are the same as for the previous 2D-doping case [84], and therefore, cannot induce different growth kinetics and one can refer to an indirect influence. Nominally, when the compressive strain is induced via the LSAO substrate, 2D-doping in related La_2CuO_4-based systems demonstrate superconducting transition temperatures over 35K [55]. However, in this case, the superconducting transition temperatures are around 25 K instead [245].

The octahedral distortions at oxide heterostructure interfaces are crucially affected by local elemental distribution [89] and have a direct link to the magnetic [153] and electronic [16,79] properties. Therefore, I further conducted STEM-ABF and STEM-HAADF imaging (Figure 6.1.5) that are appropriate methods to quantify the local distortions when combined. Basal (in-plane) and apical (out-of-plane) O–O and La–La interatomic distortions are measured on ABF (Figure 6.1.5a) and HAADF (Figure 6.1.5c) images, respectively. Measured distances versus the number of Cu-O (or Mn-O) layers, which are visible in this particular projection, are displayed in Figure 6.1.5b,d.

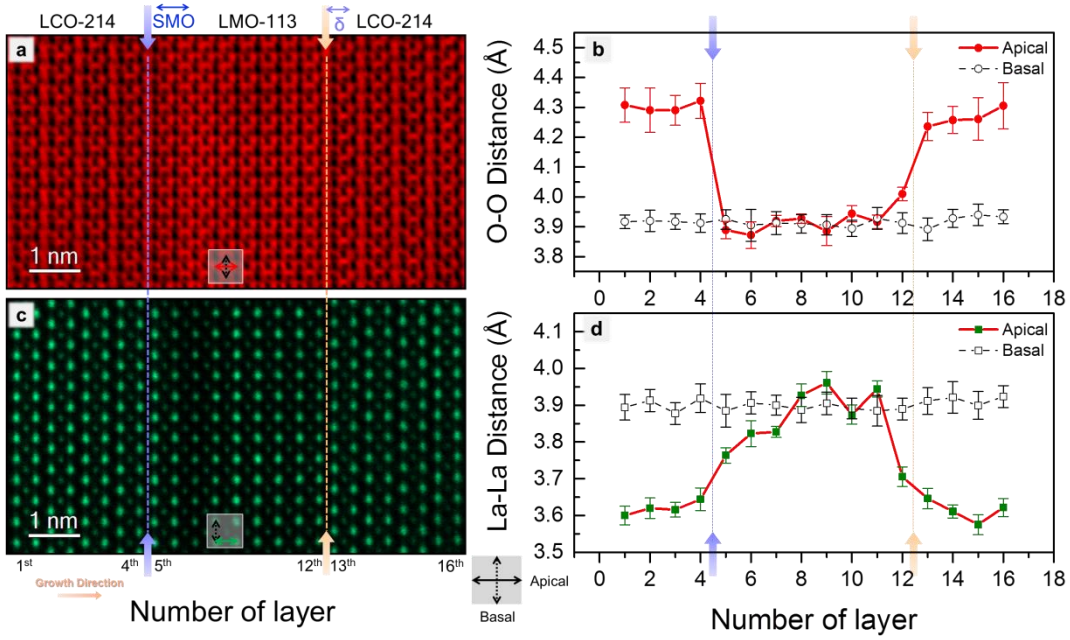

Figure 6.1.5. a) STEM-ABF image displaying all atomic column positions including O-column positions. b) O–O interatomic distances along basal (in-plane) and apical (out-of-plane) directions exhibit the variations across the interfaces. c) The STEM-HAADF image displays the coherent interfaces and the weaker contrast in the Sr-rich region (1-2 MLs). d) La–La interatomic distances along basal (in-plane) and apical (out-of-plane) directions exhibit the variations across the interfaces. The blue and orange arrows on the images indicate the nominal 214-113 and 113-214 interfaces. The apical and basal distances are indicated with straight and dashed lines, respectively. The error bars give the 95% confidence interval (corresponding to 2 times the standard error) of the average of 14 unit cells of the perovskite lattice along the basal (in-plane) direction.

First of all, the basal (in-plane) interatomic distances are about the same along the layers and are measured around 3.90 Å for both of the O–O and La–La basal (in-plane) distances (Figures 6.1.5b,d). This is an indication of the compressive in-plane epitaxial strain induced by the substrate. Regarding the O–O interatomic distance, the larger distances measured in cuprate layers (~ 4.30 ± 0.05 Å) compared to manganite layers, which saturates around 3.90Å, show an abrupt decrease after the 4th layer. Interesting findings stand out when both Sr-containing interfaces are taken into consideration and compared. In particular, the abrupt increase of O–O distance at the last unit cell of the manganite layer (i.e. 12th layer) is noteworthy. Such increase may be related to the space-charge region formed next to the nominal interface. [55] Moreover, the gradual increase of O–O interatomic (apical) distances starting from 13th layer is an example of an anti-Jahn–Teller distortion as observed in homogenously-doped La_2CuO_4 systems. [33] This gradual increase instead of an abrupt change is

due to the longer Sr tail in growth direction. The measurements also showed that, instead of a sharp transition, the apical O–O distances shows a gradual increase just after the 113-214 interface, which suggests that the 214-113 interface is sharper than the 113-214 interface.

Another point to consider is the local effect of substituting La^{3+} cations with Sr^{2+} cations, for which the measurement of La-La apical interatomic distances provides direct information (Figure 6.1.5d). In particular, while in the first LCO layer the La–La distances are constant (~3.61 Å), in the last Sr-containing unit cell of SMO-LMO contact (i.e. 7^{th} layer), the distance is measured as 3.82±0.04 Å. This is followed by the LMO layer with a La–La distance measured as 3.93±0.04 Å which demonstrates that the presence of a larger (i.e. Sr^{2+}) cation in the system suppresses the La–La interatomic distances. Besides, on the 113-214 interface, (again, similar to O–O distances) a smooth transition of the interatomic distances is observed, and this can be explained via the Sr redistribution – with a decay length of 1.3 nm – in growth direction after the nominal interface.

Conclusion

In conclusion, in order to examine the interface formation and the structural and chemical sharpness at the interfaces, ALL-oxide MBE grown lanthanum cuprate-lanthanum manganite heterostructures are probed utilizing comprehensive STEM techniques. The investigations demonstrate the differences of Sr profiles together with the interrelated local lattice deformations that affect the interface sharpness. The observations not only substantiate the tunability of Sr redistribution at oxide heterostructures interfaces via employing different phases but also indicate that sharper interfaces can be obtained via 113-214 contacts. It is further suggested that hetero-epitaxial contacts can be used as a tool to tailor the sharpness of the interfaces, which may lead to tune the physical properties.

7 • Nickelate-based oxide heterostructures

Abstract

In this chapter, state of the art scanning transmission electron microscopy is used to investigate the crystallographic reorientation of $NdNiO_3$ grown on [011]-oriented $NdGaO_3$ substrates. A comprehensive analysis of the microscopy data relates the observed reorientation from the [011]-phase (α-phase) to the [101]-phase (β-phase) to the specific [011]-directionality of the substrate induced epitaxial strain, which can be understood within the framework of DFT+*U* calculations. In addition, the calculations reveal enhanced NiO_6 octahedral breathing distortions for tensile strained β-phases of $NdNiO_3$, which can rationalize recent reports of enhanced metal-insulator transition temperatures in similar $NdNiO_3$-$NdGaO_3$ heterostructures. The observation of a crystallographic reorientation within an epitaxial thin film suggests a new route to tune material properties in heterostructures for future applications in functional devices.

7.1 Structural reconstruction in $NdNiO_3$ thin films

Introduction

Over the last years, technical advances in the synthesis of epitaxial thin films have allowed to stabilize materials of extraordinary stoichiometry and to tailor their properties in an unprecedented fashion. [1,2,4,250] Along these lines, in addition to molecular beam epitaxy (see previous chapters), ablation techniques such as pulsed laser deposition (PLD) [14,15] enable the epitaxial combination of transition metal oxides (TMOs) and other material classes in artificial multilayer systems. In this unique environment, where distinct electronic, magnetic, and orbital correlations can be brought together, novel phenomena, which are not present in the constituents alone, can emerge. [3,4] Prominent examples for such phenomena are induced electronic and magnetic phase transitions [251], orbital reconstructions [6], and interface superconductivity. [9,10]

A profound understanding of the mechanisms leading to the occurrence of novel phases is of utmost importance and enables their controlled appearance, as required for their exploitation in future functional devices. One approach to gain deeper insights explores the materials' response to a variation of external parameters like strain [86,252], doping [79], or electric [253] and magnetic fields. In the case of perovskite TMOs, it was reported that, in addition to the aforementioned parameters, the oxygen octahedral network at the interfaces plays a key role. [33,254–256] The peculiar interfacial epitaxial connection of the substrate or a buffer layer and the deposited film material imposes structural constraints that allow to widely tune emergent material properties, due to the close relation between crystal lattice and electronic, magnetic, and orbital correlations.

In more detail, it was found by means of scanning transmission electron microscopy (STEM) [152,153] that the octahedral coupling between TMO perovskite materials does not only transfer epitaxial strain but also octahedral rotations of the underlying substrate or buffer layer, yielding a modification of properties such as the magnetic anisotropy. [153] In general, the material-substrate relation in the closest interface is of one-to-one type, i.e. the material adopts the in-plane lattice parameters, the octahedral tilt pattern, and the crystallographic orientation of the substrate, while with increasing film thickness these parameters relax towards the bulk values of the material. For particular material combinations, however, epitaxial films can adopt the substrate's tilt pattern even on length scales of several tens of nm away from the interface. [257] In case of matching crystallographic symmetries of substrate and epitaxially deposited film, the film material's unit cells are expected to coincide in their orientation with the substrate, i.e. the substrate orientation determines the orientation of the film.

In this work, spherical aberration (C_s) corrected [104] STEM is used to investigate heterostructures of the perovskite $NdNiO_3$ (NNO) and the paramagnetic insulator $NdGaO_3$ (NGO). TMO heterostructures containing RNiO$_3$ (R = rare earth element) have recently attracted wide-spread interest following theoretical predictions of possible high-T_c superconductivity. [58] In the octahedral environment of the RNiO$_3$ perovskite structure the Ni^{3+} ions are coordinated to six O ions, formally providing Ni with $3d^7$ (t_{2g}^6 e_g^1) configuration. The degree of the Ni–O–Ni bond angle distortion determines the transition temperature for the phase transition from the high temperature paramagnetic metallic state to the insulating and antiferromagnetic ground state, occurring for all members of the RNiO$_3$ family, except for R = La. [258] Moreover, the metal-insulator transition coincides with a structural phase transition from orthorhombic to monoclinic symmetry characterized by a octahedral

breathing distortion yielding two inequivalent Ni sites $Ni^{3+\delta}$ and $Ni^{3-\delta}$. For the prototypical rare-earth nickelate NNO, which in a thin film undergoes a metal-insulator and paramagnetic-antiferromagnetic transition at ~150 K [259], it was shown that the metal-insulator transition temperature is significantly elevated to ~335 K, when NNO films are epitaxially grown on [101] oriented (β-phase) NGO substrates. [260] It was speculated that the specific lattice matching condition between the orthorhombic NNO and NGO for [101] orientation might yield a transfer of the NGO octahedral rotations (i.e. the Ga–O–Ga bond angles) to the NNO octahedral rotations (i.e. the Ni–O–Ni bond angles) not only in proximity to the substrate-film interface, but across the whole thickness of the studied 17 nm thick NNO film. Such an alternation of the Ni–O–Ni bond angle distortions would tune the hopping integral between the O *2p* and Ni *3d* orbitals and therewith increase the effective electronic bandwidth of the system, which could explain the elevated metal-insulator transition temperature.

Here, a similar material system is investigated, i.e. an NNO thin film epitaxially grown on a [011]-oriented (α-phase) NGO substrate. From high-angle annular dark-field (HAADF) [105] and annular bright-field (ABF) [106,107] imaging it is found that the NNO film reorients after a few unit cells from [011] to [101] orientation (α to β-phase), as opposed to maintaining the [011] orientation given by the substrate. Such reorientation is revealed in both, the local Nd- and Ni-site displacements and the alteration of Ni–O–Ni bond angles across the interface region and the film. To rationalize the unexpected emergence of the β-phase on an α-phase substrate, DFT+*U* calculations are employed to simulate epitaxial strain along different crystallographic directions, reproducing the observed phase reorientation and predicting the absence of reorientation for growth on β-phase substrates. Further, from the ABF analyses, the previously suggested transfer of the NGO octahedral rotations across the full thickness of an NNO film is not confirmed, but instead a relaxation of the NNO octahedral rotations (i.e. the Ni–O–Ni bond angles) to bulk-like values after a few unit cells from the substrate-film interface is revealed. Furthermore, the DFT+*U* calculations show that in the tensile strained β-phase the monoclinic breathing distortion can be enhanced. Such behavior correlates with an elevated metal-insulator transition temperature, and hence is consistent with the reported increase of the transition temperature in ref. [260].

Results

Several NNO samples were grown by PLD by G. Cristiani and Dr. G. Logvenov (MPI-FKF). Here, the focus is on an NNO thin film with a thickness of 11.4 nm grown on a NGO substrate (Figure 7.1.1a) with [011] orientation (α-phase), i.e. the NGO substrate surface corresponds to a (011) plane (Figure 7.1.1b). Both, bulk NNO and NGO exhibit the orthorhombic space group *Pbnm* at room-temperature. The lattice parameters are a = 5.428 Å, b = 5.498 Å, and c = 7.709 Å in the case of NGO [261] and a = 5.387 Å, b = 5.383 Å, and c = 7.610 Å in the case of NNO. [262] In this work, the main focus is on the α and β substrate orientations, corresponding to the cuts perpendicular to the (111) body diagonal of the pseudocubic unit cell. Note that, while in the simplified pseudocubic reference frame all body diagonals are equivalent, the (011) and (101) planes (α-and β-planes) of the orthorhombic *Pbnm* unit cell of NNO and NGO are not (Figure 7.1.1a). In a typical epitaxial film growth scenario involving a perovskite TMO material deposited on a compatible oxide substrate, the thin film orients in congruence with the substrate. Moreover, the epitaxial film-substrate relation is expected to be particularly robust for substrates with surfaces perpendicular to one of the pseudocubic

body diagonals (e.g. α- and β-orientation), due to the 3-fold interconnectivity of the octahedral network across an epitaxial interface (Figure 7.1.1b).

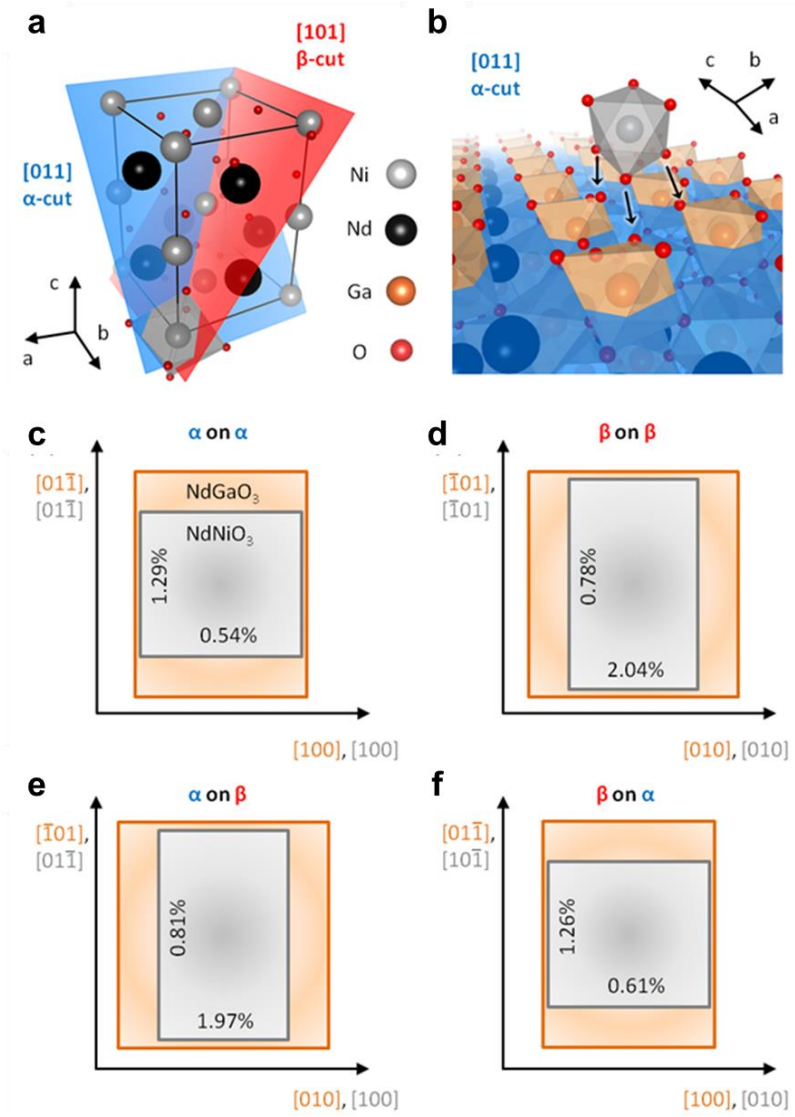

Figure 7.1.1. (a) Depiction of the $NdNiO_3$ unit cell (black lines) in orthorhombic space group *Pbnm*. The planes corresponding to the [011] –and [101]– cut (α- and β-cut) are indicated in blue and red, respectively. For clarity only one NiO_6 octahedron (gray) is superimposed to the unit cell. (b) Schematic of the interconnectivity of the octahedral network across the epitaxial $NdNiO_3$–$NdGaO_3$ interface. One NiO_6 octahedron (gray) is shown in proximity to the α-cut $NdGaO_3$ substrate surface (blue). Each interfacial $NdNiO_3$ octahedron connects to three $NdGaO_3$ octahedra (black arrows). (c)-(f) Illustration of the in-plane epitaxial strain induced to the $NdNiO_3$ unit cell (gray rectangular) by an underlying $NdGaO_3$ substrate (orange rectangular) for different combinations of α -and β-cuts. The indicated in-plane directions of the projected unit cells lie within the α- and β-planes. Unit cell dimensions are exaggerated for clarity. The numbers are the strain magnitudes along these directions calculated as explained in the text. Note that the effective strains for the growth modes α on α (c) and β on α (f) are closely similar.

The larger NGO unit cell dimensions yield tensile in-plane strain for all epitaxial combinations of the NNO unit cell to an NGO substrate. The magnitude of the epitaxial strain along the main in-plane directions depends strongly on the combination of orientations of the two materials. The schematics illustrating the epitaxial film-substrate relation are depicted in Figure 7.1.1c-f with the gray and orange rectangulars corresponding to the in-plane projections of an NNO and NGO unit cell in α- and β-orientation, respectively. The calculated effective strain $(l_{NGO}-l_{NNO})/l_{NNO}$ with l being the lattice parameter along the respective main crystallographic direction, based on the material's bulk lattice parameters at room temperature, yields ~1.3% along the [01-1] and ~0.5% strain along the [100] direction for α-oriented NNO on α-NGO and ~0.8% along the [-101] and ~2.0% strain along the [010] direction for β-NNO on β-NGO. The (at this point) hypothetical combination of α-NNO on β-NGO (Figure 7.1.1e) yields a similar magnitude of strain along the in-plane directions as β-NNO on β-NGO (Figure 7.1.1d). The same applies for β-NNO on α-NGO (Figure 7.1.1f) and α-NNO on α-NGO (Figure 7.1.1c). As a consequence, simple strain minimization cannot explain a potential occurrence of reconstructed phases such as α on β or β on α (Figure 7.1.1e,f).

Aberration-corrected STEM investigations provide valuable local information on structural details and the chemical composition at oxide heterostructure interfaces. First, the crystalline quality and the cation intermixing, particularly in the $NdNiO_3$-$NdGaO_3$ interface region, are examined. An overview STEM-HAADF image of the sample together with an EDS line scan across the interface is presented in Figure 7.1.2. The low magnification STEM-HAADF image (Figure 7.1.2a) acquired along the [011] direction of the NNO substrate reveals the high-quality epitaxial growth of the $NdNiO_3$ film as well as a defect-free structure. The NNO film (light gray) and the NGO substrate (dark gray) can be discerned by their gray-shades in the image due to the presence of a small difference of atomic weights of Ni and Ga (Z_{Ni} = 28 and Z_{Ga} = 31) providing *Z*-contrast information in HAADF imaging. [105] Complementary LAADF imaging, which exposes defects in its contrast [109], confirms the absence of any crystallographic stacking faults in the epitaxial NNO layer on a larger- (i.e. micrometer-) scale (see Figure 7.1.2c). The local chemical properties of the interface are identified by atomically-resolved EDS line scans acquired across the interface as shown in Figure 7.1.2b. The scan profiles of Ni-K (gray), Ga-K (orange), and Nd-L (black) lines reveal the chemical intermixing of Ga-Ni at the interface, which is limited to 2-3 monolayers (MLs) corresponding to <1.5 nm along [011] direction.

After revealing the high quality of the sample, a detailed investigation of the structural distortions and the local octahedral network at the NGO-NNO interface is conducted by STEM-HAADF and by STEM-ABF imaging, respectively. Figure 7.1.3 shows the STEM images together with the corresponding data analysis. The nominal interface is defined in accordance with Figure 7.1.2b and indicated by an orange line serving as a guide to the eye. The high-resolution STEM-HAADF image (Figure 7.1.3a) not only displays the coherent interface region between NGO and NNO but unveils two different phases in the sample: (i) the α-oriented substrate and (ii) a β-oriented NNO film far from the substrate with a gradual reconstruction from α to β in proximity to the interface. The presence of the α-orientation is qualitatively deduced from an overlay of a simulated NGO crystal structure projection to the zig-zag pattern of the atomic Nd-Ga columns (left inset Figure 7.1.3a), and congruently, the β-orientation is deduced from an overlay of the NNO crystal structure projection to the straight columns of Nd–Ni (right inset Figure 7.1.3a).

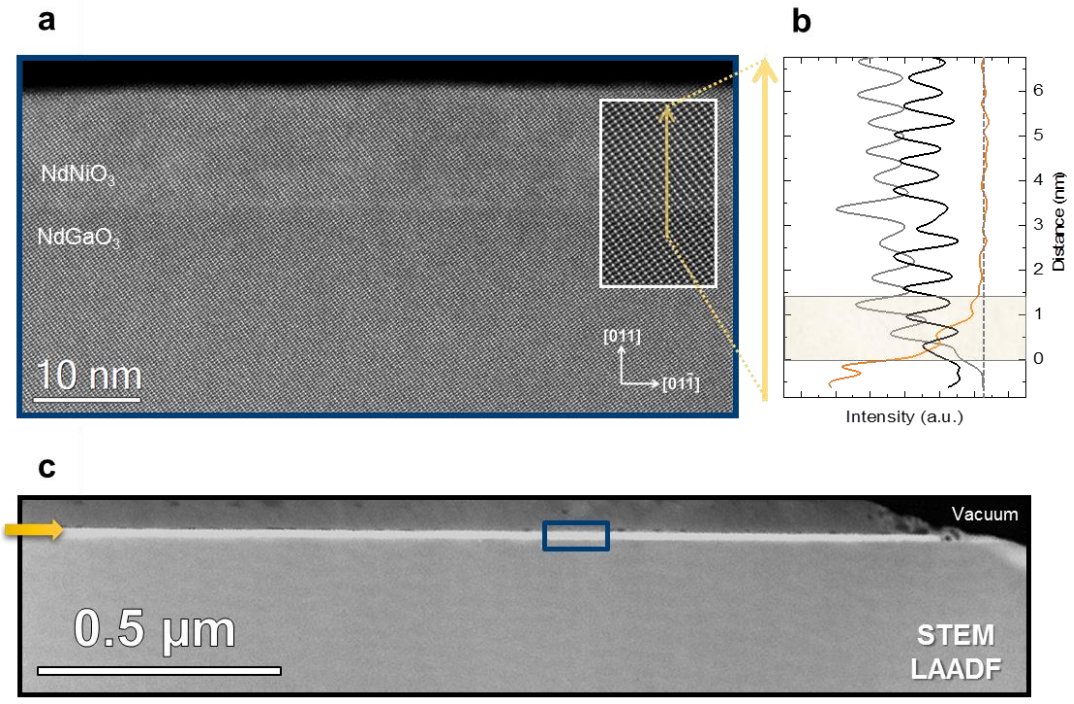

Figure 7.1.2. a) STEM-HAADF image of the $NdNiO_3$ thin film with a thickness of 11.4 nm on a [011] oriented $NdGaO_3$ substrate. The image illustrates the high epitaxial quality and the defect-free structure of the film. The inset is a high-resolution STEM-HAADF image of the film-substrate interface region. b) EDS line scan profiles along the [011] growth direction indicated by the yellow arrow presenting the chemical composition of the $NdGaO_3$-$NdNiO_3$ interface. The orange, black, and gray lines correspond to the EDS intensity of the Ga K, Nd L, Ni K, and lines, respectively. Intermixing of Ni and Ga atomic species in the interface region of ~1.5 nm is marked by the shaded area. The interface is defined at 0 nm and the dashed line corresponds to zero intensity of the EDS. c) STEM-LAADF image with $NdNiO_3$ epitaxial layer indicated by the orange arrow. No structural defects and/or structural grains can be detected, substantiating high crystalline quality. The layer on top of $NdNiO_3$ is the glue from the specimen preparation. The blue box represents the dimensions of the STEM-HAADF image in (a).

This unexpected observation is indicative of a phase reconstruction and demands a quantitative analysis of the local atomic displacements. To this end, the Nd-site displacements, in particular, the interatomic distance variations for the out-of-plane and in-plane directions are quantified. The detailed analyses are employed using the recently developed software Oxygen Octahedra Picker tool [125] that provides the required precision (see Section 3.2.5). The results can be extracted from the panel (b) and (c) displaying the out-of-plane Nd–Nd interatomic distance ($d_{Nd\text{-}Nd}$) while moving away from the interface (orange line), which is indicated here as the number of Ni–O planes. Please note that each data point in (b) and (c) corresponds to the average of 8 atomic columns. Obviously, a strong zig-zag behaviour evolves as a function of increasing number of Ni–O planes corresponding to an alteration in the structure. In more detail, with the present calibration, the out-of-plane Nd–Nd distances in the NGO substrate are determined as 2.68 ± 0.04 Å, whereas a decrease to 2.59 ± 0.02 Å is observed in the 4th Ni–O plane after the nominal interface. The sharp decrease is followed by a narrow-range (5-6 MLs) with Nd–Nd interatomic distances around $d_{Nd–Nd}$ = 2.65 Å. Starting from the 11th Ni–O plane, the fluctuation (or absolute difference) in $d_{Nd–Nd}$ between the adjacent Ni–O planes increases and exceeds 0.016 ± 0.05 Å and saturates. Next, the in-plane Nd–Nd interatomic distances are considered (Figure 7.1.3c) and a constant $d_{Nd–Nd}$ ~3.80 Å is observed. The entire Nd cation

sublattice of the film is coherently strained. This interpretation is also confirmed by the absence of any extended defects in the structure (c.f. Figure 7.1.2).

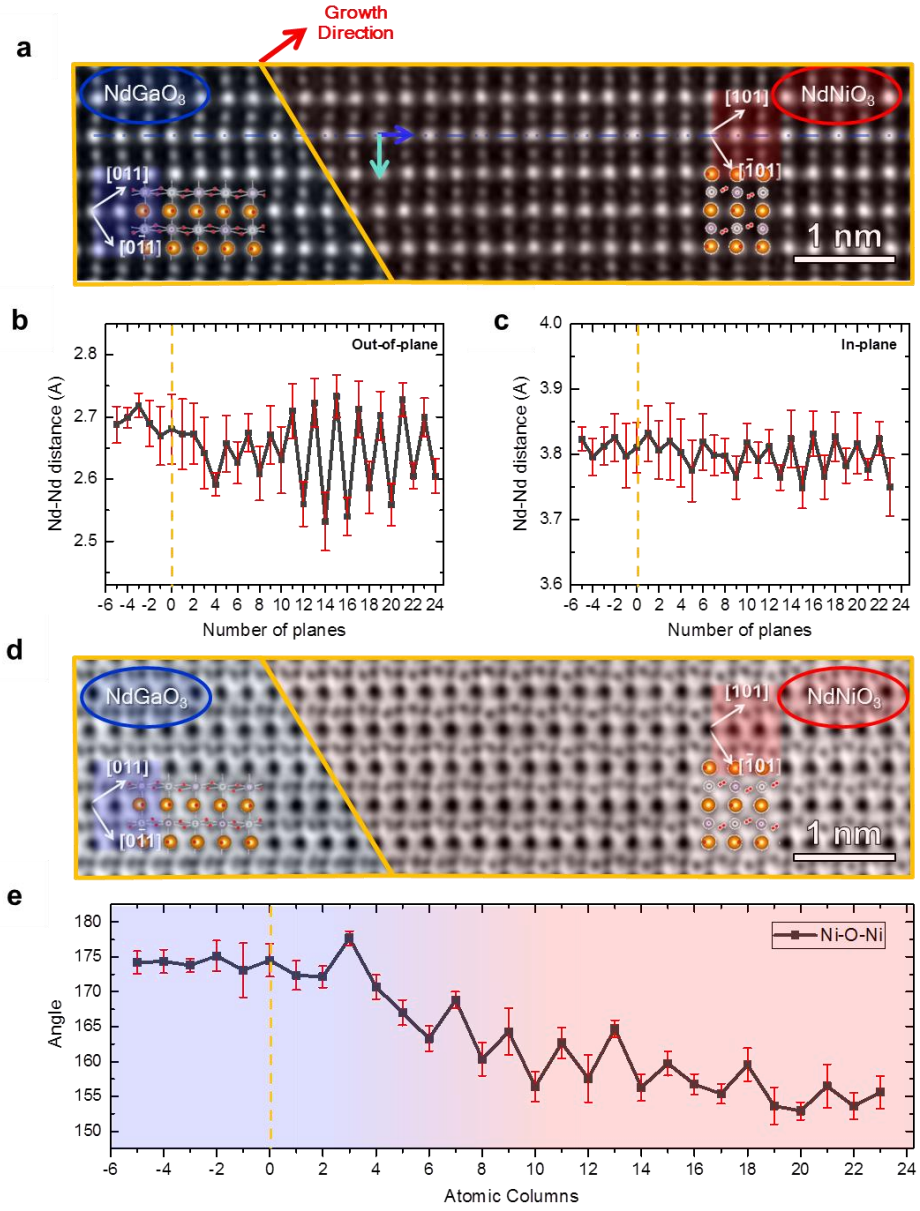

Figure 7.1.3. a) STEM-HAADF image taken along the epitaxial layer including the substrate/epitaxial layer interface. Blue and green arrows indicate measured out-of-plane and in-plane Nd–Nd interatomic distances, respectively, shown in (b) and (c). d) STEM-ABF image, simultaneously acquired with the STEM-HAADF image in (a), providing the oxygen column positions, and (e) Ni–O–Ni bond angle measurements performed on the ABF image shown in (d). The orange lines and the dashed lines mark the nominal interface in the images and the plots, respectively. The error bars of the bond angle determination (95% confidence interval, corresponding to 2 times the standard error) is less than 1º. The blue and red colored areas are guides for the eye indicating the α- and β-phases, respectively.

To gain deeper insights on the interface-induced reconstruction, I have used the STEM-ABF technique, which allows imaging of light elements [105], i.e. oxygen in the present case. A STEM-ABF image of the interface region is presented in Figure 7.1.3d with the entire set of clearly resolved atomic columns in the structure, which are Nd–O, Ga, Ni and O atomic columns in this projection. It should be emphasized that the STEM-ABF image (Figure 7.1.3d) was simultaneously acquired with the STEM-HAADF image presented in Figure 7.1.3a. Focusing on the Ni and O atomic columns, it is obvious that the Ni–O–Ni pattern exhibits a clear transition from a straight line in NGO to a zig-zag pattern in NNO away from the interface. This indicates a reorientation of the crystallographic unit cell which can be corroborated quantitatively by measuring the bond angles between the cation sublattices along the growth direction, namely the Ga–O–Ga angles in the substrate and the Ni–O–Ni angles in the interfacial region and beyond. The analyses averaging 9 atomic columns (Figure 7.1.3e shows a section of the analyzed image) give a projected Ga–O–Ga bond angle of 174° ± 1°. However, a decrease of 2° of this bond angle is observed just after the interface (i.e. 7th and 8th columns). In the consecutive columns, the measured Ni–O–Ni angle indicates a transition between two different phases. Such transformation to a β-phase is characterized by a saturation of the Ni–O–Ni angles around 155° ± 1.2°. The value of ~155° extracted for the Ni–O–Ni angles is consistent with the bond angle of bulk NNO, while NGO exhibits a bond angle of 153° in the corresponding projection of the β phase.

While the presence of the reconstruction is clear from the experimental STEM data and the detailed analyses, the mechanism behind its occurrence is not directly evident, as elucidated earlier in the text and in the strain minimization consideration of Figure 7.1.1c–f. Therefore, DFT+*U* calculations representing an α- and β-oriented NGO substrate, respectively (Figure 7.1.4) were performed by Dr. Z. Zhong and Dr. P. Hansmann (MPI-FKF). An effective Hubbard *U* of 2 eV, typical for nickelates [263,264], was employed. In Figure 7.1.4, the DFT ground-state energy calculated as a function of the out-of-plane lattice spacing "*d*" for NGO α-phase and NGO β-phase are presented, respectively. For the α-phase and β-phase calculations, the spacing *d* correspond to the distance between consecutive NiO_3 planes along the [011] and [101] directions, respectively. Figure 7.1.4a,b shows the energies in dependence of relative spacing $d_0 = d/d_{bulk}$. While the in-plane atomic distances were fixed to the values of NGO in (011) and (101) planes, the out-of-plane distances were allowed to vary in the calculations to account for the effect of tensile strain. For both types of substrate cuts, i.e. α-NGO (Figure 7.1.4a) and β-NGO (Figure 7.1.4b), it is revealed that the β-NNO phase/orientation is energetically favourable compared to the α-NNO phase/orientation within the error bar of the experimentally obtained relative out-of-plane lattice plane spacing of 0.989 ± 0.04 Å. This explains the experimentally observed reorientation of $NdNiO_3$ grown on α-cut $NdGaO_3$. For these small values of the relative spacing d_0, the calculation yields a phase (α'-phase) with α-orientation but an altered octahedral tilt pattern, i.e. symmetry corresponding to the crystallographic space group $R\bar{3}c$. While bulk LNO exhibits this space group, to the best of our knowledge, there are no experimental reports observing NNO in space group $R\bar{3}c$. Since moreover the α'-phase does not yield a global minimum, this phase is not discussed further here. Instead, the β-phase is considered in more detail in the following. The most striking feature of the calculated NNO β-phase in the global minima of Figure 7.1.4a,b is an enhancement of the monoclinic breathing distortion. The Ni–O bond disproportionation for α and β-induced tensile strain (Ni–O bond lengths 1.97 Å and 1.90 Å for long and short bond lengths, respectively) is two times larger than that of the bulk case (1.94 Å and 1.91 Å).

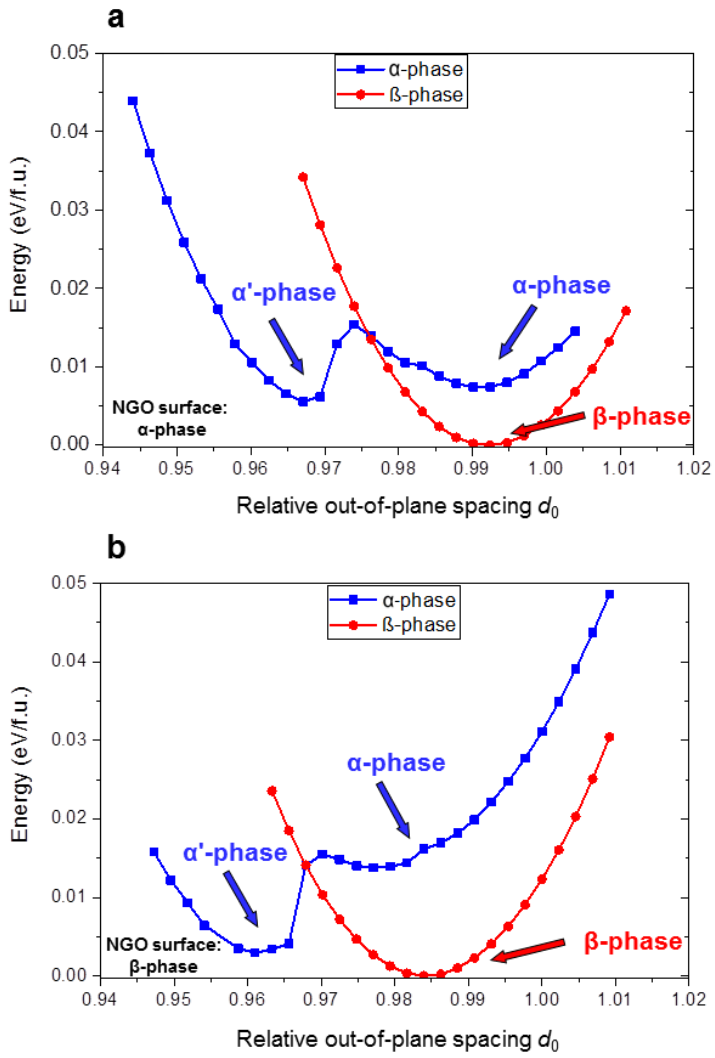

Figure 7.1.4. DFT+*U* ground state for different epitaxial configurations depicted in Figure 7.1.1(e-f). (a) In-plane lattice constants of $NdNiO_3$ are fixed at the values corresponding to the α-cut $NdGaO_3$, while the $NdNiO_3$ out-of-plane lattice constant is allowed to relax, simulating the effects of epitaxy on an α-$NdGaO_3$ substrate surface. The $NdNiO_3$ in-plane directions are [100] and [01-1], and the out-plane is [011] for the α-phase calculation (blue curve). For the β-phase calculation, in-plane directions are [010] and [-101] and the out-plane direction is [101] (red curve). The global minimum is obtained for the β-phase calculation indicating the energetically most favorable state that corresponds to β-phase $NdNiO_3$ unit cells in epitaxy to the α-phase $NdGaO_3$ substrate. This explains the experimentally observed reorientation of $NdNiO_3$ grown on α-cut $NdGaO_3$. Furthermore, the magnitude of the octahedral breathing distortion in the $NdNiO_3$ β-phase ground state is strongly enhanced which promotes its emergence. (b) Analogous calculation to (a), but with $NdNiO_3$ in-plane lattice fixed at values corresponding to β-cut $NdGaO_3$. The global minimum is obtained within the beta-phase calculation suggesting that no reorientation takes place in case $NdNiO_3$ is grown on β-cut $NdGaO_3$.

Discussion

The present study is an important example for non-trivial occurrence of phase reconstructions. As illustrated in Figure 7.1.1c-f a simple consideration of strain minimization cannot explain the observed α-to-β phase reconstruction. By means of STEM imaging, however, several important insights on the investigated system could be gained. First, the high quality of the $NdNiO_3$ film in terms of epitaxy and coherency of the crystal structure could be corroborated (Figure 7.1.2a,c). This makes it unlikely that the observed α-to-β phase reconstruction is due to accumulation of defects and stacking faults in the crystal lattice. Chemical intermixing at the $NdGaO_3$–$NdNiO_3$ interface (Figure 7.1.2b), which typically is a consequence of growth kinetics and surface segregation [79,84], was revealed to be limited to only 1-1.5 nm in the growth direction. The transition region [265] of the reorientation of the epitaxially connected α and β layers was, however, determined to extend up to ~10-12 ML away from the film-substrate interface (Figure 7.1.3a). This length scale is significantly longer than the chemical intermixing region, thus interfacial disorder as a major driving mechanism for the phase reconstruction can also be ruled out. The STEM-HAADF and STEM-ABF image analysis gave a detailed quantification of the α and β phases, and the transition region in terms of Nd, Ni, and O atomic positions as well as the Ni–O–Ni bond angles. It is shown that the Ni–O–Ni angle is relaxed to the value of ~155º after the transition region implying that the NGO octahedral rotations have not been transferred across the whole NNO film. Deeper insights on the mechanism and the energy landscape behind the phase reconstruction were provided by the DFT+*U* calculations. A global minimum in the energy landscape for the strain induced by an α-phase substrate is obtained for NNO in β-phase orientation, rationalizing the experimentally observed phase reconstruction (Figure 7.1.4a). On the other hand, for a substrate orientation corresponding to the β-phase, also the β-phase NNO exhibits the global minimum, i.e. no reconstruction will take place in this case (Figure 7.1.4b). The second important result of the calculation is that the magnitude of the octahedral breathing distortion in the NNO β-phase ground state is strongly enhanced as compared to bulk NNO. This promotes its emergence over the α-phase and also gives an explanation for the elevated metal-insulator transition temperature reported in ref. [260].

Conclusion

In conclusion, a comprehensive study of the structural properties and the interface chemistry of epitaxial $NdNiO_3$ thin films grown on $NdGaO_3$ substrates revealed a substrate induced crystallographic reconstruction. The atomically-resolved STEM investigations provided a unique local probe of the samples and allowed to quantify not only structural deformations but also modifications of the octahedral network (i.e. the alteration of Ni–O–Ni bond angles across the interface region). DFT+*U* calculations corroborated the reconstruction found from the STEM analysis. Thus, the present work emphasizes the importance of epitaxial strain and local structural details at interfaces for the emergence of novel phases in thin films and heterostructures. The methodology used can be applied to similar oxide material systems and help to improve the understanding of strongly correlated interactions occurring at interfaces.

8. Epilogue

Abstract

This chapter gives a brief overview to the study: The aim and the motivation of the thesis are blended with the outcomes and the conclusions obtained within the thesis.

In this thesis, I looked for an answer to the following question: "To which extent can epitaxial oxide heterostructures and interfaces be controlled and identified?" For this purpose, various projects were conducted in which not only the growth of La_2CuO_4-based systems are performed but also the structural and chemical identifications and octahedral distortions at the interfaces are comprehensively investigated. Through the projects, different factors such as (i) dopant size effects, (ii) two-dimensional doping (i.e. δ-doping), (iii) growth temperature gradient, (iv) contact of different phases, (v) layer-thickness variations, (vi) different substrates and their influences on the interface structures and/or on the functionalities are examined. Besides, the applications of STEM imaging and quantification as well as the analytical techniques are extensively employed, which are associated with the interface structures of oxide heterostructures.

It is revealed for La_2CuO_4 metal-insulator bilayer systems that the different cationic radii of the dopants (Ba^{2+}, Sr^{2+}, Ca^{2+}) remarkably affect the superconducting mechanisms (i.e. bulk vs interface), as a consequence of dopant redistribution near the interface. In the case of the $La_{2-x}Ca_xCuO_4/La_2CuO_4$ and $La_{2-x}Sr_xCuO_4/La_2CuO_4$ systems, the interfaces were found to be sharper, and thereby, striking interface effects, i.e. electronic redistribution, are predominant. However, in the case of $La_{2-x}Ba_xCuO_4/La_2CuO_4$, high-temperature superconductivity (HTSC) is rather ascribed to "classical" homogeneous doping determined by wide cationic intermixing. Moreover, the dopant distribution has a remarkable effect on the O–O distances, which are suggested to be related to different mechanisms leading to HTSC: While the sharp interfaces are correlated with Jahn–Teller distortion, anti-Jahn–Teller distortion is dominant for the homogeneous doping (Ba-doping) case. On the other hand, for 2D-doping of La_2CuO_4, it is found that the cationic dopant profiles are highly asymmetric with different sharpnesses: Abrupt at the downward side of the interface and broadened in growth direction. Conversely, the hole distribution, as measured by STEM-EELS, is symmetric across the interface and is decoupled from the dopant profile at the downward interface. This indicates that hole doping is achieved on the two sides of the Sr-doped plane by two distinct mechanisms: Heterogeneous doping at the downward side of the interface and homogeneous doping at the upward side.

In the case of lanthanum cuprate–lanthanum nickelate multilayers, where LNO is employed as two different phases (i.e. 214-$La_{2-x}Sr_xNiO_4$ and 113-$LaNiO_3$), different properties, in addition to structural considerations, are studied. For La_2CuO_4-$La_{2-x}Sr_xNiO_4$ contact, a chemically sharp interface inducing a hole accumulated space-charged layer is detected by STEM-EELS analyses, while a certain tendency for Sr to migrate from $La_{2-x}Sr_xNiO_4$ to La_2CuO_4 that gives rise to a 'less' sharp interface. Moreover, concerning the thermoelectric properties of La_2CuO_4–$LaNiO_3$ heterostructures, the importance of the choice of the individual layer thicknesses is revealed: The thinner the individual La_2CuO_4 and $LaNiO_3$ layers, the more chemical intermixing at the interfaces occurs, which directly influences the physical properties.

As far as the heterojunctions of $La_2CuO_4/LaMnO_3$ layers are concerned, it is found that dissimilar Sr profiles are present in cuprate and manganite phases, which lead to different interface sharpness suggesting the tunability of Sr redistribution using oxide hetero-structural contacts. Moreover, the quantification of local octahedral distortions indicates that 113-214 interfaces are sharper compared to 214-113 interfaces. Concerning the $NdNiO_3$ thin films, the realization of a structural reorientation from the [011]-phase to the [101]-phase could be understood via DFT+*U* calculations suggesting enhanced NiO_6 octahedral breathing distortions.

In conclusion, the exciting output of this thesis can be summarized as the following:

(i) The choice of the dopant (size) directly affects the interface sharpness, namely, the dopant re-distribution, local octahedral distortions and thereby the interface functionalities in La_2CuO_4 based systems.

(ii) Two-dimensional doping (i.e. δ-doping) of La_2CuO_4 in the form of superlattices results in different dopant distribution at both sides of the interfaces due to the growth kinetics and correlatively induces the different superconducting mechanisms at two sides of the interfaces.

(iii) The defect chemistry and the transfer of the species can induce space-charge regions in both homoepitaxial (e.g. δ-doping of La_2CuO_4) and heteroepitaxial (e.g. La_2CuO_4 - $La_{2-x}Sr_xNiO_4$ contacts) oxide systems with sharp interfaces.

(iv) The choice of the layer thickness in heterojunctions, e.g. La_2CuO_4-$LaNiO_3$ contacts, is of great importance and may result in the unintentional occurrence of different phases or solid solutions.

(v) The dopant distribution of the same element (i.e. Sr) in different materials exhibit different elemental distribution even at consecutive interfaces.

(vi) In $NdNiO_3$ films, a reconstruction of the crystallographic orientation is detected when tensile strain is imposed by a [011]-oriented $NdGaO_3$ substrate.

In summary, in addition to the remarkable capabilities of ALL-oxide MBE system, the feasibility of using spherical aberration corrected STEM to quantitatively describe the elemental distribution, charge distribution and the local atomic distances in LCO-based interfaces are discussed. Although numerous oxide heterostructures with different novel properties have been studied, this thesis provides a comprehensive overlook to homoepitaxial and heteroepitaxial interfaces. This work underlines that various factors affect the interface profiles and give rise to different physical properties, although atomic-precise engineering and identification are possible.

This page intentionally left blank

9 • Appendices

9.1 A : List of publications

Published: During PhD

1. Y. E. Suyolcu, Y. Wang, F. Baiutti, W. Sigle, G. Cristiani, J. Maier, G. Logvenov, P. A. van Aken, "Aberration-Corrected Scanning Transmission Electron Microscopy of La_2CuO_4-based Superconducting Interfaces at the Stuttgart Center for Electron Microscopy" *JEOL News*, 53(1), 8-17, 2018. **(Invited; Front Cover)** [266]
2. Y. E. Suyolcu, Y. Wang, W. Sigle, F. Baiutti, G. Cristiani, J. Maier, G. Logvenov, P. A. van Aken, "Octahedral Distortions at High-temperature Superconducting La_2CuO_4 Interfaces: Visualizing Jahn–Teller Effects" *Advanced Materials Interfaces*, **4**, 1700737, 2017. **(Frontispiece Cover)** [89]
3. Y. E. Suyolcu, Y. Wang, F. Baiutti, A. Al-Temimy, G. Gregori, W. Sigle, G. Cristiani, J. Maier, P. A. van Aken, G. Logvenov, "Dopant size effects on novel functionalities: High-temperature interfacial superconductivity", *Scientific Reports*, **7**, 453, 2017. [79]
4. M. Hepting, R. J. Green, Z. Zhong, M. Bluschke, Y. E. Suyolcu, S. Macke, A. Frano, S. Catalano, M. Gibert, R. Sutarto, F. He, G. Cristiani, G. Logvenov, Y. Wang, P. A. van Aken, P. Hansmann, M. Le Tacon, J.-M. Triscone, G. A. Sawatzky, B. Keimer, E. Benckiser; "Complex magnetic order in nickelate slabs", *Nature Physics*, **10**, 1097–1102, 2018. [267]
5. P. Kaya, G. Gregori, F. Baiutti, P. Yordanov, Y. E. Suyolcu, G. Cristiani, F. Wrobel, E. Benckiser, B. Keimer, P. A. van Aken, H.-U. Habermeier, G. Logvenov and J. Maier, "High Temperature Thermoelectricity in $LaNiO_3$-La_2CuO_4 Heterostructures ", *ACS Appl. Mater. Interfaces*, **10**(26), 22786-22792, 2018. [238]
6. F. Baiutti, G. Gregori, Y. E. Suyolcu, Y. Wang, G. Cristiani, W. Sigle, P. A. van Aken, G. Logvenov and J. Maier; "High-temperature superconductivity at the lanthanum cuprate/lanthanum-strontium nickelate interface", *Nanoscale*, **10**(18), 8712-8720, 2018. [205]
7. Y. Wang, Y. E. Suyolcu, U. Salzberger, K. Hahn, V. Srot, W. Sigle, P. A. van Aken, "Correcting the linear and nonlinear distortions for atomically resolved STEM spectrum and diffraction imaging", *Microscopy*, **67**, i114-i122, 2018. [129]
8. F. Baiutti, G. Gregori, Y. Wang, Y. E. Suyolcu, G. Cristiani, P. A. van Aken, J. Maier, G. Logvenov, "Cationic Redistribution at Epitaxial Interfaces in Superconducting Two-Dimensionally Doped Lanthanum Cuprate Films", *ACS Appl. Mater. Interfaces*, **8**, 27368-27375, 2016. [84]
9. Y. Wang, U. Salzberger, W. Sigle, Y. E. Suyolcu, P. A. van Aken, "Oxygen Octahedra Picker: a software tool to extract quantitative information from STEM images", *Ultramicroscopy*, **168**, 46-52, 2016. **(Front Cover)** [125]

Published: Earlier Work

10. M. Korkmaz, B. Arikan, Y. E. Suyolcu, B. Aslan, U. Serincan, "Performance evaluation of InAs/GaSb superlattice photodetector grown on GaAs substrate using AlSb interfacial misfit array", *Semicond. Sci. Technol*., **33**, 035002, 2018.
11. S. Ozdemir, Y. E. Suyolcu, S. Turan, B. Aslan, "Influence of the growth conditions on the optical and structural properties of self-assembled InAs/GaAs quantum dots for low As/In ratio", *Applied Surface Science*, **392**, 817-825, 2017.
12. B. Arikan, G. Korkmaz, Y. E. Suyolcu, B. Aslan, U. Serincan, "On the crystallographic characterization of InAs/GaSb type-II superlattices: The effect of interfaces for fixed layer thicknesses", *Thin Solid Films*, **548**, 288-291, 2013.

Unpublished: PhD Work

13. G. Kim, Y. Khaydukov, M. Bluschke, Y. E. Suyolcu, G. Cristiani, K. Son, C. Dietl, T. Keller, E. Weschke, P. A. van Aken, G. Logvenov and B. Keimer, "Tunable perpendicular exchange bias in oxide heterostructures", *submitted*.
14. Y. E. Suyolcu, G. Cristiani, A. Bussmann-Holder, P. A. van Aken & G. Logvenov, "Understanding of the surface reconstruction during epitaxial growth of $(LaSr)_2CuO_4$ thin films", *in preparation*.
15. Y. E. Suyolcu, M. Hepting, Z. Zhong, Y. Wang, G. Cristiani, G. Logvenov, P. Hansmann, E. Benckiser, B. Keimer, P.A. van Aken, "Interface Induced Reconstruction in $NdNiO_3$ Thin Films", *in preparation*.

9.2 B : Biographical note

Education

Ph.D.,
Materials Science
2014-2018

Max Planck Institute for Solid State Research;
Technical University of Darmstadt (TUD); Germany

Supervisors: Prof. Dr. Peter A. van Aken
Prof. Dr. Hans-Joachim Kleebe

M. Sc.,
Nanotechnology
2010-2013

Department of Materials Science & Engineering;
Department of Advanced Technologies; Graduate School of Sciences,
Anadolu University, Eskisehir, Turkey.

Supervisors: Assoc. Prof. Dr. Bulent Aslan
Prof. Dr. Servet Turan

9.3 C : Honors & awards

- Award: **Young Scientist Award**, E-MRS 2017 Spring Meeting, 22-26 May 2017, Strasbourg, France.
- Award: 2016 **Student Award**, (Presidential Scholar Award) Microscopy & Microanalysis (M&M) 2016, 24-28 July 2016, Columbus (Ohio), USA.
- **Cover figure** for the work in *JEOL News*: Aberration-Corrected Scanning Transmission Electron Microscopy of La_2CuO_4-based Superconducting Interfaces at the Stuttgart Center for Electron Microscopy" (2018).
- **Cover figure** (frontispiece cover) for the work in *Advanced Materials Interfaces*: "Octahedral Distortions at High-temperature Superconducting La_2CuO_4 Interfaces: Visualizing Jahn–Teller Effects" (2017).
- Scholarship: Deutsche Gesellschaft für Elektronenmikroskopie (DGE) **Travel Scholarship** for attending "19th International Microscopy Congress" (IMC19), Sydney, Australia.
- Scholarship: **Young Researchers Scholarship** for attending "16th European Microscopy Congress" European Microscopy Society (EMS), (EMC2016), Lyon, France.
- Student Scholarship(s): Deutsche Gesellschaft für Elektronenmikroskopie (DGE) **Student Scholarship(s)** for attending
  i. "Microscopy & Microanalysis (M&M) 2017, St. Louis (Missouri), USA;
  ii. "16th European Microscopy Congress" (EMC2016), Lyon, France;
  iii. "Microscopy Conference 2015" (MC2015), Göttingen, Germany.
- Scholarship: Anadolu University Scientific Research Unit, **Travel Scholarship** (full bursary), for attending 15th European Microscopy Congress (EMC2012), Manchester, England
- Scholarship/Stipend: **Max Planck Society Research Scholarship**, for PhD research in Max Planck Institute for Solid State Research (2014-2018).
- Scholarship/Stipend: The Scientific and Technological Research Council of Turkey (**TUBITAK**), within the project called:" Growth and Characterization of GaSb and InAs layers on GaAs Substrate by Molecular Beam Epitaxy". (2012-2014)
- Scholarship/Stipend: Undersecretariat for Defence Industries (SSM) Turkey –**Student Researcher Scholarship**, within the project called: "Development of InAs/GaSb Infrared Photodetector Technology (KOFDE)". (2011-2013)
- Grant: Anadolu University Scientific Research Unit: **Grant** for the Scientific Research Project entitled "Characterization of Epitaxially Grown GaSb/InAs Superlattice Structures by Electron Microscopy" (with project leader Assoc. Prof. Dr. Bulent Aslan)

List of Figures

Figure 3.1.3. The specular spot (00) (red) and Bragg spot (10) (blue) oscillations are recorded during the growth of $La_{1.6}$ $Ba_{0.4}CuO_4/La_2CuO_4$ bilayer. The intensities were integrated over selected areas, and one oscillation corresponds to a half u.c. thickness of the La_2CuO_4-based crystal structure. The dashed lines indicate the nominal M–I interface.

Figure 3.1.4. RHEED images obtained during the growth of optimum (x =0.16) Sr-doped La_2CuO_4. The two additional streaks in (a) and four additional streaks in (b) indicate the "half" and the "complete" deposition of the Cu–O layer, respectively.

Figure 3.1.5. RHEED images obtained during the growth of $La_{1.84}Sr_{0.16}CuO_4$ films grown on (a) (100) STO and (b) (001) LSGO substrates inducing tensile strain: Three diffraction lines refer to the 4a width (in-plane) atomic ordering for both cases. (c) RHEED image after the deposition of the Cu layer during the growth of $La_{1.84}Ca_{0.16}CuO_4$ film on LSAO substrate exhibits three diffraction lines similarly.

Figure 3.1.6. RHEED images of epitaxial $La_{1.84}Sr_{0.16}CuO_4$ films acquired after the Cu layer deposition in (a) vacuum and (b) after ozone annealing. The oxidation atmosphere causes different surface reconstructions.

Figure 3.3.1. Cross-sectional simple illustration model of the ray diagram, optical axis, spherical aberration corrector, and detector positions for HAADF, ABF and EELS spectrum imaging. Please note that, nominally, an EEL spectrum is formed at the end of the spectrometer (see Figure 3.3.5 for an example).

Figure 3.3.2. a) STEM-HAADF image taken of a Ca-doped bilayer and b) absolute thickness profile obtained from the EELS spectrum image showing the homogeneous thickness of the sample.

Figure 3.3.3. Steps of TEM specimen preparation: a) diamond wire saw used for cutting, b) grinding and wedge polishing with the Allied MultiPrep system [102], c) sample glued on a half grid and d) argon ion-milled sample with apparent thickness fringes as observed in the light microscope.

Figure 3.3.4. A plan-view illustration of HAADF and ABF detectors. Representative HAADF (darker, outer) and ABF (inner, brighter) experimental images taken from the $SrTiO_3$ specimen are bestrewed on the detector schematics. Please note that the experimental images are illustrated for a better presentation; nominally, there is no image formation on the detector, instead, a diffraction pattern is detected.

Figure 3.3.5. a) Simultaneously acquired STEM-HAADF and b) STEM-ABF images of (4) LSMO / (8) SRO multilayer sample presenting the coherent interfaces as well as projecting all possible atomic column positions. The images taken in [1-10] direction were processed with a multivariate weighted principal component analysis routine (MSA Plugin in Digital Micrograph) to decrease the noise level.

Figure 3.3.6. a) Schematic diagram of a general EELS spectrum. b) The origin of the ELNES intensity which reflects the unoccupied DOS above the Fermi level. Reproduced with permission from Ref. [120]. c) Experimental EELS spectrum from obtained Ba-doped La_2CuO_4 bilayer sample showing O-K, Ba-$M_{5,4}$, La-$M_{5,4,}$ and Cu-$L_{3,2}$ edges.

Figure 3.3.7. Sr (La)–Sr (La) (a; left column) and O-O (b; right column) interatomic (out-of-plane and in-plane) distances obtained from (4) LSMO / (8) SRO PLD grown samples. The interatomic distances measured by the O–O picker tool reveal the "constant" in-plane interatomic distances substantiating the epitaxial growth. Out-of-plane measurements employed for both on HAADF and ABF images show interesting local distortions: (i) the La (Sr)-La (Sr) interatomic distances in SRO/LSMO are different from those in LSMO/SRO, (ii) similar to La(Sr)–La(Sr) interatomic distances, O–O distances are larger in the SRO/LSMO interface compared to LSMO/SRO. The blue and green arrows on the images indicate the nominal SRO–LSMO and LSMO–SRO interfaces.

Figure 3.3.8. Illustration of a raster scan in scanning transmission electron microscopy. The schematic presents the fast and slow scanning directions. Note that the fast scan direction is composed of many small steps instead of one long scan.

Figure 3.3.9. (a) Non-linear distortion partially corrected STEM-EELS SI data, (b)–(e) atomic-column-resolved Nd-$M_{4,5}$ (red), V-$L_{2,3}$ (green), Ga-$L_{2,3}$ (blue), and La-$M_{4,5}$ (magenta) elemental maps extracted from the distortion-corrected SI.

Figure 4.1.1. Structural model of the $La_{1.6}A_{0.4}CuO_4/La_2CuO_4$ bilayers grown on the LSAO substrate. The bilayers are composed of two different layers: (i) overdoped (metallic, M) $La_{1.6}A_{0.4}CuO_4$ and undoped (insulator, I) La_2CuO_4, respectively.

Figure 4.1.2. RHEED patterns of the three different bilayers: a) LCCO/LCO, b) LSCO/LCO, c) LBCO/LCO. AFM images of the top surface of the three different bilayers: d) LCCO/LCO, e) LSCO/LCO, f) LBCO/LCO. One can observe the different surface morphology, in particular, in the case of LBCO/LCO, secondary phase precipitates can be observed (some are marked by blue arrows). The atomic steps with heights of less than one unit cell (u.c.) are attributed to a small substrate miscut angle (~0.1°). g) rms roughness values of three bilayers versus cation radius (pm). Reproduced from *Suyolcu et al.* [79].

Figure 4.1.3. High magnification AFM images of three different bilayers: a) LCCO/LCO, b) LSCO/LCO, c) LBCO/LCO. Line scan profiles obtained from the AFM images given in a-c: d) LCCO/LCO, e) LSCO/LCO, f) LBCO/LCO. One can observe the different surface morphology. In the case of LBCO/LCO, secondary phase precipitations can be observed with up to 3-4 nm height. g) The critical thickness of the LBCO film versus Ba concentration at which RHEED patterns indicate nucleation of secondary phase precipitates. The top inset RHEED image has extra diffraction spots in comparison to the bottom RHEED image. h) AFM image of a 15 u.c. thick LBCO (x = 0.18) film on LSAO (001) substrate. Reproduced from Suyolcu *et al.* [79].

Figure 4.1.4. XRD θ-2θ scans for three different bilayers: a) LCCO/LCO, b) LSCO/LCO, and c) LBCO/LCO and d) *c*-axis lattice parameter versus ionic radii of dopants in three different bilayers: LCCO/LCO, LSCO/LCO, and LBCO/LCO. Reproduced from Suyolcu *et al.* [79].

Figure 4.1.5. Transport measurements for three different bilayers. The upper panels show resistance versus temperature for a) LCCO/LCO, b) LSCO/LCO, c) LBCO/LCO, whereas the bottom panels show the real (Re) and imaginary (Im) parts of mutual inductance measurements for d) LCCO/LCO, e) LSCO/LCO, f) LBCO/LCO. Reproduced from Suyolcu *et al.* [79].

Figure 4.1.6. Dependence of T_c on the average *c*-axis lattice parameter. The red squares show the T_c values measured in Ca-, Sr-, and Ba-doped bilayers in the present study, whereas the black circles refer to I–M (La_2CuO_4 / $La_{1.56}Sr_{0.44}CuO_4$), S (superconducting; $La_2CuO_{4+\delta}$), M–I ($La_{1.56}Sr_{0.44}CuO_4$ / La_2CuO_4) and M–S ($La_{1.56}Sr_{0.44}CuO_4$ / $La_2CuO_{4+\delta}$) structures as reported in Ref. [52]. Reproduced from Suyolcu *et al.* [79].

Figure 4.1.7. Atomically resolved STEM imaging and EELS spectrum imaging. a) HAADF image showing the growth quality, a defect-free structure and coherent interfaces of LCCO/LCO. b) High magnification of the area highlighted by the red rectangle in a. In d, f, and h, RGB elemental maps (La = green, Cu = red, dopant = blue) are shown. In e, g and i the Ca-, Sr- and Ba-doped bilayers dopant distributions, as obtained from the maps in (d), (f), and (h), are displayed. Reproduced from Suyolcu *et al.* [79].

Figure 4.1.8. Dopant distribution of the Ba-doped bilayer as a plot of intensity vs. distance obtained from the map in Figure 4.2.2d. The vertical lines indicate the nominal interfaces and dashed lines indicate zero intensity. Reproduced from Suyolcu *et al.* [79].

Figure 4.1.9. Illustration of two different superconductivity mechanisms observed in M–I bilayers: Interface superconductivity (HT-IS; i.e. Sr- and Ca-doping, top) vs. bulk superconductivity (HTSC; i.e. Ba-doping, bottom). Due to different dopant distribution based on the dopant size (i.e. Ca and Sr vs. Ba), different superconducting mechanisms are induced. The turquoise arrows indicate the nominal M–I interface position.

Figure 4.1.10. STEM-HAADF images showing coherent interfaces of a) Ba- (LBCO), b) Sr- (LSCO), and c) Ca- (LCCO) doped bilayers. The HAADF images were taken along the [100] direction of the LSAO substrate. Reproduced from Suyolcu *et al.* [89].

Figure 4.1.11. Atomically resolved EELS spectrum image of the Ba-doped bilayer. a) Simultaneously acquired HAADF image. (b–d) Atomically resolved Cu-L_{23} edge, La-M_{45} edge, and Ba-M_{45} edge elemental maps. The arrows indicate the nominal interface positions. Reproduced from Suyolcu *et al.* [89].

Figure 4.1.12. Atomically resolved EELS spectrum image of the Sr-doped bilayer. a) Simultaneously acquired HAADF image. (b–d) Atomically resolved Cu-$L_{2,3}$ edge, La-$M_{4,5}$ edge, and Sr-$L_{2,3}$ edge elemental maps. The arrows indicate the nominal interface positions. Reproduced from Suyolcu *et al.* [89].

Figure 4.1.13. Atomically resolved EELS spectrum image of the Ca-doped bilayer. a) Simultaneously acquired HAADF image. (b–d) Atomically resolved Cu-L_{23} edge, La-M_{45} edge, and Ca-L_{23} edge elemental maps. The arrows indicate the nominal interface positions. Reproduced from Suyolcu *et al.* [89].

Figure 4.1.14 ABF images showing coherent interfaces and all atomic column positions including O-positions for the a) Ba-, b) Sr-, and c) Ca-doped bilayers. The yellow arrows indicate the nominal interface positions. d) Illustration of measured apical and basal O–O distances on a magnified (and colored) section obtained from (b). Reproduced from Suyolcu *et al.* [89].

Figure 4.1.15 Graphs showing the concentration per CuO_2 block for the a) Ba-, b) Sr-, and c) Ca-doped bilayers. The horizontal dashed lines delimitate the region corresponding to the superconducting phase. (d–f) O–O atomic column spacing along the apical (red) and basal (green) directions for the LBCO/LCO, LSCO/LCO, and LCCO/LCO bilayers, respectively. The yellow arrows indicate the nominal interface positions. The error bars represent the 95% confidence interval (corresponding to 2 times the standard error) of the average of 14 unit cells of LCO along the basal direction. Reproduced from Suyolcu *et al.* [89].

Figure 4.1.16. High-resolution STEM-HAADF image and quantitative analyses of the structural distortion in the Ba-, Sr-, and Ca-doped bilayers: a) representative STEM-HAADF image of LBCO/LCO bilayer given as a guide for the eyes; b), c) and d) La–La atomic column spacings along the basal (green) and apical (red) directions for the Ba-, Sr-, and Ca-doped bilayers, respectively. The error bars represent the 95% confidence interval (corresponding to 2 times the standard error) of the average of 14 unit cells of LCO along the basal direction. Reproduced from Suyolcu *et al.* [89].

Figure 4.1.17. Dependence of local lattice parameter on the cation radii of dopants (i.e. Ba^{2+}, Sr^{2+}, and Ca^{2+}). Reproduced from *Suyolcu et al.* [89].

Figure 4.2.1. a) Resistivity vs temperature curves for Sr (black line), Ba (blue line), Ca (orange line) two-dimensionally doped La_2CuO_4 (N = 9). The resistance values have been normalized by multiplication with the number of superlattice repetitions (M). b) AFM micrograph of Ba δ-doped La_2CuO_4 multilayer indicating the high tendency of secondary phase formation in the structure. Reproduced from *Bauitti et al*. [84].

Figure 4.2.2. HAADF images for a) Ca, b) Sr, and c) Ba δ-doped multilayers. All images exhibit the structural quality of the samples. [84]

Figure 4.2.3. The respective elemental maps and averaged concentration profiles from atomically resolved EELS spectroscopy are shown in (a, b), (c, d), and (e, f) for Ca-, Sr-, and Ba- doping, respectively. Black dashed lines are used as a guide and indicating "0" nm. (g) Average extension, resulting from EELS data analysis, of the, Ca, Sr, and Ba redistribution widths at the upward side (solid diamonds) and at the downward side (open circles) of the interface, as a function of the dopant ionic size mismatch with La. (h) Redistribution width ratio (upward/downward) for Ca-, Sr-, and Ba-two-dimensionally doped La_2CuO_4. Error bars express the standard deviation of the mean. Reproduced from *Bauitti et al*. [84].

Figure 4.2.4. a) HAADF image showing some extended defects originating from Dy-doped area b) HAADF image of Dy two-dimensionally doped La_2CuO_4. c) Dy-L intensity profile acquired by EDX during a linescan across several Dy-containing planes in a defect-free region. Reproduced from *Bauitti et al*. [84].

Figure 4.2.5. a) HAADF image of a Sr δ-doped La_2CuO_4 structure, in which the doped regions (collimated with arrows) have been deposited at gradually decreasing (~35 ºC) temperatures. b) Sr-$L_{2,3}$ EELS profile linescan acquired along the growth direction. The smoothed data (red) is given with the raw data (black) and the error bars are smaller than the symbols. c) The Sr average redistribution length as resulting from EELS analyses for the downward and upward sides of the interface are reported in (b). Reproduced from *Bauitti et al*. [84]. In order to allow for a better comparison, the data have been normalized with respect to the reference values (interfaces grown at 600 ºC).

Figure 4.2.6. a) HAADF image of a Sr δ-doped La_2CuO_4 multilayer grown on LSAT substrate presenting the overview of the sample. White arrows indicate the δ-doped regions and orange arrows indicate the structural defect. b) High magnification of the area highlighted by the blue rectangle in a. c) Sr-$L_{3,2}$ (red) and La-$M_{5,4}$ (green) EELS profile linescans acquired along the growth direction. Black arrows indicate the Sr distribution tendencies on both sides of nominal δ-doping and dashed lines indicate zero intensity.

Figure 4.2.7. (a) Fitting of the Sr concentration profile across the nominally doped interface (marked by the black dotted line). The blue circles represent the Sr experimental profile as retrieved from the STEM-EELS analysis reported in ref 16. At the downward interface side, the experimental data are fitted using a Gaussian function, which simulates the evolution of a delta-dopant profile upon thermal diffusion. At the upward interface side, the fitting curve (green line) stems from the Muraki equation, $x_n = x_0(1 - P)\, P^{n-1}$, with fitting parameters $x_0 = 0.78$ and $P = 0.58$. In particular, the stars represent the resulting concentration of each (La,A)O−(La,A)O−CuO_2 constituting block (labeled with n). In panels b−d, a sketch of the cationic intermixing process based on thermodynamical considerations is shown ("entropic model"). In panel b, the last undoped La_2CuO_4 constituting block (labeled with n = 1) is depicted on the surface of the film, together with the incoming two-dimensionally doped La_2CuO_4 block (n = 2) (note that, for simplicity, the growth process is pictured as "block-by-block" deposition, rather than as the real atomic-layer by atomic-layer). Here the film (excluding the last La_2CuO_4 constituting block) is labeled as "bulk La_2CuO_4". Imposing the equilibrium conditions to be verified between the surface and the incoming block (n = 1 and n = 2) results in the A-cation being equally distributed between these two, as shown in panel c. Afterwards, when the next block (n = 3) is deposited, the situation evolves as follows: n = 1 now pertains to the bulk phase, i.e., is no more involved in the mixing process, whereas the blocks n = 2 and n = 3 share the same A-cation amount in order to establish conditions of thermodynamic equilibrium. The resulting dopant distribution after this iteration is sketched in panel d (for each step, the "active" blocks are highlighted in red). Such a process can be formally described by the Muraki equation having P = 0.5 (dotted green line in panel a, resulting $x_0 = 0.69$). Reproduced from *Bauitti et al.* [84].

Figure 5.1.1: Electrical properties of LCO / LSNO structures. a) Resistance curves as a function of temperature, for a set of superlattices (N = 2.5) having different doping levels x of LSNO. In order to allow for a direct comparison between the curves, the resistance values have been normalized to R (T = 273 K). b) Dependence of T_c on the doping level x for LCO / LSNO superlattices for a set of representative samples (the corresponding R vs T curves are reported in (a)). c) R vs T for LCO (bottom layer) / LSNO (top layer) bilayers and d) R vs T for LSNO (bottom layer) / LCO (top layer) bilayers for representative doping levels x (refer to Figure 5.1.1a for the color legend). Reproduced from Bauitti *et al*. [205].

Figure 5.1.2. Dependence of T_c with the LCO thickness for LCO / LSNO superlattices. a) R vs T curves for 1 x $La_{1.56}Sr_{0.44}CuO_4$ + S x (2.5 x $La_{0.7}Sr_{1.3}NiO_4$ + N x La_2CuO_4) superlattices, for different LCO thicknesses N. b) T_c values as a function of the thickness of the LCO phase N for the $La_{0.7}Sr_{1.3}NiO_4/La_2CuO_4$ superlattices, whose R vs T curves are reported in (a). Reproduced from Bauitti *et al.* [205].

Figure 5.1.3. Low-magnification STEM-HAADF images of (a) x = 0.8 and (b) x = 0.4 LCO/LSNO/LCO trilayers. The images demonstrate the epitaxial quality and the defect-free structures for both samples. Depending on the different doping (i.e. Sr doping) of the samples the image contrasts are different.

Figure 5.1.4. STEM imaging and EDX spectroscopy for LCO / LSNO / LCO trilayers. In panels a) and c), HAADF images of structures in which the doping level of LSNO are x = 0.8 and x = 0.4, respectively, are displayed. EDX linescans for Ni and Sr are shown in panels b (for x = 0.8) and d (x = 0.4). Reproduced from Bauitti *et al.* [205].

Figure 5.1.5. **HR-STEM investigations at the La_2CuO_4 / $La_{0.7}Sr_{1.3}NiO_4$ / La_2CuO_4 interfaces**. a) HAADF image of a the superlattice structure (N = 9). b) Spatial elemental distribution, extracted from the EELS spectrum image across a $La_{0.7}Sr_{1.3}NiO_4$ region and neighboring LCO areas (the analyzed region is highlighted by the orange rectangle in panel (a)). The color code is as follows: La-green, Cu-red, Ni-orange, Sr-blue. c) EDX signal for Sr (blue) and Ni (orange) (top panel), together with the simultaneously acquired O-K edge prepeak profile as obtained by an EELS linescan (red line, bottom panel). The blue and red arrows indicate the upper limits for the Sr and holes distributions, respectively. Reproduced from Bauitti *et al.* [205].

Figure 5.1.6. (a) HAADF image showing the line along which the EELS and EDXS line scan was acquired. (b) Raw EDXS spectrum image. (c) EELS spectrum image of the O-K edge after background subtraction. (d) Oxygen-K edge from different positions as indicated in Figure (a). The intensity of the pre-edge peak has been quantified by multi-Gaussian peak fitting using a non-linear least square (NLLS) routine for all spectra in the line scan profile across several interfaces. Reproduced from Bauitti *et al*. [205].

Figure 5.1.7. Sketch of the thermodynamic situation at the boundary layers of LCO and LSNO (if both are equilibrated with the same oxygen partial pressure and a net transfer of holes and vacancies occurs from LSNO to LCO). a) The condition of thermodynamic equilibrium for the defect species (the abbreviations *v, i, p, n* are used for the building units oxygen vacancies, oxygen interstitials, electrons and holes respectively) and with the external oxygen partial pressure defines a horizontal profile for the electrochemical potential of V ($\tilde{\mu}_V = \mu_V + 2F\varphi$) and p ($\tilde{\mu}\_p = \mu\_p + F\varphi$), as well as for the chemical potential of oxygen $\mu_O = -\mu_V + 2\mu_p$. Therefore, as a consequence of the difference in the bulk chemical potentials for the defect species, the bending of μ_V and μ_p at the interface is expected. b) Resulting charge concentration profiles at the interface. Reproduced from Bauitti *et al*. [205].

Figure 5.2.1. a) Electrical conductivity and b) Seebeck coefficient of superlattices with different individual layer thicknesses, as a function of temperature. Reproduced from Kaya *et al*. [238]

Figure 5.2.2. a), b) and c) low, intermediate and high-magnification HAADF images of the thick-layered sample grown on LSAO substrate, respectively. d) XRD pattern of the sample and e) EDXS line scan profiles of Ni (red) and Cu (blue) along the green arrow in (b) and (c). Reproduced from Kaya *et al*. [238].

Figure 5.2.3. a), b) and c) low-, intermediate- and high-magnification HAADF images of the thin-layered sample grown on LSAO substrate (inset images indicate the corresponding red and green rectangular regions, blue dashed line indicates the 113-structure). d) XRD pattern of the sample and e) EDXS line scan profiles of Ni (red) and Cu (blue) along the green arrow in (b) and (c). Reproduced from Kaya *et al*. [238]

Figure 5.2.4. Seebeck coefficient (blue) and electrical conductivity (black) of superlattices with thick constituent layer as a function of temperature obtained experimentally and calculated by applying the parallel slab model. Reproduced from Kaya *et al*. [238]

Figure 6.1.1. Basic sketches of the (a) thick-LCO (N = 9) and (b) thin-LCO samples (N = 3). Both of the samples are composed of 21 repetitions.

Figure 6.1.2. (a) Low magnification STEM-HAADF images of the thick-LCO SL demonstrate the high-quality epitaxy. (b) STEM-HAADF image intensity profile along the orange arrow in Fig. 1a, averaged along the perpendicular direction. The image intensity indicates the periodicity of the contrast related to the Sr distribution at the interfaces. (c) High-magnification image of the area highlighted by the red rectangle in (a) confirming the structurally coherent 214-113 and 113-214 interfaces.

Figure 6.1.3. (a) Low magnification STEM-HAADF images of the thin-LCO SL demonstrate the high-quality epitaxy. (b) STEM-HAADF image intensity profile along the orange arrow in Fig. 1a, averaged along the perpendicular direction. The image intensity indicates the periodicity of the contrast related to the Sr distribution at the interfaces. (c) High-magnification image of the area highlighted by the red rectangle in (a) confirming the structurally coherent 214-113 and 113-214 interfaces.

Figure 6.1.4. The atomically resolved elemental maps obtained via EELS spectroscopy, are displayed in panels a), b), c) and d) for Sr (blue), La (green), Mn (red), and Cu (cyan) respectively. e) displays the overlay of the three elements. f) shows the Sr distribution profiles across both interfaces. The linear distortion in the experimental spectrum image is corrected via STEM SI Warp software [129] for the Sr profile plot in (f). Please note that, for clarity, the nominal $SrMnO_3$ and Sr δ-doped La_2CuO_4 layers are shaded light-blue.

Figure 6.1.5. a) STEM-ABF image displaying all atomic column positions including O-column positions. b) O–O interatomic distances along basal (in-plane) and apical (out-of-plane) directions exhibit the variations across the interfaces. c) The STEM-HAADF image displays the coherent interfaces and the weaker contrast in the Sr-rich region (1-2 MLs). d) La–La interatomic distances along basal (in-plane) and apical (out-of-plane) directions exhibit the variations across the interfaces. The blue and orange arrows on the images indicate the nominal 214-113 and 113-214 interfaces. The apical and basal distances are indicated with straight and dashed lines, respectively. The error bars give the 95% confidence interval (corresponding to 2 times the standard error) of the average of 14 unit cells of the perovskite lattice along the basal (in-plane) direction.

Figure 7.1.1. (a) Depiction of the $NdNiO_3$ unit cell (black lines) in orthorhombic space group *Pbnm*. The planes corresponding to the [011] –and [101]– cut (α- and β-cut) are indicated in blue and red, respectively. For clarity only one NiO_6 octahedron (gray) is superimposed to the unit cell. (b) Schematic of the interconnectivity of the octahedral network across the epitaxial $NdNiO_3$–$NdGaO_3$ interface. One NiO_6 octahedron (gray) is shown in proximity to the α-cut $NdGaO_3$ substrate surface (blue). Each interfacial $NdNiO_3$ octahedron connects to three $NdGaO_3$ octahedra (black arrows). (c)-(f) Illustration of the in-plane epitaxial strain induced to the $NdNiO_3$ unit cell (gray rectangular) by an underlying $NdGaO_3$ substrate (orange rectangular) for different combinations of α -and β-cuts. The indicated in-plane directions of the projected unit cells lie within the α- and β-planes. Unit cell dimensions are exaggerated for clarity. The numbers are the strain magnitudes along these directions calculated as explained in the text. Note that the effective strains for the growth modes α on α (c) and β on α (f) are closely similar.

Figure 7.1.2. a) STEM-HAADF image of the $NdNiO_3$ thin film with a thickness of 11.4 nm on a [011] oriented $NdGaO_3$ substrate. The image illustrates the high epitaxial quality and the defect-free structure of the film. The inset is a high-resolution STEM-HAADF image of the film-substrate interface region. b) EDS line scan profiles along the [011] growth direction indicated by the yellow arrow presenting the chemical composition of the $NdGaO_3$-$NdNiO_3$ interface. The orange, black, and gray lines correspond to the EDS intensity of the Ga K, Nd L, Ni K, and lines, respectively. Intermixing of Ni and Ga atomic species in the interface region of ~1.5 nm is marked by the shaded area. The interface is defined at 0 nm and the dashed line corresponds to zero intensity of the EDS. c) STEM-LAADF image with $NdNiO_3$ epitaxial layer indicated by the orange arrow. No structural defects and/or structural grains can be detected, substantiating high crystalline quality. The layer on top of $NdNiO_3$ is the glue from the specimen preparation. The blue box represents the dimensions of the STEM-HAADF image in (a).

Figure 7.1.3. a) STEM-HAADF image taken along the epitaxial layer including the substrate/epitaxial layer interface. Blue and green arrows indicate measured out-of-plane and in-plane Nd–Nd interatomic distances, respectively, shown in (b) and (c). d) STEM-ABF image, simultaneously acquired with the STEM-HAADF image in (a), providing the oxygen column positions, and (e) Ni–O–Ni bond angle measurements performed on the ABF image shown in (d). The orange lines and the dashed lines mark the nominal interface in the images and the plots, respectively. The error bars of the bond angle determination (95% confidence interval, corresponding to 2 times the standard error) is less than 1°. The blue and red colored areas are guides for the eye indicating the α- and β-phases, respectively.

Figure 7.1.4. DFT+*U* ground state for different epitaxial configurations depicted in Figure 7.1.1(e-f). a) In-plane lattice constants of $NdNiO_3$ are fixed at the values corresponding to the α-cut $NdGaO_3$, while the $NdNiO_3$ out-of-plane lattice constant is allowed to relax, simulating the effects of epitaxy on an α-$NdGaO_3$ substrate surface. The $NdNiO_3$ in-plane directions are [100] and [01-1], and the out-plane is [011] for the α-phase calculation (blue curve). For the β-phase calculation, in-plane directions are [010] and [-101] and the out-plane direction is [101] (red curve). The global minimum is obtained for the β-phase calculation indicating the energetically most favorable state that corresponds to β-phase $NdNiO_3$ unit cells in epitaxy to the α-phase $NdGaO_3$ substrate. This explains the experimentally observed reorientation of $NdNiO_3$ grown on α-cut $NdGaO_3$. Furthermore, the magnitude of the octahedral breathing distortion in the $NdNiO_3$ β-phase ground state is strongly enhanced which promotes its emergence. b) Analogous calculation to (a), but with $NdNiO_3$ in-plane lattice fixed at values corresponding to β-cut $NdGaO_3$. The global minimum is obtained within the beta-phase calculation suggesting that no reorientation takes place in case $NdNiO_3$ is grown on β-cut $NdGaO_3$.

Symbols and abbreviations

List of most used abbreviations

ABF	Annular bright field
AFM	Atomic force microscopy
ALL	Atomic-layer-by-layer
EDXS	Energy dispersive X-ray spectroscopy
EELS	Electron energy loss spectroscopy
HAADF	High-angle annular dark field
HT-IS	High-temperature interface superconductivity
HTSC	High-temperature superconductivity
LBCO	$La_{2-x}Ba_xCuO_4$
LCO	La_2CuO_4
LCCO	$La_{2-x}Ca_xCuO_4$
LSCO	$La_{2-x}Sr_xCuO_4$
LNO	La_2NiO_4; $LaNiO_3$
LSAO	$LaSrAlO_4$
MBE	Molecular beam epitaxy
MSA	Multivariate statistical analysis
NNO	$NdNiO_3$
NGO	$NdGaO_3$
PCA	Principal component analyses
STEM	Scanning transmission electron microscopy
STO	$SrTiO_3$
TEM	Transmission electron microscopy
TMO	Transition metal oxide
RHEED	Reflection high-energy electron diffraction
XRD	X-ray diffraction

List of most used symbols

$h^{\bullet}$	Electron hole according to the Kröger-Vink notation
δ	Oxygen nonstoichiometry
ρ	Electrical resistivity
n	Electron concentration
P	Pressure
p	Electron hole concentration
T	Temperature
T_c	Superconducting critical temperature
$V_O^{\bullet\bullet}$	Oxygen vacancy according to the Kröger-Vink notation
O_i''	Oxygen interstitial according to the Kröger-Vink notation

Declaration

Hereby I declare that this thesis titled, "Atomic-Scale Control and Characterization of Oxide Heterostructures: Correlating Interfacial Structure and Novel Functionalities" has been independently carried out by me at the Stuttgart Center for Electron Microscopy (StEM), Max Planck Institute for Solid State Research in partial fulfillment of the requirements for the degree of Doctor of Natural Science (Dr. rer. nat.) in Materials Science from the Technical University of Darmstadt (TU Darmstadt). I certify that the work presented in this thesis is, to the best of my knowledge and belief, original and contains no material previously published or written by another person, except where due reference and permission is made.

Stuttgart
13.11.2018

Y. Eren Suyolcu

MAX-PLANCK-GESELLSCHAFT

TECHNISCHE UNIVERSITÄT DARMSTADT

Bibliography

[1] D.G. Schlom, J. Mannhart, Oxide electronics: Interface takes charge over Si, Nat. Mater. 10 (2011) 168–169. doi:10.1038/nmat2965.

[2] J. Mannhart, D.G. Schlom, Oxide Interface - An Opportunity for Electronics, Science. 327 (2010) 1607–1611. doi:10.1126/science.1181862.

[3] P. Zubko, S. Gariglio, M. Gabay, P. Ghosez, J.-M. Triscone, Interface Physics in Complex Oxide Heterostructures, Annu. Rev. Condens. Matter Phys. 2 (2011) 141–165. doi:10.1146/annurev-conmatphys-062910-140445.

[4] H.Y. Hwang, Y. Iwasa, M. Kawasaki, B. Keimer, N. Nagaosa, Y. Tokura, Emergent phenomena at oxide interfaces, Nat. Mater. 11 (2012) 103–113. doi:10.1038/nmat3223.

[5] J.B. Torrance, P. Lacorre, A.I. Nazzal, E.J. Ansaldo, Ch. Niedermayer, Systematic study of insulator-metal transitions in perovskites $RNiO_3$ (R=Pr,Nd,Sm,Eu) due to closing of charge-transfer gap, Phys. Rev. B. 45 (1992) 8209–8212. doi:10.1103/PhysRevB.45.8209.

[6] J. Chakhalian, J.W. Freeland, H.-U. Habermeier, G. Cristiani, G. Khaliullin, M. van Veenendaal, B. Keimer, Orbital Reconstruction and Covalent Bonding at an Oxide Interface, Science. 318 (2007) 1114–1117. doi:10.1126/science.1149338.

[7] S. Jin, M. McCormack, T.H. Tiefel, R. Ramesh, Colossal magnetoresistance in La-Ca-Mn-O ferromagnetic thin films (invited), J. Appl. Phys. 76 (1994) 6929–6933. doi:10.1063/1.358119.

[8] Y. Tokura, Y. Tomioka, Colossal magnetoresistive manganites, J. Magn. Magn. Mater. 200 (1999) 1–23. doi:10.1016/S0304-8853(99)00352-2.

[9] N. Reyren, S. Thiel, A.D. Caviglia, L.F. Kourkoutis, G. Hammerl, C. Richter, C.W. Schneider, T. Kopp, A.-S. Rüetschi, D. Jaccard, M. Gabay, D.A. Muller, J.-M. Triscone, J. Mannhart, Superconducting Interfaces Between Insulating Oxides, Science. 317 (2007) 1196–1199. doi:10.1126/science.1146006.

[10] A. Gozar, G. Logvenov, L.F. Kourkoutis, A.T. Bollinger, L.A. Giannuzzi, D.A. Muller, I. Bozovic, High-temperature interface superconductivity between metallic and insulating copper oxides, Nature. 455 (2008) 782–785. doi:10.1038/nature07293.

[11] C. He, A.J. Grutter, M. Gu, N.D. Browning, Y. Takamura, B.J. Kirby, J.A. Borchers, J.W. Kim, M.R. Fitzsimmons, X. Zhai, V.V. Mehta, F.J. Wong, Y. Suzuki, Interfacial Ferromagnetism and Exchange Bias in $CaRuO_3/CaMnO_3$ Superlattices, Phys. Rev. Lett. 109 (2012) 197202. doi:10.1103/PhysRevLett.109.197202.

[12] A. Ohtomo, H.Y. Hwang, A high-mobility electron gas at the $LaAlO_3/SrTiO_3$ heterointerface, Nature. 427 (2004) 423–426. doi:10.1038/nature02308.

[13] H. Ohta, S. Kim, Y. Mune, T. Mizoguchi, K. Nomura, S. Ohta, T. Nomura, Y. Nakanishi, Y. Ikuhara, M. Hirano, H. Hosono, K. Koumoto, Giant thermoelectric Seebeck coefficient of a two-dimensional electron gas in $SrTiO_3$, Nat. Mater. 6 (2007) 129–134. doi:10.1038/nmat1821.

[14] S.A. Chambers, Epitaxial Growth and Properties of Doped Transition Metal and Complex Oxide Films, Adv. Mater. 22 (2010) 219–248. doi:10.1002/adma.200901867.

[15] D.G. Schlom, L.-Q. Chen, X. Pan, A. Schmehl, M.A. Zurbuchen, A Thin Film Approach to Engineering Functionality into Oxides, J. Am. Ceram. Soc. 91 (2008) 2429–2454. doi:10.1111/j.1551-2916.2008.02556.x.

[16] Y.E. Suyolcu, Y. Wang, W. Sigle, G. Cristiani, G. Logvenov, P.A. van Aken, Linking Dopant Distribution and Interatomic Distortions at $La_{1.6}M_{0.4}CuO_4/La_2CuO_4$ Superconducting Interfaces, Microsc. Microanal. 22 (2016) 308–309. doi:10.1017/S1431927616002397.

[17] J. Maier, Nanoionics: ion transport and electrochemical storage in confined systems, Nat. Mater. 4 (2005) 805–815. doi:10.1038/nmat1513.

[18] R. Ramesh, N.A. Spaldin, Multiferroics: progress and prospects in thin films, Nat. Mater. 6 (2007) nmat1805. doi:10.1038/nmat1805.

[19] V.M. Goldschmidt, Die Gesetze der Krystallochemie, Naturwissenschaften. 14 (1926) 477–485. doi:10.1007/BF01507527.

[20] D. Lee, H.N. Lee, Controlling Oxygen Mobility in Ruddlesden–Popper Oxides, Materials. 10 (2017) 368. doi:10.3390/ma10040368.

[21] J.H. Van Vleck, Theory of the Variations in Paramagnetic Anisotropy Among Different Salts of the Iron Group, Phys. Rev. 41 (1932) 208–215. doi:10.1103/PhysRev.41.208.

[22] Y. Tokura, N. Nagaosa, Orbital Physics in Transition-Metal Oxides, Science. 288 (2000) 462–468. doi:10.1126/science.288.5465.462.

[23] H.A. Jahn, E. Teller, Stability of Polyatomic Molecules in Degenerate Electronic States. I. Orbital Degeneracy, Proc. R. Soc. Lond. Math. Phys. Eng. Sci. 161 (1937) 220–235. doi:10.1098/rspa.1937.0142.

[24] J. Kanamori, Crystal Distortion in Magnetic Compounds, J. Appl. Phys. 31 (1960) S14–S23. doi:10.1063/1.1984590.

[25] M. A. Halcrow, Jahn–Teller distortions in transition metal compounds, and their importance in functional molecular and inorganic materials, Chem. Soc. Rev. 42 (2013) 1784–1795. doi:10.1039/C2CS35253B.

[26] Kamimura, H., Theory of Copper Oxide superconductors, Springer, New York, 2005.

[27] J.B. Boyce, F. Bridges, T. Claeson, T.H. Geballe, C.W. Chu, J.M. Tarascon, X-ray-absorption studies of the high-T_c superconductors $La_{1.8}Sr_{0.2}CuO_4$ and $La_{1.8}Ba_{0.2}CuO_4$, Phys. Rev. B. 35 (1987) 7203–7206. doi:10.1103/PhysRevB.35.7203.

[28] M.W. Lufaso, P.M. Woodward, Jahn–Teller distortions, cation ordering and octahedral tilting in perovskites, Acta Crystallogr. B. 60 (2004) 10–20. doi:10.1107/S0108768103026661.

[29] D. Haskel, V. Polinger, E.A. Stern, Where do the doped holes go in $La_{2-x}Sr_xCuO_4$? A close look by XAFS, in: AIP Conf. Proc., AIP Publishing, 1999: pp. 241–246. doi:10.1063/1.59594.

[30] V. Polinger, D. Haskel, E.A. Stern, Dopant Induced Enhancement of the Jahn–Teller Effect in Perovskite Cuprates, in: M.D. Kaplan, G.O. Zimmerman (Eds.), Vibronic Interact. Jahn–Teller Eff. Cryst. Mol., Springer Netherlands, 2001: pp. 215–219. doi:10.1007/978-94-010-0985-0_23.

[31] K. Shiraishi, Dr. of Science Thesis, University of Tokyo, 1988.

[32] P.G. Radaelli, D.G. Hinks, A.W. Mitchell, B.A. Hunter, J.L. Wagner, B. Dabrowski, K.G. Vandervoort, H.K. Viswanathan, J.D. Jorgensen, Structural and superconducting properties of $La_{2-x}Sr_xCuO_4$ as a function of Sr content, Phys. Rev. B. 49 (1994) 4163–4175. doi:10.1103/PhysRevB.49.4163.

[33] Y. Wang, F. Baiutti, G. Gregori, G. Cristiani, U. Salzberger, G. Logvenov, J. Maier, P.A. van Aken, Atomic-Scale Quantitative Analysis of Lattice Distortions at Interfaces of Two-Dimensionally Sr-Doped La_2CuO_4 Superlattices, ACS Appl. Mater. Interfaces. 8 (2016) 6763–6769. doi:10.1021/acsami.5b12813.

[34] H. Zhou, Y. Yacoby, V.Y. Butko, G. Logvenov, I. Božović, R. Pindak, Anomalous expansion of the copper-apical-oxygen distance in superconducting cuprate bilayers, Proc. Natl. Acad. Sci. 107 (2010) 8103–8107. doi:10.1073/pnas.0914702107.

[35] H. Kamimura, T. Hamada, S. Matsuno, H. Ushio, A Novel Approach to the Polaronic Metallic State of Cuprate Superconductors and the d-Wave Pairing Mechanism, J. Supercond. 15 (2002) 379–385. doi:10.1023/A:1021078415473.

[36] S.-W. Cheong, J.D. Thompson, Z. Fisk, Properties of La_2CuO_4 and related compounds, Phys. C Supercond. 158 (1989) 109–126. doi:10.1016/0921-4534(89)90306-7.

[37] P. Babkevich, D. Prabhakaran, C.D. Frost, A.T. Boothroyd, Magnetic spectrum of the two-dimensional antiferromagnet La_2CoO_4 studied by inelastic neutron scattering, Phys. Rev. B. 82 (2010) 184425. doi:10.1103/PhysRevB.82.184425.

[38] K. Yamada, M. Matsuda, Y. Endoh, B. Keimer, R.J. Birgeneau, S. Onodera, J. Mizusaki, T. Matsuura, G. Shirane, Successive antiferromagnetic phase transitions in single-crystal La_2CoO_4, Phys. Rev. B. 39 (1989) 2336–2343. doi:10.1103/PhysRevB.39.2336.

[39] W. Paulus, A. Cousson, G. Dhalenne, J. Berthon, A. Revcolevschi, S. Hosoya, W. Treutmann, G. Heger, R. Le Toquin, Neutron diffraction studies of stoichiometric and oxygen intercalated La_2NiO_4 single crystals, Solid State Sci. 4 (2002) 565–573. doi:10.1016/S1293-2558(02)01299-2.

[40] J.G. Bednorz, K.A. Müller, Possible high T_c superconductivity in the Ba−La−Cu−O system, Z. Für Phys. B Condens. Matter. 64 (1986) 189–193. doi:10.1007/BF01303701.

[41] A. Schilling, M. Cantoni, J.D. Guo, H.R. Ott, Superconductivity above 130 K in the Hg–Ba–Ca–Cu–O system, Nature. 363 (1993) 56–58. doi:10.1038/363056a0.

[42] C.W. Chu, L. Gao, F. Chen, Z.J. Huang, R.L. Meng, Y.Y. Xue, Superconductivity above 150 K in $HgBa_2Ca_2Cu_3O_{8+\delta}$ at high pressures, Nature. 365 (1993) 323–325. doi:10.1038/365323a0.

[43] L. Gao, Y.Y. Xue, F. Chen, Q. Xiong, R.L. Meng, D. Ramirez, C.W. Chu, J.H. Eggert, H.K. Mao, Superconductivity up to 164 K in $HgBa_2Ca_{m-1}Cu_mO_{2m+2+\delta}$ (m=1, 2, and 3) under quasihydrostatic pressures, Phys. Rev. B. 50 (1994) 4260–4263. doi:10.1103/PhysRevB.50.4260.

[44] B. Keimer, S.A. Kivelson, M.R. Norman, S. Uchida, J. Zaanen, From quantum matter to high-temperature superconductivity in copper oxides, Nature. 518 (2015) 179–186. doi:10.1038/nature14165.

[45] H. Sato, A. Tsukada, M. Naito, A. Matsuda, $La_{2-x}Sr_xCuO_y$ epitaxial thin films (x=0 to 2): Structure, strain, and superconductivity, Phys. Rev. B. 61 (2000) 12447–12456. doi:10.1103/PhysRevB.61.12447.

[46] Y. Ando, S. Komiya, K. Segawa, S. Ono, Y. Kurita, Electronic Phase Diagram of High-T_c Cuprate Superconductors from a Mapping of the In-Plane Resistivity Curvature, Phys. Rev. Lett. 93 (2004) 267001. doi:10.1103/PhysRevLett.93.267001.

[47] L. Taillefer, Scattering and Pairing in Cuprate Superconductors, Annu. Rev. Condens. Matter Phys. 1 (2010) 51–70. doi:10.1146/annurev-conmatphys-070909-104117.

[48] J. Bardeen, L.N. Cooper, J.R. Schrieffer, Theory of Superconductivity, Phys. Rev. 108 (1957) 1175–1204. doi:10.1103/PhysRev.108.1175.

[49] M. Hashimoto, I.M. Vishik, R.-H. He, T.P. Devereaux, Z.-X. Shen, Energy gaps in high-transition-temperature cuprate superconductors, Nat. Phys. 10 (2014) 483–495. doi:10.1038/nphys3009.

[50] H. Keller, A. Bussmann-Holder, K.A. Müller, Jahn–Teller physics and high-T_c superconductivity, Mater. Today. 11 (2008) 38–46. doi:10.1016/S1369-7021(08)70178-0.

[51] G. Logvenov, A. Gozar, I. Bozovic, High-Temperature Superconductivity in a Single Copper-Oxygen Plane, Science. 326 (2009) 699–702. doi:10.1126/science.1178863.

[52] V.Y. Butko, G. Logvenov, N. Božović, Z. Radović, I. Božović, Madelung Strain in Cuprate Superconductors – A Route to Enhancement of the Critical Temperature, Adv. Mater. 21 (2009) 3644–3648. doi:10.1002/adma.200803850.

[53] H. Sato, M. Naito, Increase in the superconducting transition temperature by anisotropic strain effect in (001) $La_{1.85}Sr_{0.15}CuO_4$ thin films on $LaSrAlO_4$ substrates, Phys. C Supercond. 274 (1997) 221–226. doi:10.1016/S0921-4534(96)00675-2.

[54] J.-P. Locquet, J. Perret, J. Fompeyrine, E. Mächler, J.W. Seo, G. Van Tendeloo, Doubling the critical temperature of $La_{1.9}Sr_{0.1}CuO_4$ using epitaxial strain, Nature. 394 (1998) 453–456. doi:10.1038/28810.

[55] F. Baiutti, G. Logvenov, G. Gregori, G. Cristiani, Y. Wang, W. Sigle, P.A. van Aken, J. Maier, High-temperature superconductivity in space-charge regions of lanthanum cuprate induced by two-dimensional doping, Nat. Commun. 6 (2015) 8586. doi:10.1038/ncomms9586.

[56] S. Shinomori, Y. Okimoto, M. Kawasaki, Y. Tokura, Insulator-Metal Transition in $La_{2-x}Sr_xNiO_4$, J. Phys. Soc. Jpn. 71 (2002) 705–708. doi:10.1143/JPSJ.71.705.

[57] P. Briois, F. Perry, A. Billard, Structural and electrical characterisation of lanthanum nickelate reactively sputter-deposited thin films, Thin Solid Films. 516 (2008) 3282–3286. doi:10.1016/j.tsf.2007.08.107.

[58] J. Zhang, A.S. Botana, J.W. Freeland, D. Phelan, H. Zheng, V. Pardo, M.R. Norman, J.F. Mitchell, Large orbital polarization in a metallic square-planar nickelate, Nat. Phys. 13 (2017) 864–869. doi:10.1038/nphys4149.

[59] M.L. Medarde, Structural, magnetic and electronic properties of $RNiO_3$ perovskites (R = rare earth), J. Phys. Condens. Matter. 9 (1997) 1679. doi:10.1088/0953-8984/9/8/003.

[60] F. Wrobel, Structural and electronic properties of nickelate heterostructures, (2016). doi:http://dx.doi.org/10.18419/opus-8924.

[61] F. Baiutti, Heterogeneous doping and superconductivity in La_2CuO_4-based heterostructures, University of Stuttgart, 2015. http://elib.uni-stuttgart.de/handle/11682/6901 (accessed October 28, 2016).

[62] A. Bhattacharya, S.J. May, Magnetic Oxide Heterostructures, Annu. Rev. Mater. Res. 44 (2014) 65–90. doi:10.1146/annurev-matsci-070813-113447.

[63] P. Ravindran, A. Kjekshus, H. Fjellvåg, A. Delin, O. Eriksson, Ground-state and excited-state properties of $LaMnO_3$ from full-potential calculations, Phys. Rev. B. 65 (2002) 064445. doi:10.1103/PhysRevB.65.064445.

[64] I. Loa, P. Adler, A. Grzechnik, K. Syassen, U. Schwarz, M. Hanfland, G.Kh. Rozenberg, P. Gorodetsky, M.P. Pasternak, Pressure-Induced Quenching of the Jahn–Teller Distortion and Insulator-to-Metal Transition in $LaMnO_3$, Phys. Rev. Lett. 87 (2001) 125501. doi:10.1103/PhysRevLett.87.125501.

[65] H. Chen, A.J. Millis, Phase diagram of $Sr_{1-x}Ba_xMnO_3$ as a function of chemical doping, epitaxial strain, and external pressure, Phys. Rev. B. 94 (2016) 165106. doi:10.1103/PhysRevB.94.165106.

[66] J.J. Adkin, M.A. Hayward, $BaMnO_{3-x}$ Revisited: A Structural and Magnetic Study, Chem. Mater. 19 (2007) 755–762. doi:10.1021/cm062055r.

[67] Y. Syono, S. Akimoto, K. Kohn, Structure Relations of Hexagonal Perovskite-Like Compounds ABX_3 at High Pressure, J. Phys. Soc. Jpn. 26 (1969) 993–999. doi:10.1143/JPSJ.26.993.

[68] R. Søndenå, P. Ravindran, S. Stølen, T. Grande, M. Hanfland, Electronic structure and magnetic properties of cubic and hexagonal $SrMnO_3$, Phys. Rev. B. 74 (2006) 144102. doi:10.1103/PhysRevB.74.144102.

[69] K.R. Poeppelmeier, M.E. Leonowicz, J.C. Scanlon, J.M. Longo, W.B. Yelon, Structure determination of $CaMnO_3$ and $CaMnO_{2.5}$ by X-ray and neutron methods, J. Solid State Chem. 45 (1982) 71–79. doi:10.1016/0022-4596(82)90292-4.

[70] P.W. Anderson, Antiferromagnetism. Theory of Superexchange Interaction, Phys. Rev. 79 (1950) 350–356. doi:10.1103/PhysRev.79.350.

[71] J.B. Goodenough, Theory of the Role of Covalence in the Perovskite-Type Manganites [La, *M*(II)]MnO_3, Phys. Rev. 100 (1955) 564–573. doi:10.1103/PhysRev.100.564.

[72] C. Zener, Interaction between the d-Shells in the Transition Metals. II. Ferromagnetic Compounds of Manganese with Perovskite Structure, Phys. Rev. 82 (1951) 403–405. doi:10.1103/PhysRev.82.403.

[73] N. Nguyen, J. Choisnet, M. Hervieu, B. Raveau, Oxygen defect K_2NiF_4-type oxides: The compounds $La_{2-x}Sr_xCuO_{4-x/2+\delta}$, J. Solid State Chem. 39 (1981) 120–127. doi:10.1016/0022-4596(81)90310-8.

[74] J. Maier, G. Pfundtner, Defect chemistry of the high-T_c superconductors, Adv. Mater. 3 (1991) 292–297. doi:10.1002/adma.19910030605.

[75] L. Shen, P. Salvador, T.O. Mason, K. Fueki, High temperature electrical properties and defect chemistry of $La_{2-x}Ca_xCuO_{4-y}$ superconductors—II. Defect structure modeling, J. Phys. Chem. Solids. 57 (1996) 1977–1987. doi:10.1016/S0022-3697(95)00324-X.

[76] A.R. Moodenbaugh, Y. Xu, M. Suenaga, T.J. Folkerts, R.N. Shelton, Superconducting properties of $La_{2-x}Ba_xCuO$, Phys. Rev. B. 38 (1988) 4596–4600. doi:10.1103/PhysRevB.38.4596.

[77] A.R. Moodenbaugh, R.L. Sabatini, Y. Xu, J. Ochab, J.G. Huber, Solubility of Ca in superconducting $La_{2-x}Ca_xCuO_4$, Phys. C Supercond. 198 (1992) 103–108. doi:10.1016/0921-4534(92)90272-E.

[78] J. Maier, Physical Chemistry of Ionic Materials: Ions and Electrons in Solids, John Wiley & Sons, Ltd, Chichester, UK, 2004. doi:10.1002/0470020229.

[79] Y.E. Suyolcu, Y. Wang, F. Baiutti, A. Al-Temimy, G. Gregori, G. Cristiani, W. Sigle, J. Maier, P.A. van Aken, G. Logvenov, Dopant size effects on novel functionalities: High-temperature interfacial superconductivity, Sci. Rep. 7 (2017) 453. doi:10.1038/s41598-017-00539-4.

[80] J.B. Torrance, Y. Tokura, A.I. Nazzal, A. Bezinge, T.C. Huang, S.S.P. Parkin, Anomalous Disappearance of High-T_c Superconductivity at High Hole Concentration in Metallic $La_{2-x}Sr_xCuO_4$, Phys. Rev. Lett. 61 (1988) 1127–1130. doi:10.1103/PhysRevLett.61.1127.

[81] D.E. Rice, D.J. Buttrey, An X-Ray Diffraction Study of the Oxygen Content Phase Diagram of $La_2NiO_{4+\delta}$, J. Solid State Chem. 105 (1993) 197–210. doi:10.1006/jssc.1993.1208.

[82] J.P. Tang, R.I. Dass, A. Manthiram, Comparison of the crystal chemistry and electrical properties of $La_{2-x}A_xNiO_4$ (A = Ca, Sr, and Ba), Mater. Res. Bull. 35 (2000) 411–424. doi:10.1016/S0025-5408(00)00234-8.

[83] J. Maier, Space charge regions in solid two-phase systems and their conduction contribution-I. Conductance enhancement in the system ionic conductor-'inert' phase and application on AgC1:Al_2O_3 and AgC1:SiO_2, J. Phys. Chem. Solids. 46 (1985) 309–320. doi:10.1016/0022-3697(85)90172-6.

[84] F. Baiutti, G. Gregori, Y. Wang, Y.E. Suyolcu, G. Cristiani, P.A. van Aken, J. Maier, G. Logvenov, Cationic Redistribution at Epitaxial Interfaces in Superconducting Two-Dimensionally Doped Lanthanum Cuprate Films, ACS Appl. Mater. Interfaces. 8 (2016) 27368–27375. doi:10.1021/acsami.6b09739.

[85] F. Wrobel, A.F. Mark, G. Christiani, W. Sigle, H.-U. Habermeier, P.A. van Aken, G. Logvenov, B. Keimer, E. Benckiser, Comparative study of $LaNiO_3/LaAlO_3$ heterostructures grown by pulsed laser deposition and oxide molecular beam epitaxy, Appl. Phys. Lett. 110 (2017) 041606. doi:10.1063/1.4975005.

[86] D.G. Schlom, L.-Q. Chen, C.-B. Eom, K.M. Rabe, S.K. Streiffer, J.-M. Triscone, Strain Tuning of Ferroelectric Thin Films, Annu. Rev. Mater. Res. 37 (2007) 589–626. doi:10.1146/annurev.matsci.37.061206.113016.

[87] I. Bozovic, G. Logvenov, I. Belca, B. Narimbetov, I. Sveklo, Epitaxial Strain and Superconductivity in $La_{2-x}Sr_xCuO_4$ Thin Films, Phys. Rev. Lett. 89 (2002) 107001. doi:10.1103/PhysRevLett.89.107001.

[88] C.L. Jia, X.H. Zeng, X.X. Xi, K. Urban, Microstructure and residual strain in La_2CuO_4 thin

films on $LaSrAlO_4$-buffered $SrTiO_3$ substrates, Phys. Rev. B. 64 (2001) 075416. doi:10.1103/PhysRevB.64.075416.

[89] Y.E. Suyolcu, Y. Wang, W. Sigle, F. Baiutti, G. Cristiani, G. Logvenov, J. Maier, P.A. van Aken, Octahedral Distortions at High-Temperature Superconducting La_2CuO_4 Interfaces: Visualizing Jahn–Teller Effects, Adv. Mater. Interfaces. 4 (2017) 1700737. doi:10.1002/admi.201700737.

[90] D.G. Schlom, J.N. Eckstein, E.S. Hellman, S.K. Streiffer, J.S. Harris, M.R. Beasley, J.C. Bravman, T.H. Geballe, C. Webb, K.E. von Dessonneck, F. Turner, Molecular beam epitaxy of layered Dy- Ba- Cu- O compounds, Appl. Phys. Lett. 53 (1988) 1660–1662. doi:10.1063/1.100443.

[91] M.G. Lagally, D.E. Savage, Quantitative Electron Diffraction from Thin Films, MRS Bull. 18 (1993) 24–31. doi:10.1557/S0883769400043414.

[92] G.J.H.M. Rijnders, G. Koster, D.H.A. Blank, H. Rogalla, In situ monitoring during pulsed laser deposition of complex oxides using reflection high energy electron diffraction under high oxygen pressure, Appl. Phys. Lett. 70 (1997) 1888–1890. doi:10.1063/1.118687.

[93] T. Terashima, Y. Bando, K. Iijima, K. Yamamoto, K. Hirata, K. Hayashi, K. Kamigaki, H. Terauchi, Reflection high-energy electron diffraction oscillations during epitaxial growth of high-temperature superconducting oxides, Phys. Rev. Lett. 65 (1990) 2684–2687. doi:10.1103/PhysRevLett.65.2684.

[94] I. Bozovic, J.N. Eckstein, Analysis of Growing Films of Complex Oxides by RHEED, MRS Bull. 20 (1995) 32–38. doi:10.1557/S0883769400044870.

[95] W. Braun, Monitoring surface roughness during film growth using modulated RHEED intensity oscillations, J. Cryst. Growth. 477 (2017) 34–39. doi:10.1016/j.jcrysgro.2016.12.082.

[96] R.D. Shannon, Revised effective ionic radii and systematic studies of interatomic distances in halides and chalcogenides, Acta Crystallogr. Sect. A. 32 (1976) 751–767. doi:10.1107/S0567739476001551.

[97] G. Kim, G. Christiani, G. Logvenov, S. Choi, H.-H. Kim, M. Minola, B. Keimer, Selective formation of apical oxygen vacancies in $La_{2-x}Sr_xCuO_4$, Phys. Rev. Mater. 1 (2017) 054801. doi:10.1103/PhysRevMaterials.1.054801.

[98] Y.E. Suyolcu, G. Cristiani, P.A. van Aken, G. Logvenov, Understanding of the surface reconstruction during epitaxial growth of $(LaSr)_2CuO_4$ thin films, (unpublished results).

[99] W. Lee, J.W. Han, Y. Chen, Z. Cai, B. Yildiz, Cation Size Mismatch and Charge Interactions Drive Dopant Segregation at the Surfaces of Manganite Perovskites, J. Am. Chem. Soc. 135 (2013) 7909–7925. doi:10.1021/ja3125349.

[100] C.B. Carter, D.B. Williams, eds., Transmission Electron Microscopy, Springer International Publishing, Cham, 2016. doi:10.1007/978-3-319-26651-0.

[101] S.J. Pennycook, P.D. Nellist, eds., Scanning Transmission Electron Microscopy, Springer New York, New York, NY, 2011. doi:10.1007/978-1-4419-7200-2.

[102] Allied High Tech - MultiPrep™ Polishing System - 8", (n.d.). http://www.alliedhightech.com/Equipment/multiprep-polishing-system-8 (accessed February 9, 2017).

[103] T. Malis, S.C. Cheng, R.F. Egerton, EELS log-ratio technique for specimen-thickness measurement in the TEM, J. Electron Microsc. Tech. 8 (1988) 193–200. doi:10.1002/jemt.1060080206.

[104] M. Haider, S. Uhlemann, E. Schwan, H. Rose, B. Kabius, K. Urban, Electron microscopy image enhanced, Nature. 392 (1998) 768–769. doi:10.1038/33823.

[105] S.J. Pennycook, D.E. Jesson, High-resolution incoherent imaging of crystals, Phys. Rev. Lett. 64 (1990) 938–941. doi:10.1103/PhysRevLett.64.938.

[106] S.D. Findlay, N. Shibata, H. Sawada, E. Okunishi, Y. Kondo, T. Yamamoto, Y. Ikuhara, Robust

atomic resolution imaging of light elements using scanning transmission electron microscopy, Appl. Phys. Lett. 95 (2009) 191913. doi:10.1063/1.3265946.

[107] E. Okunishi, I. Ishikawa, H. Sawada, F. Hosokawa, M. Hori, Y. Kondo, Visualization of Light Elements at Ultrahigh Resolution by STEM Annular Bright Field Microscopy, Microsc. Microanal. 15 (2009) 164–165. doi:10.1017/S1431927609093891.

[108] S.D. Findlay, N. Shibata, H. Sawada, E. Okunishi, Y. Kondo, Y. Ikuhara, Dynamics of annular bright field imaging in scanning transmission electron microscopy, Ultramicroscopy. 110 (2010) 903–923. doi:10.1016/j.ultramic.2010.04.004.

[109] Z. Yu, D.A. Muller, J. Silcox, Study of strain fields at a-Si/c-Si interface, J. Appl. Phys. 95 (2004) 3362–3371. doi:10.1063/1.1649463.

[110] S.J. Pennycook, Z-contrast stem for materials science, Ultramicroscopy. 30 (1989) 58–69. doi:10.1016/0304-3991(89)90173-3.

[111] S.E. Maccagnano-Zacher, K.A. Mkhoyan, E.J. Kirkland, J. Silcox, Effects of tilt on high-resolution ADF-STEM imaging, Ultramicroscopy. 108 (2008) 718–726. doi:10.1016/j.ultramic.2007.11.003.

[112] J.T. Held, S. Duncan, K.A. Mkhoyan, Effects of small-angle mistilts on dopant visibility in ADF-STEM imaging of nanocrystals, Ultramicroscopy. 177 (2017) 53–57. doi:10.1016/j.ultramic.2017.03.008.

[113] K.A. Mkhoyan, S.E. Maccagnano-Zacher, E.J. Kirkland, J. Silcox, Effects of amorphous layers on ADF-STEM imaging, Ultramicroscopy. 108 (2008) 791–803. doi:10.1016/j.ultramic.2008.01.007.

[114] L. Jones, H. Yang, T.J. Pennycook, M.S.J. Marshall, S.V. Aert, N.D. Browning, M.R. Castell, P.D. Nellist, Smart Align—a new tool for robust non-rigid registration of scanning microscope data, Adv. Struct. Chem. Imaging. 1 (2015) 8. doi:10.1186/s40679-015-0008-4.

[115] L. Jones, S. Wenner, M. Nord, P.H. Ninive, O.M. Løvvik, R. Holmestad, P.D. Nellist, Optimising multi-frame ADF-STEM for high-precision atomic-resolution strain mapping, Ultramicroscopy. 179 (2017) 57–62. doi:10.1016/j.ultramic.2017.04.007.

[116] D. Zhou, K. Müller-Caspary, W. Sigle, F.F. Krause, A. Rosenauer, P.A. van Aken, Sample tilt effects on atom column position determination in ABF–STEM imaging, Ultramicroscopy. 160 (2016) 110–117. doi:10.1016/j.ultramic.2015.10.008.

[117] P. Gao, A. Kumamoto, R. Ishikawa, N. Lugg, N. Shibata, Y. Ikuhara, Picometer-scale atom position analysis in annular bright-field STEM imaging, Ultramicroscopy. 184 (2018) 177–187. doi:10.1016/j.ultramic.2017.09.001.

[118] Q.M. Ramasse, F.S. Hage, D.M. Kepaptsoglou, P. Abellan, J. Yates, R.J. Nicholls, H.C. Nerl, V. Nicolosi, K. Winther, K. Thygesen, P.Z.E. Khoury, W.P. Hess, F. Azough, R. Freer, Recent Applications of Sub-20meV Monochromated STEM-EELS: from Phonon to Core Losses in Real and Momentum Spaces, Microsc. Microanal. 22 (2016) 964–965. doi:10.1017/S1431927616005663.

[119] W. Sigle, Analytical Transmission Electron Microscopy, Annu. Rev. Mater. Res. 35 (2005) 239–314. doi:10.1146/annurev.matsci.35.102303.091623.

[120] R. Brydson, N. Hondow, Electron Energy Loss Spectrometry and Energy Dispersive X-ray Analysis, in: R. Brydson (Ed.), Aberration-Corrected Anal. Transm. Electron Microsc., John Wiley & Sons, Ltd, 2011: pp. 163–210. doi:10.1002/9781119978848.ch7.

[121] R.F. Egerton, Electron energy-loss spectroscopy in the TEM, Rep. Prog. Phys. 72 (2009) 016502. doi:10.1088/0034-4885/72/1/016502.

[122] The use of MLLS fitting approach to resolve overlapping edges in the EELS spectrum at the atomic level | Gatan, Inc., (n.d.). http://www.gatan.com/use-mlls-fitting-approach-resolve-overlapping-edges-eels-spectrum-atomic-level (accessed August 22, 2016).

[123] Y. Wang, M.R.S. Huang, U. Salzberger, K. Hahn, W. Sigle, P.A. van Aken, Towards atomically

resolved EELS elemental and fine structure mapping via multi-frame and energy-offset correction spectroscopy, Ultramicroscopy. 184 (2018) 98–105. doi:10.1016/j.ultramic.2017.10.014.

[124] M. Bosman, M. Watanabe, D.T.L. Alexander, V.J. Keast, Mapping chemical and bonding information using multivariate analysis of electron energy-loss spectrum images, Ultramicroscopy. 106 (2006) 1024–1032. doi:10.1016/j.ultramic.2006.04.016.

[125] Y. Wang, U. Salzberger, W. Sigle, Y. Eren Suyolcu, P.A. van Aken, Oxygen octahedra picker: A software tool to extract quantitative information from STEM images, Ultramicroscopy. 168 (2016) 46–52. doi:10.1016/j.ultramic.2016.06.001.

[126] C. Ophus, J. Ciston, C.T. Nelson, Correcting nonlinear drift distortion of scanning probe and scanning transmission electron microscopies from image pairs with orthogonal scan directions, Ultramicroscopy. 162 (2016) 1–9. doi:10.1016/j.ultramic.2015.12.002.

[127] A.B. Yankovich, C. Zhang, A. Oh, T.J.A. Slater, F. Azough, R. Freer, S.J. Haigh, R. Willett, P.M. Voyles, Non-rigid registration and non-local principle component analysis to improve electron microscopy spectrum images, Nanotechnology. 27 (2016) 364001. doi:10.1088/0957-4484/27/36/364001.

[128] J.S. Jeong, K.A. Mkhoyan, Improving Signal-to-Noise Ratio in Scanning Transmission Electron Microscopy Energy-Dispersive X-Ray (STEM-EDX) Spectrum Images Using Single-Atomic-Column Cross-Correlation Averaging, Microsc. Microanal. 22 (2016) 536–543. doi:10.1017/S1431927616000635.

[129] Y. Wang, Y.E. Suyolcu, U. Salzberger, K. Hahn, V. Srot, W. Sigle, V. Aken, P. A, Correcting the linear and nonlinear distortions for atomically resolved STEM spectrum and diffraction imaging, Microscopy. 67 (2018) i114–i122. doi:10.1093/jmicro/dfy002.

[130] A. Tsukazaki, A. Ohtomo, T. Kita, Y. Ohno, H. Ohno, M. Kawasaki, Quantum Hall Effect in Polar Oxide Heterostructures, Science. 315 (2007) 1388–1391. doi:10.1126/science.1137430.

[131] A. Brinkman, M. Huijben, M. van Zalk, J. Huijben, U. Zeitler, J.C. Maan, W.G. van der Wiel, G. Rijnders, D.H.A. Blank, H. Hilgenkamp, Magnetic effects at the interface between non-magnetic oxides, Nat. Mater. 6 (2007) 493–496. doi:10.1038/nmat1931.

[132] J. Biscaras, N. Bergeal, A. Kushwaha, T. Wolf, A. Rastogi, R.C. Budhani, J. Lesueur, Two-dimensional superconductivity at a Mott insulator/band insulator interface $LaTiO_3/SrTiO_3$, Nat. Commun. 1 (2010) 89. doi:10.1038/ncomms1084.

[133] C.H. Ahn, J.-M. Triscone, J. Mannhart, Electric field effect in correlated oxide systems, Nature. 424 (2003) 1015–1018. doi:10.1038/nature01878.

[134] G. Logvenov, V.V. Butko, C. DevilleCavellin, J. Seo, A. Gozar, I. Bozovic, Engineering interfaces in cuprate superconductors, Phys. B Condens. Matter. 403 (2008) 1149–1150. doi:10.1016/j.physb.2007.10.351.

[135] V.M. Loktev, Yu.G. Pogorelov, Model for modulated electronic configurations in selectively doped multilayered La_2CuO_4 nanostructures, Phys. Rev. B. 78 (2008) 180501. doi:10.1103/PhysRevB.78.180501.

[136] S. Smadici, J.C.T. Lee, S. Wang, P. Abbamonte, G. Logvenov, A. Gozar, C.D. Cavellin, I. Bozovic, Superconducting Transition at 38 K in Insulating-Overdoped La_2CuO_4-$La_{1.64}Sr_{0.36}CuO_4$ Superlattices: Evidence for Interface Electronic Redistribution from Resonant Soft X-Ray Scattering, Phys. Rev. Lett. 102 (2009) 107004. doi:10.1103/PhysRevLett.102.107004.

[137] A. Suter, E. Morenzoni, T. Prokscha, B.M. Wojek, H. Luetkens, G. Nieuwenhuys, A. Gozar, G. Logvenov, I. Božović, Two-Dimensional Magnetic and Superconducting Phases in Metal-Insulator $La_{2-x}Sr_xCuO_4$ Superlattices Measured by Muon-Spin Rotation, Phys. Rev. Lett. 106 (2011) 237003. doi:10.1103/PhysRevLett.106.237003.

[138] E. Stilp, A. Suter, T. Prokscha, E. Morenzoni, H. Keller, B.M. Wojek, H. Luetkens, A. Gozar, G. Logvenov, I. Božović, Magnetic phase diagram of low-doped $La_{2-x}Sr_xCuO_4$ thin films studied by

low-energy muon-spin rotation., Phys. Rev. B. 88 (2013) 064419. doi:10.1103/PhysRevB.88.064419.

[139] Y. Yacoby, H. Zhou, R. Pindak, I. Božović, Atomic-layer synthesis and imaging uncover broken inversion symmetry in $La_{2-x}Sr_xCuO_4$ films, Phys. Rev. B. 87 (2013) 014108. doi:10.1103/PhysRevB.87.014108.

[140] J. Wu, O. Pelleg, G. Logvenov, A.T. Bollinger, Y.-J. Sun, G.S. Boebinger, M. Vanević, Z. Radović, I. Božović, Anomalous independence of interface superconductivity from carrier density, Nat. Mater. 12 (2013) 877–881. doi:10.1038/nmat3719.

[141] V.A. Gasparov, I. Božović, Complex conductance of ultrathin $La_{2-x}Sr_xCuO_4$ films and heterostructures, Low Temp. Phys. 41 (2015) 965–970. doi:10.1063/1.4935694.

[142] C. Panagopoulos, M. Majoros, T. Nishizaki, H. Iwasaki, Weak Magnetic Order in the Normal State of the High-Tc Superconductor $La_{2-x}Sr_xCuO_4$, Phys. Rev. Lett. 96 (2006) 047002. doi:10.1103/PhysRevLett.96.047002.

[143] G. Logvenov, A. Gozar, V.Y. Butko, A.T. Bollinger, N. Bozovic, Z. Radovic, I. Bozovic, Comprehensive study of high-T_c interface superconductivity, J. Phys. Chem. Solids. 71 (2010) 1098–1104. doi:10.1016/j.jpcs.2010.03.014.

[144] A.T. Bollinger, G. Dubuis, J. Yoon, D. Pavuna, J. Misewich, I. Božović, Superconductor-insulator transition in $La_{2-x}Sr_xCuO_4$ at the pair quantum resistance, Nature. 472 (2011) 458–460. doi:10.1038/nature09998.

[145] J. Pereiro, A.T. Bollinger, G. Logvenov, A. Gozar, C. Panagopoulos, I. Božović, Insights from the study of high-temperature interface superconductivity, Philos. Trans. R. Soc. Lond. Math. Phys. Eng. Sci. 370 (2012) 4890–4903. doi:10.1098/rsta.2012.0219.

[146] G. Logvenov, A. Gozar, I. Bozovic, High Temperature Interface Superconductivity, J. Supercond. Nov. Magn. 26 (2013) 2863–2865. doi:10.1007/s10948-013-2215-3.

[147] I. Bozovic, C. Ahn, A new frontier for superconductivity, Nat. Phys. 10 (2014) 892–895. doi:10.1038/nphys3177.

[148] A. Gozar, I. Bozovic, High temperature interface superconductivity, Phys. C Supercond. Its Appl. 521–522 (2016) 38–49. doi:10.1016/j.physc.2016.01.003.

[149] H. Sato, A. Tsukada, M. Naito, A. Matsuda, Absence of 1/8 anomaly in strained thin films of $La_{2-x}Ba_xCuO_4$, Phys. Rev. B. 62 (2000) R799–R802. doi:10.1103/PhysRevB.62.R799.

[150] F. Baiutti, G. Cristiani, G. Logvenov, Towards precise defect control in layered oxide structures by using oxide molecular beam epitaxy, Beilstein J Nanotechnol. 5 (2014) 596–602. doi:10.3762/bjnano.5.70.

[151] R. Aso, D. Kan, Y. Shimakawa, H. Kurata, Control of Structural Distortions in Transition-Metal Oxide Films through Oxygen Displacement at the Heterointerface, Adv. Funct. Mater. 24 (2014) 5177–5184. doi:10.1002/adfm.201303521.

[152] D. Kan, R. Aso, R. Sato, M. Haruta, H. Kurata, Y. Shimakawa, Tuning magnetic anisotropy by interfacially engineering the oxygen coordination environment in a transition metal oxide, Nat. Mater. 15 (2016) 432–437. doi:10.1038/nmat4580.

[153] Z. Liao, M. Huijben, Z. Zhong, N. Gauquelin, S. Macke, R.J. Green, S. Van Aert, J. Verbeeck, G. Van Tendeloo, K. Held, G.A. Sawatzky, G. Koster, G. Rijnders, Controlled lateral anisotropy in correlated manganite heterostructures by interface-engineered oxygen octahedral coupling, Nat. Mater. 15 (2016) 425–431. doi:10.1038/nmat4579.

[154] Y.-M. Kim, A. Kumar, A. Hatt, A.N. Morozovska, A. Tselev, M.D. Biegalski, I. Ivanov, E.A. Eliseev, S.J. Pennycook, J.M. Rondinelli, S.V. Kalinin, A.Y. Borisevich, Interplay of Octahedral Tilts and Polar Order in $BiFeO_3$ Films, Adv. Mater. 25 (2013) 2497–2504. doi:10.1002/adma.201204584.

[155] S.D. Findlay, Y. Kohno, L.A. Cardamone, Y. Ikuhara, N. Shibata, Enhanced light element imaging in atomic resolution scanning transmission electron microscopy, Ultramicroscopy. 136 (2014)

31–41. doi:10.1016/j.ultramic.2013.07.019.

[156] E. Bousquet, M. Dawber, N. Stucki, C. Lichtensteiger, P. Hermet, S. Gariglio, J.-M. Triscone, P. Ghosez, Improper ferroelectricity in perovskite oxide artificial superlattices, Nature. 452 (2008) 732–736. doi:10.1038/nature06817.

[157] E.J. Moon, R. Colby, Q. Wang, E. Karapetrova, C.M. Schlepütz, M.R. Fitzsimmons, S.J. May, Spatial control of functional properties via octahedral modulations in complex oxide superlattices, Nat. Commun. 5 (2014) 5710. doi:10.1038/ncomms6710.

[158] S.H. Chang, Y.J. Chang, S.Y. Jang, D.W. Jeong, C.U. Jung, Y.-J. Kim, J.-S. Chung, T.W. Noh, Thickness-dependent structural phase transition of strained $SrRuO_3$ ultrathin films: The role of octahedral tilt, Phys. Rev. B. 84 (2011) 104101. doi:10.1103/PhysRevB.84.104101.

[159] R. Aso, D. Kan, Y. Fujiyoshi, Y. Shimakawa, H. Kurata, Strong Dependence of Oxygen Octahedral Distortions in $SrRuO_3$ Films on Types of Substrate-Induced Epitaxial Strain, Cryst. Growth Des. 14 (2014) 6478–6485. doi:10.1021/cg501340e.

[160] D. Kan, R. Aso, H. Kurata, Y. Shimakawa, Phase control of a perovskite transition-metal oxide through oxygen displacement at the heterointerface, Dalton Trans. 44 (2015) 10594–10607. doi:10.1039/C4DT03749A.

[161] Z. Liao, Z. Li, J. Zhu, Coupling Between Strain and Oxygen Octahedral Distortions in Epitaxially Strained $GdScO_3/SrTiO_3$ Heterostructure, J. Am. Ceram. Soc. (2016) n/a-n/a. doi:10.1111/jace.14371.

[162] D. Mihailovic, Inter-site Pair Superconductivity: Origins and Recent Validation Experiments, in: A. Bussmann-Holder, H. Keller, A. Bianconi (Eds.), High-T_c Copp. Oxide Supercond. Relat. Nov. Mater., Springer International Publishing, 2017: pp. 201–212. doi:10.1007/978-3-319-52675-1_16.

[163] E.F. Schubert, Delta doping of III–V compound semiconductors: Fundamentals and device applications, J. Vac. Sci. Technol. Vac. Surf. Films. 8 (1990) 2980–2996. doi:10.1116/1.576617.

[164] J.S. Kim, S.S.A. Seo, M.F. Chisholm, R.K. Kremer, H.-U. Habermeier, B. Keimer, H.N. Lee, Nonlinear Hall effect and multichannel conduction in $LaTiO_3/SrTiO_3$ superlattices, Phys. Rev. B. 82 (2010) 201407. doi:10.1103/PhysRevB.82.201407.

[165] K. Nishio, M. Matvejeff, R. Takahashi, M. Lippmaa, M. Sumiya, H. Yoshikawa, K. Kobayashi, Y. Yamashita, Delta-doped epitaxial La:$SrTiO_3$ field-effect transistor, Appl. Phys. Lett. 98 (2011) 242113. doi:10.1063/1.3600782.

[166] S. Stemmer, S.J. Allen, Two-Dimensional Electron Gases at Complex Oxide Interfaces, Annu. Rev. Mater. Res. 44 (2014) 151–171. doi:10.1146/annurev-matsci-070813-113552.

[167] D.G. Ouellette, P. Moetakef, T.A. Cain, J.Y. Zhang, S. Stemmer, D. Emin, S.J. Allen, High-density Two-Dimensional Small Polaron Gas in a Delta-Doped Mott Insulator, Sci. Rep. 3 (2013) srep03284. doi:10.1038/srep03284.

[168] Y. Kozuka, M. Kim, C. Bell, B.G. Kim, Y. Hikita, H.Y. Hwang, Two-dimensional normal-state quantum oscillations in a superconducting heterostructure, Nature. 462 (2009) 487–490. doi:10.1038/nature08566.

[169] B. Jalan, S. Stemmer, S. Mack, S.J. Allen, Two-dimensional electron gas in δ-doped $SrTiO_3$, Phys. Rev. B. 82 (2010) 081103. doi:10.1103/PhysRevB.82.081103.

[170] Y. Kozuka, M. Kim, H. Ohta, Y. Hikita, C. Bell, H.Y. Hwang, Enhancing the electron mobility via delta-doping in $SrTiO_3$, Appl. Phys. Lett. 97 (2010) 222115. doi:10.1063/1.3524198.

[171] J. Maier, Ionic conduction in space charge regions, Prog. Solid State Chem. 23 (1995) 171–263. doi:10.1016/0079-6786(95)00004-E.

[172] J.M. Moison, C. Guille, F. Houzay, F. Barthe, M. Van Rompay, Surface segregation of third-column atoms in group III-V arsenide compounds: Ternary alloys and heterostructures, Phys. Rev. B. 40 (1989) 6149–6162. doi:10.1103/PhysRevB.40.6149.

[173] K. Muraki, S. Fukatsu, Y. Shiraki, R. Ito, Surface segregation of In atoms during molecular beam epitaxy and its influence on the energy levels in InGaAs/GaAs quantum wells, Appl. Phys. Lett. 61 (1992) 557–559. doi:10.1063/1.107835.

[174] M. Gibert, M. Viret, A. Torres-Pardo, C. Piamonteze, P. Zubko, N. Jaouen, J.-M. Tonnerre, A. Mougin, J. Fowlie, S. Catalano, A. Gloter, O. Stéphan, J.-M. Triscone, Interfacial Control of Magnetic Properties at $LaMnO_3/LaNiO_3$ Interfaces, Nano Lett. 15 (2015) 7355–7361. doi:10.1021/acs.nanolett.5b02720.

[175] L.F. Kourkoutis, D.A. Muller, Y. Hotta, H.Y. Hwang, Asymmetric interface profiles in $LaVO_3/SrTiO_3$ heterostructures grown by pulsed laser deposition, Appl. Phys. Lett. 91 (2007) 163101. doi:10.1063/1.2798060.

[176] S.J. May, A.B. Shah, S.G.E. te Velthuis, M.R. Fitzsimmons, J.M. Zuo, X. Zhai, J.N. Eckstein, S.D. Bader, A. Bhattacharya, Magnetically asymmetric interfaces in a $LaMnO_3/SrMnO_3$ superlattice due to structural asymmetries, Phys. Rev. B. 77 (2008) 174409. doi:10.1103/PhysRevB.77.174409.

[177] O. Dehaese, X. Wallart, F. Mollot, Kinetic model of element III segregation during molecular beam epitaxy of III- III'- V semiconductor compounds, Appl. Phys. Lett. 66 (1995) 52–54. doi:10.1063/1.114180.

[178] Y.N. Drozdov, N.V. Baidus', B.N. Zvonkov, M.N. Drozdov, O.I. Khrykin, V.I. Shashkin, Segregation of indium in InGaAs/GaAs quantum wells grown by vapor-phase epitaxy, Semiconductors. 37 (2003) 194–199. doi:10.1134/1.1548664.

[179] J. Massies, F. Turco, A. Saletes, J.P. Contour, Experimental evidence of difference in surface and bulk compositions of $Al_xGa_{1-x}As$, Al_xIn_{1-x} As and $Ga_xIn_{1-x}As$ epitaxial layers grown by molecular beam epitaxy, J. Cryst. Growth. 80 (1987) 307–314. doi:10.1016/0022-0248(87)90076-5.

[180] E.L. Pankratov, Dynamics of δ-dopant redistribution during heterostructure growth, Eur. Phys. J. B. 57 (2007) 251–256. doi:10.1140/epjb/e2007-00173-8.

[181] N. Nakagawa, H.Y. Hwang, D.A. Muller, Why some interfaces cannot be sharp, Nat. Mater. 5 (2006) 204–209. doi:10.1038/nmat1569.

[182] P.R. Willmott, S.A. Pauli, R. Herger, C.M. Schlepütz, D. Martoccia, B.D. Patterson, B. Delley, R. Clarke, D. Kumah, C. Cionca, Y. Yacoby, Structural Basis for the Conducting Interface between $LaAlO_3$ and $SrTiO_3$, Phys. Rev. Lett. 99 (2007) 155502. doi:10.1103/PhysRevLett.99.155502.

[183] M. Luysberg, M. Heidelmann, L. Houben, M. Boese, T. Heeg, J. Schubert, M. Roeckerath, Intermixing and charge neutrality at $DyScO_3/SrTiO_3$ interfaces, Acta Mater. 57 (2009) 3192–3198. doi:10.1016/j.actamat.2009.03.031.

[184] S.A. Chambers, M.H. Engelhard, V. Shutthanandan, Z. Zhu, T.C. Droubay, L. Qiao, P.V. Sushko, T. Feng, H.D. Lee, T. Gustafsson, E. Garfunkel, A.B. Shah, J.-M. Zuo, Q.M. Ramasse, Instability, intermixing and electronic structure at the epitaxial $LaAlO_3/SrTiO_3(001)$ heterojunction, Surf. Sci. Rep. 65 (2010) 317–352. doi:10.1016/j.surfrep.2010.09.001.

[185] R. Colby, L. Qiao, K.H.L. Zhang, V. Shutthanandan, J. Ciston, B. Kabius, S.A. Chambers, Cation intermixing and electronic deviations at the insulating $LaCrO_3/SrTiO_3(001)$ interface, Phys. Rev. B. 88 (2013) 155325. doi:10.1103/PhysRevB.88.155325.

[186] S. Kim, R. Merkle, J. Maier, Oxygen nonstoichiometry of nanosized ceria powder, Surf. Sci. 549 (2004) 196–202. doi:10.1016/j.susc.2003.12.002.

[187] R.A. De Souza, J. Zehnpfenning, M. Martin, J. Maier, Determining oxygen isotope profiles in oxides with Time-of-Flight SIMS, Solid State Ion. 176 (2005) 1465–1471. doi:10.1016/j.ssi.2005.03.012.

[188] R.A. De Souza, V. Metlenko, D. Park, T.E. Weirich, Behavior of oxygen vacancies in single-crystal $SrTiO_3$: Equilibrium distribution and diffusion kinetics, Phys. Rev. B. 85 (2012) 174109. doi:10.1103/PhysRevB.85.174109.

[189] S. Miyazawa, Y. Sekiguchi, Low-Temperature Molecular Beam Epitaxy Growth of Single Quantum Well GaAs/AlGaAs Lasers, Jpn. J. Appl. Phys. 30 (1991) L921. doi:10.1143/JJAP.30.L921.

[190] M. Naito, H. Yamamoto, H. Sato, Reflection high-energy electron diffraction and atomic force microscopy studies on homoepitaxial growth of $SrTiO_3$(001), Phys. C Supercond. 305 (1998) 233–250. doi:10.1016/S0921-4534(98)00338-4.

[191] N. Čebašek, R. Haugsrud, T. Norby, Cation transport in Sr and Cu substituted $La_2NiO_{4+\delta}$ studied by inter-diffusion, Solid State Ion. 254 (2014) 32–39. doi:10.1016/j.ssi.2013.10.041.

[192] N. Čebašek, R. Haugsrud, T. Norby, Determination of inter-diffusion coefficients for the A- and B-site in the $A_2BO_{4+\delta}$ (A = La, Nd and B = Ni, Cu) system, Solid State Ion. 231 (2013) 74–80. doi:10.1016/j.ssi.2012.11.002.

[193] U. Aschauer, R. Pfenninger, S.M. Selbach, T. Grande, N.A. Spaldin, Strain-controlled oxygen vacancy formation and ordering in $CaMnO_3$, Phys. Rev. B. 88 (2013) 054111. doi:10.1103/PhysRevB.88.054111.

[194] D.M. Kienzle, L.D. Marks, Surface transmission electron diffraction for $SrTiO_3$ surfaces, CrystEngComm. 14 (2012) 7833–7839. doi:10.1039/C2CE25204J.

[195] S. Gerhold, M. Riva, B. Yildiz, M. Schmid, U. Diebold, Adjusting island density and morphology of the $SrTiO_3$(110)-(4×1) surface: Pulsed laser deposition combined with scanning tunneling microscopy, Surf. Sci. 651 (2016) 76–83. doi:10.1016/j.susc.2016.03.010.

[196] C. Noguera, Polar oxide surfaces, J. Phys. Condens. Matter. 12 (2000) R367. doi:10.1088/0953-8984/12/31/201.

[197] A. Tschöpe, Grain size-dependent electrical conductivity of polycrystalline cerium oxide II: Space charge model, Solid State Ion. 139 (2001) 267–280. doi:10.1016/S0167-2738(01)00677-4.

[198] C.-C. Chen, L. Fu, J. Maier, Synergistic, ultrafast mass storage and removal in artificial mixed conductors, Nature. 536 (2016) 159–164. doi:10.1038/nature19078.

[199] E. Navickas, Y. Chen, Q. Lu, W. Wallisch, T.M. Huber, J. Bernardi, M. Stöger-Pollach, G. Friedbacher, H. Hutter, B. Yildiz, J. Fleig, Dislocations Accelerate Oxygen Ion Diffusion in $La_{0.8}Sr_{0.2}MnO_3$ Epitaxial Thin Films, ACS Nano. 11 (2017) 11475–11487. doi:10.1021/acsnano.7b06228.

[200] P. Lupetin, G. Gregori, J. Maier, Mesoscopic Charge Carriers Chemistry in Nanocrystalline $SrTiO_3$, Angew. Chem. Int. Ed. 49 (2010) 10123–10126. doi:10.1002/anie.201003917.

[201] K.K. Adepalli, M. Kelsch, R. Merkle, J. Maier, Influence of Line Defects on the Electrical Properties of Single Crystal TiO_2, Adv. Funct. Mater. 23 (2013) 1798–1806. doi:10.1002/adfm.201202256.

[202] G. Gregori, R. Merkle, J. Maier, Ion conduction and redistribution at grain boundaries in oxide systems, Prog. Mater. Sci. 89 (2017) 252–305. doi:10.1016/j.pmatsci.2017.04.009.

[203] S. Smadici, J.C.T. Lee, J. Morales, G. Logvenov, O. Pelleg, I. Bozovic, Y. Zhu, P. Abbamonte, Graded orbital occupation near interfaces in a La_2NiO_4-La_2CuO_4 superlattice, Phys. Rev. B. 84 (2011) 155411. doi:10.1103/PhysRevB.84.155411.

[204] E.J. Opila, H.L. Tuller, B.J. Wuensch, J. Maier, Oxygen Tracer Diffusion in $La_{2-x}Sr_xCuO_{4-y}$ Single Crystals, J. Am. Ceram. Soc. 76 (1993) 2363–2369. doi:10.1111/j.1151-2916.1993.tb07778.x.

[205] F. Baiutti, G. Gregori, Y. E. Suyolcu, Y. Wang, G. Cristiani, W. Sigle, P.A. van Aken, G. Logvenov, J. Maier, High-temperature superconductivity at the lanthanum cuprate/lanthanum–strontium nickelate interface, Nanoscale. 10 (2018) 8712–8720. doi:10.1039/C8NR00885J.

[206] G.D. Liu, Z.X. Zhao, G.C. Che, A possible mechanism for the effect of impurities in the CuO_2 plane of high T_c superconductors, Solid State Commun. 109 (1999) 495–499. doi:10.1016/S0038-1098(98)00591-2.

[207] M. Matsuura, M. Fujita, H. Hiraka, M. Kofu, H. Kimura, S. Wakimoto, T.G. Perring, C.D. Frost, K. Yamada, Ni-substitution effects on the spin dynamics and superconductivity in $La_{1.85}Sr_{0.15}CuO_4$, Phys. Rev. B. 86 (2012) 134529. doi:10.1103/PhysRevB.86.134529.

[208] A. Ohtomo, D.A. Muller, J.L. Grazul, H.Y. Hwang, Artificial charge-modulationin atomic-scale perovskite titanate superlattices, Nature. 419 (2002) 378–380. doi:10.1038/nature00977.

[209] F. Gunkel, R. Waser, A.H.H. Ramadan, R.A. De Souza, S. Hoffmann-Eifert, R. Dittmann, Space charges and defect concentration profiles at complex oxide interfaces, Phys. Rev. B. 93 (2016) 245431. doi:10.1103/PhysRevB.93.245431.

[210] F. Gunkel, C. Bell, H. Inoue, B. Kim, A.G. Swartz, T.A. Merz, Y. Hikita, S. Harashima, H.K. Sato, M. Minohara, S. Hoffmann-Eifert, R. Dittmann, H.Y. Hwang, Defect Control of Conventional and Anomalous Electron Transport at Complex Oxide Interfaces, Phys. Rev. X. 6 (2016) 031035. doi:10.1103/PhysRevX.6.031035.

[211] X. He, A. Gozar, R. Sundling, I. Božović, High-precision measurement of magnetic penetration depth in superconducting films, Rev. Sci. Instrum. 87 (2016). doi:10.1063/1.4967004.

[212] K.F. Garrity, First-principles search for *n*-type oxide, nitride, and sulfide thermoelectrics, Phys. Rev. B. 94 (2016) 045122. doi:10.1103/PhysRevB.94.045122.

[213] J. He, Y. Liu, R. Funahashi, Oxide thermoelectrics: The challenges, progress, and outlook, J. Mater. Res. 26 (2011) 1762–1772. doi:10.1557/jmr.2011.108.

[214] I. Terasaki, Y. Sasago, K. Uchinokura, Large thermoelectric power in $NaCo_2O_4$ single crystals, Phys. Rev. B. 56 (1997) R12685–R12687. doi:10.1103/PhysRevB.56.R12685.

[215] D.M. Rowe, CRC Handbook of Thermoelectrics, CRC Press, 1995.

[216] I. Pallecchi, F. Telesio, D. Li, A. Fête, S. Gariglio, J.-M. Triscone, A. Filippetti, P. Delugas, V. Fiorentini, D. Marré, Giant oscillating thermopower at oxide interfaces, Nat. Commun. 6 (2015) 6678. doi:10.1038/ncomms7678.

[217] J. Ravichandran, A.K. Yadav, W. Siemons, M.A. McGuire, V. Wu, A. Vailionis, A. Majumdar, R. Ramesh, Size effects on thermoelectricity in a strongly correlated oxide, Phys. Rev. B. 85 (2012) 085112. doi:10.1103/PhysRevB.85.085112.

[218] P. Brinks, G. Rijnders, M. Huijben, Size effects on thermoelectric behavior of ultrathin Na_xCoO_2 films, Appl. Phys. Lett. 105 (2014) 193902. doi:10.1063/1.4901447.

[219] P. Yordanov, P. Wochner, S. Ibrahimkutty, C. Dietl, F. Wrobel, R. Felici, G. Gregori, J. Maier, B. Keimer, H.-U. Habermeier, Perovskite substrates boost the thermopower of cobaltate thin films at high temperatures, Appl. Phys. Lett. 110 (2017) 253101. doi:10.1063/1.4986778.

[220] K. Fischer, C. Stoiber, A. Kyarad, H. Lengfellner, Anisotropic thermopower in tilted metallic multilayer structures, Appl. Phys. A. 78 (2004) 323–326. doi:10.1007/s00339-003-2326-y.

[221] S. Heinze, H.-U. Habermeier, G. Cristiani, S. Blanco Canosa, M. Le Tacon, B. Keimer, Thermoelectric properties of $YBa_2Cu_3O_{7-\delta}$–$La_{2/3}Ca_{1/3}MnO_3$ superlattices, Appl. Phys. Lett. 101 (2012) 131603. doi:10.1063/1.4754707.

[222] A. Wold, B. Post, E. Banks, Rare Earth Nickel Oxides, J. Am. Chem. Soc. 79 (1957) 4911–4913. doi:10.1021/ja01575a022.

[223] N. Nguyen, F. Studer, B. Raveau, Oxydes ternaires de cuivre a valence mixte de type K_2NiF_4 deficitaires en oxygene:Evolution progressive d'un etat semi-conducteur vers un etat semi-metallique des oxydes $La_{2-x}Sr_xCuO_{4-x/2+\delta}$, J. Phys. Chem. Solids. 44 (1983) 389–400. doi:10.1016/0022-3697(83)90066-5.

[224] A.P. Gonçalves, I.C. Santos, E.B. Lopes, R.T. Henriques, M. Almeida, M.O. Figueiredo, Transport properties of the oxides $Y_{1-x}Pr_xBa_2Cu_3O_{7-\delta}$ ($0 \leq x \leq 1$): Effects of band filling and lattice distortion on superconductivity, Phys. Rev. B. 37 (1988) 7476–7481. doi:10.1103/PhysRevB.37.7476.

[225] A.P.G. Kutty, S.N. Vaidya, Effect of pressure on the thermoelectric power and resistivity of some high-T_c oxides, High Temp. High Press. 20 (1988) 475–478.

[226] W.J. Macklin, P.T. Moseley, On the use of oxides for thermoelectric refrigeration, Mater. Sci. Eng. B. 7 (1990) 111–117. doi:10.1016/0921-5107(90)90015-4.

[227] S.I. Seok, D.S. Park, S.J. Park, The effect of Cu-sites doping on electrical properties of La_2CuO_4 as thermoelectric material, J. Mater. Sci. Mater. Electron. 6 (1995) 140–143. doi:10.1007/BF00190544.

[228] A.A. Sattar, K.M. El-Shokrofy, A.M. Samy, I. Kashif, A.A. Ghani, High-temperature anomalies of the electrical resistivity and thermoelectric power in $La_{(2-x)}R_xCuO_4$ (R = Y and Fe; x = 0.0 and 0.05), J. Phys. Appl. Phys. 30 (1997) 266. doi:10.1088/0022-3727/30/2/013.

[229] J.E. Rodriguez, YBCO samples as a possible thermoelectric material, in: 2005: pp. 3605–3608. doi:10.1002/pssc.200461769.

[230] Y. Liu, Y.-H. Lin, B.-P. Zhang, H.-M. Zhu, C.-W. Nan, J. Lan, J.-F. Li, High-Temperature Thermoelectric Properties in the $La_{2-x}R_xCuO_4$ (R: Pr, Y, Nb) Ceramics, J. Am. Ceram. Soc. 92 (2009) 934–937. doi:10.1111/j.1551-2916.2009.02952.x.

[231] Y. Horiuchi, W. Tamura, T. Fujii, I. Terasaki, In-plane thermoelectric properties of heavily underdoped high-temperature superconductor $Bi_2Sr_2CaCu_2O_{8+\delta}$, Supercond. Sci. Technol. 23 (2010) 065018. doi:10.1088/0953-2048/23/6/065018.

[232] N. Gayathri, A.K. Raychaudhuri, X.Q. Xu, J.L. Peng, R.L. Greene, Electronic conduction in $LaNiO_{3-x}$: the dependence on the oxygen stoichiometry x, J. Phys. Condens. Matter. 10 (1998) 1323. doi:10.1088/0953-8984/10/6/015.

[233] J. Maier, Physical Chemistry of Ionic Materials: Ions and Electrons in Solids, 1 edition, Wiley, Chichester ; Hoboken, NJ, 2004.

[234] H.Y. Hwang, Perovskites: Oxygen vacancies shine blue, Nat. Mater. 4 (2005) 803–804. doi:10.1038/nmat1515.

[235] Z. Xu, K. Jin, L. Gu, Y. Jin, C. Ge, C. Wang, H. Guo, H. Lu, R. Zhao, G. Yang, Evidence for a Crucial Role Played by Oxygen Vacancies in $LaMnO_3$ Resistive Switching Memories, Small. 8 (2012) 1279–1284. doi:10.1002/smll.201101796.

[236] M. Crespin, P. Levitz, L. Gatineau, Reduced forms of $LaNiO_3$ perovskite. Part 1.—Evidence for new phases: $La_2Ni_2O_5$ and $LaNiO_2$, J. Chem. Soc. Faraday Trans. 2 Mol. Chem. Phys. 79 (1983) 1181–1194. doi:10.1039/F29837901181.

[237] Lisauskas, V, Vengalis, B., Sliuziene, K., Pyragas, V., Epitaxial Growth and Oxygen Nonstoichiometry of Magnetron–Sputtered Conductive $LaNiO_{3-\delta}$ Thin Films, Phys. Chem. Solid State. (2008) 350.

[238] P. Kaya, G. Gregori, F. Baiutti, P. Yordanov, Y.E. Suyolcu, G. Cristiani, F. Wrobel, E. Benckiser, B. Keimer, P.A. van Aken, H.-U. Habermeier, G. Logvenov, J. Maier, High-Temperature Thermoelectricity in $LaNiO_3$–La_2CuO_4 Heterostructures, ACS Appl. Mater. Interfaces. (2018). doi:10.1021/acsami.8b02153.

[239] F. Wrobel, B. Geisler, Y. Wang, G. Christiani, G. Logvenov, M. Bluschke, E. Schierle, P.A. van Aken, B. Keimer, R. Pentcheva, E. Benckiser, Digital modulation of the nickel valence state in a cuprate-nickelate heterostructure, Phys. Rev. Mater. 2 (2018) 035001. doi:10.1103/PhysRevMaterials.2.035001.

[240] J.-Y. Tak, S.-M. Choi, W.-S. Seo, H.K. Cho, Thermoelectric properties of a doped $LaNiO_3$ perovskite system prepared using a spark-plasma sintering process, Electron. Mater. Lett. 9 (2013) 513–516. doi:10.1007/s13391-013-0034-0.

[241] N. Kieda, S. Nishiyama, K. Shinozaki, N. Mizutani, Nonstoichiometry and electrical properties of La_2CuO_4 and $La_2(Cu, Ni)O_4$, Solid State Ion. 49 (1991) 85–88. doi:10.1016/0167-2738(91)90072-J.

[242] I. Terasaki, High-temperature oxide thermoelectrics, J. Appl. Phys. 110 (2011) 053705. doi:10.1063/1.3626459.

[243] A. Frano, S. Blanco-Canosa, E. Schierle, Y. Lu, M. Wu, M. Bluschke, M. Minola, G. Christiani, H.U. Habermeier, G. Logvenov, Y. Wang, P.A. van Aken, E. Benckiser, E. Weschke, M. Le Tacon, B. Keimer, Long-range charge-density-wave proximity effect at cuprate/manganate interfaces, Nat. Mater. 15 (2016) 831–834. doi:10.1038/nmat4682.

[244] G.M. De Luca, G. Ghiringhelli, C.A. Perroni, V. Cataudella, F. Chiarella, C. Cantoni, A.R. Lupini, N.B. Brookes, M. Huijben, G. Koster, G. Rijnders, M. Salluzzo, Ubiquitous long-range antiferromagnetic coupling across the interface between superconducting and ferromagnetic oxides, Nat. Commun. 5 (2014) 5626. doi:10.1038/ncomms6626.

[245] G. Kim, Y. Khaydukov, M. Bluschke, Y.E. Suyolcu, G. Cristiani, E. Weschke, K. Son, C. Dietl, T. Keller, P.A. van Aken, G. Logvenov, B. Keimer, Tunable perpendicular exchange bias in oxide heterostructures, Phys. Rev. Mater. (2019).

[246] P.G. Radaelli, G. Iannone, M. Marezio, H.Y. Hwang, S.-W. Cheong, J.D. Jorgensen, D.N. Argyriou, Structural effects on the magnetic and transport properties of perovskite $A_{1-x}A'_xMnO_3$ (x=0.25, 0.30), Phys. Rev. B. 56 (1997) 8265–8276. doi:10.1103/PhysRevB.56.8265.

[247] G.H. Jonker, J.H. Van Santen, Ferromagnetic compounds of manganese with perovskite structure, Physica. 16 (1950) 337–349. doi:10.1016/0031-8914(50)90033-4.

[248] A. Bhattacharya, S.J. May, S.G.E. te Velthuis, M. Warusawithana, X. Zhai, B. Jiang, J.-M. Zuo, M.R. Fitzsimmons, S.D. Bader, J.N. Eckstein, Metal-Insulator Transition and Its Relation to Magnetic Structure in $(LaMnO_3)_{2n}/(SrMnO_3)_n$ Superlattices, Phys. Rev. Lett. 100 (2008) 257203. doi:10.1103/PhysRevLett.100.257203.

[249] A.B. Shah, Q.M. Ramasse, S.J. May, J. Kavich, J.G. Wen, X. Zhai, J.N. Eckstein, J. Freeland, A. Bhattacharya, J.M. Zuo, Presence and spatial distribution of interfacial electronic states in $LaMnO_3$-$SrMnO_3$ superlattices, Phys. Rev. B. 82 (2010) 115112. doi:10.1103/PhysRevB.82.115112.

[250] M. Lorenz, M.S.R. Rao, T. Venkatesan, E. Fortunato, P. Barquinha, R. Branquinho, D. Salgueiro, R Martins, E. Carlos, A. Liu, F.K. Shan, M. Grundmann, H. Boschker, J. Mukherjee, M. Priyadarshini, N. DasGupta, D.J. Rogers, F.H. Teherani, E.V. Sandana, P. Bove, K. Rietwyk, A. Zaban, A. Veziridis, A. Weidenkaff, M. Muralidhar, M Murakami, S. Abel, J. Fompeyrine, J. Zuniga-Perez, R. Ramesh, N.A. Spaldin, S. Ostanin, V. Borisov, I. Mertig, V Lazenka, G. Srinivasan, W. Prellier, M. Uchida, M. Kawasaki, R. Pentcheva, P. Gegenwart, F.M. Granozio, J Fontcuberta, N. Pryds, The 2016 oxide electronic materials and oxide interfaces roadmap, J. Phys. Appl. Phys. 49 (2016) 433001. doi:10.1088/0022-3727/49/43/433001.

[251] M. Imada, Metal-insulator transitions, Rev. Mod. Phys. 70 (1998) 1039–1263. doi:10.1103/RevModPhys.70.1039.

[252] A. Vailionis, H. Boschker, W. Siemons, E.P. Houwman, D.H.A. Blank, G. Rijnders, G. Koster, Misfit strain accommodation in epitaxial ABO_3 perovskites: Lattice rotations and lattice modulations, Phys. Rev. B. 83 (2011) 064101. doi:10.1103/PhysRevB.83.064101.

[253] R. Scherwitzl, P. Zubko, I.G. Lezama, S. Ono, A.F. Morpurgo, G. Catalan, J.-M. Triscone, Electric-Field Control of the Metal-Insulator Transition in Ultrathin $NdNiO_3$ Films, Adv. Mater. 22 (2010) 5517–5520. doi:10.1002/adma.201003241.

[254] H.Y. Qi, M.K. Kinyanjui, J. Biskupek, D. Geiger, E. Benckiser, H.-U. Habermeier, B. Keimer, U. Kaiser, Local octahedral rotations and octahedral connectivity in epitaxially strained $LaNiO_3/LaGaO_3$ superlattices, J. Mater. Sci. 50 (2015) 5300–5306. doi:10.1007/s10853-015-9077-y.

[255] J.Y. Zhang, H. Kim, E. Mikheev, A.J. Hauser, S. Stemmer, Key role of lattice symmetry in the metal-insulator transition of $NdNiO_3$ films, Sci. Rep. 6 (2016) 23652. doi:10.1038/srep23652.

[256] K. Hirai, R. Aso, Y. Ozaki, D. Kan, M. Haruta, N. Ichikawa, H. Kurata, Y. Shimakawa, Melting of Oxygen Vacancy Order at Oxide–Heterostructure Interface, ACS Appl. Mater. Interfaces. (2017).

doi:10.1021/acsami.7b08134.

[257] Z. Liao, R.J. Green, N. Gauquelin, S. Macke, L. Li, J. Gonnissen, R. Sutarto, E.P. Houwman, Z. Zhong, S. Van Aert, J. Verbeeck, G.A. Sawatzky, M. Huijben, G. Koster, G. Rijnders, Long-Range Domain Structure and Symmetry Engineering by Interfacial Oxygen Octahedral Coupling at Heterostructure Interface, Adv. Funct. Mater. 26 (2016) 6627–6634. doi:10.1002/adfm.201602155.

[258] G. Catalan, Progress in perovskite nickelate research, Phase Transit. 81 (2008) 729–749. doi:10.1080/01411590801992463.

[259] U. Staub, G.I. Meijer, F. Fauth, R. Allenspach, J.G. Bednorz, J. Karpinski, S.M. Kazakov, L. Paolasini, F. d'Acapito, Direct Observation of Charge Order in an Epitaxial $NdNiO_3$ Film, Phys. Rev. Lett. 88 (2002) 126402. doi:10.1103/PhysRevLett.88.126402.

[260] S. Catalano, M. Gibert, V. Bisogni, F. He, R. Sutarto, M. Viret, P. Zubko, R. Scherwitzl, G.A. Sawatzky, T. Schmitt, J.-M. Triscone, Tailoring the electronic transitions of $NdNiO_3$ films through (111)pc oriented interfaces, APL Mater. 3 (2015) 062506. doi:10.1063/1.4919803.

[261] L. Vasylechko, L. Akselrud, W. Morgenroth, U. Bismayer, A. Matkovskii, D. Savytskii, The crystal structure of $NdGaO_3$ at 100 K and 293 K based on synchrotron data, J. Alloys Compd. 1–2 (2000) 46–52. doi:10.1016/S0925-8388(99)00603-9.

[262] J.L. García-Muñoz, M.A.G. Aranda, J.A. Alonso, M.J. Martínez-Lope, Structure and charge order in the antiferromagnetic band-insulating phase of $NdNiO_3$, Phys. Rev. B. 79 (2009) 134432. doi:10.1103/PhysRevB.79.134432.

[263] J. Varignon, M.N. Grisolia, J. Íñiguez, A. Barthélémy, M. Bibes, Complete phase diagram of rare-earth nickelates from first-principles, Npj Quantum Mater. 2 (2017) 21. doi:10.1038/s41535-017-0024-9.

[264] A. Hampel, C. Ederer, Interplay between breathing mode distortion and magnetic order in rare-earth nickelates $RNiO_3$ within DFT+*U*, Phys. Rev. B. 96 (2017) 165130. doi:10.1103/PhysRevB.96.165130.

[265] A. Vailionis, H. Boschker, Z. Liao, J.R.A. Smit, G. Rijnders, M. Huijben, G. Koster, Symmetry and lattice mismatch induced strain accommodation near and away from correlated perovskite interfaces, Appl. Phys. Lett. 105 (2014) 131906. doi:10.1063/1.4896969.

[266] Y.E. Suyolcu, Y. Wang, F. Baiutti, W. Sigle, G. Cristiani, G. Gregori, G. Logvenov, J. Maier, P.A. van Aken, Aberration-Corrected Scanning Transmission Electron Microscopy of La_2CuO_4-based Superconducting Interfaces at the Stuttgart Center for Electron Microscopy, JEOL News. 53 (2018) 8–17.

[267] M. Hepting, R.J. Green, Z. Zhong, M. Bluschke, Y.E. Suyolcu, S. Macke, A. Frano, S. Catalano, M. Gibert, R. Sutarto, F. He, G. Cristiani, G. Logvenov, Y. Wang, P.A. van Aken, P. Hansmann, M.L. Tacon, J.-M. Triscone, G.A. Sawatzky, B. Keimer, E. Benckiser, Complex magnetic order in nickelate slabs, Nat. Phys. (2018) 1. doi:10.1038/s41567-018-0218-5.

This page intentionally left blank